

Statistical Photoionization Theory of Atoms in Soft XUV Free-Electron Laser Fields

A thesis submitted for the degree of
Doctor of Philosophy (PhD)

Dublin City University
(DCU)
School of Physical Sciences

Military University of Technology
(MUT)
Institute of Optoelectronics



Tejaswi Katravulapally

B.Tech, M.Sc.

Supervisors:

Dr. Lampros Nikolopoulos

Dr. hab.inz Karol Janulewicz

February 2021



Statistical Photoionization Theory of Atoms in Soft XUV Free-Electron Laser Fields

Thesis presented by

Tejaswi Katravulapally

B.Tech, M.Sc.

Dr. Lampros Nikolopoulos
(Promoter)
Dublin City University

Dr. hab.inz Karol Janulewicz
(Co-Promoter)
Military University of Technology

Doctoral Studies Panel Membership:

Dr. Lampros Nikolopoulos

Dr. hab.inz Karol Janulewicz

Erasmus Mundus Joint Doctorate, EXTATIC

February 2021



Declaration

I hereby certify that this material, which I now submit for assessment on the programme of study leading to the award of Doctor of Philosophy is entirely my own work, and that I have exercised reasonable care to ensure that the work is original, and does not to the best of my knowledge breach any law of copyright, and has not been taken from the work of others save and to the extent that such work has been cited and acknowledged within the text of my work.

Signed: Tejanus (Candidate)
ID No.: 16212552
Date: February 3, 2021

Dedication

To my father who always encourages me in the pursuit of my dreams,
To my mother who is ever caring and loving,
To my wife who is literally my better half,
To my cute little daughter Varali who brought a new dimension into my life,
And to my beloved Master E.K.

Acknowledgements

I would like to first thank my supervisor Dr. Lampros Nikolopoulos who not only guided the direction of my research and encouraged me to explore new domains but also even entertained my unplanned knocks on his office door for any conceptual discussions. Without his moral support and necessary guidance in the times of need, my life in Dublin would not have been as smooth. I would like to thank Prof. John Costello, for his ever cheerful and enriching insights during the group discussions and other times. I thank the whole school of physics at DCU for providing with necessary means to pursue my research.

I would like to thank Dr. hab.inz Karol Janulewicz for his support and guidance during the period of my mobility stay at MUT. I am grateful for the academic suggestions given by Prof. Henryk Fiedorowicz which added a necessary push to the work. I also thank the whole team of Institute of Optoelectronics at MUT for hosting my mobility there and providing me with necessary research means.

I would like to thank William and Cathal for their help in the early stages of my work. I would like to thank my colleagues Adam and Andrew who brought vibrance to the office time by bringing up intriguing question-answer sessions. I would like to thank Muhammad, Sadaf, Hu Lu, Aris, Ismail (MUT) and other post-grads who were always ready to help. I would like to thank Ray for his ever quick support and constant patience in regard to any technical issues that arose.

Without the constant support from my parents and my wife, I would not have been where I am today. I am thankful to Dr. Amit Neogi who occasionally offered useful advises. I am ever grateful for my alumnus friend Damien who made my non-academic life an active adventure. There are many more people to whom I convey my thanks and gratitude but might have forgotten the names at the moment. I hope they know that I am always grateful.

This work is funded by the Education, Audiovisual and Culture Executive Agency (EACEA) EXTATIC-Erasmus Mundus Joint Doctorate Programme and I wish to thank the whole EXTATIC-EMJD team.

Contents

Declaration	i
Dedication	ii
Acknowledgements	iii
Glossary of acronyms	vii
Glossary of symbols	viii
List of Figures	xi
List of Tables	xvi
Abstract	xvii
Streszczenie	xviii
1 Introduction	1
2 Basics of statistical description of laser pulses	9
2.1 Basic concepts	9
2.1.1 Random variable	9
2.1.2 Probability density function (PDF)	9
2.1.3 Stochastic processes and ensembles	10
2.1.4 Time average vs ensemble average & Ergodicity	10
2.1.5 Second order probability densities	10
2.1.6 Autocorrelation function (AC)	11
2.1.7 Stationary random process	11
2.2 Chaotic light - an example	11
2.2.1 Ensemble Average	13
2.2.2 Autocorrelation function and coherence time	13
2.2.3 Degree of coherence	15
2.2.4 Types of correlation shapes	15
2.2.5 Stationarity of the field	17
2.3 Conclusion	17
3 Numerical simulation of the temporal fluctuations of the FEL pulses	19
3.1 Gaussian pdf	19
3.2 FEL field and amplitude	20
3.3 FEL wavepacket	21
3.4 Generation of random wavepackets	22
3.4.1 Random numbers	22

3.4.2	Random wavepackets	24
3.5	Field and intensity fluctuations	24
3.6	Degree of temporal coherence: 1st and 2nd order	26
3.6.1	Ensemble average	27
3.6.2	Degree of coherence:	27
3.6.3	Ensemble average of FEL field intensity	29
3.6.4	Non-Stationarity and non-ergodicity of the FEL field	29
3.7	Frequency domain	30
3.7.1	Discrete Fourier Transform	30
3.7.2	Intensity profile	31
3.8	Conclusion	32
4	Density matrix equations of motion	33
4.1	Nature of the laser field used	33
4.2	Two-level atom	35
4.2.1	Operators of interest	35
4.2.2	Amplitude equations formulation	36
4.2.3	Density-Matrix formulation	37
4.2.4	Rotating wave approximation and interaction picture	39
4.3	Strong-field DM equations of AIS ionization	39
4.4	Conclusion	49
5	Ab-initio calculation of helium bound and continuum states: Fano parameters and AIS	51
5.1	Atomic structure calculations	51
5.2	Calculation of the Fano Parameters of the AIS	54
5.3	Photoionization cross section, position and width of the AIS	56
5.3.1	Calculation of q_a, d_{ga}, d_{gc}	57
5.3.2	Extra channel	59
5.4	Conclusion	59
6	Simple theory of averaging	61
6.1	Stochastic field modelling	61
6.2	Approach-1: Retaining the form of EOMs	62
6.2.1	Results and discussions: Neon	66
6.3	Approach - 2: Eliminating the coherence equation	69
6.3.1	Approximations	71
6.3.2	Different Scenarios of AC function	73
6.3.3	Results and discussions: helium	75
6.4	Conclusions and limitations	78
7	Perturbative theory of ensemble averaging	81
7.1	Extended DM-EOMs	82
7.2	The Formalism	85
7.2.1	Liouville - Equation, Matrices and Operators	85
7.2.2	Infinite expansion of Evolution operator	87
7.2.3	Cumulant-expansion vs moment-expansion	89
7.2.4	The cumulant-expansion	90
7.2.5	The first two non-vanishing terms	92
7.2.6	Equations for the bound-part	93
7.2.7	Equations for the continuum populations	95
7.3	The case of a Gaussian random field	96

7.4	Conclusion	98
8	Helium in 60.16 eV FEL radiation	101
8.1	Comparison with the Monte Carlo calculations	103
8.1.1	Monte Carlo method	103
8.1.2	Comparison	103
8.2	Comparison with the Fano-convolution method	106
8.3	Validity of the approximate expressions	107
8.4	Effects of intensity correlation	109
8.5	Comparison with the simple averaging method	109
8.6	Effects of the field AC shape:	111
8.7	Effects of τ_c	112
8.8	Conclusion	113
9	Li⁺ in 150.2 eV FEL radiation	115
9.1	The AIS lineshape	117
9.2	Effects of the coherence time	118
9.3	Effects of the pulse duration	118
9.4	Conclusion	120
10	Summary and outlook	123
10.1	Overall summary	123
10.2	Outlook - Future work	124
A	Laplace transform and pole approximation	137
A.1	Laplace transform and its inverse	137
A.2	Pole approximation	137
B	Moments and cumulants	140
B.1	Overview	140
B.2	Moments and cumulants relation:	141
B.3	Zero mean - Gaussian case	142
C	Cumulant-expansion terms	143
D	Derivation of $S_{1t}(\delta)$ and $S_{2t}(0)$	146
D.1	Gaussian AC	146
D.1.1	Closed form expression of $S_{1t}(\delta)$ - Gaussian AC	147
D.1.2	Closed form expression of $S_{2t}(0)$ - Gaussian AC	149
D.2	Lorentzian AC	150
D.2.1	Closed form expression of $S_{1t}(\delta)$ - Lorentzian AC	151
D.2.2	Closed form expression of $S_{2t}(0)$ - Lorentzian AC	152
E	Atomic units - conversion	154

Glossary of acronyms

<i>wlog</i>	without loss of generality
a.u.	atomic units
AC	autocorrelation
AIS	autoionizing state
AMO	Atomic Molecular Optical
CI	configuration interaction
DA	decorrelation approximation
DFT	Discrete Fourier Transform
DM	density matrix
EOMs	equations of motion
FEL	Free-Electron Laser
FERMI	Free-Electron laser Radiation for Multidisciplinary Investigations
FLASH	Free-Electron Laser in Hamburg
FWHM	full width at half maximum
HS	Hilbert space
IP	interaction picture
laser	light amplification by stimulated emission of radiation
LCLS	Linac Coherent Light Source
LHS	left hand side of an equation
MC	Monte Carlo
ODE	ordinary differential equation
pdf	probability density function
RHS	right hand side of an equation
RMSW	root mean square width
RV	random variable
RWA	rotating wave approximation
SACLA	Spring-8 Angstrom Compact Free Electron Laser
SASE	Self Amplified Spontaneous Emission
SDE	stochastic differential equation
TDSE	time dependent Schrödinger equation
TISE	time independent Schrödinger equation
XFEL	X-ray Free-Electron Laser

Glossary of symbols

$C_{n_1 l_1 n_2 l_2}^{nL}$	CI coefficients
$C_n(t_1, t_2, \dots, t_n)$	n^{th} order cumulant
$E(t)$	semi-classical dipole approximated electric field
E_a	energy position of AIS resonant state
$E_{0R}(t)$	real electric field envelope of $E(t)$
$L_b(t)$	bound-part Liouville matrix
$L_c(t)$	continuum-part Liouville matrix
$M_n(t_1, t_2, \dots, t_n)$	n^{th} order moment
M	a measure of number of modes in a fluctuating pulse
$P_{nl}(r)$	radial wavefunction
R	finite box radius in which an atomic system is confined to
$S_{1t}(\delta)$	related to time dependent frequency spectrum
$S_{2t}(0)$	related to field's average energy standard deviation
Δ	complex detuning
Γ_a	autoionization width
$\Omega(t)$	Rabi oscillations
$\overline{U}_b^\dagger(t, t_i)$	complex conjugate of the deterministic time-evolution unitary operator
$\overline{U}_b(t, t_i)$	deterministic time-evolution unitary operator
\overline{X}	ensemble average of the quantity X
$\Phi_{E_n L}(\mathbf{r}_1, \mathbf{r}_2)$	two electron wavefunctions
∇^2	Laplacian operator
$\mathcal{A}(Z)$	an atomic/ionic system with atomic number Z
\mathcal{D}	interference matrix element
$\mathcal{E}(t)$	complex field envelope
$\mathcal{E}_0(t)$	slowly varying deterministic envelope of $\mathcal{E}(t)$
\mathcal{E}_0	peak amplitude of the complex field envelope
$\mathcal{I}(t)$	instantaneous intensity envelope
\mathcal{I}_0	peak value of intensity envelope
\mathcal{L}	Laplace transform
χ	chirp factor
$\delta(x)$	Dirac delta function
δ_0	near resonant detuning
$\delta_l(\mathbf{E})$	scattering phase shift of ejected electron
δ_\pm	averaged dynamic detunings
δ_{ij}	Kronecker delta whose value is 1 for $i = j$ and 0 for $i \neq j$
δ	complex detuning
$\epsilon(t)$	complex random process which models the fluctuations of $\mathcal{E}(t)$
\forall	for all

γ_a	peak of photoionization width from $ a\rangle$ to $ c'\rangle$
γ_c	peak of photoionization width from $ c\rangle$ to $ c''\rangle$
γ_g	peak of the photoionization width from $ g\rangle$ to $ c\rangle$
$\hat{U}(t)$	time evolution operator
$\hat{H}(t)$	total Hamiltonian
\hat{H}^R	Radiation Hamiltonian
\hat{H}^a	field-free Hamiltonian
\hat{H}^o	clubbed field free and radiation Hamiltonian
\hat{d}	the dipole operator
i	imaginary complex number $\sqrt{-1}$
\in	belonging to
\mathbf{k}	wave vector whose magnitude is related to the wavelength by $ k = \frac{2\pi}{\lambda}$
$ a\rangle$	AIS
$ c\rangle$	continuum states
$ g\rangle$	ground state
\mathcal{P}	principal part of an integral
$\mathcal{Y}_{l_1 l_2}^{LM_L}(\Omega_1, \Omega_2)$	bipolar spherical harmonics
\mathcal{F}	Fourier transform
ω	central tunable frequency of the field
$\hat{D}(t)$	the semi-classical field matter interaction operator
\hat{V}	electron-electron (inter electronic) interaction operator
$\hat{h}(r_i)$	one-electron Hamiltonian
$\phi_{n_1 l_1 n_2 l_2}^L(\mathbf{r}_1, \mathbf{r}_2)$	two electron basis state
$\langle \rangle$	ensemble average
\mathbf{r}	position vector
$\rho(t)$	density matrix before RWA
$\rho_{ij}(t)$	density matrix element before RWA
$\sigma(t)$	density matrix after RWA
$\sigma_1(E)$	one-photon cross section as a function of energy E
$\sigma_b(t)$	bound-part density matrix
$\sigma_c(t)$	continuum-part density matrix
$\sigma_{ij}(t)$	density matrix element after RWA
τ_c	coherence time
τ_p	pulse duration
τ_{fwhm}	full width at half maximum
τ_{rmsw}	root mean square width
$\tilde{L}(t)$	fluctuating interaction matrix
$\tilde{U}(t)$	evolution operator involving fluctuating interaction matrices
\tilde{X}	residual fluctuations of the quantity X
cc	complex conjugate
$d_{ac'}$	dipole transition matrix element between $ a\rangle$ and $ c'\rangle$
$d_{cc''}$	dipole transition matrix element between $ c\rangle$ and $ c''\rangle$
d_{ga}	dipole transition matrix element between $ g\rangle$ and $ a\rangle$
d_{gc}	dipole transition matrix element between $ g\rangle$ and $ c\rangle$
$g_1(\tau)$	first order degree of temporal coherence
$g_2(\tau)$	second order degree of temporal coherence
q_a	Fano asymmetry parameter
s_a	peak intensity of ac-Stark shift of AIS
s_g	peak intensity of ac-Stark shift of ground state

t_i	initial time, often takes the value of either 0 or <i>infty</i>
t	the usual time variable
Im	Imaginary part
Re	Real part

List of Figures

2.1	Depiction of random fluctuations in an emission of chaotic light by 7 atoms. Each of the 7 random arrows is a phasor i.e., complex exponential associated with one of the 7 radiating atoms. The blue double-dashed arrow is the resultant phasor having a resultant amplitude $f(t)$ and phase $\Phi(t)$. For each realization of the same ensemble of 7 atoms give different field amplitudes $f_i(t)$ and phases $\Phi_i(t)$ for $i = 1, 2$. (The figure is adapted from the 3rd chapter of ref [45] and extended)	12
2.2	Physically understanding the AC of a function. The solid curve is a real random function varying in time. The dotted curve is the same function shifted in time. These can be assumed to be the real parts of the chaotic field envelope and a time-shifted version of itself, respectively. The shift is given by τ . As τ increases, it can be understood from the figure that the magnitude of the product of both the curves decreases.	14
2.3	Different forms of first order degree of coherence function as a function of the time difference τ (arb. units). $g_1(\tau)_{gauss}$ has a Gaussian lineshape and $g_1(\tau)_{lorentz}$ has a Lorentzian lineshape. Both have characteristic coherence time of 0.2 (arb units). The width (root mean square width or full width at half maxima) of these pulses is proportional to the coherence time τ_c	16
2.4	Different forms of second order degrees of coherence as a function of the time difference τ (arb units). $g_2(\tau)_{gauss}$ has a shifted Gaussian shape and $g_2(\tau)_{lorentz}$ has a shifted Lorentzian shape as per their relation to first order degree of coherence.	16
3.1	Schematic showing the process of micro bunching and generation of coherent radiation as the randomly arriving electrons pass through the length of the undulator. The figure is adapted from reference [10].	20
3.2	This plot shows the real part of a random FEL wavepacket. Its fast oscillating part due to the tunable resonance frequency $\omega = 60.16$ eV (2.211 a.u.) is shown with a black-solid curve whereas the envelope is shown with a red-dashed curve, having a width proportional to $\tau_{wp} = 0.29$ fs (11.99 a.u.). A reference Gaussian curve (green-dot-dashed) has also been fitted to show that the envelope is indeed Gaussian.	22
3.3	Probability distribution for $N_e = 1000$ random variables which are Gaussian distributed with zero mean and variance $\tau_b = 4.99$ is depicted in the black dot-dashed curve. Number of bins used is 100. An ensemble average over 300 ensembles is depicted as the red curve whereas the ideal Gaussian distribution is depicted as the green dashed curve.	24

3.4	Real part of a set of 10 random FEL wavepackets, separated temporally according to the Gaussian distribution of the arrival times of the associated electrons at the entrance of the undulator, is shown here. The center of each wavepacket denotes the arrival time of j^{th} electron, denoted by t_j . The generation of the wavepackets follow chronological ordering i.e., the values of $i = 1, 2, \dots, 10$ denote particular increasing times at which they were generated. The disordered placement of the wavepackets in the figure suggest the randomness involved in their arrival times.	25
3.5	Superposition of a thousand random wavepackets resulting in a fluctuating profile of an FEL field whose real part is plotted here. The tunable resonance frequency $\omega = 60.16$ eV (2.211 a.u.) and the Gaussian envelope of each random wavepacket has a width proportional to $\tau_{wp} = 0.29$ fs (11.99 a.u.). Coherence time τ_c of the pulse is 0.5 fs.	25
3.6	Superposition of intensities of a thousand random pulses, for five different pulse realizations. The tunable resonance frequency $\omega = 60.16$ eV (2.211 a.u.) and the Gaussian envelope of each random wavepacket has a width proportional to $\tau_{wp} = 0.29$ fs (11.99 a.u.). The red solid curve shows the ensemble average over many ensembles.	26
3.7	Black-dashed curve: Simulated first order coherence function having parameters of Table 3.1. Red-solid curve: Analytical Gaussian fit having a width of $\tau_c = 0.5$ fs.	28
3.8	Black-dashed curve: Simulated second order coherence function, having parameters of Table 3.1. Red-solid curve: Analytical shifted-Gaussian form obtained from Eq. (3.11b) having a width of $\tau_c = 0.5$ fs	29
3.9	Red solid curve: Ensemble average of the instantaneous intensity $\langle \mathcal{E}(t) ^2 \rangle$ over three hundred pulse shots, with parameters of Table 3.1. Black dot-dashed curve: An analytical Gaussian fit of Eq. (3.12) with a width of $\tau_p = 7$ fs (289.38 a.u.).	30
3.10	Frequency spectrum of a pulse with central frequency $\omega = 60.16$ eV, coherence time $\tau_c = 0.5$ fs and total pulse duration $\tau_p = 7$ fs. The black-solid curve represents the averaged spectrum, blue-dashed curve is its Gaussian fit with a width of ~ 1.31 eV while the red dot-dashed curve is the spectrum corresponding to one of the FEL pulse's single shot realizations.	31
4.1	A two level atomic system with ground state $ g\rangle$ with eigenenergy E_g and excited state $ e\rangle$ with eigenenergy E_e . It interacts with a coherent laser pulse of central frequency $\omega \approx \omega_{eg} = E_e - E_g$, where $E_e > E_g$. This introduces an intensity dependent oscillation between the states, called Rabi oscillations, denoted by $\Omega(t)$. The dotted boundary around the two levels, suggest that the two level system may also be a sub-system in focus i.e., part of a bigger system which is studied in isolation.	35
4.2	Schematic of an extended two-level system where one of the two states is degenerate with continuum.	40
4.3	Schematic of Laplace transform and a change of s-variable to z-variable.	42
4.4	Schematic showing the Fano picture of an atom when it interacts with a laser pulse of frequency ω . The direct channel of photoionization $\gamma_g(t)$, the indirect channel via Rabi oscillations $\Omega(t)$ and autoionization Γ_a are shown. The energy shifts s_g and s_a are included and depicted as the thick lines for the corresponding states.	48
5.1	Schematic of a two electron system where e_i and \mathbf{r}_i represent the i^{th} electron and its position vector with respect to the origin O.	52

5.2	Photoionization cross section profile (black solid curve) calculated for helium using the method discussed in this chapter following the methodology of [67, 68]. A Fano-formula fit (red-dashed curve) is also shown which gives the parameters as obtained in Table 5.1.	54
5.3	Schematic showing the energy levels in Helium in Fano-representation. $ g\rangle$ is considered to be at 0 eV. The energy positions shows are not to the scale.	55
6.1	Schematic of the interaction of a near resonant FEL field with neon atom. ω is the tunable resonance frequency, $ c\rangle$ is the continuum Γ_a is the Auger-decay width and $\Omega(t)$ denotes the Rabi oscillations.	63
6.2	Ground-state population of neon after interacting with an ensemble of fluctuating pulses whose average form is slowly varying square shape. The solid curves are obtained by solving the averaged DM-EOMs Eq. (6.8) - Eq. (6.11) whereas the dashed curves mimic the data from the reference [29]. The green and blue curves represent the ground-state population of Neon whereas the red and the black ones represent the averaged intensity profile.	67
6.3	Auger-electron yield of Neon after interacting with a coherent pulse of Gaussian shaped envelope. The solid curves are obtained by solving the averaged DM-EOMs Eq. (6.8) - Eq. (6.11) when $\frac{1}{\tau_c} \rightarrow 0$ whereas the double-dot-dashed curves mimic the data from the reference [29].	67
6.4	Comparison of the Auger-yields for coherent pulse (solid curves) with that of stochastic pulse (double-dot-dashed curves) of $\tau_c = 0.15$ fs. The τ_{rmsw} for the black curves is 0.5 fs, for the red curves is 2 fs and for the green curves is 10 fs.	68
6.5	Comparison of the Auger-yields for coherent pulse (solid curves) with that of stochastic pulse (double-dot-dashed curves) of $\tau_c = 3.3$ fs. The τ_{rmsw} for the black curves is 0.5 fs, for the red curves is 2 fs and for the green curves is 10 fs.	69
6.6	Schematic of the interaction of a near resonant FEL field with helium atom. ω is the tunable resonance frequency, $ c\rangle$ is the continuum, $\gamma_g(t)$ is the photoionization width, Γ_a is the autoionization width and $\Omega(t)$ denotes the Rabi oscillations.	70
6.7	The effect of smoothing the familiar Fano-lineshape, caused by averaging the fluctuations can be clearly seen in this figure. The red-dashed curve with highest peak is obtained for a deterministic pulse whereas the black-solid curve is obtained for a stochastic pulse. A Gaussian correlation is attributed to the field having a coherence time of $\tau_c = 0.5$ fs (20.67 a.u.). For both the coherent and chaotic pulses the peak intensity is 10^{13} W/cm ² and the pulse duration is $\tau_p = 7$ fs (289.38 a.u.).	76
6.8	Validity of population approximation relative to the raw form of the averaged DM-EOMs. The black solid curve represents the yield profile obtained from the raw form of EOMs whereas the red-dashed curve represents the yield profile obtained after the invocation of population approximation. A Gaussian correlation is attributed to the field having a coherence time of $\tau_c = 0.5$ fs (20.67 a.u.). and a pulse duration of $\tau_p = 7$ fs (289.38 a.u.).	77
6.9	Influence of different correlation types on the ionization yield lineshape. The black solid curve utilises a Gaussian correlation whereas the red dashed curve utilises a Lorentzian correlation. Both the correlation types have a coherence time of $\tau_c = 0.5$ fs (20.67 a.u.) and a pulse duration of $\tau_p = 7$ fs (289.38 a.u.). It can be seen how distinct each lineshape is.	78

7.1	Sketch of the near-resonant excitation or ionization scheme, which includes the depiction of further channels of ionization, with a FEL field	82
8.1	Ionization scheme of He in a 60.16 eV FEL radiation. $ g\rangle$ $1s^2$ is the ground state, $ a\rangle$ $2s2p$ is the auto-ionizing state, $ c\rangle$ is the continuum above the ionized state of He^+ $1s$ and the $ c''\rangle$ is the continuum above the ionized state He^{2+} . The energies depicted on the right are not to scale but only give an idea of the values of the levels.	102
8.2	Single-ionization yield for one realization of the random pulse (red-solid curve), and its corresponding ensemble average obtained from the averaged EOMs (black-dashed curve) and the MC method (blue-dashed curve and is calculated over 300 pulse realizations). The yields were obtained at the resonance frequency 60.16 eV and for $\tau_p = 7$ fs, $\tau_c = 0.5$ and peak intensity $10^{13}\text{W}/\text{cm}^2$	104
8.3	Comparison of ionization yields obtained from the Monte Carlo method (red solid curve) and averaged density matrix equations (black dashed curve) for peak intensities of 10^{13} W/cm^2 , 10^{14} W/cm^2 and 10^{15} W/cm^2 (top to bottom respectively). $\gamma_c = 0$ a.u. Other parameters are $\tau_p = 7$ fs, $\tau_c = 0.5$ fs ($M = 14$).	104
8.4	Comparison of ionization yields obtained from the Monte Carlo method (red solid curve) and averaged density matrix equations (black dashed curve) for peak intensities of 10^{13} W/cm^2 , 10^{14} W/cm^2 and 10^{15} W/cm^2 (top to bottom respectively). $\gamma_c = 0.426$ a.u. Other parameters are $\tau_p = 7$ fs, $\tau_c = 0.5$ fs ($M = 14$).	105
8.5	Comparison of He^+ yield when its further ionization ($\text{He}^+ \rightarrow \text{He}^{2+}$) is taken into account (red-dashed curves) and when it is not (black-solid curves), for the peak intensities 10^{14} W/cm^2 -(plot (a)) and 10^{15} W/cm^2 -(plot (b)). The yields were obtained at the resonance frequency 60.16 eV and for $\tau_p = 7$ fs, $\tau_c = 0.5$ fs ($M = 14$).	106
8.6	Amplitude of intensity profile in frequency domain. The black-solid curve represents the averaged spectrum, blue-dashed curve is its Gaussian fit with a width of ~ 1.31 eV while the red dot-dashed curve is the spectrum corresponding to one of the FEL pulse's single shot realizations.	107
8.7	He^+ yields using the convolution of the AIS Fano-shape with the averaged pulse profile (green dashed line), Eq. (8.3), the averaged EOMs (black line) and the MC approach (red line) The yields were obtained at the resonance frequency 60.16 eV and for $\tau_p = 7$ fs, $\tau_c = 0.5$ and peak intensity $10^{13}\text{W}/\text{cm}^2$. The scaling factor for the convolution profile so as to match the other profiles is 80.	108
8.8	Comparison of the ionization yields obtained by approximate (red dashed curve) and non-approximate expressions (black solid curve) for the S_{1t} and S_{2t} terms for the peak intensities of 10^{13} W/cm^2 , 10^{14} W/cm^2 and 10^{15} W/cm^2 from top to bottom, respectively. Gaussian correlation is used and the γ_c channel is included. Other parameters are $\tau_p = 7$ fs, $\tau_c = 0.5$ fs ($M = 14$).	108
8.9	Comparison of the ionization yields obtained when the intensity correlation $S_{2t}(0)$ is included (black solid curve) and not included (red dashed curve) in the averaged DM-EOMs equations, for different peak intensities.	109

8.10	Comparison of the ionization yield of helium obtained by perturbative averaging method (black-solid curve) and simple averaging method (red-dashed curve) for the peak intensities of 10^{13} W/cm ² , 10^{14} W/cm ² and 10^{15} W/cm ² from top to bottom, respectively. Gaussian correlation is used and the γ_c channel is not included. Other parameters are $\tau_p = 7$ fs, $\tau_c = 0.5$ fs ($M = 14$).	110
8.11	Comparison of ionization yields obtained from the Gaussian correlation (black solid curve) and Lorentzian correlation (red dashed curve) for peak intensities of 10^{13} W/cm ² , 10^{14} W/cm ² and 10^{15} W/cm ² (top to bottom respectively). The figures (a), (b) and (c) are obtained when the area under the $g_1(\tau)$ is kept the same for both the correlations. $\tau_{c_{gauss}} = 0.5$ fs and $\tau_{c_{lorentz}} = 0.31$ fs.	111
8.12	Comparison of ionization yields obtained from the Gaussian correlation (black solid curve) and Lorentzian correlation (red dashed curve) for peak intensities of 10^{13} W/cm ² , 10^{14} W/cm ² and 10^{15} W/cm ² (top to bottom respectively). The figures (a), (b) and (c) are obtained when the correlation time $\tau_c = 0.5$ fs is maintained the same.	112
8.13	Comparison of the ionisation yield obtained by using Gaussian form of the field's autocorrelation function at 10^{13} W/cm ² for different coherence times τ_c : 2 fs (black-curve), 4 fs (red-curve), 6 fs (green-curve) and 8 fs (blue-curve). At resonance, the yield is highest for the longest coherence time and it gradually decreases as the τ_c is decreased. The pulse duration used is $\tau_p = 45$ fs.	113
9.1	Ionization scheme of Li ⁺ in a 150.2 eV FEL radiation. $ g\rangle$ 1s ² is the ground state, $ a\rangle$ 2s2p is the auto-ionizing state, $ c\rangle$ is the continuum above the ionized state of Li ²⁺ 1s and the $ c''\rangle$ is the continuum above the ionized state Li ³⁺ . The energies depicted on the right are not to scale but only give an idea of the values of the levels.	116
9.2	The effect of smoothing the familiar Fano-profile, caused by averaging the fluctuations can be clearly seen in this figure. The red-dashed curve with highest peak is obtained for a deterministic pulse whereas the black-solid curve is obtained for a stochastic pulse with coherence time of 1.3 fs (53.74 a.u.). The peak intensity is 10^{13} W/cm ² and the pulse duration $\tau_p = 12.7$ fs (525.02 a.u.).	117
9.3	Effect of coherence time on the ionization yield. As τ_c increases, the ionization yield also increases, near resonance. The peak intensity is 10^{13} W/cm ² and the pulse duration $\tau_p = 12.7$ fs (525.02 a.u.).	119
9.4	Effect of pulse duration on the ionization yield. The coherence time used is $\tau_c = 3$ fs (124.02 a.u.) and the peak intensities are: 10^{13} W/cm ² for (a), 10^{14} W/cm ² for (b) and 10^{15} W/cm ² for (c).	119
9.5	Effect of peak intensity on the population of Li ²⁺ . The peak intensities used are: 10^{13} W/cm ² for (a), 10^{14} W/cm ² for (b) and 10^{15} W/cm ² for (c). Black-solid curve is when the further ionization channel is ignored ($\gamma_c = 0$) and the red-dashed curve is when the further ionization channel is considered. The pulse duration $\tau_p = 20$ fs (826.8 a.u.) and the coherence time $\tau_c = 3$ fs (124.02 a.u.).	120
A.1	The scheme of integration of an inverse Laplace transform along the vertical contour line L_1 which has all its singularities strictly to the left of it.	138
A.2	Integration scheme for pole-approximation.	138

List of Tables

3.1	FEL field parameters used in simulation as well as reference typical values. .	21
3.2	Important FEL facilities and some of the related field parameters, for relative comparison, taken from references [5, 10, 53–55]. τ_{fwhm} is the FWHM pulse duration, ω is the central operating frequency, $\frac{\Delta\omega}{\omega}$ is the relative fractional bandwidth, PPS is the number of pulses per second and PE is the pulse energy.	32
5.1	Atomic parameters obtained for He(2s2p) AIS resonance in a.u.	57
6.1	Atomic parameters in a.u. used for the neon resonant Auger decay.	66
6.2	Atomic parameters for the He(2s2p) AIS resonance and field parameters in a.u.; The values for the effective matrix element d_{ga} is calculated by $4 d_{ga} ^2 = q_a^2 \Gamma_a \gamma_g$	75
8.1	Atomic structure parameters for the He system in a.u.	101
9.1	Atomic structure parameters for the Li ⁺ system in a.u.	117
E.1	Useful conversion factors relating to atomic units.	154

Abstract

Statistical Photoionization Theory of Atoms in Soft XUV Free-Electron Laser Fields

Tejaswi Katravulapally

The goal is to develop a rigorous theory to study the effects of stochastic fluctuations of self amplified spontaneous emission free-electron laser (SASE FEL) on the near-resonant ionization of atomic/ionic systems. To this end, density matrix equations of motion are utilised in their raw form for the sake of Monte Carlo simulations and in their particular averaged forms. First, a couple of simpler averaging methods were used to quickly understand the general behavior of the interaction of fluctuating fields with atoms. To this end, the particular case of neon (Ne) and helium (He) were used, where the effects of the interplay of the pulse duration and the coherence time on the oscillations of the yield profile, which manifest due to Rabi oscillations, were studied in comparison to a coherent pulse. Second, a rigorous method of perturbative approach is developed, which is based on the expansion in terms of multitime cumulants which are a particular combination of the field's coherence functions. The range of validity of the model is tested in terms of the field's coherence temporal length and peak intensity. Particularly, the photoionization of helium (He) and lithium ion (Li^+) via their doubly-excited state $2s2p\ ^1P$ has been studied with the interacting FEL's 1st-order coherence function modelled as square-exponentially dependent. The traditional asymmetric resonant Fano-profile is broadened and is shown to acquire a Voigt profile. The effects of pulse duration, coherence time and peak intensity on the lineshape are clearly shown. The two approaches of averaging were compared and the supremacy of the latter is shown. When compared to Monte Carlo, it is seen that the rigorous averaging approach results in competing values up to higher peak intensities. This suggests that in the scenarios of low coherence time and peak intensities, the averaging method developed in this thesis is highly preferable over the traditional Monte Carlo given its high computational demands.

Streszczenie

Statystyczna Teoria Fotojonizacji Atomów w Słabych Polach Promieniowania Laserów na Swobodnych Elektronach w Zakresie Ekstremalnego Ultrafioletu.

Tejaswi Katravulapally

Celem pracy jest rozwinięcie ścisłej teorii do badania wpływu stochastycznych fluktuacji sygnału lasera na swobodnych elektronach pracującego w reżimie samowzmocnionej emisji spontanicznej (SASE FEL) na quasi-rezonansową jonizację układów atomowych lub jonowych. W tym celu, równania macierzy gęstości zostały użyte w ich wyjściowej formie z korzyścią dla symulacji metodą Monte-Carlo oraz w ich szczególnej, uśrednionej formie. Po pierwsze, użyto kilka prostszych metod uśredniania dla szybkiego zrozumienia ogólnego zachowania się procesu oddziaływania fluktuujących pól z atomami. Do tego celu zostały użyte atomy neonu (Ne) i helu (He), w których wpływ wzajemnej zależności pomiędzy długością impulsu i czasem koherencji na profil krzywej uzysku elektronów, manifestowany w wyniku oscylacji Rabięgo, był badany przez porównanie z tzw. impulsem koherentnym. Po drugie, została rozwinięta ścisła metoda rachunku zaburzeń, oparta na rozwinięciu w funkcji kumulantów wieloczasowych będących szczególną kombinacją funkcji koherencji pola. Zakres ważności modelu został zweryfikowany dla zależności od czasowej koherencji pola i szczytowej gęstości mocy impulsu. W szczególności, fotojonizacja helu (He) i jonu litu (Li^+) poprzez podwójnie wzbudzony stan $2s2p\ ^1P$ były badane przy funkcji koherencji pierwszego rzędu lasera na swobodnych elektronach modelowanej jako kwadratowo-eksponencjalna zależność. Tradycyjnie asymetryczny rezonansowy profil Fano poszerza się i jak pokazano w pracy, nabywa cech profilu Voigta. Wpływ długości impulsu, czasu koherencji i szczytowej gęstości mocy na profil linii jest jasno pokazany. Porównane zostały dwie metody uśredniania i wyższość jednej z nich została udowodniona. Z obliczeń wynika wyraźnie, że ścisła metoda uśredniania daje rezultaty konkurencyjne w porównaniu do metody Monte Carlo, aż do wysokich gęstości mocy szczytowej. To sugeruje, że w sytuacjach z danymi zawierającymi niskie wartości czasu koherencji i mocy szczytowej, metoda uśredniania rozwinięta w tej pracy ma znaczącą przewagę nad tradycyjną metodą Monte Carlo, biorąc pod uwagę wysokie potrzeby odnośnie mocy obliczeniowej w przypadku tej ostatniej.

Chapter 1

Introduction

Interaction of light and matter is what makes the visible world beautiful. Imagine the sunrise over the coastal sea or moon light reflected on a snowy house. All such plethora of vibrant sceneries and vivid beauties of nature are the result of light being scattered, reflected or refracted over and through many objects. This is only a macroscopic understanding. How does light actually interacts with matter? What actually happens when it interacts with matter? It is the motto of Atomic Molecular Optical (AMO) physics to explore this question. The subject of the present thesis is one of the building blocks of the ever expanding grand field of AMO physics.

In the pursuit of understanding the interaction dynamics of light and matter the core element is the availability of a proper light source. When a target atom remains the same, the dynamics depend on the type of light that shines on it. The invention of laser has revolutionized the way of understanding the internal structure of atoms and related dynamics phenomena. In their initial days of development, the long-wavelength lasers suffered from statistical fluctuations which lead to the development of rigorous theories that tackled the situation in a sophisticated manner [1–4]. As the technology evolved, the fluctuations in the source weakened giving rise to more coherent and stable laser fields (in terms of temporally varying amplitude and phase), such as *Ti:sapphire laser*. Typically at 800 nm wavelength, when the pulse duration is ~ 25 fs, the *Ti:sapphire laser* can operate at the peak intensity of approximately $6 \times 10^{15} \text{ W/cm}^2$ [5]. But these lasers are limited in many respects, such as output power, tunable frequency, frequency range, etc. Some of these limitations cannot be overcome due to the way the lasers are generated. For example, the tunability is dependent on the quantum levels involved in the atomic/molecular transitions of the active medium or the output power is limited by the heat dissipation problems, etc. [6].

There arose a new revolution with the generation of free-electron lasers (FELs) at various sites such as FLASH (2005), LCLS (2009), FERMI (2011), SACLA(2011), Swiss-FEL(2016), European XFEL (2017), which has made available intense, ultrafast (femtosecond scale) and coherent radiation sources in the soft and hard X-ray wavelength regime (20 eV-10.2 KeV) [7–9]. A glance at some of the parameters of these FELs can be had by looking at Table 3.1 on page 21 and Table 3.2 on 32 along with references therein. In contrast to the other lasers, FELs have femtosecond pulse duration, can reach keV photon

energies, highly tunable and can operate at peak intensities as high as 10^{18} W/cm² [10]. A detailed history relating to the FELs can be found in the references [10, 11].

FEL light is generated from *self amplified spontaneous emission* (SASE) which inherently has noise properties. This renders the output radiation's amplitude and phase to temporally fluctuate [12–14]. On the other hand FEL radiation has some of the most desirable properties such as good tunability, wide frequency range, ultra short pulse durations and very high pulse peak intensities [14, 15]. They are sufficiently short (\sim few femtoseconds) and hence compare with sub-femtosecond atomic characteristic time scales [7–9, 16, 17]. These ultrashort pulse durations combined with ultrahigh intensities help in the time-resolved studies of atomic/molecular dynamics [18]. Another important property of a high energy X-ray FEL radiation is that it can interact with the the inner most electrons of an atomic system directly, a property which is in contrast with long-wavelength laser (i.e., Ti:sapphire). Usually in the latter, the outermost electrons obstructs the probing of the inner regions even in the cases where sufficient energies are available in the form of multi-photon absorption. All these desirable properties of FELs created a sustained stir of interest, since more than a decade, and enhanced the exploration of the topics concerning atomic dynamics under short-wavelength fluctuating radiation field. Due to this, a similar situation as for the initial phase of the long-wavelength lasers, in terms of statistical descriptions, has arisen now for the SASE FEL interaction studies.

Theoretically speaking, the dynamics of laser and matter interaction is studied using the language of mathematics i.e., one has to use a mathematical interface of dynamics equations of motion (EOMs). When the laser has statistical properties, the dynamics involved will imbibe a similar nature and renders the EOMs stochastic. Often, these equations involve differential equations and hence this constitutes the dynamics to be studied under the frame work of *stochastic differential equations* which incorporate the dynamical quantities as stochastic processes [19–22]. To describe the statistics of the dynamical quantities such as excited populations, ionization yield, electron's angular spectrum, etc., many rigorous studies were undertaken for the long wavelength sources [1–4]. In the recent past, the same rigour and depth have been applied in the related explorations of FELs [9, 23–27].

FEL principle lies in the interaction of electromagnetic fields and accelerated electrons which results in self amplified spontaneous emission (SASE) rather than in the stimulated emission of radiation of an atom/molecular medium [14]. This SASE FEL inherits stochastic properties from the stochastic properties of the shot noise associated with the electron beam [28]. In the context of these fluctuating FELs, there are certain class of experiments, called multi-shot experiments, which collect the data over a repeated sets of different random pulses. Because FEL analyser exhibits shot-to-shot fluctuations, the data obtained for each shot are completely random compared to the other. Therefore the end result will be effectively an average of the data set over all the random pulse shots. To describe this theoretically, one can resort to the Monte Carlo (MC) approach which emulates an experimental scenario i.e., solves the set of EOMs for the random pulse shots and then takes an average over all the shots [29–31]. But, when one needs to work in the

frequency space (e.g. spectrum - profiles), along with time evolution, as the pulse profile changes randomly for each and every frequency, the computational demand increases rapidly [32]. Also, not much insight into the dynamics is gained nor can one predict the nature of observables when the statistical nature of an interacting laser is given, through the MC approach. So, the MC method is only a brute-force method but not an intuitive or an ingenious technique. It solves the bare minimum purpose but does not provide much insight into the exploration.

There is another approach one can embark upon in order to study the aforementioned multi-shot problems, theoretically. It is the method of *Ensemble averaging*. Different random shots mentioned above form a set of mathematical objects called *ensembles* (see 2.1.3) and if one can devise certain procedures to incorporate these ensembles and convert the stochastic EOMs into deterministic EOMs (via ensemble averaging), then it would help reduce the computational complexity in greater lengths [32, 33]. This is because, once the EOMs are deterministic, obtainment of a simple solution (averaged observables) for the equations is a lot quicker than taking a repeated average such as in MC method.

Typical MC calculations in this work took more than 35 hours to compute. This is because, the MC method is repetitive. For each central frequency of the field one needs to simulate a new random field-profile and propagate the equations of motion in time. For example, to obtain the red curve of Fig. 8.3 of Chapter 8 the number of photon frequencies between 52-68 eV were chosen to be 600. To obtain a proper smoothness of the observable through the Monte Carlo approach, at least 300 simulations had to be performed. Therefore, a total of $600 \times 300 = 180000$ runs were required. In addition, for each of these 180000 runs a proper random field needed to be generated which is not modelled analytically. Each particular realization (out of 180000) required about 1000 randomly chosen time points (within the pulse duration). All these factors contribute to the large computational times.

On the other hand, the stochastic averaging approaches took approximately 7-10 minutes to compute because of the deterministic nature of the equations of motion. Also, in an averaging approach the EOMs can be represented in the form of experimentally accessible quantities such as autocorrelation spectrum, coherence time, field's energy, etc., [34], which arise explicitly due to the process of ensemble averaging. This latter attribute is insightful and helps one to predict the nature of the outcome beforehand or at least gauge what would happen when the type of the statistics involved in the interacting laser changes.

The above forms the motivation behind the present work. The goal in this thesis is to develop a mathematically rigorous *perturbative theory of statistically averaged atomic dynamics governing the non-linear photoionization processes in a fluctuating FEL field*. Due to the short-wavelength radiation typical ionization schemes include two-photon resonant ionization, autoionization, sequential double photoionization, etc.

The model of the FEL is assumed to be the one of Krinsky and Li [35] who treat the startup SASE, which generates the FEL light, as a shot-noise process [36–38]. It is important to note that in the present work a square exponential form is used for the time

varying first order autocorrelation (AC) function $\sim e^{-(t_1-t_2)^2/2\tau_c^2}$. This is different from the generally assumed exponential form $\sim e^{-|t_1-t_2|/2\tau_c}$ of the early long-wavelength lasers' first order AC function. Either the latter was applied when dealing with FELs [27] or the former was applied only in a MC framework [23, 26]. To date, as per the knowledge of the author, the square exponential form of the field's AC function was not applied to the FEL's interaction in a stochastic averaging framework, other than in MC.

The three major parts of the present thesis are concerned with: a) The field, b) The EOMs and c) The method of averaging. Depending on the type of the field used, the EOMs give different results for the same atomic/ionic system. Therefore, the Chapters 2 and 3 are dedicated to the study of the statistical properties of a random field and what they mean precisely in the context of a fluctuating FEL pulse. Next, a proper mathematical interface i.e., a set of EOMs, including the atomic parameters (and hence the atom part is also covered here), is needed to study the laser and matter interactions. This is developed in the Chapters 4 and 5. Finally when the laser output is stochastic, one needs certain averaging techniques. Two methods: a quick simpler method as well as a mathematically rigorous method (the main part of the thesis) are developed and applied to different atomic/ionic systems in the remaining chapters (6 to 9). At the end a general conclusion and an outlook are given after which follow necessary appendices. This is the structure and theme of the thesis.

It may be noted that for the sake of clarity, atomic units (a.u.) are also provided where necessary. The values for the experimental observables such as ionization yields and population of states are obtained using double-precision floating point format of the arithmetic numbers involved in the calculations. Runge-Kutta fourth order method (see [39]) was used to solve the coupled partial differential equations.

A brief overview of each of the aforementioned chapters is given below.

- **Chapter 2:** In order to thoroughly deal with the process of statistical averaging later on, a basic overview on different statistical terminology is given in the first part of this chapter. The second part considers the example of chaotic light, to give a practical meaning to these definitions.
- **Chapter 3:** Part of the present thesis uses a simulated FEL pulse. Hence, there is a need to show that the simulated FEL field is in line with the theoretical statistical characteristics, such as those given in the references [35, 40]. So, extending some of the concepts of the previous chapter, this chapter aims to explore explicitly different statistical properties of the simulated FELs.
- **Chapter 4:** To deal with real life experimental scenarios, it is often best practice to use the density matrix (DM) approach introduced by John von Neumann [41]. This chapter aims to derive necessary DM-EOMs which form basic elements for the core analysis of the present work. To this end, the chapter starts with a two-level system interacting with a monochromatic coherent laser, develops amplitude equations and transforms them into DM-EOMs. Then, a general picture of multi-level atom is given, which includes a single autoionizing state (AIS) (for example 2s2p

in the helium atom) and corresponding DM-EOMs are derived in the framework of the Fano picture [42, 43]. These final DM-EOMs, with some added channels of ionization, depending on the context, form a basic set of equations to which the later stochastic averaging methods are applied to.

- **Chapter 5:** The DM-EOMs contain certain parameters which need to be evaluated before embarking upon solving them, for example, photoionization width, autoionization width, resonance energy position, etc. The theoretical methodology to obtain the values of these parameters starting from the calculation of two electron wavefunctions is presented in this chapter.
- **Chapter 6:** The previously derived DM-EOMs equations can be solved to find the observables such as ionization yields. Those equations assume a coherent pulse. When the pulse fluctuates, it affects the way of obtaining the observables as it renders the DM-EOMs stochastic. A couple of averaging methods to solve such stochastic differential equations (SDEs) are presented in this chapter, to understand the general behavior of the interaction of fluctuating laser fields with atoms. The particular case of neon (Ne) and helium (He) are used, where the effects of the interplay of the pulse duration and the coherence time of a fluctuating field on the oscillations (Rabi oscillations) of the yield profile are studied in contrast to a coherent pulse. At the end of the chapter, the difference between the two approaches and their intrinsic limitations are pointed out.
- **Chapter 7:** This chapter constitutes the core material of the thesis. The averaging methods given in the previous chapter are basic and their limitations require one to seek a thorough and all-encompassing (in terms of statistical properties) approach. A perturbative method to model the resonant ionization of atomic systems in a fluctuating laser field is developed. This method is based on an expansion in terms of the multi-time cumulants which are used to describe the field statistical properties. Using this method and a second order truncation of the aforementioned expansion, a set of averaged DM-EOMs are derived and expressed using experimentally accessible quantities such as the radiation's power spectrum and the intensity autocorrelation function.
- **Chapter 8:** The DM-EOMs derived in Chapter 7 are applied in the case of the near-resonant ionization of the helium via the $2s2p$ autoionizing state by a SASE FEL. Comparisons between the averaging methods/Monte Carlo, Fano convolution and simple methods of Chapter 6 are made. The influence of the statistical fluctuations and their strength on the resonant yield profile is discussed. The influence of different shapes of the field first order correlation function is also explored. By considering a set of practically usable set of field parameters, the effects of coherence time on the yield profile are investigated.
- **Chapter 9:** In this chapter, the DM-EOMs derived in the Chapter 7 are restructured to explicitly make visible the pulse parameters such as duration and coherence time.

The restructured EOMs are then applied for the case of a near-resonant ionization of the lithium ion via the 2s2p autoionizing state by a SASE FEL. The influence of statistical fluctuations and the FEL field parameters on the resonant profile is investigated.

- **Chapter 10:** This chapter gives an overall summary of the thesis and a brief outlook.
- **Appendices:** Useful appendices are given at the end.

Publication list of the author based on the thesis work

- Tejaswi Katravulapally and L. A. A. Nikolopoulos, *Perturbative theory of statistically averaged atomic dynamics in fluctuating laser fields*, Phys. Rev. A 102 (5 Nov. 2020), p. 053111.
<https://doi.org/10.1103/PhysRevA.102.053111>
- Tejaswi Katravulapally and Lampros A. A. Nikolopoulos, *Effects of the FEL Fluctuations on the 2s2p Li+ Auto-Ionization Lineshape*, Atoms 2020, 8, 35.
<https://doi.org/10.3390/atoms8030035>
- T Katravulapally, *Ab-initio studies of few photon ionisation of helium*, Journal of Physics: Conference Series 1289 012029 (2019).
<https://doi.org/10.1088/1742-6596/1289/1/012029>
- D. P. W. Middleton, K. N. R. Tejaswi, and L. A. A. Nikolopoulos, “A rate equation method for the sequential double ionisation, including autoionising state excitation, of a noble gas,” Central European Journal of Physics, vol. 11, pp. 1082–1090, Sept. 2013.
<https://doi.org/10.2478/s11534-013-0232-2>.

In fact, this early investigation which was undertaken by the author during summer internship of 2012 forms the reason which kindled the necessary motivation to pursue a doctoral study in the line of work presented in the following pages.

Chapter 2

Basics of statistical description of laser pulses

This chapter aims to give a brief description of some important concepts involving random and stochastic processes. The first section of the chapter deals with the mathematical definitions of some basic terms that are used throughout the thesis. The second section illustrates the physical meaning of these definitions through the example of a chaotic light.

2.1 Basic concepts

2.1.1 Random variable

A function that can take different values in a given situation or in a given set of criteria is called a *random variable* (RV). It differs from a sure variable in the sense that, when the criteria are fixed, the sure variable has a fixed set of values whereas a RV could take different set of values. Consider the famous coin-flip example. If a coin is flipped N times, then the number of heads it could take in the N flips is the RV. Denote it by \mathbf{X} . Then, \mathbf{X} can take all the values from 0 to N i.e, there could have been either 0 heads or 1 heads or... N heads in the N flips. Unless a measurement is performed, none of the values between 0 to N could be surely assigned to \mathbf{X} . Instead, one assigns a probability to the RV \mathbf{X} . Formally, $p(x) = P(\mathbf{X} = x)$ is the probability that \mathbf{X} takes the value x , where $p(x)$ is the probability mass function. In the previous coin-flip example, if $N = 10$, $p(5) = P(\mathbf{X} = 5)$ assigns the probability to the RV \mathbf{X} that the coin takes 5 heads out of total 10 flips.

2.1.2 Probability density function (PDF)

In the previous case, the RV was discrete i.e., its values belonged to a discrete range. Instead, if it were continuous, one assigns a probability density $p(x)$, where $p(x)dx$ gives the probability of \mathbf{X} taking the values in the range of $(x, x + dx)$. This $p(x)$ is often abbreviated as pdf.

2.1.3 Stochastic processes and ensembles

If \mathbf{X} is a RV that changes with time ‘t’, the process or the associated time evolution is called a *stochastic process*. It is denoted by $\mathbf{X}(t)$ and the related pdf is denoted by $p(x, t)$, with the meaning that $p(x, t)dx$ gives the probability of the RV which takes a value within the range $(x, x + dx)$ at a time t . For each measurement in time, the stochastic process yields a set of realizations of $\mathbf{X}(t)$. A collection of such realizations is called an *ensemble*. Formally, if ‘i’ denotes the ith measure in time, then the set $\{ {}^1\mathbf{X}(t), {}^2\mathbf{X}(t) \dots {}^i\mathbf{X}(t) \dots \}$, for all positive integer values of ‘i’ is called an *ensemble* of realizations of $\mathbf{X}(t)$.

2.1.4 Time average vs ensemble average & Ergodicity

An ensemble has different realizations of a random process evaluated at different times. This leads to two concepts of averaging: a) an average of each realization with respect to the duration of time and b) a weighted average of all the realizations of the set of ensemble with respect to the probability distribution function. The former is called a *time average* of the ith realization, denoted by $\langle {}^i\mathbf{X}(t) \rangle_t$ whereas the latter is called an *ensemble average*. An ensemble average is denoted by bold angular brackets $\langle \rangle$ throughout this thesis. So, the ensemble average of $\mathbf{X}(t)$ is denoted by $\langle \mathbf{X}(t) \rangle$. The same concepts extends to a function of RV, say $G[\mathbf{X}(t)]$. The following expressions explicitly formulate the said averages

$$\langle {}^i x(t) \rangle_t = \lim_{T \rightarrow \infty} \frac{1}{2T} \int_{-T}^T {}^i x(t) dt \quad (2.1a)$$

$$\langle G[{}^i x(t)] \rangle_t = \lim_{T \rightarrow \infty} \frac{1}{2T} \int_{-T}^T G[{}^i x(t)] dt \quad (2.1b)$$

$$\langle x(t) \rangle = \int_{\forall x} x p(x, t) dx \quad (2.1c)$$

$$\langle G[x(t)] \rangle = \int_{\forall x} G(x) p(x, t) dx \quad (2.1d)$$

If a random process is such that the time average equals the ensemble average i.e., $\langle {}^i x(t) \rangle_t = \langle x(t) \rangle$ or $\langle G[{}^i x(t)] \rangle_t = \langle G[x(t)] \rangle$, then such a process is called *ergodic*. It physically suggests that a sample function of an ergodic random process contains the whole information related to its statistical ensemble behaviour [44].

2.1.5 Second order probability densities

The pdf $p(x, t)$ contains information of $x(t)$, evaluated at particular time ‘t’. There is no more information. For example, if one needs to obtain $\langle x(t_1)x(t_2) \rangle$ i.e., the ensemble average of product of RVs evaluated at two time points, the $p(x, t)$ can not help. One requires additional probability density function - something that has more information. Let $p(x, t) = p_1(x, t)$ i.e., it is a first order pdf. Then what is required for the afore-

mentioned ensemble average is a second order pdf $p_2(x_1, x_2; t_1, t_2)$ with the meaning that $p_2(x_1, x_2; t_1, t_2)dx_1dx_2$ gives the probability that the RV $x(t)$ takes a value belonging to the range $(x_1, x_1 + dx_1)$ at t_1 and takes a value belonging to the range $(x_2, x_2 + dx_2)$ at t_2 . Higher order pdfs p_3, p_4, \dots have similar extension in logic.

2.1.6 Autocorrelation function (AC)

Using the above second order pdf one can calculate the autocorrelation (AC) function of a RV, which is of high importance in associating its relation at one point of time to that of the other. More generally one should include complex RVs. If one such complex RV is $z(t) = x(t) + iy(t)$ and its pdf is given by $p_2(z_1, z_2; t_1, t_2)$, then $p_2(z_1, z_2; t_1, t_2)d^2z_1d^2z_2$ gives the probability that $z(t)$ takes a value in the elemental area $d^2z_1 = dx_1dy_1$ at t_1 and a value in the elemental area $d^2z_2 = dx_2dy_2$ at t_2 . Autocorrelation of this complex RV, $AC(t_1, t_2)$ is given by:

$$AC(t_1, t_2) = \langle z(t_1)z^*(t_2) \rangle = \int_{\forall z} z_1z_2^*p_2(z_1, z_2; t_1, t_2)d^2z_1d^2z_2 \quad (2.2)$$

By extending the same logic, one can compute higher order pdfs and thus higher order autocorrelation functions.

2.1.7 Stationary random process

A stochastic process is said to be *stationary* if none of its probability densities vary when a time translation is performed i.e., their values are independent on where the origin of time is. Physically it means that the statistical properties of a random process do not vary with time. Formally, this is expressed as [44]:

$$p_n(x_1, x_2, \dots, x_n; t_1, t_2, \dots, t_n) = p_n(x_1, x_2, \dots, x_n; t_1 + \tau, t_2 + \tau, \dots, t_n + \tau) ; \forall \tau \quad (2.3)$$

Generally, the first and second order pdfs play a major role and if one considers only the mean & AC and if they are invariant under time translation, such processes are termed *wide sense stationary*. If all of the PDFs are invariant under time translation, then such random processes are termed *strict sense stationary*. If the random process does not obey either of the aforementioned time-translation equivalence, then it is termed *non-stationary*.

2.2 Chaotic light - an example

Previous sections are a collection of definitions in a generalized mathematical form. The goal of this chapter is to better the understanding of the statistical properties of free electron laser of the next chapter. Before embarking on this goal, a simple physical example incorporating some of the concepts of previously dealt stochastic processes needs to be given. This helps to visualize the concepts better.

The core of this work revolves around classical electromagnetic field (EMF) interacting with quantized atoms. This means, a classical form of EMF, which satisfies the classical

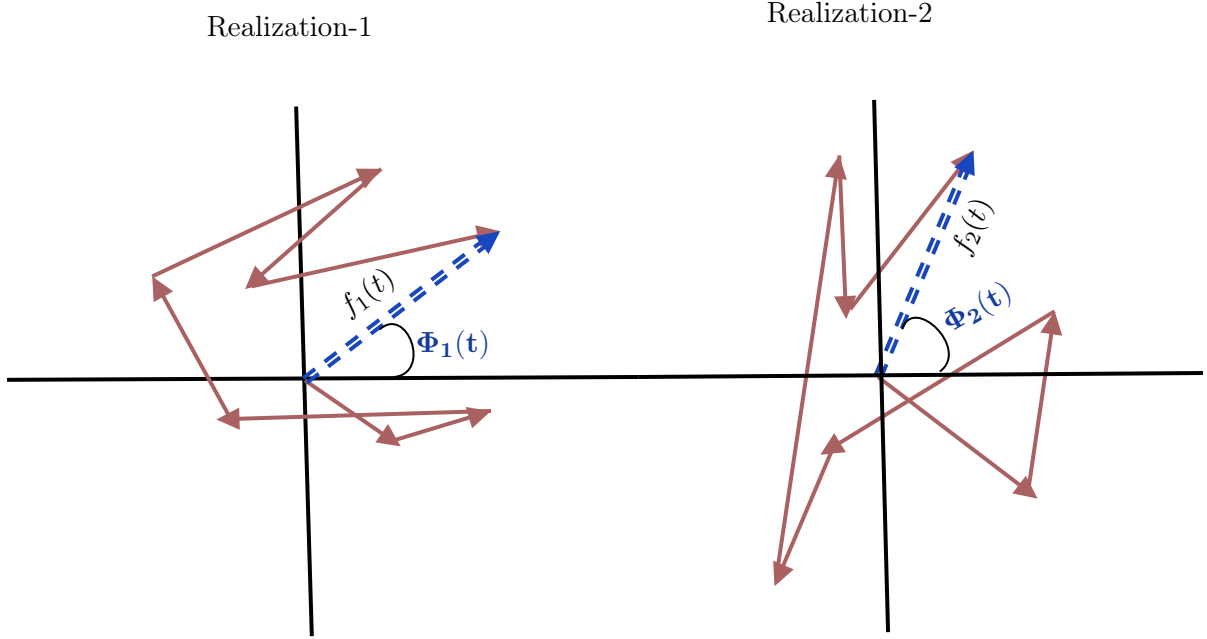


Figure 2.1: Depiction of random fluctuations in an emission of chaotic light by 7 atoms. Each of the 7 random arrows is a phasor i.e., complex exponential associated with one of the 7 radiating atoms. The blue double-dashed arrow is the resultant phasor having a resultant amplitude $f(t)$ and phase $\Phi(t)$. For each realization of the same ensemble of 7 atoms give different field amplitudes $f_i(t)$ and phases $\Phi_i(t)$ for $i = 1, 2$. (The figure is adapted from the 3rd chapter of ref [45] and extended)

Maxwell's equations, is used as the interacting light with a quantum-mechanical atom (i.e., the atomic states are described quantum mechanically). Let the form of such a field be

$$E(\mathbf{r}, t) = E_{0R}(t) \cos(\omega t + \phi(t)) \quad (2.4)$$

where $E(t)$ is the real electric field having a central frequency of ω , phase $\phi(t)$ and real field envelope of $E_{0R}(t)$. Generally the time variable is denoted by t in this work. Though it is the real-field that actually interacts, analytically speaking it is more useful to deal with complex envelopes for their rich mathematical "agility". Therefore, the real electric field ¹ can be modeled using a complex field envelope $\mathcal{E}(t)$, which is dipole approximated, as

$$E(t) = \mathcal{E}(t)e^{i\omega t} + cc \quad ; \quad \mathcal{E}(t) = \frac{1}{2}E_{0R}(t)e^{i\phi(t)}$$

where cc is the complex conjugate (of the first summand). Knowing the behavior of $\mathcal{E}(t)$ helps understanding the behavior of the total field and hence from here on, the concentration will be on $\mathcal{E}(t)$.

Consider a gas of atoms radiating light from its excited state and that amplitude and phase of this radiation changes as and when another atom collides with it. These collisions can be modeled by a random-walk problem [45]. The emitted light as a whole embodies this randomness. This randomness affects the amplitude as well as the phase of the radiation. In such scenarios, it is better to write the radiation emitted by each of the, say N atoms,

¹Note that throughout this thesis i represents the imaginary complex number $i = \sqrt{-1}$

as

$$\mathcal{E}_i(t) = \frac{1}{2} E_{0R}(t) e^{i\phi_i(t)} \quad (2.5)$$

where, the subscript i is to suggest that the above expression is associated with single atom and that there is a whole ensemble of such expressions for all the atoms emitting the light. The final field emitted by the gas of atoms is nothing but a superposition of all the individual fields emitted by each atom. The final form of observed field is

$$\mathcal{E}_{final}(t) = \sum_{i=1}^N \frac{1}{2} E_{0R}(t) e^{i\phi_i(t)} = f(t) e^{i\Phi(t)} \quad (2.6)$$

where, $f(t)$ is the resultant amplitude and $\Phi(t)$ is the resultant phase of the vector sum of all the complex exponentials. These complex exponentials are called *phasors*. Phasor is a complex quantity having an amplitude and a phase. Fig. 2.1 depicts these random phasors for the radiations emitted by 7 atoms (just for example sake only 7 atoms are taken but in real life the number of atoms will be very large) and their net resultant field phasor.

All the atoms under consideration form an ensemble and so also the radiation emitted by them. By the very nature of the randomness, the resultant radiation emitted by this ensemble varies from each batch of radiation emitted i.e., the resultant amplitude $f(t)$ as well as the phase $\Phi(t)$ fluctuate randomly. This gives rise to so called amplitude and phase fluctuations in the field. This is shown by the two figures in Fig. 2.1, where, the left part is for one realization of emission and the right part is for another. It can be clearly seen that (in general) $f_1(t) \neq f_2(t)$ and $\Phi_1(t) \neq \Phi_2(t)$. This results in fluctuations of the total field envelope $\mathcal{E}(t)$.

2.2.1 Ensemble Average

It was just shown that the emitted field can be represented by an ensemble of statistically uncorrelated pulses. Therefore, one can evaluate an ensemble average which is the first characteristic of a random process. An ensemble average was previously defined in Eq. (2.1d). By the very nature of the random-walk problem, the probability of $f(t)$ having a positive real value is equal to that of it having a negative real value. Therefore the ensemble average gives a value of 0.

$$\langle \mathcal{E}(t) \rangle = 0$$

2.2.2 Autocorrelation function and coherence time

To characterize a random process, its AC takes priority after the ensemble average function. The AC is formally defined in Eq. (2.2). But, it should be tailored for the present situation. AC of the emitted electric field means an ensemble average of product of the field with its time shifted complex conjugate. A uniform distribution, over a time interval T , is assumed for the random fluctuations. That means, the probability density to be used is

$$p_{uni}(t) = \frac{1}{T} ; \forall t \in [0, T]$$

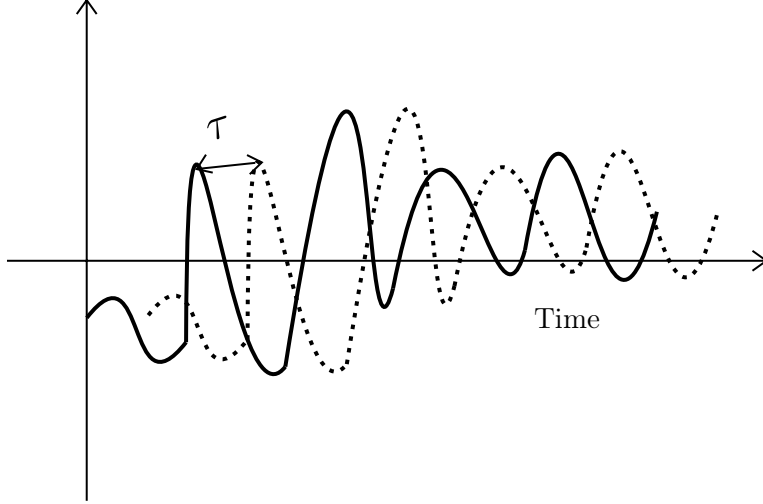


Figure 2.2: Physically understanding the AC of a function. The solid curve is a real random function varying in time. The dotted curve is the same function shifted in time. These can be assumed to be the real parts of the chaotic field envelope and a time-shifted version of itself, respectively. The shift is given by τ . As τ increases, it can be understood from the figure that the magnitude of the product of both the curves decreases.

Therefore, the AC of the field that is given by its definition is

$$\langle \mathcal{E}(t)\mathcal{E}^*(t - \tau) \rangle = \frac{1}{T} \int_T \mathcal{E}(t)\mathcal{E}^*(t - \tau) dt$$

An AC function contains the information as to how well the field is correlated to itself at two different points in time domain. For example, consider a field-envelope whose values are real. In Fig. 2.2 are plotted the example curves denoting such random field envelope and its time-shifted version, having a shift of τ . The value of AC function consists of a time integral of the product of both these functions. That means, the overlap between both the curves determines the value of the integral. Therefore, as τ increases, there is less overlap between the two curves and hence the absolute value of AC function decreases in its value. It has a maximum value at $\tau = 0$.

The duration of τ in which the field stays coherent or has some non-zero value of AC function and after which becomes incoherent or has a close to zero value of AC function, is called *coherence time*, denoted by τ_c . This is defined formally, in terms of the first order degree of temporal coherence function $g_1(\tau)$ (Eq. (2.7a)), by the relation ²

$$\tau_c \equiv \int_{-\infty}^{\infty} d\tau |g_1(\tau)|^2$$

²For non-stationary fields, the coherence time can also be defined by $\tau_c \equiv \int_{-\infty}^{\infty} d\tau \left| \frac{\langle \mathcal{E}(t - \frac{\tau}{2})\mathcal{E}^*(t + \frac{\tau}{2}) \rangle}{\langle |\mathcal{E}(t)|^2 \rangle} \right|^2$

If this τ_c is large, the field stays coherent for longer time shifts. If τ_c is very small, the field loses its coherence properties very fast. For example, filtered sunlight ($\tau_c \sim 2$ fs [46]), synchrotron radiation ($\tau_c \sim 1.6$ fs [47]), FELs ($\tau_c \sim 6$ fs [48]), LEDs ($\tau_c \sim 67$ fs [46]), etc., have very low coherence time. Single mode He-Ne laser on the other hand, for example, is coherent for longer time shifts ($\tau_c \sim 1\mu\text{s}$ [46]). Of course the values given above are only to give a sense of the order of magnitude. The actual values depend on the exact bandwidth as well as the operating central frequency.

2.2.3 Degree of coherence

A degree of measure of coherence can also be characterized by a function called *degree of temporal coherence* [45]. These functions are expressed in terms of normalized AC functions. For a fully coherent light, the first order degree of coherence function take a constant value of 1 (or a constant value for the first order AC function), whereas for a fully incoherent light, they take the value of 0 (or a delta function for the first order AC function). Realistic fluctuations have a value between 0 and 1 (AC function has some finite width and line shape).

The degree of first order temporal coherence $g_1(\tau)$ and the degree of second order temporal coherence $g_2(\tau)$ are expressed in terms of normalized AC functions of the field and its intensity as follows:

$$g_1(\tau) = \frac{\langle \mathcal{E}(t)\mathcal{E}^*(t-\tau) \rangle}{\sqrt{\langle |\mathcal{E}(t)|^2 \rangle \langle |\mathcal{E}(t-\tau)|^2 \rangle}} \quad (2.7a)$$

$$g_2(\tau) = \frac{\langle |\mathcal{E}(t)|^2 |\mathcal{E}(t-\tau)|^2 \rangle}{\langle |\mathcal{E}(t)|^2 \rangle \langle |\mathcal{E}(t-\tau)|^2 \rangle} \quad (2.7b)$$

$$g_2(\tau) = 1 + |g_1(\tau)|^2 \quad (2.7c)$$

2.2.4 Types of correlation shapes

There always exists a bandwidth and hence a line shape for spectrum of emission. This is called *broadening*. Broadly speaking, there exists two types of broadening lineshapes for a chaotic light [45].

Gaussian:

$$|g_1(\tau)_{gauss}| = e^{-\frac{\tau^2}{2\tau_c^2}} \quad (2.8a)$$

$$|g_2(\tau)_{gauss}| = 1 + e^{-\frac{\tau^2}{\tau_c^2}} \quad (2.8b)$$

Lorentzian:

$$|g_1(\tau)_{lorentz}| = e^{-\frac{|\tau|}{2\tau_c}} \quad (2.8c)$$

$$|g_2(\tau)_{lorentz}| = 1 + e^{-\frac{|\tau|}{\tau_c}} \quad (2.8d)$$

The shape of these coherence functions are shown in Figs. 2.3 and 2.4, respectively.

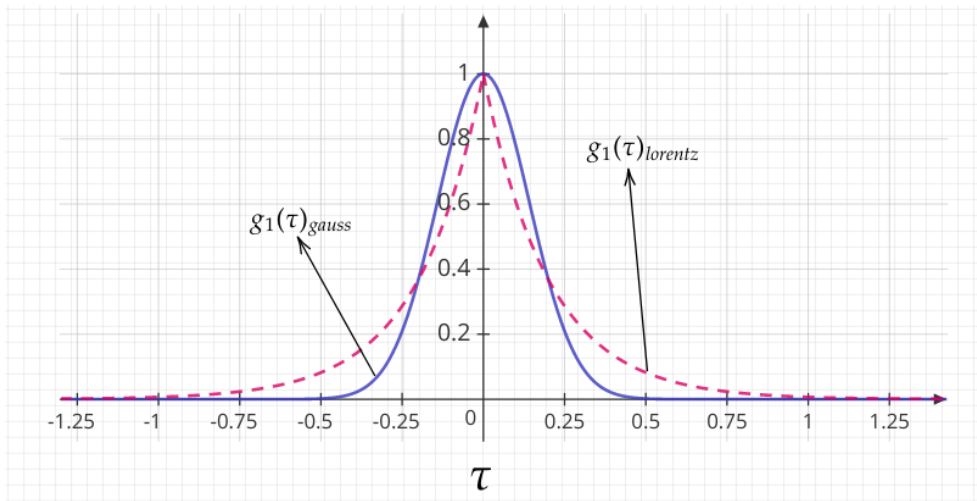


Figure 2.3: Different forms of first order degree of coherence function as a function of the time difference τ (arb. units). $g_1(\tau)_{\text{gauss}}$ has a Gaussian lineshape and $g_1(\tau)_{\text{lorentz}}$ has a Lorentzian lineshape. Both have characteristic coherence time of 0.2 (arb units). The width (root mean square width or full width at half maxima) of these pulses is proportional to the coherence time τ_c

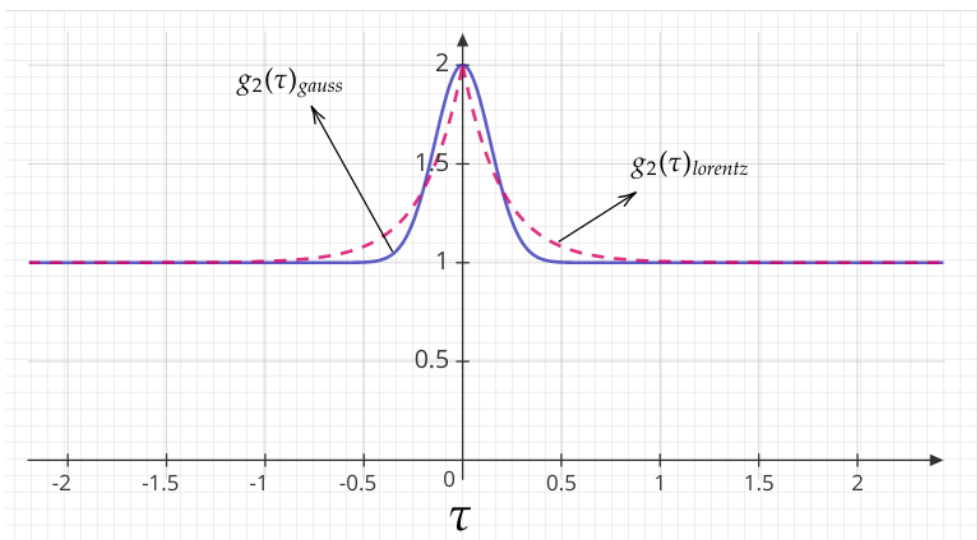


Figure 2.4: Different forms of second order degrees of coherence as a function of the time difference τ (arb units). $g_2(\tau)_{\text{gauss}}$ has a shifted Gaussian shape and $g_2(\tau)_{\text{lorentz}}$ has a shifted Lorentzian shape as per their relation to first order degree of coherence.

2.2.5 Stationarity of the field

The field is said to be stationary if its first and second order correlation functions are not explicitly dependent on time. If the functions, whose degrees of coherence are depicted by Fig. 2.3 and Fig. 2.4, are of the form

$$\langle \mathcal{E}(t)\mathcal{E}^*(t-\tau) \rangle_{gauss} = f_{0g} e^{-\frac{\tau^2}{2\tau_c^2}} \quad (2.9)$$

$$\langle \mathcal{E}(t)\mathcal{E}^*(t-\tau) \rangle_{lorentz} = f_{0l} e^{-\frac{\tau}{2\tau_c}} \quad (2.10)$$

where f_{0g} or f_{0l} are constants of time (constant amplitudes), then the field is said to be *stationary* because of its exclusive dependence on τ alone.

But, there also exists some random processes that have time dependent correlation functions. In those cases the fields are said to be *non-stationary*. Explicit form of non-stationary fields, having a close relation to the previously discussed correlation shapes, can be thought of as follows

$$\langle \mathcal{E}(t)\mathcal{E}^*(t-\tau) \rangle_{gauss} = f_g(t) e^{-\frac{\tau^2}{2\tau_c^2}} \quad (2.11)$$

$$\langle \mathcal{E}(t)\mathcal{E}^*(t-\tau) \rangle_{lorentz} = f_l(t) e^{-\frac{\tau}{2\tau_c}} \quad (2.12)$$

where, all the time dependence is now incorporated into $f_l(t)$ and $f_g(t)$ envelope functions. Thus, such AC functions having explicit time dependence are not stationary. That means, the statistical quantities driving the physical observation change with time and hence also the associated observations.

An example to understand the concept of stationarity is the interference patterns obtained from Mach-Zehnder interferometer [45]. The AC functions occur when one evaluates the average intensity of the output fringes. A time dependent AC will imply that these fringes are also time dependent and will vary in their intensity as time changes. A stationary field produces temporally constant fringe patterns. This kind of variations are to be understood by the terms stationary or non-stationary fields.

2.3 Conclusion

A basic overview of the statistical definitions were provided. These definitions were explained in terms of chaotic light for a better picture. A chaotic light has its amplitude and phase varying randomly. This chapter in conjunction with the Appendix B gives a brief foundation in regard to the statistical nature of FELs and the averaging methods involving their interactions.

Chapter 3

Numerical simulation of the temporal fluctuations of the FEL pulses

The generation of a self amplified spontaneous emission free-electron laser (SASE FEL) pulse, inherently has noise properties. Consider a close-up look at how the radiation is emitted from a FEL generator, as described in ref [10, 14] and depicted in Fig. 3.1. Many electrons randomly arrive at the undulator, a device that generates spatially alternating magnetic fields (represented by the array of red and blue cuboids in Fig. 3.1). As the electron bunches travel across the undulator, they start to oscillate due to the alternating magnetic field and radiate electromagnetic fields. The fields emitted by each electron interact with the other electrons to form so called micro-bunches, a crucial phenomenon for the generation of SASE. This leads to the production of partially coherent radiation. There is a lot of physics involved here. The most important aspect for this work is the statistics of random arrival times of the electrons which in-turn determine the statistics of the emitted radiation field.

A computer simulation of a random SASE FEL field is a complex task. So, a considerable part of this chapter concentrates on the methodology used for the related simulation. The remaining part of the chapter aims to test the statistical nature of the simulated random FEL field through the corresponding analytical expressions derived in refs [35, 37], both in time and frequency domains. The theoretical formulation of the basic statistical concepts was already described in the Chapter 2. The present chapter extends on this and focuses down on the application under study (SASE FEL).

3.1 Gaussian pdf

Consider an electron bunch arriving at some point along its path within the undulator. Each electron of this bunch arrives at a random time, denoted by ' t_j ' which is a *random variable*. This random arrival time of each electron in the bunch has an associated pdf. It can be modelled according to the nature of the inherent randomness. As suggested in

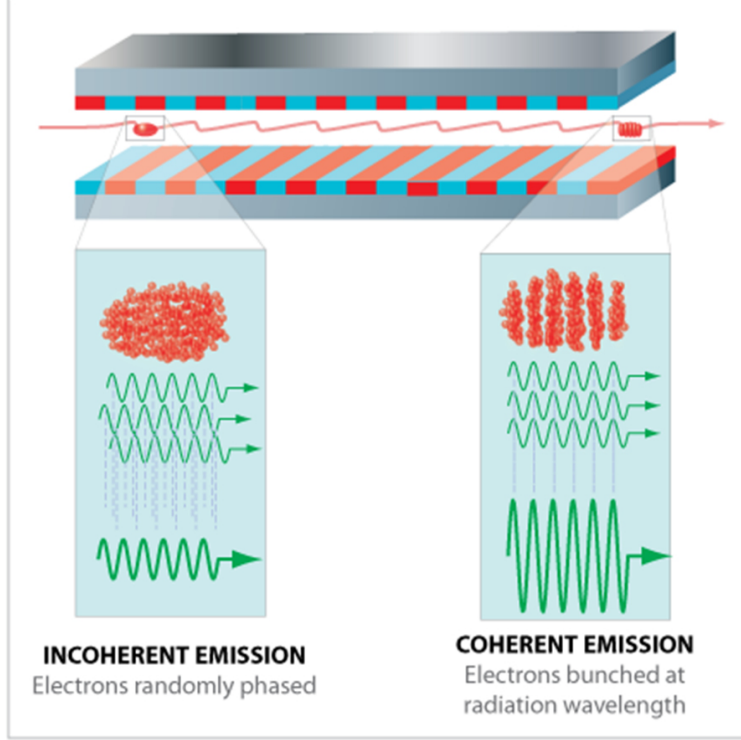


Figure 3.1: Schematic showing the process of micro bunching and generation of coherent radiation as the randomly arriving electrons pass through the length of the undulator. The figure is adapted from reference [10].

[35], a Gaussian form often fits well the said distribution in a FEL pulse. A Gaussian pdf ($p_{gauss}(t_j)$) of the random time variable ‘ t_j ’ is given by:

$$p_{gauss}(t_j) = \frac{1}{\sqrt{2\pi}\tau_b} \exp\left(-\frac{t_j^2}{2\tau_b^2}\right) \quad (3.1)$$

where, τ_b is the standard deviation or temporal width of the probability distribution and $p_{gauss}(t_j)dt_j$ gives the probability that an electron of the bunch arrives at the undulator entrance between the times t_j and $t_j + dt_j$.

3.2 FEL field and amplitude

The generated field grows along the path length z of the undulator. The point of consideration here is the time evolution and hence the field at a fixed z (exit of undulator). Given that the arrival time of the electrons is distributed via Eq. (3.1), a FEL field $E(t)$ and its complex envelope $\mathcal{E}(t)$ (similar to the general form discussed in the section 2.2), at a fixed point of the undulator, are modeled as [35]:

$$E(t) = \mathcal{E}(t) \exp(i\omega t) + cc \quad (3.2a)$$

$$\mathcal{E}(t) = \mathcal{E}_0 \sum_{j=1}^{N_e} \exp\left(i\omega t_j - \frac{(t - t_j)^2}{4\tau_{wp}^2} \chi^*\right) \quad (3.2b)$$

Parameters	Meaning	Simulation	Typical FEL
τ_p	pulse duration	7 fs	45 fs [49]
τ_c	coherence time	0.5 fs	3.9 fs [49]
ω	central tunable frequency	60.16 eV	20 eV - 20 keV [10]
τ_{wp}	wavepacket width	0.29 fs	0.95 fs [49]
τ_b	electron bunch duration	4.99 fs	< 20 fs [50]
\mathcal{I}_0	peak intensity	$10^{13} - 10^{15}$ W/cm ²	up to 10^{20} W/cm ² [51]
N_e	number of electrons in a bunch	1000	$\geq 10^6$ [10]
L	number of ensembles	300	-

Table 3.1: FEL field parameters used in simulation as well as reference typical values.

where \mathcal{E}_0 is the peak amplitude of the complex field envelope, N_e is the number of electrons in a bunch, τ_{wp} is the characteristic wavepacket width, ω is the central tunable resonance frequency and the complex chirp factor χ is given by $1 - \frac{\iota}{\sqrt{3}}$, where $\iota = \sqrt{-1}$.

To understand and connect the dots between the previously defined statistical definitions and FEL pulses, one needs to consider Eqs. (3.2a) and (3.2b) against the background of the role played by the random variable t_j . Table 3.1 gives the parameters used in obtaining all of the plots (Fig. 3.2 - Fig. 3.10) in this chapter. In the up-coming chapters detailing the averaging methods, the most used parameters from the aforementioned table are pulse duration (τ_p), coherence time (τ_c) and central frequency (ω). The other parameters are used only in the MC method.

3.3 FEL wavepacket

The formulation in Eq. (3.2b) suggests that the model of the field envelope includes a superposition of the random Gaussian wavepackets emitted by each of the N_e electrons. One such wavepacket has the form

$$\mathcal{E}_j(t) = \mathcal{E}_0 \exp \left(i\omega t_j - \frac{(t - t_j)^2}{4\tau_{wp}^2} \chi^* \right)$$

where $\mathcal{E}_j(t)$ implies the complex envelope of the j^{th} wavepacket emitted by the j^{th} electron in the bunch. This wavepacket has an envelope with the real part having a Gaussian form and a fast oscillating sinusoidal part. The Gaussian envelope has a width proportional to τ_{wp} and the central tunable resonance frequency ω , characterising the fast oscillating part. In Fig. 3.2 one can see the real part of this simulated wavepacket plotted in the time domain. A Gaussian fit, with a width and amplitude that matches the parameters of the real part of the envelope has also been plotted for reference. The central time of this wavepacket is t_j which is nothing else but the random arrival time of j^{th} electron.

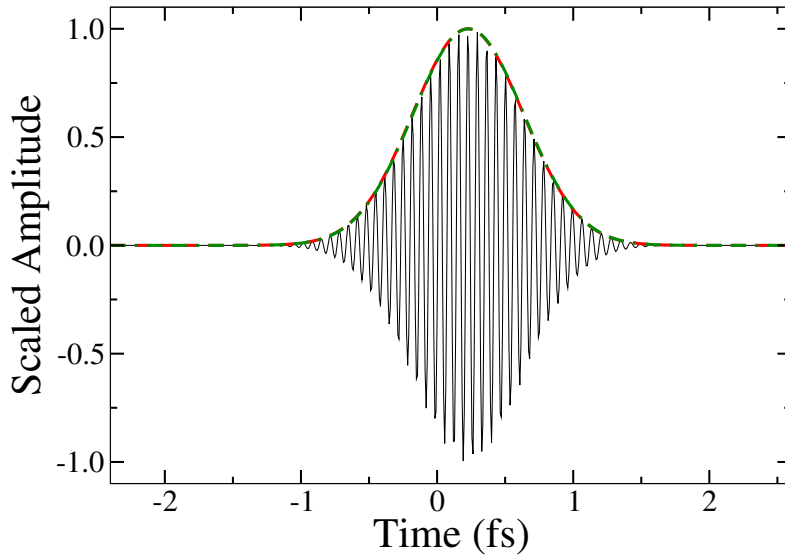


Figure 3.2: This plot shows the real part of a random FEL wavepacket. Its fast oscillating part due to the tunable resonance frequency $\omega = 60.16$ eV (2.211 a.u.) is shown with a black-solid curve whereas the envelope is shown with a red-dashed curve, having a width proportional to $\tau_{wp} = 0.29$ fs (11.99 a.u.). A reference Gaussian curve (green-dot-dashed) has also been fitted to show that the envelope is indeed Gaussian.

3.4 Generation of random wavepackets

3.4.1 Random numbers

To generate a random field, one first needs to generate a set of random wavepackets for which it is needed to generate a set of random time series $\{t_j\}$ according to the Gaussian distribution given by Eq. (3.1). This is the essence of the procedure to generate a random time profile for Eq. (3.2b). Eq. (3.1) suggests that when $t_j = 0$, one obtains a maximum probability of its occurrence and as the value of t_j moves away from 0, the probability of its occurrence decreases.

Speaking in terms of computation it is difficult to reproduce an experimental FEL pulse. But, with the presently available tools, one can closely mimic the statistics involved and try to reproduce a simulation of an FEL pulse. So, the task at hand is two-fold: first to simulate a fluctuating FEL pulse and second to check its statistical behavior. Both these tasks are accomplished in this work.

The thesis utilises the C++11 standard version of the C++ programming language to model and generate the desired random FEL pulse. As pointed earlier, one needs to first have a set of random numbers to be associated with random arrival times of electrons. For this task, C++11 offers two tools: a random number engine and a random distribution.

- **Engine:** The job of the engine is to generate numbers that are very hard to predict. As a computer is a deterministic device, the numbers it generates are pseudorandom in nature (not completely random per se). But certain algorithms make sure that

the randomness is of high quality. There are some good predefined random engines available in the library of c++ some of which are given in reference [52]. The thesis uses an engine called ‘*default_random_engine* f (seed)’ which serves the purpose fairly well as it is a balanced option among the available engines in terms of computational cost and randomization. The ‘f’ is the engine’s name (user defined) and the seed helps increase the randomness every time the engine is activated. For example the seed can be the clock’s time in a computer or the output of another random number generator, etc.

- **Distribution:** With the engine ready, there needs to be a distribution pattern assigned to the engine. Uniform distribution, normal distribution, etc., are some of the common distributions of random numbers. This brings in context to the generation of the random numbers. As pointed earlier, one requires Gaussian distribution in order to simulate an FEL field. This is achieved by utilising a predefined distribution function ‘*normal_distribution*<type> d (μ, σ)’ where ‘d’ is the user-defined name for distribution, μ is the mean and σ is the variance of the Gaussian distribution. In the view of Eq. (3.1), $\mu = 0$ and $\sigma = \tau_b$.

The engine will then generate random numbers which are distributed with a zero mean and τ_b variance and these numbers change every time they are generated due to the ever changing seed.

Coming back to the task of generating random FEL pulses, consider a set of $N_e = 1000$ random numbers (t_j) generated using the above generators (engine + distribution). To check the probability distribution of the generated numbers, one can divide the total time span into $N_b = 100$ bins. A bin is a time interval with a certain probability of occurrence associated with it. Any randomly generated number has to fall in one of the N_b bins and hence every number is associated with a certain probability p_i of occurrence, which is given by the number of random numbers in the corresponding bin (frequency) divided by total number of random numbers generated i.e.,

$$p_i(t_j) = \frac{\text{frequency of } t_j}{N_e} \quad (3.3)$$

For a single set of random numbers t_j , the black dash-dotted plot in Fig. 3.3 shows the probability of occurrence of each of the t_j in 100 bins.

When a different set of $\{t_j\}$ is generated, the numbers fall into different bins and hence the probability associated with the bins change. This is the concept of ensembles seen in Chapter 2. Let L be the number of such ensembles. When one takes an average of all such L probability distributions of occurrence of generated numbers, one achieves the ideal Gaussian distribution of the numbers given by Eq. (3.1). In Fig. 3.3, the red dashed curve is obtained when the average is taken over $L = 300$ different realizations of t_j . A zero mean Gaussian fit with the standard deviation of $\tau_b = 4.99$ is also plotted as the green-dashed curve to suggest the trend. So, the random numbers generated are indeed of Gaussian nature and hence can be inserted in Eq. (3.2b) to generate the random field.

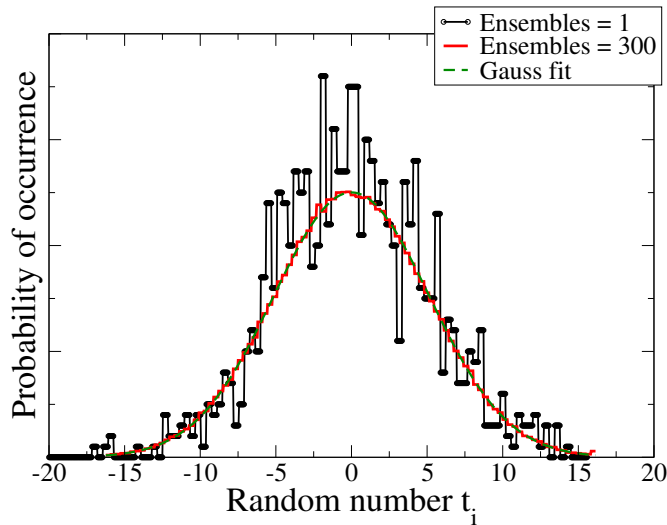


Figure 3.3: Probability distribution for $N_e = 1000$ random variables which are Gaussian distributed with zero mean and variance $\tau_b = 4.99$ is depicted in the black dot-dashed curve. Number of bins used is 100. An ensemble average over 300 ensembles is depicted as the red curve whereas the ideal Gaussian distribution is depicted as the green dashed curve.

3.4.2 Random wavepackets

Utilising a single set of $\{t_j\}$ generated from the above method, ten wavepackets are simulated and plotted in Fig. 3.4. Though each t_j , the central time of each wavepacket, is sequentially evolved in time, as they take random values, each of the pulses can be seen to be randomly spaced in time. This results in a temporally fluctuating profile as discussed later on.

3.5 Field and intensity fluctuations

The previously described randomly spaced Gaussian wavepackets, centered at random times t_j , can be superposed with each other in time. This results in a continuously fluctuating profile whose real part is plotted in Fig. 3.5 where approximately 1000 randomly simulated Gaussian wavepackets were superposed. This profile fluctuates from shot to shot in a FEL.

As it is intensity that is measured by photo-detectors in an experiment, it will therefore be of interest to know how the intensity profile of a FEL pulse fluctuates. The instantaneous intensity of a pulse is given by

$$\mathcal{I}(t) = \mathcal{E}(t)\mathcal{E}^*(t) \quad (3.4)$$

One FEL ‘realization’ or one FEL ‘shot’ implies a superposition of the intensities of individual random wavepackets obtained from one set of arrival times of the electrons. In Fig. 3.6, the random instantaneous intensity profile, calculated with Eq. (3.4) for five different realizations are simulated and plotted. One can see how spiky and random the

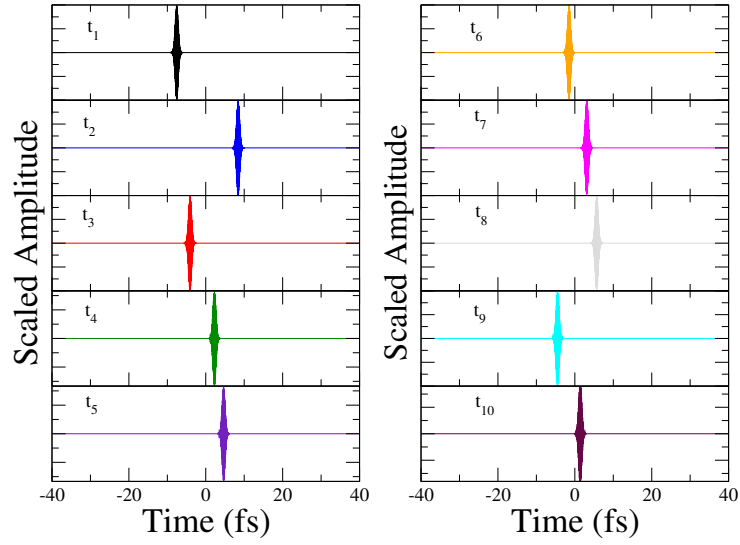


Figure 3.4: Real part of a set of 10 random FEL wavepackets, separated temporally according to the Gaussian distribution of the arrival times of the associated electrons at the entrance of the undulator, is shown here. The center of each wavepacket denotes the arrival time of j^{th} electron, denoted by t_j . The generation of the wavepackets follow chronological ordering i.e., the values of $i = 1, 2, \dots, 10$ denote particular increasing times at which they were generated. The disordered placement of the wavepackets in the figure suggest the randomness involved in their arrival times.

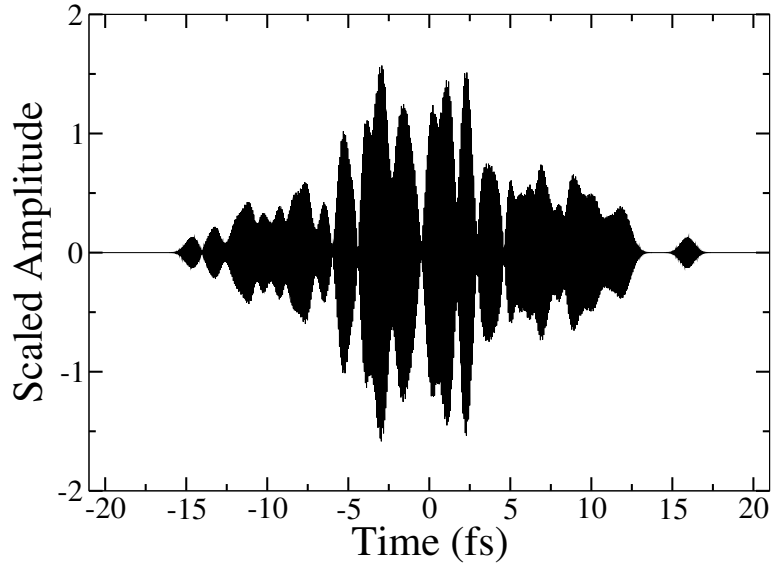


Figure 3.5: Superposition of a thousand random wavepackets resulting in a fluctuating profile of an FEL field whose real part is plotted here. The tunable resonance frequency $\omega = 60.16 \text{ eV}$ (2.211 a.u.) and the Gaussian envelope of each random wavepacket has a width proportional to $\tau_{wp} = 0.29 \text{ fs}$ (11.99 a.u.). Coherence time τ_c of the pulse is 0.5 fs.

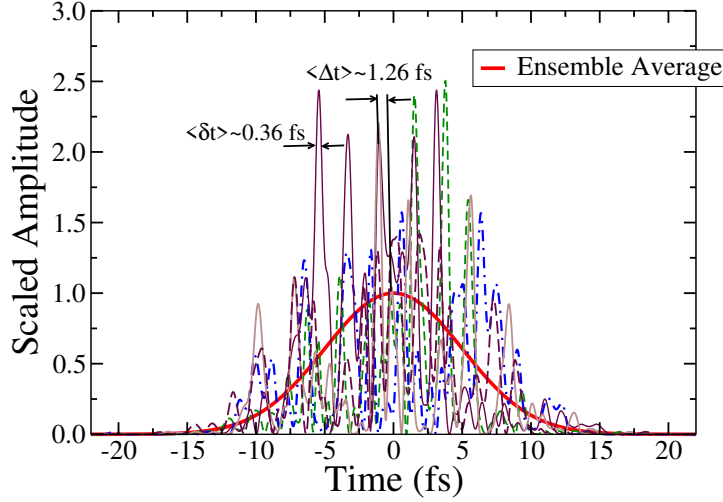


Figure 3.6: Superposition of intensities of a thousand random pulses, for five different pulse realizations. The tunable resonance frequency $\omega = 60.16 \text{ eV}$ (2.211 a.u.) and the Gaussian envelope of each random wavepacket has a width proportional to $\tau_{wp} = 0.29 \text{ fs}$ (11.99 a.u.). The red solid curve shows the ensemble average over many ensembles.

profile is from shot to shot. This is one of the characteristics of the SASE FELs. It is to be noted that the scaling of the corresponding field and intensity plots is chosen such a way that the peak magnitude of the ensemble average of the intensity profile is 1.

One of the checks one can perform at this point, to see if the generated single shots are indeed emulating single shots of SASE FELs, is to see if the average spike width and average spike separation of a single shot FEL intensity profile give the theoretical values in line with the analytical expressions derived in [35]. Using the parameters of Table 3.1, one obtains

- **Average spike separation:** $\langle \Delta t \rangle \approx \sqrt{2\pi} \times \sqrt{3}\tau_{wp} \approx 1.26 \text{ fs}$.
- **Average spike width:** $\langle \delta t \rangle \approx \sqrt{\frac{3}{2}}\tau_{wp} \approx 0.36 \text{ fs}$.
- **Number of random spikes:** This is given by $\sqrt{\frac{2}{3}}\frac{\tau_p}{\tau_{wp}} \approx 19$.

Here, the non-bold angular brackets denote the average over the peaks of single profile rather than over an ensemble. These three criteria are satisfied in the generated single shot FEL profiles as depicted in Fig. 3.6.

3.6 Degree of temporal coherence: 1st and 2nd order

Before moving to the topic of the degree of coherence, it is better to explain how the ensemble average is computed.

3.6.1 Ensemble average

Consider a random time signal $\mathbf{X}(t)$ where ‘t’ is the random variable. Though it is ideally continuous, for computation sake, it is sampled into discrete set of $\mathbf{X}_i(t_j)$ where the index ‘i’ is for the i^{th} ensemble and ‘j’ is for the discretized random variable. An ensemble average of $\mathbf{X}(t)$ with a probability distribution of its random variable as $p(t)$ is then defined in discrete form as

$$\langle \mathbf{X}(t) \rangle = \frac{1}{L} \sum_i \sum_j p_i(t_j) \mathbf{X}_i(t_j) \quad (3.5)$$

Similarly, one computes the autocorrelation function of a discretized function as

$$\langle \mathbf{X}(t) \mathbf{X}^*(t - \tau) \rangle = \frac{1}{L} \sum_i \sum_j p_i(t_j) \mathbf{X}_i(t_j) \mathbf{X}_i^*(t_j - \tau) \quad (3.6)$$

with L as the number of ensemble realizations and $p_i(t_j)$ as the frequency of occurrence defined by Eq. (3.3). Inserting the expression of $\mathcal{E}(t)$ from Eq. (3.2b) into the above equation, one can compute the autocorrelation of the FEL field amplitude which helps with the computation of the degree of coherence.

3.6.2 Degree of coherence:

In the previous chapter a measure of coherence was defined in terms of normalised AC functions. An autocorrelation function of a FEL field contains the information as to how well the FEL is correlated to itself at two different points in time. This information is the core of the coherence properties. The FEL field’s degree of first order temporal coherence $g_1(\tau)$ and the degree of second order temporal coherence $g_2(\tau)$ are expressed in terms of normalised autocorrelation functions of field and intensity as follows:

$$g_1(\tau) = \frac{\langle \mathcal{E}(t) \mathcal{E}^*(t - \tau) \rangle}{\sqrt{\langle |\mathcal{E}(t)|^2 \rangle \langle |\mathcal{E}(t - \tau)|^2 \rangle}} \quad (3.7a)$$

$$g_2(\tau) = \frac{\langle |\mathcal{E}(t)|^2 |\mathcal{E}(t - \tau)|^2 \rangle}{\langle |\mathcal{E}(t)|^2 \rangle \langle |\mathcal{E}(t - \tau)|^2 \rangle} = \frac{\langle \mathcal{I}(t) \mathcal{I}(t - \tau) \rangle}{\langle \mathcal{I}(t) \rangle^2} \quad (3.7b)$$

$$g_2(\tau) = 1 + |g_1(\tau)|^2 \quad (3.7c)$$

These expressions can be computed as explored earlier. Analytically, for the present case of random FEL field, as in Eq. (3.2b), one can utilize the simplified expression given in reference [35] for the autocorrelation of the field amplitude of Eq. (3.2b)

$$\langle \mathcal{E}(t) \mathcal{E}^*(t - \tau) \rangle_{gauss} = \frac{N_e \tau_{wp} \mathcal{E}_0^2}{\sqrt{\tau_b^2 + \tau_{wp}^2}} e^{-\frac{t^2 + (t - \tau)^2}{2\tau_p^2}} e^{-\frac{i(t^2 - (t - \tau)^2)}{2\sqrt{3}\tau_p^2}} e^{-\frac{\tau^2}{2\tau_c^2}} \quad (3.8)$$

where, \mathcal{E}_0 is the peak amplitude of the FEL field, N_e is the number of electrons in a bunch, τ_{wp} is the characteristic wavepacket width, τ_b is the standard deviation of the normal

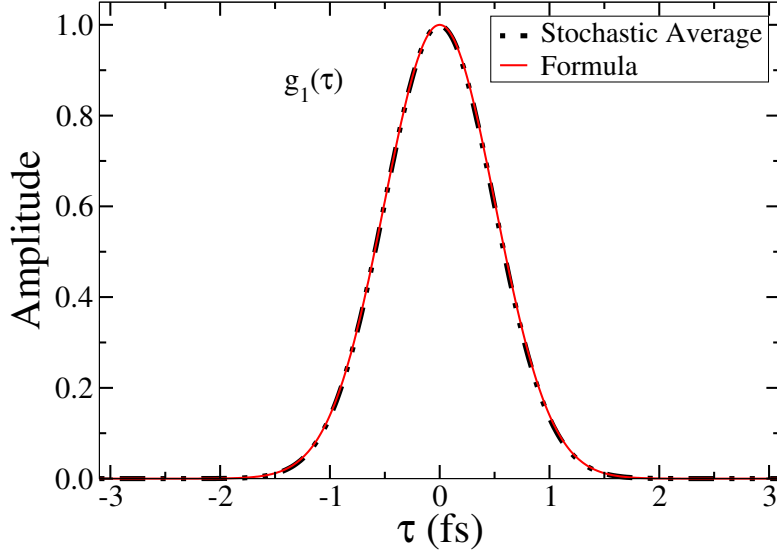


Figure 3.7: Black-dashed curve: Simulated first order coherence function having parameters of Table 3.1. Red-solid curve: Analytical Gaussian fit having a width of $\tau_c = 0.5$ fs.

distribution used and $k = 1/\sqrt{3}$. They are related [35] to each other through:

$$\tau_p = \sqrt{2(\tau_b^2 + \tau_{wp}^2)} \quad ; \quad \frac{\sqrt{2}\tau_b}{\tau_p} = \frac{\sqrt{3}\tau_{wp}}{\tau_c} \quad (3.9)$$

For brevity of computations, one can proceed to construct a scaled field amplitude and then compute the coherence functions. Begin by defining a scaled field amplitude $\epsilon(t)$, as

$$\mathcal{E}(t) = \mathcal{E}_0 \sqrt{\frac{\sqrt{2}N_e\tau_{wp}}{\tau_p}} e^{-\frac{\chi^* t^2}{2\tau_p^2}} \epsilon(t) = \mathcal{E}_0(t)\epsilon(t) \quad (3.10)$$

With this scaled field amplitude and using the Eq. (3.8), the $g_1(\tau)$ and $g_2(\tau)$ turn out to have the following stationary profile:

$$g_1(\tau) = \langle \epsilon(t)\epsilon^*(t-\tau) \rangle = e^{-\frac{\tau^2}{2\tau_c^2}} \quad (3.11a)$$

$$g_2(\tau) = \langle |\epsilon(t)|^2 |\epsilon(t-\tau)|^2 \rangle = 1 + e^{-\frac{\tau^2}{\tau_c^2}} \quad (3.11b)$$

In Fig. 3.7, the degree of first order coherence function, simulated using 1000 random times, 1000 bins and 300 ensembles is plotted. The Gaussian form obtained through the end-formula of Eq. (3.11a) is also plotted. In Fig. 3.8, the degree of second order coherence function simulated using same set of parameters is plotted and compared with the shifted Gaussian form obtained by Eq. (3.11b). For all these simulations, the parameters are taken from Table 3.1. In both cases, one can see that the theoretical and simulated graphs for the first and second order degree of temporal coherence match closely.

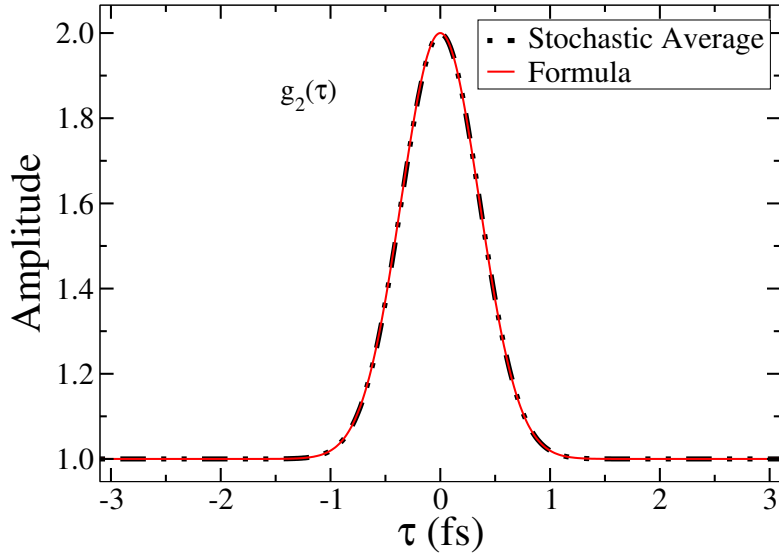


Figure 3.8: Black-dashed curve: Simulated second order coherence function, having parameters of Table 3.1. Red-solid curve: Analytical shifted-Gaussian form obtained from Eq. (3.11b) having a width of $\tau_c = 0.5$ fs

3.6.3 Ensemble average of FEL field intensity

Different realizations of intensity profiles in Fig. 3.6 constitute a family of ensemble of the random FEL field intensity. This implies that an ensemble average of intensity forms one of the primary tools to probe the statistical nature of FEL fluctuations. One can compute the ensemble average of intensity by making $\tau = 0$ in the computed AC function. One can also obtain the analytical expression of the same, from Eq. (3.8) evaluated at $\tau = 0$ i.e.,

$$\langle \mathcal{I}(t) \rangle = \langle \mathcal{E}(t) \mathcal{E}^*(t) \rangle = \frac{\sqrt{2} N_e \tau_{wp}}{\tau_p} \mathcal{E}_0^2 e^{-\frac{t^2}{\tau_p^2}} = \mathcal{I}_0 e^{-\frac{t^2}{\tau_p^2}} \quad (3.12)$$

Fig. 3.9 shows both of these simulated and analytically plotted curves for the ensemble average of the FEL intensity. The closeness of the curves suggest the accuracy of the simulations. In Fig. 3.6 the ideal ensemble average was shown as the red solid curve which indeed shows the averaged nature of the intensity fluctuations.

3.6.4 Non-Stationarity and non-ergodicity of the FEL field

Finally, one can see that the mean of FEL field intensity, as given in Eq. (3.12) and the autocorrelation of FEL field, as given in Eq. (3.8) are both time-dependent. This renders the processes involving random FEL pulses non-stationary. That means, as time proceeds, the statistical properties of FELs also change and vary. Also, the time average of the field is not equal to its ensemble average. One time averaged single shot does not contain information regarding the whole set of ensemble of shots. Therefore FELs are non-ergodic.

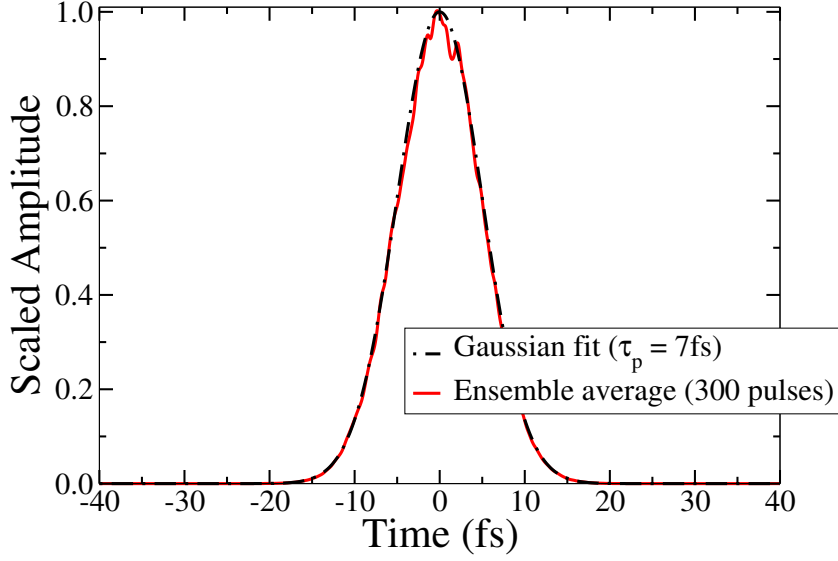


Figure 3.9: Red solid curve: Ensemble average of the instantaneous intensity $\langle |\mathcal{E}(t)|^2 \rangle$ over three hundred pulse shots, with parameters of Table 3.1. Black dot-dashed curve: An analytical Gaussian fit of Eq. (3.12) with a width of $\tau_p = 7$ fs (289.38 a.u.).

3.7 Frequency domain

Until now, the simulated FEL field's characteristics were explored in the time domain. This is because for the later input of an FEL pulse in the concerned EOMs, it is the random time profile as well as the ensemble averaged time profile that are needed. But it is a well known fact that the time-domain characteristics manifest into frequency domain characteristics via the Fourier transform and the experimental observables are often measured in frequency domain. So, this section is dedicated to see if the frequency domain characteristics of the simulated random FEL pulse follows the theoretical implications suggested by Krinsky and Li in reference [35].

3.7.1 Discrete Fourier Transform

When a time signal $f(t)$ is defined over a continuous time variable 't', its Fourier transform (represented by \mathcal{F}) is given by

$$F(\omega) = \mathcal{F}[f(t)] = \int_{-\infty}^{\infty} f(t)e^{-i\omega t} dt \quad (3.13)$$

where ω represents the frequency domain variable. The implementation of the above form in a computer is not possible due to the involvement of continuous time or continuous frequency variables. It is the discrete Fourier transform (DFT) that is to be used in place of the continuous Fourier transform. For a signal $x(n)$, its DFT $X(k)$, is obtained as

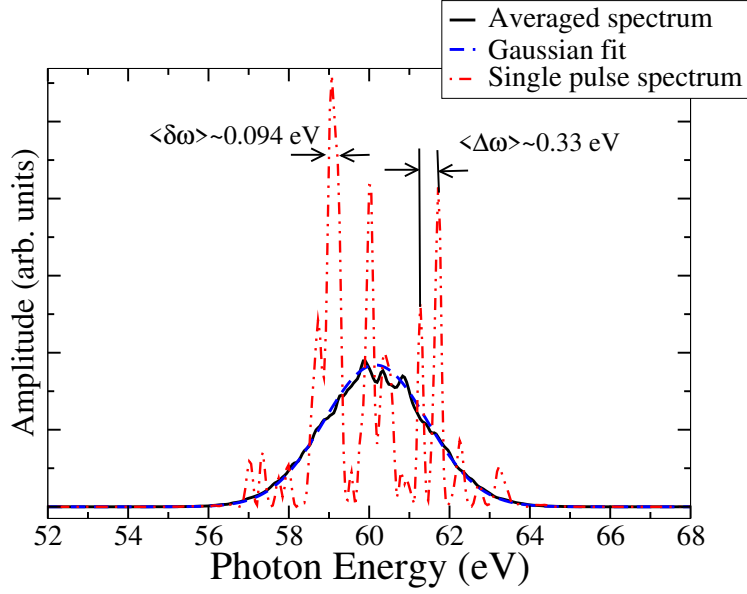


Figure 3.10: Frequency spectrum of a pulse with central frequency $\omega = 60.16 \text{ eV}$, coherence time $\tau_c = 0.5 \text{ fs}$ and total pulse duration $\tau_p = 7 \text{ fs}$. The black-solid curve represents the averaged spectrum, blue-dashed curve is its Gaussian fit with a width of $\sim 1.31 \text{ eV}$ while the red dot-dashed curve is the spectrum corresponding to one of the FEL pulse's single shot realizations.

follows:

$$X(k) = \sum_{n=0}^{N-1} x(n) e^{-\frac{2\pi i}{N} kn} \quad (3.14)$$

The ω is related to k by $\omega = 2\pi k$ and t is related to n by $t = n/N$. As the sample size N increases, the DFT profile approaches the Fourier transform profile of Eq. (3.13).

3.7.2 Intensity profile

One can first generate a random time domain FEL field $\mathcal{E}(t)$ as suggested in the previous sections and then use Eq. (3.14) to generate a frequency domain FEL field $\mathcal{E}(\omega)$. But it is the intensity that is measured and one can use the following relation to obtain the frequency domain intensity.

$$\mathcal{I}(\omega) = \mathcal{E}(\omega)\mathcal{E}^*(\omega) \quad (3.15)$$

Just like the single-shot $\mathcal{I}(t)$ profile obtained in Fig. 3.6, the frequency domain FEL pulse also should show random spikes and shot to shot variation in the profile shape. One of the single shots frequency domain random intensity profile is plotted in Fig. 3.10 (as a red double-dot dashed curve). Krinsky and Li suggest in [35] that the average of the intensity spike width and their spacing in the frequency domain relates to the pulse duration. The quantitative relations are given below,

- **Average spike separation:** $\langle \Delta\omega \rangle \approx \frac{\sqrt{\pi}}{\tau_p} \approx 0.33 \text{ eV}$.
- **Average spike width:** $\langle \delta\omega \rangle \approx \frac{1}{\tau_p} \approx 0.094 \text{ eV}$.

FEL Facilities	Location	τ_{fwhm}	ω	$\frac{\Delta\omega}{\omega}$	PPS	PE
FLASH	Hamburg	50-200 fs	30-300 eV	1%	5000	10–500 μJ
FERMI	Trieste	150 fs	20-300 eV	.1%	10	< 30 μJ
LCLS	Stanford	2-100 fs	.25-10 keV	.2-.5%	120	2–6 mJ
SACLA	Hyogo	20-30 fs	4.5-15 keV	.2-.25%	60	80–250 μJ
SwissFEL	Canton of Aargau	1-20 fs	2-12 keV	.2-.5%	100	.01-1 μJ
EU XFEL	Hamburg	<100 fs	.25-25 keV	.1%	27000	0.03-8.5 μJ

Table 3.2: Important FEL facilities and some of the related field parameters, for relative comparison, taken from references [5, 10, 53–55]. τ_{fwhm} is the FWHM pulse duration, ω is the central operating frequency, $\frac{\Delta\omega}{\omega}$ is the relative fractional bandwidth, PPS is the number of pulses per second and PE is the pulse energy.

where the non-bold angular brackets suggest an average over the number of spikes. These are depicted in Fig. 3.10. When 300 such random pulses are chosen and averaged, the black solid curve is obtained. It is fitted with a Gaussian curve of width 1.31 eV. Let the spectral bandwidth of averaged FEL pulse be σ_ω . This relates (see [35]) to the time domain parameters via

$$\sigma_\omega = \frac{1}{\tau_{wp}\sqrt{3}} = \frac{\tau_p}{\tau_c\tau_b\sqrt{2}} \quad (3.16)$$

Inserting the values from Table 3.1, one should obtain the spectral bandwidth to be $\sigma_\omega \approx 1.31$ eV which is what the Gaussian fit suggests. Therefore, the ensemble average of the frequency domain intensity profile not only emulates single-shot spectrum of SASE FEL, but also gives good ensemble average profiles. This suggests with certainty that the frequency domain characteristics in the simulation of the random FEL pulses are all in order.

3.8 Conclusion

The goal of the thesis is to study the atomic/ionic interactions under randomly fluctuating FELs. So it is inevitable to study the nature of FELs in the light of statistical definitions. As the following chapters utilize a simulated FEL pulse, the accuracy of such simulated field needs to be tested in comparison to the theoretical definitions. These aspects were discussed in the present chapter. Starting from the modelling equation of random FEL, the chapters went on to explain its subtleties and dived into the characterization of the FEL in terms of ensemble average and coherence functions. It was shown that the simulated FEL indeed shows high accuracy in terms of the statistics involved not only in the time domain, but also in the frequency domain. With such a good simulated FEL at hand, one can insert it into the DM-EOMs, to be developed soon, and study the affects of fluctuations of FELs on their interactions with atomic/ionic systems. To give a practical perspective, Table 3.1 and Table 3.2 show the parameters used in some of the important FEL facilities.

Chapter 4

Density matrix equations of motion

Chapter 3 described the statistical nature of FELs. This is the first part in the goal of understanding the interaction dynamics of FEL fields with matter. The next part is to formulate a mathematical interface that allows one to probe it. A proper construction of the necessary tools involving the statistical fluctuations of FELs is considered in Chapters 6 and 7. Prior to that, a bridge needs to be constructed in order to cross the study of interaction of coherent fields over to that of stochastic fields. The present chapter aims to lay the foundations for this bridge.

The plan is to first start with a simple system - e.g. a two-level atom - and see how a quasi-monochromatic field interacts with it. Understanding this is the basic brick for all the concepts to be explored later. After having briefly touched upon the aforesaid topic, the scenario is extended to include a set of continuum states in which is embedded a discrete autoionizing state (AIS) (i.e., a bound state degenerate with the surrounding continuum) in the atomic system. The latter extension is to cater for the study of resonant photoionization processes. The said formulation allows one to deal with observables like ionization yield or kinetic energies of ejected electrons, etc., of real life experiments. Both the two-level system (TLS) and the extended systems are modeled using amplitude equations as well as density matrix (DM) equations. But as one proceeds to the later chapter(s) of the thesis, they inevitably stick to DM equations for the simple reason that amplitude equations are no longer solvable for an interacting stochastic fields involving ensembles. For this reason and for the reason of giving a clear idea as to how the involvement of stochastic fields affects the mathematical interface, this chapter describes both the amplitude equations and DM equations.

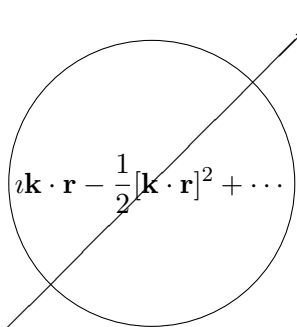
4.1 Nature of the laser field used

As far as this chapter is concerned, the goal is to understand the interaction of a coherent laser field with an atom. The following properties are therefore assumed for the interacting laser.

- Consider a laser beam. There exists a thickness to this beam which is characterised by the angle of deviation of the propagating light rays with respect to the axis of

propagation. If this angle is assumed to be very small, it is called paraxial approximation. The electric field is thus assumed to be **paraxial**.

- The field is **fully temporally coherent**. This means, the degree of coherence function $\mathbf{g}_1(\tau)$, as in Eq. (3.11a), gives a constant value of 1. This suggests that, the field is correlated in time or can be said to have a full memory of itself.
- The field is **quasi-monochromatic**. This implies that the bandwidth of the laser frequency, that surrounds the central frequency is very small. If Δ_ω represents the bandwidth and ω represents the central frequency, then the assumption of quasi-monochromatic field implies the following relation: $\Delta_\omega/\omega \ll 1$
- The field is assumed to be **dipole approximated**. In general, the field is spatially dependent. With wave vector \mathbf{k} ($|\mathbf{k}| = \frac{2\pi}{\lambda}$, where λ is the wavelength) and position vector \mathbf{r} , the general field's expression is given by $E(\mathbf{r}, t) = f(t) \exp[i\mathbf{k} \cdot \mathbf{r} + i\omega t]$. But often the wavelength of the field is far greater than the atomic dimensions under consideration i.e., $|\mathbf{k} \cdot \mathbf{r}| = 2\pi \frac{|\mathbf{r}|}{\lambda} \ll 1$. For example, consider typical wavelength of Ti:sapphire laser, which is around 800 nm (1.55 eV), interacting with hydrogen atom. This gives (using Bohr radius) $|\mathbf{k} \cdot \mathbf{r}| = 2\pi \frac{0.0529 \text{ nm}}{800 \text{ nm}} \approx 0.0004 \ll 1$. Take another example of FEL operating at 20.7 nm (60 eV), interacting with same system. This gives, $|\mathbf{k} \cdot \mathbf{r}| = 2\pi \frac{0.0529 \text{ nm}}{20.7 \text{ nm}} \approx 0.016 \ll 1$. Therefore, this approximation is widely valid. This allows one to use the so called dipole approximation which entails to shrink the equation

$$\exp[i\mathbf{k} \cdot \mathbf{r}] = 1 + i\mathbf{k} \cdot \mathbf{r} - \frac{1}{2}[\mathbf{k} \cdot \mathbf{r}]^2 + \dots \approx 1$$


Physically, it just means that the spatial variation of the field is negligible. So, a dipole approximated field implies a field that is only time dependent i.e.,

$$E(\mathbf{r}, t) = E(t)$$

- The explicit form of the dipole approximated field to be used is

$$E(t) = \mathcal{E}(t)e^{i\omega t} + cc \quad (4.1)$$

where $E(t)$ is the real electric field of the laser and $\mathcal{E}(t)$ is its complex envelope (whose deterministic part can be square or Gaussian or any other shape) and ω is the central frequency. The field is assumed to be linearly polarized in the $\hat{\mathbf{z}}$ direction and propagating in the $\hat{\mathbf{y}}$ direction.

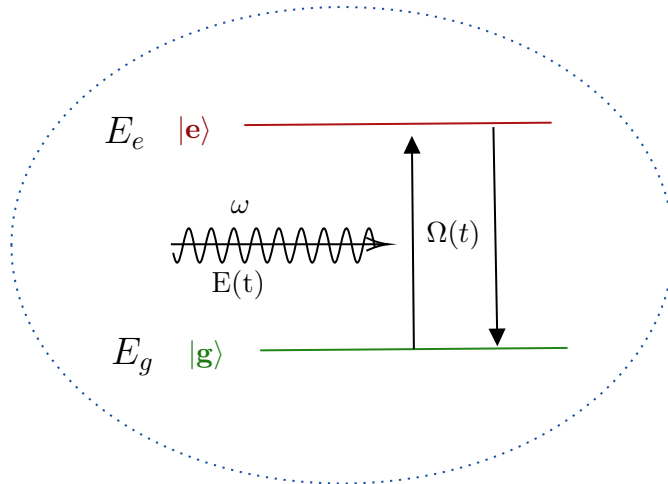


Figure 4.1: A two level atomic system with ground state $|g\rangle$ with eigenenergy E_g and excited state $|e\rangle$ with eigenenergy E_e . It interacts with a coherent laser pulse of central frequency $\omega \approx \omega_{eg} = E_e - E_g$, where $E_e > E_g$. This introduces an intensity dependent oscillation between the states, called Rabi oscillations, denoted by $\Omega(t)$. The dotted boundary around the two levels, suggest that the two level system may also be a sub-system in focus i.e., part of a bigger system which is studied in isolation.

4.2 Two-level atom

Any system can be characterised by its state - like spin, energy, position, momentum, etc. A two-level system then implies a totality of a system in which exists two separate non-identical states. For example, an electron with a spin, which can be either $+\frac{1}{2}$ or $-\frac{1}{2}$ can be considered as a two-level system. Mathematically, a state of a system is represented by the elements (or vectors or state-kets/bras) of Hilbert space (HS). In the language of matrices, they are represented by column and row matrices. Physical observables of the system, like spin or momentum, are represented by operators or square matrices, acting on the elements of this HS.

A Two-level system is spanned by 2-dimensional HS and hence is completely characterised by two mutually orthonormal state-kets (called basis). Using Dirac's notation, let them be $|g\rangle$ and $|e\rangle$. As the thesis deals with laser-atom interactions, let the two-level system be a two-level atom. In this case, $|g\rangle$ can be the ground state and $|e\rangle$ can be the excited state. The following conditions hold for this system:

- $\langle g|g\rangle = 1$ and $\langle e|e\rangle = 1 \implies$ criteria for normality
- $\langle g|e\rangle = \langle e|g\rangle = 0 \implies$ criteria for orthogonality
- $|g\rangle\langle g| + |e\rangle\langle e| = 1 \implies$ both the kets span all of the 2-dimensional HS

4.2.1 Operators of interest

When such a two-level atom is placed under the influence of a laser field, with the assumptions as in section.4.1, the following operators come into play.

- **Laser-Atom interaction operator** is given by $\hat{D}(t) = \hat{d}E(t)$ where \hat{d} is the dipole operator. Given a charge e and the position operator \mathbf{r} , the dipole operator is given

by $\hat{d} = er$. The matrix elements of \hat{d} represent transitions from one state to the other, called dipole transitions. So when this operator is sandwiched between two states, it gives the probability of transition from one state to the other. If the states are equal, by the assumptions of the field and the system under consideration, the value is 0 i.e., $\langle i|\hat{D}(t)|j\rangle = d_{ij}E(t)(1 - \delta_{ij})$, where δ_{ij} is the Kronecker delta symbol whose value is 1 for $i = j$ and 0 for $i \neq j$, $\forall i, j = g, e$.

- **Field free Hamiltonian** is denoted by $\hat{\mathcal{H}}^a$. This is the Hamiltonian of the system when no laser field is interacting with it. When this acts on a state-ket, it results in an eigenvalue equation, whose eigenvalue is the state's energy (E_g or E_e) i.e., $\hat{\mathcal{H}}^a|i\rangle = E_i|i\rangle$, $\forall i = g, e$.
- **Total Hamiltonian** is denoted by $\hat{\mathcal{H}}(t)$. It is given by $\hat{\mathcal{H}}(t) = \hat{\mathcal{H}}^a + \hat{D}(t)$ i.e., it is a superposition of the Hamiltonian when there is no field and the field-matter interaction operator.

With this preliminary background, one can proceed to analyse the two-level system's interaction and develop the so-called *amplitude equations*.

4.2.2 Amplitude equations formulation

First, consider the state of the above system under a laser field as in Fig. 4.1. When no measurement is performed, the state of the system is said to be a superposition of two levels i.e., there exists a probability for its existence to be in either of its states. Let the state ket of the system at any time 't', while the laser is interacting with the atom, be $|\psi(t)\rangle$. It is given by the following expression.

$$|\psi(t)\rangle = c_g(t)|g\rangle + c_e(t)|e\rangle \quad (4.2)$$

Here, $c_i(t)$ is called the amplitude for the state $|i\rangle$ and $|c_i(t)|^2$ gives the probability of existence of the system in the state $|i\rangle$, $\forall i = e, g$. For a two-level system, the following relation holds. It suggests that the total probability of finding the system in one of the two levels is 1.

$$|c_g(t)|^2 + |c_e(t)|^2 = 1$$

The next step is to consider the time-dependent Schrödinger equation (TDSE).

$$i\frac{\partial}{\partial t}|\psi(t)\rangle = \hat{\mathcal{H}}(t)|\psi(t)\rangle = [\hat{\mathcal{H}}^a + \hat{D}(t)]|\psi(t)\rangle \quad (4.3)$$

Substituting the Eq. (4.2) into Eq. (4.3), and then taking the inner-product on both sides of the above equality with $\langle g|$ and $\langle e|$, and utilising their orthonormality property, one obtains the following coupled differential equations.

$$\begin{aligned} \frac{d}{dt}c_g(t) &= -iE_g c_g(t) - id_{ge}[\mathcal{E}(t)e^{-i\omega t} + \mathcal{E}(t)e^{i\omega t}]c_e(t) \\ \frac{d}{dt}c_e(t) &= -iE_e c_e(t) - id_{ge}[\mathcal{E}(t)e^{-i\omega t} + \mathcal{E}(t)e^{i\omega t}]c_g(t) \end{aligned}$$

Here, matrix element $\langle i|\hat{d}|j\rangle = d_{ij}$ denotes the transition dipole matrix element whose values are 0 for $i = j$ and $d_{ij} = d_{ji}$, $\forall i \neq j$ and $i, j = g, e$. Basically, d_{ge} represents the strength of the laser introducing a state transition to the atomic system.

Rabi oscillations

Define a new term $\Omega(t) = d_{ge}\mathcal{E}(t)$, which represents the so called **Rabi oscillations**. They are the field dependent oscillations introduced by the interacting laser into the populations of the atomic states via the dipole moment transition matrix element $d_{ge} = \langle e|d|g\rangle$ and the field amplitude $\mathcal{E}(t)$. The magnitude of this term is called Rabi frequency. A small digression is necessary here. The nature of manifestation of these oscillations can be seen when one solves the two-level system for exact resonance (see example, [56, 57]). The ground-state population for a two-level system (after neglecting the fast oscillating terms) is given as

$$|C_g(t)|^2 = \cos^2(\Omega t) ; \quad \Omega = d_{ge}|\mathcal{E}(t)|$$

Thus, it can be seen that the ground state oscillates sinusoidally with a frequency proportional to Ω . This is the reason for it to be called a *frequency*.

The new equations, including the notation of Rabi oscillations will now look like

$$\frac{d}{dt}c_g(t) = -\imath E_g c_g(t) - \imath[\Omega(t)e^{-\imath\omega t} + \Omega(t)e^{\imath\omega t}]c_e(t) \quad (4.4a)$$

$$\frac{d}{dt}c_e(t) = -\imath E_e c_e(t) - \imath[\Omega(t)e^{-\imath\omega t} + \Omega(t)e^{\imath\omega t}]c_g(t) \quad (4.4b)$$

The above coupled differential equations, can now be solved by existing methods, for specific field shapes of $\mathcal{E}(t)$. The solutions, along with some initial conditions (like $c_g(t=0) = 1$ and $c_e(t=0) = 0$), give the time evolution of the amplitudes $c_g(t)$ and $c_e(t)$. The modulus squared of these amplitudes i.e., $|c_g(t)|^2$ and $|c_e(t)|^2$ give the probability of finding the atomic state in either of the states. Thus, one has at this juncture successfully modeled and solved a two-level system under the laser influence.

There exists, yet another approach for the study of laser-atom interactions. It is the *density matrix* (DM) approach. In the following, an outline is given as to what these density matrices are and then the procedure to arrive at a set of solvable DM-EOMs, for a two-level system.

4.2.3 Density-Matrix formulation

The approach of amplitude equations can be further extended by incorporating rotating wave approximation, i.e., ignoring the fast oscillating terms in the coupled differential equations (see 4.2.4) and solving for the time evolution of the newly transformed equations [56]. But when the interacting laser is fluctuating, it brings in the concept of ensembles and their averages. The use of density matrices is well known in such situations (see e.g. [58, 59]). In the following, a brief overview on the DM approach is given. Let $\rho(t)$ denote

the **density matrix**. It is formally defined as a outer product of the state ket $|\psi(t)\rangle$, i.e.,

$$\rho(t) = |\psi(t)\rangle\langle\psi(t)| \quad (4.5)$$

If the state ket is expressed in terms of basis states, as in Eq. (4.2), then the density operator turns out to be

$$\rho(t) = \sum_{i,j} c_i(t)c_j^*(t)|i\rangle\langle j| = \sum_{i,j} \rho_{ij}(t)|i\rangle\langle j| ; \quad \rho_{ij}(t) = c_i(t)c_j^*(t) \quad (4.6)$$

where, $\rho_{ij}(t)$ are the matrix elements. When this operator is sandwiched between the basis states, one obtains the matrix form of $\rho(t)$

$$\rho(t) = \begin{pmatrix} \rho_{gg}(t) & \rho_{ge}(t) \\ \rho_{eg}(t) & \rho_{ee}(t) \end{pmatrix}$$

where each element of the density matrix is given by the following relation, which is obtained by utilising the orthonormal property of the basis states, i.e.,

$$\begin{aligned} \rho_{mn}(t) &= \langle m| \left[\sum_{i,j} c_i(t)c_j^*(t)|i\rangle\langle j| \right] |n\rangle = \sum_{i,j} c_i(t)c_j^*(t)\langle m|i\rangle\langle j|n\rangle \\ &\Rightarrow \begin{pmatrix} \rho_{gg}(t) & \rho_{ge}(t) \\ \rho_{eg}(t) & \rho_{ee}(t) \end{pmatrix} = \begin{pmatrix} |c_g(t)|^2 & c_g(t)c_e^*(t) \\ c_e(t)c_g^*(t) & |c_e(t)|^2 \end{pmatrix} \end{aligned}$$

The structure of the diagonal elements of the density-matrix $\rho_{ii}(t) = |c_i(t)|^2$ suggests that they represent the populations of the two-level system i.e., the probability of the system being found in either of the states. So, $\rho_{gg}(t)$ and $\rho_{ee}(t)$ are called the *populations*. The structure of the off-diagonal elements of the density matrix $\rho_{ij}(t) = c_i(t)c_j^*(t)$, for $i \neq j$, suggests that they represent the interference terms i.e., the coefficients are representatives of the coherence properties of the states. That is why, $\rho_{ge}(t)$ and $\rho_{eg}(t)$ are called *coherences*. They carry the phase information which is crucial for understanding the coherence properties.

Time evolution of DM elements

Starting from the Liouville equation $i\dot{\rho}(t) = [\hat{\mathcal{H}}, \rho(t)]$, one can derive the following relation for the time evolution of the DM elements

$$\frac{d}{dt}\rho_{ij}(t) = c_i(t)\dot{c}_j^*(t) + \dot{c}_i(t)c_j^*(t) \quad (4.7)$$

Using the Eq. (4.7), Eq. (4.4a) and Eq. (4.4b) one can proceed to evaluate the time evolution of the density matrix elements in terms of amplitude equations. For the present

two-level system, the following set of coupled differential equations are obtained.

$$\frac{d}{dt}\rho_{gg}(t) = 2\text{Im}[(\Omega(t)e^{-i\omega t} + \Omega(t)e^{i\omega t})\rho_{eg}(t)] \quad (4.8a)$$

$$\frac{d}{dt}\rho_{ee}(t) = -2\text{Im}[(\Omega(t)e^{-i\omega t} + \Omega(t)e^{i\omega t})\rho_{eg}(t)] \quad (4.8b)$$

$$\frac{d}{dt}\rho_{eg}(t) = -i(E_e - E_g)\rho_{eg} - i[\Omega(t)e^{-i\omega t} + \Omega(t)e^{i\omega t}](\rho_{gg}(t) - \rho_{aa}(t)) \quad (4.8c)$$

$$\rho_{ge}(t) = \rho_{eg}^*(t) \quad (4.8d)$$

4.2.4 Rotating wave approximation and interaction picture

When there is an interacting field, which can be treated perturbatively, one is at an advantage by moving to what is called *interaction picture* (IP) (see e.g. [60, 61]). Effectively, to transform to IP a new set of density matrices $\sigma(t)$ and their matrix elements $\sigma_{ij}(t)$ are to be defined as follows

$$\sigma_{ij}(t) = \begin{cases} \rho_{ij}(t)e^{-i\omega t}, & i \neq j \\ \rho_{ij}(t), & i = j \end{cases} \quad (4.9)$$

where, the central laser frequency is assumed to be at resonance i.e., $\omega \approx \omega_i - \omega_j = E_i - E_j$.

This introduces two kinds of exponentials in the EOMs of the two-state system: (a) oscillating with a frequency of $\Delta = \omega - \omega_{eg}$, which is the difference or detuning that exists between the central laser frequency and the exact resonance and (b) oscillating with higher frequencies of $\omega + \omega_{eg}$. When $\Delta \ll \omega$ one can invoke the rotating wave approximation (RWA) in the IP which entails to effectively remove the fast oscillating terms i.e., one can assume $e^{i(\omega + \omega_{eg})t} \sim 0$ and $e^{i\Delta t} \sim 1$. The final form of time-dependent density matrix equations, for the two-level system will look like

$$\frac{d}{dt}\sigma_{gg}(t) = 2\text{Im}[\Omega(t)\sigma_{eg}(t)] \quad (4.10a)$$

$$\frac{d}{dt}\sigma_{ee}(t) = -2\text{Im}[\Omega(t)\sigma_{eg}(t)] \quad (4.10b)$$

$$\frac{d}{dt}\sigma_{eg}(t) = -i\Delta\sigma_{eg} - i\Omega(t)[\sigma_{gg}(t) - \sigma_{aa}(t)] \quad (4.10c)$$

$$\sigma_{ge}(t) = \sigma_{eg}^*(t) \quad (4.10d)$$

4.3 Strong-field DM equations of AIS ionization

The previous sections laid basic bricks for furthering the theory of laser-matter interactions. The core interest of this thesis lies in the study of the effects of fluctuating laser fields on autoionizing lineshapes. To achieve that goal, the next step after a brief description of a two-level system is to extend the same to a system which is close to a real atom. The thesis is mostly concerned with 2-electron systems and this is taken as a prototype here.

Consider the ground state $|g\rangle$, replace the previously considered bound excited state $|e\rangle$ with a doubly excited bound state or an autoionizing state (AIS) $|a\rangle$ and continuum $|c\rangle$. The eigenenergy of the AIS lies above the first ionization threshold i.e., E_a is degenerate

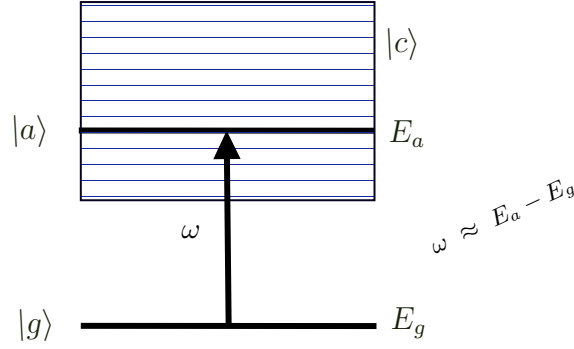


Figure 4.2: Schematic of an extended two-level system where one of the two states is degenerate with continuum.

with the surrounding E_c . For example, in helium, $|g\rangle$ is $1s^2$ and $|a\rangle$ is $2s2p$. The $E_{2s2p} \sim 60.16$ eV is greater than the first ionization threshold which is ~ 24.587 eV.

Consider Fig. 4.2. The schematic shows the states under consideration prior to the interaction of laser. Under Fano model, when a near resonant laser field interacts with such system, a modification of AIS and continuum states occur which arises due to their coupling via the non-zero matrix element of the electron-electron Coulomb interaction operator $\hat{V} = \frac{1}{|\mathbf{r}_1 - \mathbf{r}_2|}$. This coupling modifies the previously bound state $|a\rangle$ to a quasi-bound state i.e, it becomes very short lived. The same coupling also modifies the continua close to the degenerate level. The field couples the ground state to the modified AIS and the continua via the corresponding matrix elements of the laser-atom interaction operator $\hat{D}(t)$.

With this preliminary backdrop, a derivation of a set of amplitude equations and thus the corresponding DM-EOMs will be given in the following. A resolvent operator approach as described in reference [43] is followed. In this approach, it helps to consider a quantized EM field rather than a classical field. When the field duration is of the order of few fs (much shorter than typical spontaneous emission duration ~ 1 ns) and the number of photons are such that one can ignore the quantum fluctuations, then the field can be practically approximated as a classical one [60, 62]. This implies that at the end of the following procedure, one can apply the classical limit to the field and obtain semi-classical EOMs for the type of fields that this thesis is concerned with (high intense and ultra short).

To the already defined operators of 4.1, the following may be now added:

- **Electron-electron Coulomb interaction operator:** $\hat{V} = \frac{1}{|\mathbf{r}_1 - \mathbf{r}_2|}$ where \mathbf{r}_i represents the position vector of an electron with respect to the origin of some reference frame.
- **Radiation Hamiltonian:** $\hat{\mathcal{H}}^R|n\rangle = n\omega|n\rangle$ where n represents the number of photons each having an energy ω (note that atomic units are being used).
- **Laser-atom interaction operator:** It is now given by \hat{D} whose classical limit is the previously described $\hat{d}E(t)$.

Considering the atom as well as the quantised field as one system, the total Hamiltonian

now takes the form

$$\hat{\mathcal{H}} = \underbrace{\hat{\mathcal{H}}^a + \hat{\mathcal{H}}^R}_{\hat{\mathcal{H}}^o} + \hat{V} + \hat{D} = \underbrace{\hat{\mathcal{H}}^o}_{\hat{\mathcal{H}}^o} + \hat{V} + \hat{D} \quad (4.11)$$

The field free- and radiation- Hamiltonians can be clubbed to form a new Hamiltonian $\hat{\mathcal{H}}^o$. The total Hamiltonian is time independent because the radiation-part is also included in the Hamiltonian i.e., the system has no change in the total energy due to the law of energy conservation (assuming no losses exist). This time independence plays a crucial role in the following derivation.

Let the atom absorb 1 photon and excite. If the ground state of the total system has n -photons then the excited state has $n-1$ photons. Without loss of generality (abbreviated by *wlog*) one can start with one photon ($n = 1$) for the radiation state (if an ensemble of atoms is considered, then it means 1-photon for the radiation state, per atom). So, *wlog* the radiation state n need not be represented exclusively, as its eigenvalue ω (energy of the photon in a.u.) keeps track of it. The state kets along with the action of the Hamiltonian $\hat{\mathcal{H}}^o$ is given below

$$\begin{aligned} \hat{\mathcal{H}}^o|g; n\rangle &= (E_g + n\omega)|g; n\rangle \xrightarrow{wlog} \hat{\mathcal{H}}^o|g\rangle = (E_g + \omega)|g\rangle \\ \hat{\mathcal{H}}^o|a; n-1\rangle &= (E_a - (n-1)\omega)|a; n-1\rangle \xrightarrow{wlog} \hat{\mathcal{H}}^o|a\rangle = E_a|a\rangle \\ \hat{\mathcal{H}}^o|c; n-1\rangle &= (E_c - (n-1)\omega)|c; n-1\rangle \xrightarrow{wlog} \hat{\mathcal{H}}^o|c\rangle = E_c|c\rangle \end{aligned}$$

It is also to be noted that the state kets are orthonormal i.e., $\langle p|q\rangle = \delta_{pq} \forall p, q = g, a, c$ where δ_{pq} is the Kronecker delta.

With all these tools, and again noting the time independence of the total Hamiltonian, consider the time-dependent Schrödinger equation (TDSE) and find the time evolution of the system state wavefunction $\psi(t)$.

$$i\frac{\partial}{\partial t}\psi(t) = \hat{\mathcal{H}}\psi(t) \quad (4.13a)$$

$$\implies \psi(t) = e^{-i\hat{\mathcal{H}}t}\psi(0) = \hat{U}(t)\psi(0) \quad (4.13b)$$

where $\hat{U}(t)$ is the time evolution operator, known from inspection, and $\psi(0) \equiv |g\rangle$. Taking the Laplace transform(\mathcal{L}) (Eq. (A.1)) of the wavefunction one obtains

$$\mathcal{L}[\psi(t)] = \int_0^\infty e^{-\imath s} e^{-i\hat{\mathcal{H}}t}\psi(0)dt = \frac{1}{s + i\hat{\mathcal{H}}}\psi(0) \quad (4.14)$$

Apply the change of variable $s = -\imath z$. This entails to changing the complex-plane and the line of integration. See Fig. 4.3 where the limits of integration of L_1 (belonging to s -plane) are from $(a, -\infty)$ to (a, ∞) and after the transformation ($z = \imath s$) the limits of integration of L_2 (belonging to z -plane) become (∞, a) to $(-\infty, a)$. Now taking inverse

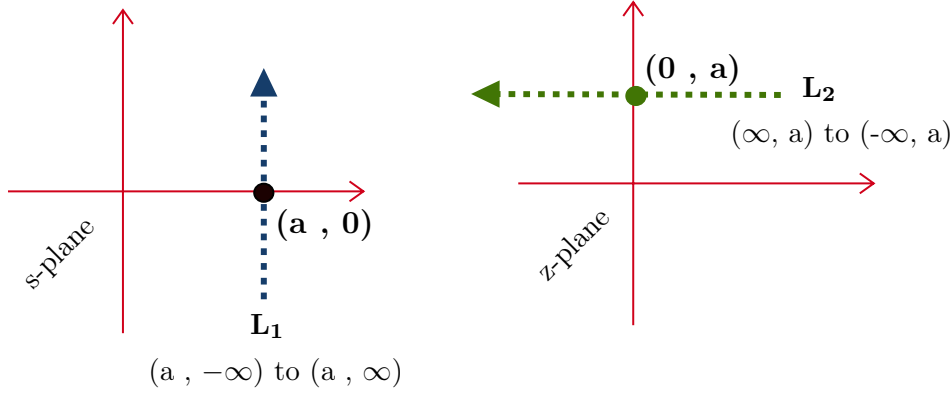


Figure 4.3: Schematic of Laplace transform and a change of s -variable to z -variable.

Laplace transform (Eq. (A.2)), along L_2 , one obtains

$$\begin{aligned}
 \psi(t) &= \frac{1}{2\pi i} \int_{L_2} e^{-izt} \frac{1}{-iz + i\hat{\mathcal{H}}} \psi(0) d(-iz) \\
 &= \frac{1}{2\pi i} \int_{L_2} e^{-izt} \left(\frac{1}{z - \hat{\mathcal{H}}} \right) \psi(0) dz \\
 &= \frac{1}{2\pi i} \int_{L_2} e^{-izt} G(z) \psi(0) dz
 \end{aligned} \tag{4.15a}$$

The function $G(z)$ is called the *resolvent* operator given by [43, 63]

$$\begin{aligned}
 G(z) &\equiv \frac{1}{z - \hat{\mathcal{H}}} \\
 G(z)(z - \hat{\mathcal{H}}) &\equiv 1
 \end{aligned} \tag{4.16a}$$

Inspecting Eq. (4.13b), Eq. (4.15a) and Eq. (A.2), the time evolution operator can be expressed in terms of the inverse Laplace transform (in the z -plane) of the resolvent,

$$\hat{U}(t) = \frac{1}{2\pi i} \int_{L_2} e^{-izt} G(z) dz = \mathcal{L}^{-1}[G(z)] \tag{4.17}$$

Assuming that the only kets involved are the ground state $|g\rangle$ (eigenenergy E_g), autoionizing state $|a\rangle$ (eigenenergy E_a) and a single set of continuum $|c\rangle$ states (eigenenergies E_c), a closure relation can be constructed by taking their outer product.

$$\hat{P} = |g\rangle\langle g| + |a\rangle\langle a| + \int dE_c |c\rangle\langle c| = 1 \tag{4.18}$$

A small digression is necessary here in relation to the reasons why an integration is taken over a set of energy values for the outer product of the continuum states $|c\rangle$ (see further developments in chapter 18 of reference [64]). Let $\langle r|c\rangle$ represent the continuum radial wavefunctions. Let the product $\langle r|c\rangle\langle c'|r\rangle dr d\epsilon$ denote the probability that a free electron of the continuum lies inside a shell of radius r of a width dr , and a kinetic energy which is within $d\epsilon$ having a center ϵ' . Then the normalization condition of this wavefunction is

given by

$$\int_{\Delta_\epsilon} \int_0^\infty \langle r|c\rangle \langle c'|r\rangle dr d\epsilon = \int_{\Delta_\epsilon} \delta(\epsilon - \epsilon') d\epsilon = \begin{cases} 0; & \text{for } \epsilon' \text{ outside } \Delta_\epsilon \\ 1; & \text{for } \epsilon' \text{ inside } \Delta_\epsilon \end{cases} \quad (4.19)$$

where $\delta(x)$ is the Dirac delta function ¹ and the Δ_ϵ considered is a very small but finite energy interval. This specific choice of normalization suggests that the dimension of a continuum state $\langle r|c\rangle$ is given by $[E^{-\frac{1}{2}}L^{-\frac{1}{2}}]$ and it is different from that of a bound state which is $[L^{-\frac{1}{2}}]$. With the present notation, ϵ is E_c . The outer product of the continuum states ² $|c\rangle \langle c| = \langle r|c\rangle \langle c'|r\rangle$ therefore has a dimension of $[E^{-\frac{1}{2}}L^{-\frac{1}{2}}E^{-\frac{1}{2}}L^{-\frac{1}{2}}] = [E^{-1}L^{-1}]$, which means it represents a quantity ‘per unit energy’ (the length dimension matches the other outer terms of the bound states) and hence in the closure relation of \hat{P} one needs to integrate the $|c\rangle \langle c|$ over the range of continuum energies.

It is beneficial to note that there are two expressions for the identity operator ($\mathbb{1} \equiv 1$) viz. Eq. (4.16a) and Eq. (4.18) which will be exploited in the upcoming steps. Start by inserting Eq. (4.18) into Eq. (4.13b) i.e,

$$\begin{aligned} |\psi(t)\rangle &= \hat{U}(t) |\psi(0)\rangle = \hat{U}(t) |g\rangle = \mathbb{1} \cdot \hat{U}(t) |g\rangle = \hat{P} \cdot \hat{U}(t) |g\rangle \\ &= \left[|g\rangle \langle g| + |a\rangle \langle a| + \int_c dE_c |c\rangle \langle c| \right] \hat{U}(t) |g\rangle \\ &= U_{gg}(t) |g\rangle + U_{ag}(t) |a\rangle + \int_c dE_c U_{cg}(t) |c\rangle \end{aligned} \quad (4.20)$$

Keeping the above relation along with $U_{lm}(t) = \frac{1}{2\pi i} \int_{L_2} e^{-izt} G_{lm}(z) dz$ in mind, let Eq. (4.16a) be considered now. Insert Eq. (4.18) and sandwich it between the eigenstates under consideration by utilising their orthonormal relation,

$$\begin{aligned} 1 &= \langle g|g\rangle = \langle g| \mathbb{1} |g\rangle = \langle g| (z - \hat{\mathcal{H}}) \mathbb{1} G |g\rangle = \langle g| (z - \hat{\mathcal{H}}) P G |g\rangle \\ &\implies \langle g| (z - \hat{\mathcal{H}}) P G |g\rangle = 1 \end{aligned} \quad (4.21a)$$

$$\begin{aligned} 0 &= \langle a|g\rangle = \langle a| \mathbb{1} |g\rangle = \langle a| (z - \hat{\mathcal{H}}) \mathbb{1} G |g\rangle = \langle a| (z - \hat{\mathcal{H}}) P G |g\rangle \\ &\implies \langle a| (z - \hat{\mathcal{H}}) P G |g\rangle = 0 \end{aligned} \quad (4.21b)$$

$$\begin{aligned} 0 &= \langle c|g\rangle = \langle c| \mathbb{1} |g\rangle = \langle c| (z - \hat{\mathcal{H}}) \mathbb{1} G |g\rangle = \langle c| (z - \hat{\mathcal{H}}) P G |g\rangle \\ &\implies \langle c| (z - \hat{\mathcal{H}}) P G |g\rangle = 0 \end{aligned} \quad (4.21c)$$

The next step is to expand $\hat{\mathcal{H}}$ using Eq. (4.11) in the above expressions and compress the sandwiched terms to their matrix element forms. In doing so, only few terms will remain and the rest will become zero due to the nature of the operator that is sandwiched in between the eigenstates. In qualitative terms, the field-matter interaction operator \hat{D} cannot participate in the transition of an electron from the autoionizing state to the degenerate continuum (or vice versa) and the electron-electron Coulomb interaction operator \hat{V} can-

¹ $\delta(x) = \begin{cases} +\infty; & x = 0 \\ 0; & x \neq 0 \end{cases}$

²One can exploit the closure relation $\int |r\rangle \langle r| dr = 1$

not drive the system from ground state to the continuum or to the doubly excited state (or vice versa). This is summarised quantitatively in the following,

$$\langle l | \hat{\mathcal{H}}^o | m \rangle = \mathcal{H}_{lm}^o = \delta_{lm} E_l + \delta_{gl} \delta_{gm} \omega \quad ; \quad \forall l, m = g, a, c \quad (4.22)$$

$$\langle l | \hat{V} | m \rangle = \begin{cases} 0 & ; \text{ for } (l \vee m = g) \vee (l = m) \\ V_{lm} & ; \text{ otherwise} \end{cases} \quad (4.23)$$

$$\langle l | \hat{D} | m \rangle = \begin{cases} 0 & ; \forall l, m = a, c \\ D_{lm} & ; \text{ otherwise} \end{cases} \quad (4.24)$$

where in Eq. (4.23) \vee represents logical OR operator. Utilising these and proceeding further,

$$\begin{aligned} & \langle g | (z - \hat{\mathcal{H}}) P G | g \rangle = 1 \\ \implies & \langle g | (z - \hat{\mathcal{H}}^o - \hat{V} - \hat{D}) \hat{P} G | g \rangle = 1 \\ \implies & \langle g | z \hat{P} G | g \rangle - \langle g | \hat{\mathcal{H}}^o \hat{P} G | g \rangle - \langle g | \hat{V} \hat{P} G | g \rangle - \langle g | \hat{D} \hat{P} G | g \rangle = 1 \\ \implies & z G_{gg} - E'_g G_{gg} - \underbrace{\langle g | \hat{\mathcal{V}} \hat{P} | g \rangle}_{\circlearrowleft 0} G | g \rangle - \left[D_{ga} \langle a | + \int dE_c D_{gc} \langle c | \right] G | g \rangle = 1 \\ \implies & (z - E'_g) G_{gg} - D_{ga} G_{ag} - \int dE_c D_{gc} G_{cg} = 1 \end{aligned} \quad (4.25a)$$

Similarly,

$$\begin{aligned} & \langle a | (z - \hat{\mathcal{H}}) \hat{P} G | g \rangle = 0 \\ \implies & (z - E_a) G_{ag} - D_{ga} G_{gg} - \int dE_c \mathcal{V}_{ac} G_{cg} = 0 \end{aligned} \quad (4.25b)$$

and

$$\begin{aligned} & \langle c | (z - \hat{\mathcal{H}}) \hat{P} G | g \rangle = 0 \\ \implies & (z - E_c) G_{cg} - D_{cg} G_{gg} - V_{ca} G_{ag} = 0 \end{aligned} \quad (4.25c)$$

The equations (4.25) are obtained by utilising the closure \hat{P} , expanding the total Hamiltonian of Eqs. (4.21). In the above equations $E'_g = E_g + \omega$. The Eqs. (4.25) are algebraic equations. The task now is to solve Eq. (4.25c) for G_{cg} .

$$G_{cg} = \frac{1}{z - E_c} (D_{cg} G_{gg} + V_{ca} G_{ag}) \quad (4.26)$$

Inserting this expression into Eq. (4.25a) gives

$$(z - E'_g) G_{gg} - D_{ga} G_{ag} - \int dE_c \frac{1}{z - E_c} D_{gc} (D_{cg} G_{gg} + V_{ca} G_{ag}) = 1 \quad (4.27)$$

Consider the operator $\frac{1}{z - \hat{\mathcal{H}}}$. When it acts on $\psi(0)$, it results in $\frac{1}{z - (E_g + \omega)}$. So, z has a real pole which implies, the contour L_2 of the integration (Fig. 4.3) approaches the real axis. That means, z can be approximated by the limit: $\lim_{\eta \rightarrow +0} E_g + \omega + \eta$ or $\lim_{\eta \rightarrow +0} E'_g + \eta$.

Using this, the previous equation can be rewritten as

$$(z - E'_g)G_{gg} - D_{ga}G_{ag} - \lim_{\eta \rightarrow +0} \int dE_c \frac{1}{E'_g + i\eta - E_c} D_{gc} (D_{cg}G_{gg} + V_{ca}G_{ag}) = 1 \quad (4.28)$$

Looking at the last summand, it is desirable to invoke the so called *pole approximation* [43, 65], whose identity is given in Eq. (4.29) and whose proof is given in Appendix A.2. The integration is to be understood as being carried out through the pole ($E_c = E_g + \omega = E'_g$).

$$\lim_{\eta \rightarrow +0} \int dE_c \frac{f(E_c)}{E'_g + i\eta - E_c} = \mathcal{P} \int dE_c \frac{f(E_c)}{E'_g - E_c} - i\pi \int dE_c \delta(E'_g - E_c) f(E_c) \quad (4.29)$$

In the above equation, $f(E_c) = D_{gc}(D_{cg}G_{gg} + V_{ca}G_{ag})$ and \mathcal{P} is the principal part of the integral that follows it (refer Appendix A.2). As one can see in the proof of the pole approximation, the condition in which it is valid is when $f(E_c)$ is a slowly and smoothly varying function of E_c around the range of the integrating resonance energies. That means, the Eq. (4.29) is valid only when the matrix elements in the numerator of Eq. (4.28) are smoothly and slowly varying functions of the continuum energy.

$$\begin{aligned} & (z - E'_g)G_{gg} - D_{ga}G_{ag} - \left[\mathcal{P} \int_{-E_1}^{E_2} dE_c \frac{f(E_c)}{E'_g - E_c} - i\pi \int_{-E_1}^{E_2} dE_c \delta(E'_g - E_c) f(E_c) \right] = 1 \\ \implies & (z - E'_g)G_{gg} - D_{ga}G_{ag} - \mathcal{P} \int dE_c \frac{D_{gc}}{E_g + \omega - E_c} D_{cg}G_{gg} \\ & - \mathcal{P} \int dE_c \frac{D_{gc}}{E_g + \omega - E_c} V_{ca}G_{ag} + i\pi \int dE_c D_{gc} \delta(E_g + \omega - E_c) D_{cg}G_{gg} \\ & + i\pi \int dE_c D_{gc} \delta(E_g + \omega - E_c) V_{ca}G_{ag} = 1 \\ \implies & (z - E'_g)G_{gg} - D_{ga}G_{ag} - \boxed{\mathcal{P} \int dE_c \frac{|D_{gc}|^2}{E_g + \omega - E_c} G_{gg}} - \boxed{\mathcal{P} \int dE_c \frac{D_{gc}V_{ca}}{E_g + \omega - E_c} G_{ag}} \\ & + \boxed{i\pi |D_{gc}|_{E_g+\omega}^2 G_{gg}} + \boxed{i\pi [D_{gc}V_{ca}G_{ag}]_{E_g+\omega}} = 1 \\ \implies & (z - E'_g)G_{gg} - D_{ga}G_{ag} - \boxed{s_g G_{gg}} - \boxed{(D_{g\bar{E}}G_{ag} - D_{ga}G_{ag})} \\ & + \boxed{i\pi \left(\frac{\gamma_g(t)}{2\pi}\right) G_{gg}} + \boxed{i\pi \frac{D_{g\bar{E}}}{q\pi} G_{ag}} = 1 \\ \implies & (z - E'_g)G_{gg} - \underline{D_{ga}G_{ag}} - (s_g - i\frac{\gamma_g(t)}{2})G_{gg} - D_{g\bar{E}} \left(1 - \frac{i}{q}\right) G_{ag} + \underline{D_{ga}G_{ag}} = 1 \\ \implies & (z - E'_g)G_{gg} - (s_g - i\frac{\gamma_g(t)}{2})G_{gg} - \boxed{D_{g\bar{E}} \left(1 - \frac{i}{q}\right) G_{ag}} = 1 \\ \implies & (z - E'_g)G_{gg} - (s_g - i\frac{\gamma_g(t)}{2})G_{gg} - \boxed{\tilde{\Omega}(t)} G_{ag} = 1 \end{aligned}$$

Some new terms have appeared in the above derivation, that have been put in boxes, which need more exploration.

- s_g is the ac-Stark energy shift which occurs when there is an energy shift in the presence of a variable electric field [66]. In the above derivation, its expression is

given by

$$s_g = \mathcal{P} \int dE_c \frac{|D_{gc}|^2}{E_g + \omega} \quad (4.30)$$

Dimensional analysis helps in recognising the RHS of s_g as an energy term. The dimension of RHS depends on the dimension of $D_{gc} = \langle g | \hat{\mathcal{H}} | c \rangle = \int dr \langle g | r \rangle \hat{\mathcal{H}} \langle c | r \rangle$ (rest of the terms from $\hat{\mathcal{H}}$ in this sandwiched form are zero). As explored previously, the dimensions of $\langle r | c \rangle$ is $[E^{-\frac{1}{2}} L^{-\frac{1}{2}}]$, found using the normalization equation Eq. (4.19). The dimension of $\langle g | r \rangle$ is $[L^{-\frac{1}{2}}]$. The dimension of $\hat{\mathcal{H}}$ is $[E]$. Thus, the dimension of $D_{gc} = \int \underbrace{dr}_{[L]} \underbrace{\langle g | r \rangle}_{[L^{-\frac{1}{2}}]} \underbrace{\hat{\mathcal{H}}}_{[E]} \underbrace{\langle c | r \rangle}_{[E^{-\frac{1}{2}}] L^{-\frac{1}{2}}}$ is $[L L^{-\frac{1}{2}} E E^{-\frac{1}{2}} L^{-\frac{1}{2}}] = [E^{\frac{1}{2}}]$. Therefore, the dimension of $|D_{gc}|^2$ is $[E]$ and hence the terms s_g represents an energy term.

- $D_{g\bar{E}} - D_{ga}$: In the Fano picture the autoionizing state is modified due to the interaction with the surrounding continuum [42]. Let such a modified state be $|\Phi\rangle$. It has the form

$$|\Phi\rangle = |a\rangle + \mathcal{P} \int dE_c \frac{V_{ca} |c\rangle}{E'_g - E_c} \quad (4.31)$$

Define the matrix element that takes the system from ground state to the modified state as

$$\begin{aligned} D_{g\bar{E}} &= \langle g | \hat{D} | \Phi \rangle \\ &= \langle g | \hat{D} | [|a\rangle + \mathcal{P} \int dE_c \frac{V_{ca} |c\rangle}{E'_g + \omega - E_c}] \\ &= D_{ga} + \mathcal{P} \int dE_c \frac{D_{gc} V_{ca}}{E'_g - E_c} \\ \implies D_{g\bar{E}} - D_{ga} &= \mathcal{P} \int dE_c \frac{D_{gc} V_{ca}}{E'_g - E_c} \end{aligned} \quad (4.32)$$

Here, it is understood that $\bar{E} = E'_g = E_g + \omega$. Sometimes for simplicity, one takes the value of \bar{E} evaluated at E_a (provided there is very small detuning).

- q_a is the Fano asymmetry parameter, defined as follows

$$q_a = \frac{\langle \Phi | \hat{D} | g \rangle}{\pi V_{ac} \langle c | \hat{D} | g \rangle} = \frac{d_{\bar{E}g}}{\pi V_{ac} d_{cg}} \quad (4.33)$$

It compares the direct transition probability from the ground state to the continuum and the indirect transition probability to the continuum via an autoionizing state and hence q_a measures the level of interference, which causes the asymmetry in the line shape, between the two channels of ionization.

- Photoionization width

$$\gamma_g(t) = 2\pi |D_{cg}|^2 \quad (4.34)$$

After transforming to the interaction picture (IP) and application of rotating wave approximation (RWA), and in the classical limit of \hat{D} , the above term becomes

$\gamma_g(t) = 2\pi|d_{cg}|^2|\mathcal{E}(t)|^2 = \gamma_g\mathcal{I}(t)$. Therefore this is an intensity dependent width. Also, in the main derivation, this term was evaluated at $E_g + \omega$ (due to the δ function) which means, it is also dependent on the central frequency of the laser pulse.

- Complex Rabi interference term $\tilde{\Omega}(t)$

$$\tilde{\Omega}(t) = D_{g\bar{E}} \left(1 - \frac{\imath}{q_a} \right) \quad (4.35)$$

The Rabi oscillation character, which is intensity dependent, exist due to the $D_{g\bar{E}}$ and this oscillates the system to transfer between the ground state and the resonantly excited state. The interference character arises due to the q_a term.

Therefore, the first equation gives

$$\begin{aligned} (z - E'_g)G_{gg} - D_{ga}G_{ag} - \int dE_c D_{gc}G_{cg} &= 1 \\ \implies (z - \bar{E}_g + \imath\frac{\gamma_g(t)}{2})G_{gg} - \tilde{\Omega}(t)G_{ag} &= 1 \end{aligned} \quad (4.36)$$

Where the Stark energy shift is now absorbed into \bar{E}_g .

Similarly one obtains the following expression for the other equation

$$\begin{aligned} (z - E_a)G_{ag} - D_{ag}G_{gg} - \int dE_c V_{ac}G_{cg} &= 0 \\ \implies (z - \bar{E}_a + \imath\frac{\Gamma_a}{2})G_{ag} - \tilde{\Omega}(t)G_{gg} &= 0 \end{aligned} \quad (4.37)$$

where, the extra terms are defined as in the previous case :

- One obtains similar integrals but with different matrix elements and hence the physical quantities they represent change.

$$\int dE_c \frac{|V_{ca}|^2}{z - E_c} = \mathcal{P} \int dE_c \frac{|V_{ca}|^2}{E'_g - E_c} - \imath\pi(|V_{ca}(E'_g)|^2) = s_a - \imath\frac{\Gamma_a}{2} \quad (4.38)$$

The s_a is the shift of resonance energy. This is understood from the dimensional analysis of $\langle a|\hat{V}|c\rangle$ just like before. This term s_a is absorbed into \bar{E}_a in the main equation.

- Autoionization width Γ_a

$$\Gamma_a = 2\pi|V_{ca}|^2 \quad (4.39)$$

This is purely dependent on electron-electron interactions and not on the applied field. Therefore it is not intensity dependent like the photoionization width. Inverse of this width gives the rate of decay into continuum from the autoionizing state (AIS).

All these quantities are shown schematically in the Fig. 4.4. For the purpose of this work, this picture is adequate. For an extended system with more autoionization states included,

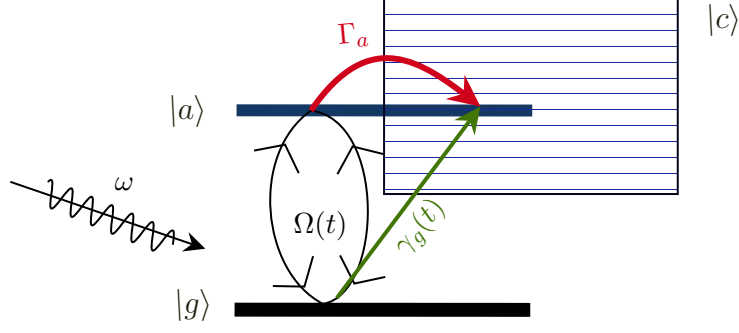


Figure 4.4: Schematic showing the Fano picture of an atom when it interacts with a laser pulse of frequency ω . The direct channel of photoionization $\gamma_g(t)$, the indirect channel via Rabi oscillations $\Omega(t)$ and autoionization Γ_a are shown. The energy shifts s_g and s_a are included and depicted as the thick lines for the corresponding states.

one may refer to [43].

Finally one obtains three equations of motion in the z-variable

$$(z - \bar{E}_g + i\frac{\gamma_g(t)}{2})G_{gg} - \tilde{\Omega}(t)G_{ag} = 1 \quad (4.40a)$$

$$(z - \bar{E}_a + i\frac{\Gamma_a}{2})G_{ag} - \tilde{\Omega}(t)G_{gg} = 0 \quad (4.40b)$$

$$(z - E_c)G_{cg} - D_{cg}G_{gg} - V_{ca}G_{ag} = 0 \quad (4.40c)$$

Applying inverse Laplace transform to these equations and noting that $C_g(t) \equiv U_{gg}(t)$, $C_a(t) \equiv U_{ag}(t)$ and $C_c(t) \equiv U_{cg}(t)$, one obtains what are known as *amplitude equations*,

$$i\dot{C}_g(t) = (\bar{E}_g - i\frac{\gamma_g(t)}{2})C_g(t) + \tilde{\Omega}(t)C_a(t) \quad (4.41a)$$

$$i\dot{C}_a(t) = (\bar{E}_a - i\frac{\Gamma_a}{2})C_a(t) + \tilde{\Omega}(t)C_g(t) \quad (4.41b)$$

$$i\dot{C}_c(t) = E_c C_c(t) + D_{cg}C_g(t) + V_{ca}C_a(t) \quad (4.41c)$$

These are called so because the $C_k(t)$, $\forall k = g, a, c$, represents the respective probability amplitude term in the Eq. (4.20), which needs to be recalled at this point. Therefore, by solving the Eqs. (4.41) one can know precisely the state wavefunction

$$|\Psi(t)\rangle = C_g(t)|g\rangle + C_a(t)|a\rangle + \int_c dE_c C_c(t)|c\rangle \quad (4.42)$$

Utilising the above Eq. (4.42), $|\dot{\Psi}(t)\rangle = -i\hat{\mathcal{H}}|\Psi(t)\rangle = \dot{U}(t)|g\rangle$, and $U_{mg}(t) \equiv C_m(t)$ $\forall m, n = g, a, c$, one can now proceed to derive time evolution of DM elements in terms of

amplitudes starting from the Liouville equation [56]

$$\imath\dot{\rho}(t) = \left[\hat{\mathcal{H}}, \rho(t) \right] = \hat{\mathcal{H}}\rho(t) - \rho(t)\hat{\mathcal{H}} \quad (4.43)$$

$$\begin{aligned} \implies \imath\dot{\rho}_{ij}(t) &= \langle i | \hat{\mathcal{H}} | \Psi(t) \rangle \langle \Psi(t) | j \rangle - \langle i | \Psi(t) \rangle \langle \Psi(t) | \hat{\mathcal{H}} | j \rangle \\ &= \langle i | \imath\dot{U}(t) | g \rangle C_j^*(t) - C_i(t) \langle g | (-\imath\dot{U}^*(t)) | j \rangle \\ &= \imath\dot{C}_i(t)C_j^*(t) + \imath C_i(t)\dot{C}_j^*(t) \\ \implies \dot{\rho}_{ij}(t) &= \dot{C}_i(t)C_j^*(t) + C_i(t)\dot{C}_j^*(t) \end{aligned} \quad (4.44)$$

Inserting the amplitude equations obtained in Eqs. (4.41) into Eq. (4.44), moving to the interaction picture by applying the transformation given by Eq. (4.9) which results in diagonal elements remaining the same whereas the off-diagonal terms changing by $\sigma_{ij}(t) = \rho_{ij}(t)e^{-\imath\omega t}$ and applying the rotating wave approximation as discussed in the section 4.2.4, the final set of density matrix equations of motion (DM-EOMs) are obtained as depicted in the boxed equations below

$$\dot{\sigma}_{gg}(t) = -\gamma_g(t)\sigma_{gg}(t) + 2\text{Im}[\Omega(t) \left(1 - \frac{\imath}{q_a} \right) \sigma_{ag}(t)] \quad (4.45a)$$

$$\dot{\sigma}_{aa}(t) = -\Gamma_a\sigma_{aa}(t) - 2\text{Im}[\Omega^*(t) \left(1 + \frac{\imath}{q_a} \right) \sigma_{ag}(t)] \quad (4.45b)$$

$$\begin{aligned} \dot{\sigma}_{ag}(t) &= \left(\imath\Delta - \frac{1}{2}(\gamma_g(t) + \Gamma_a) \right) \sigma_{ag} - \imath\Omega(t) \left(1 - \frac{\imath}{q_a} \right) \sigma_{gg}(t) \\ &\quad + \imath\Omega^*(t) \left(1 + \frac{\imath}{q_a} \right) \sigma_{aa}(t) \end{aligned} \quad (4.45c)$$

$$\dot{\sigma}_{cc}(t) = 2\text{Im}[\mathcal{D}_{cg}\sigma_{gc} + V_{ca}\sigma_{ac}] \quad (4.45d)$$

$$\dot{\sigma}_{gc}(t) = \left(\imath\Delta_1 - \frac{1}{2}\gamma_g(t) \right) \sigma_{gc} - \imath\Omega(t)\sigma_{ac}(t) + \imath\mathcal{D}_{cg}^*\sigma_{gg}(t) + \imath V_{ca}^*\sigma_{ga}(t) \quad (4.45e)$$

$$\dot{\sigma}_{ac}(t) = \left(\imath\Delta_2 - \frac{1}{2}\Gamma_a \right) \sigma_{ac} - \imath\Omega(t)\sigma_{gc}(t) + \imath\mathcal{D}_{cg}^*\sigma_{ag}(t) + \imath V_{ca}^*\sigma_{aa}(t) \quad (4.45f)$$

where, $\Delta = \omega - (\bar{E}_a - \bar{E}_g)$, $\Delta_1 = \omega - (\bar{E}_c - \bar{E}_g)$ and $\Delta_2 = (\bar{E}_c - \bar{E}_a)$ are relevant detunings. $\Omega(t) = d_{ga}\mathcal{E}(t)$, $d_{ga} = d_{ag}$, $\mathcal{D}_{cg} = d_{cg}\mathcal{E}(t)$ with dipole transition matrix element d_{cg} between $|c\rangle$ and $|g\rangle$ states and complex field envelope $\mathcal{E}(t)$.

4.4 Conclusion

The chapter aimed to develop the necessary density matrix equations to be used later on. For this purpose, it started with a two-level system and an interacting monochromatic field. From this, a set of amplitude equations were developed. Then a set of density matrix equations were developed hinting at the former's inadequacy in dealing with statistical ensembles. Then, in the framework of the Fano picture, the 2-level system is extended to a multi-level system for which corresponding DM-EOMs were derived using resolvent operator method. These equations form the starting point of the explorations of the main chapters (6 and 7) of the thesis.

Chapter 5

Ab-initio calculation of helium bound and continuum states: Fano parameters and AIS

In Chapter 4, a set of DM-EOMs were obtained for a near resonant laser interacting with an atomic system having a ground state and an AIS embedded in a continuum. To solve the set of Eqs. (4.45), certain parameters need to be calculated beforehand. They are the transition dipole matrix elements from the ground state to the continuum (d_{gc}), ground state to the AIS (d_{ga}), Fano-asymmetry parameter (q_a) and the position of AIS (E_a). Through these and the knowledge of the field applied, one obtains the photoionization width ($\gamma_g = 2\pi|d_{cg}|^2|\mathcal{E}(t)|^2$) and the autoionization width ($\Gamma_a = 2\pi|d_{ga}|^2$). This chapter gives a brief overview of theoretically achieving this goal. An ab-initio methodology developed and utilised in references [67–69], was followed here.

In the following sections, in brief, a calculation method is given for the atomic structure, the way to extract the Fano parameters from the knowledge of the photoionization cross section and the position and width of the AIS.

5.1 Atomic structure calculations

Let the two electron systems such as He atom, Li^+ ion, etc., be denoted by $\mathcal{A}(Z)$ with corresponding atomic number $Z = 2$. Then, the Hamiltonian of $\mathcal{A}(Z)$ in atomic units is given by

$$\hat{\mathcal{H}}^a(\mathbf{r}_1, \mathbf{r}_2) = \sum_{i=1,2} \hat{h}(\mathbf{r}_i) + \hat{V}(\mathbf{r}_1, \mathbf{r}_2) = \sum_{i=1}^2 \left(-\frac{1}{2} \nabla_i^2 - \frac{Z}{r_i} \right) + \frac{1}{r_{12}}, \quad (5.1)$$

where the one-electron Hamiltonian $\hat{h}(r_i)$ for each of the electrons positioned at \mathbf{r}_i (having a magnitude of r_i) and the inter-electronic potential $\hat{V}(\mathbf{r}_1, \mathbf{r}_2)$ are defined by inspection. The Laplacian operator ∇^2 , in Cartesian coordinate system, is given by $\nabla_i^2 = \left(\frac{\partial^2}{\partial x^2} + \frac{\partial^2}{\partial y^2} + \frac{\partial^2}{\partial z^2} \right)_i$. The subscript ‘i’ in the above equation denotes that the operator is applied to the i^{th} electron. A schematic of the geometry of this system is given in Fig. 5.1.

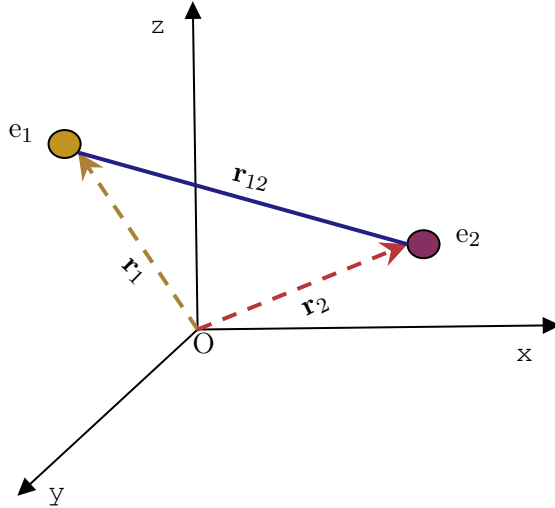


Figure 5.1: Schematic of a two electron system where e_i and \mathbf{r}_i represent the i^{th} electron and its position vector with respect to the origin O .

Consider the interaction of $\mathcal{A}(Z)$ with radiation. Under the non-relativistic approximation, the following set of entities generate the necessary Hilbert space for the needed formalism: the field-free Hamiltonian ($\hat{\mathcal{H}}^a$), the total orbital angular momentum squared (\hat{L}^2), the total spin angular momentum squared (\hat{S}^2) and their projections (\hat{L}_z and \hat{S}_z), where $\hat{L} = \hat{l}_1 + \hat{l}_2$, $\hat{S} = \hat{s}_1 + \hat{s}_2$ and \hat{l}_i, \hat{s}_i are the orbital angular momenta and spin angular momenta of each of the two-electrons. The present work considers the interacting field to be having no spin operator i.e., it does not affect the total spin angular momentum quantum number of the atomic system. Also assuming that the field is linearly polarised along the z -axis, it can be seen that the values of \hat{L}_z and \hat{S}_z do not change in the process of the interaction. Therefore $\mathcal{A}(Z)$, starting from the ground state of $|g\rangle = |1s^2, {}^1S\rangle$, after interacting with FEL, will reach such states which have $L_z = 0$, $S = 0$ and $M_S = 0$ (due to selection rules involving linear polarization in z -direction). Let all the eigenstates be denoted by $|nL\rangle$, where n corresponds to the eigenenergy E_n and L the total angular momentum.

The next step is to numerically calculate the two-electron eigenstates of $\hat{\mathcal{H}}^a$, which entails solving the eigenvalue equation for a two-electron time-independent Schrödinger equation (TISE ¹)

$$\hat{\mathcal{H}}^a \Phi_{E_n L}(\mathbf{r}_1, \mathbf{r}_2) = E_n L \Phi_{E_n L}(\mathbf{r}_1, \mathbf{r}_2), \quad (5.2)$$

where $\Phi_{E_n L}(\mathbf{r}_1, \mathbf{r}_2)$ are the eigenstates of $\hat{\mathcal{H}}^a$. The atomic system is considered to be inside of a spherical box of radius R , whose magnitude is greater than typical atomic dimensions. The Eq. (5.2) is a partial differential equation whose solution, requires certain boundary conditions. In the present scenario, this entails a vanishing wavefunction at the origin as well as at the boundary R . This makes all of the eigenstates discrete and hence the bound as well as the continuum states can be treated similarly [67, 70, 71], except for certain normalization constants.

¹Note that in general TISE is of the form $\mathcal{H}(\mathbf{r})|\phi(\mathbf{r})\rangle = E|\phi(\mathbf{r})\rangle$ whereas time-dependent Schrödinger equation (TDSE) is of the form $i\frac{\partial}{\partial t}|\psi(\mathbf{r}, t)\rangle = \mathcal{H}(\mathbf{r}, t)|\psi(\mathbf{r}, t)\rangle$.

Starting from the one electron TISE one can find the one electron states called configurations. Then using Slater determinants [72] of the one-electron states, a two-electron basis $\phi_{n_1 l_1 n_2 l_2}^L(\mathbf{r}_1, \mathbf{r}_2)$, is formed. These functions are specifically the solutions of zero-order Hamiltonian (without the electron-electron interactions), $\hat{\mathcal{H}}^{a(0)} = \hat{h}_1(\mathbf{r}_1) + \hat{h}_2(\mathbf{r}_2)$, with

$$\phi_{n_1 l_1 n_2 l_2}^L(\mathbf{r}_1, \mathbf{r}_2) = A_{12} \frac{P_{n_1 l_1}(r_1)}{r_1} \frac{P_{n_2 l_2}(r_2)}{r_2} \mathcal{Y}_{l_1 l_2}^{L0}(\Omega_1, \Omega_2), \quad (5.3)$$

where $\mathcal{Y}_{l_1 l_2}^{LM_L}(\Omega_1, \Omega_2)$ are the bipolar spherical harmonics ($M_L = 0$ here), containing the angular momentum coupling coefficients (Clebsch-Gordon coefficients) and A_{12} is the antisymmetrization operator which acts to exchange the coordinates of the two electrons. The radial functions, $P_{nl}(r)$, are calculated through the relation

$$\left[-\frac{1}{2} \frac{d^2}{dr^2} + \frac{l(l+1)}{2r^2} - \frac{Z}{r} \right] P_{nl} = \epsilon_{nl} P_{nl}(r). \quad (5.4)$$

To solve it numerically, the radial functions are expanded on a basis of B-Spline polynomials with excellent numerical properties [70, 73]. Thus, by first solving the radial functions, the one-electron states can be calculated from which the two electron uncorrelated states can be obtained. The two electron wavefunctions can now be expanded on the basis set of the known two-electron uncorrelated states (configuration interaction (CI) approach)

$$\begin{aligned} \Phi_{E_n L}(\mathbf{r}_1, \mathbf{r}_2) &= \sum_{n_1 l_1 n_2 l_2} C_{n_1 l_1 n_2 l_2}^{nL} \phi_{n_1 l_1 n_2 l_2}^L(\mathbf{r}_1, \mathbf{r}_2) \\ &= \sum_{n_1 l_1 n_2 l_2} C_{n_1 l_1 n_2 l_2}^{nL} A_{12} \frac{P_{n_1 l_1}(r_1)}{r_1} \frac{P_{n_2 l_2}(r_2)}{r_2} \mathcal{Y}_{l_1 l_2}^{L0}(\Omega_1, \Omega_2) \end{aligned} \quad (5.5)$$

Eq. (5.5) is substituted into the TISE and projected over the basis $\phi_{n_1 l_1 n_2 l_2}^L(\mathbf{r}_1, \mathbf{r}_2)$ to convert it into a matrix equation. After the usual diagonalization method, the eigenenergies E_{nL} and the CI coefficients $C_{n_1 l_1 n_2 l_2}^{nL}$ are obtained.

To give a numerical scenario, start from the set of one-electron wavefunctions already at hand ($\frac{1}{r} P_{n_i l_i} Y_{l_i m_i}$) with indices n_i corresponds to the radial quantum number and l_i corresponds to the angular momentum quantum number. To relate n_i to the principal quantum number n_p , one has to use $n_p = n_i + l_i$ [68]. As has been seen in Eq. (5.5) different 2-electron uncorrelated states are used to obtain the 2-electron wavefunction. The number of states and type of states combined depend on the context and computational requirements.

For the later calculation of the cross section, the thesis considers the following set: $1 \leq n_1 \leq 5$ and $1 \leq n_2 \leq 790$. So, the first state $(n_1, l_1) \implies (n_1 + l_1)l_1$ is combined with the second state $(n_2, l_2) \implies (n_2 + l_2)l_2$. For example, one can combine $(n_1, l_1) = (1, 0) \implies 1s$ with $(n_2, l_2) = (450, 1) \implies 452p$, etc. The maximum number of such configurations considered is 4000. The number of B-spline functions used were $n_b = 802$ whereas the order of the B-splines was $k_b = 9$. The spherical box radius R was varied between $R = 296$ a.u. to $R = 326$ a.u. with a step size of 1 a.u. Using these parameters and the methodology given later on, cross section profiles were obtained for each box

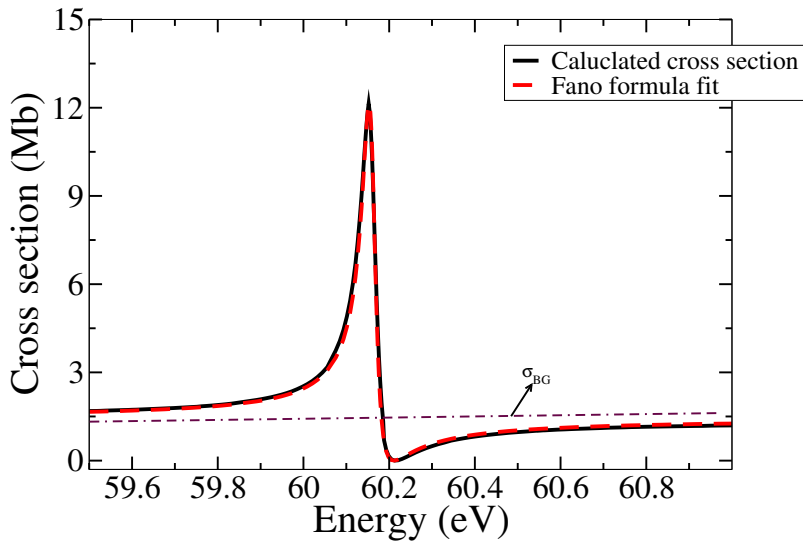


Figure 5.2: Photoionization cross section profile (black solid curve) calculated for helium using the method discussed in this chapter following the methodology of [67, 68]. A Fano-formula fit (red-dashed curve) is also shown which gives the parameters as obtained in Table 5.1.

radius. After this, the data from the aforementioned 30 boxes was merged to get the familiar cross section profile depicted in Fig. 5.2.

Coming back to the theory, a small note is in order. Assuming that the zero-energy level is set to be equivalent to the first ionization threshold of $\mathcal{A}(Z)$, if a two-electron eigenstate has an energy $E_{nL} < 0$ along with both electrons having a negative energy ($\epsilon_1, \epsilon_2 < 0$), then the two-electron state is of bound character. The electronic states with energies $E_{nL} > 0$ represent singly ionized states of $\mathcal{A}(Z)$ if the electronic energies are such that $\epsilon_1 < 0$ and $\epsilon_2 > 0$ (or vice-versa), and doubly ionized states with two ejected electrons if both of them have the electronic energies $\epsilon_i > 0$ for $i = 1, 2$.

This in brief is the approach to obtain the two-electron wavefunctions. One may wonder how these calculations related to two-electron bound and continuum states help in obtaining the necessary parameters to be inserted in the DM-EOMs (e.g. Eqs. (4.45))? The two-electron wavefunctions help in the calculation of many of the atomic quantities which in turn help in the description of the atom interaction with its environment, such as collisions, radiation, etc. Here, the particular interest is to find the values of the photoionization cross section from the ground state as well as the position and the width of the autoionizing resonance. It is these latter quantities which help in obtaining the desired parameters.

5.2 Calculation of the Fano Parameters of the AIS

In the previous chapter, Fano-representation of the atomic states was used to arrive at the DM-EOMs. In this representation the artificial separation of the two electron continuum wavefunctions leads to the concept of two channels of ionization and hence two transition

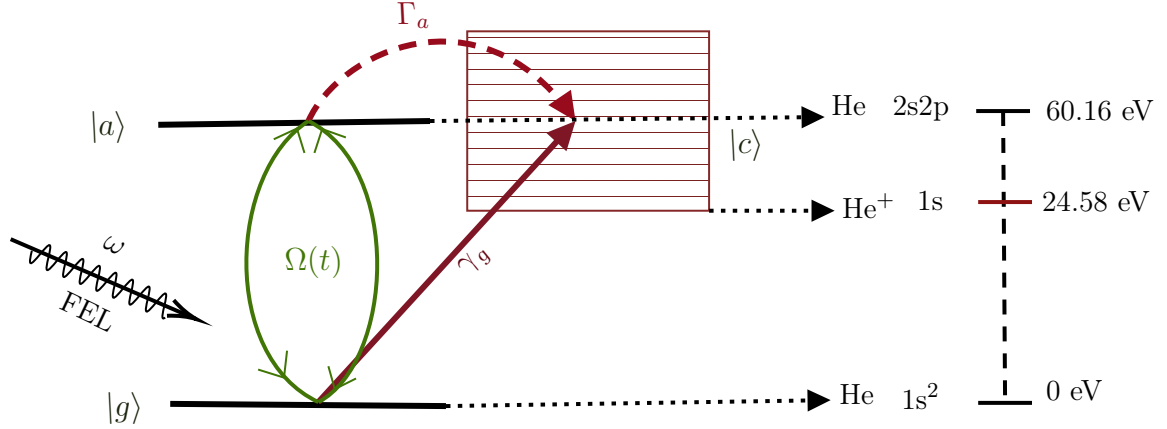


Figure 5.3: Schematic showing the energy levels in Helium in Fano-representation. $|g\rangle$ is considered to be at 0 eV. The energy positions shows are not to the scale.

amplitudes: bound-bound and bound-continuum. The former channel starts from the ground state, $|g\rangle$, by absorbing a photon and transits to the artificial Fano-bound state, $|a\rangle$ which is coupled with the Fano-continuum states, $|c\rangle$, via the electron-electron Coulomb interaction operator matrix element V_{ac} . The rate of decay from $|a\rangle$ to $|c\rangle$ is given by the AIS width, Γ_a while the rate of excitation from $|g\rangle$ to $|a\rangle$ is determined by the dipole transition matrix element, d_{ga} . Simultaneously, photoionization via a direct transition from the ground state, $|g\rangle$, to the Fano continuum, $|c\rangle$, occurs via the dipole transition matrix element d_{gc} . These two channels interfere i.e., $|g\rangle \xrightarrow{d_{ga}} |a\rangle \xrightarrow{V_{ac}} |c\rangle$ and $|g\rangle \xrightarrow{d_{gc}} |c\rangle$ interfere which leads to the famous Fano-asymmetric lineshape [42].

Let the helium atom be the target example in this chapter. The same can be easily extended to other helium like ions. For numerical purposes, the ground state $|g\rangle$ ($1s^2$) is considered to be at $E_g = 0$ eV (0 a.u.) and the FEL pulse's central frequency ω is chosen near the resonance energy of $|a\rangle$ ($2s2p$). After interacting with the near resonant laser pulse, the system may first excite into an unstable doubly excited autoionizing state $|a\rangle$ ($E_a = 60.16$ eV or 2.211 a.u.), via the field dependent Rabi oscillation $\Omega(t)$ and then ionize into the continuum through the electron-electron interaction, characterised by the autoionization width Γ_a . The system may also ionize directly into the continuum via photoionization characterised by its width $\gamma_g(t)$. The interference between these two channels of ionization is described via the asymmetry parameter q_a . This schematic is given in Fig. 5.3

It is understood from the aforementioned processes that unless one knows the values of $E_a, \Gamma_a, d_{ga}, d_{gc}$ and q_a , one can not decode the photoionization dynamics. The standard theoretical procedure to obtain these values is as follows:

- i After the calculation of the two-electron states, the photoionization cross sections are calculated.
- ii From the photoionization cross section profile, the position and width of the autoionizing resonance is obtained.
- iii From the width and positional values of the AIS, the Fano effective parameters, d_{ga}, d_{gc}, q_a are obtained.

The first step has already been discussed. In the following sections, the other steps will be explored.

5.3 Photoionization cross section, position and width of the AIS

When the helium atom starts from its initial ground state He ($1s^2$) and ends in He⁺ ($1s$) final state, the one-photon photoionization cross section $\sigma_1(E)$, in a.u., can be calculated from the formula,

$$\sigma_1(E) = \frac{4\pi^2}{c}\omega|\langle\Phi_{E_gS}|z_1 + z_2|\Phi_{EP}\rangle|^2 = \frac{4\pi^2}{c}\omega|d_{gf}|^2, \quad E = E_g + \omega, \quad (5.6)$$

where ω is the central frequency of the laser pulse, Φ_{E_gS} , Φ_{EP} represent respectively the ground and the final (near AIS) states of the system and d_{gf} denotes the corresponding transition dipole matrix element [67]. The z_1, z_2 are the electron's position operators (note that the field is assumed to be linearly polarised along the z-axis).

Using the previously calculated two electron states and following the scheme of the ab-initio calculation method developed in [67, 68], the corresponding dipole transition matrix elements and hence the one-photon cross section values for helium are calculated. The lineshape thus obtained is shown as the black-solid curve in the Fig. 5.2.

The near resonance lineshape of a cross section relates to the q_a, E_a and Γ_a via the Fano-shape formula [42, 74],

$$\sigma_1(E) = \sigma_{BG} \frac{(q_a + \epsilon)^2}{(1 + \epsilon^2)}, \quad \epsilon = \frac{E - E_a}{\frac{1}{2}\Gamma_a} \quad (5.7)$$

where, σ_{BG} is the background cross section whose value is obtained as 1.40 Mb (close to the experimental value [75, 76])². It is depicted in the Fig. 5.2 as a maroon colored dot-dashed line marked as σ_{BG} . Using the above parametric formula-fit (shown as red-dashed curve in the same figure), one obtains the required values which are given in Table 5.1. It can be seen that the theoretical values thus obtained are in close agreement with the experimental values measured in references [77–81] along with the cross section profile itself as shown in reference [76] and the references therein.

Alternatively one can first find the scattering phase shifts ($\delta_l(E)$) for the ejected electron, using the previously obtained box-limited wavefunctions and then use the following formula-fit to obtain the AIS position and corresponding width.

$$\delta_l(E) = b_0 + b_1E + b_2E^2 + \tan^{-1} \frac{\Gamma_a/2}{E_a - E}, \quad (5.8)$$

where E_a is the position of the AIS and Γ_a is the autoionizing width of this state. b_iE^i 's represent the residual background energy dependence of the phase shift. For more detailed methodologies, see e.g. Refs [76, 82]. This approach does not give q_a directly. In the next

²Units of a photoionization cross section are usually megabarns (Mb), with 1 Mb = 10^{-22} m².

section, using the maximum and minimum of the lineshape of Fig. 5.2, the value of q_a is derived.

Parameters	Values
E_a	2.211
q_a	-2.733
d_{ga}	0.0355
Γ_a	0.00137
γ_g	0.494
γ_c	0.426

Table 5.1: Atomic parameters obtained for He(2s2p) AIS resonance in a.u.

5.3.1 Calculation of q_a, d_{ga}, d_{gc}

q_a is already known if the Fano-lineshape approach is followed. If the alternate phase-shift approach is followed, then the following analysis will help in obtaining the value of q_a along with the matrix elements d_{ga} and d_{gc} .

In its simplest form, the Fano parametrization of the dipole photoionization cross section ionization expressed at energy $E = E_g + \omega = E_c = E_{nP}$ is written as,

$$|d_{gf}|^2 = |d_{gc}|^2 \frac{(q + \epsilon)^2}{1 + \epsilon^2} = |d_{gc}|^2 \left(1 + \frac{q_a^2 - 1 + 2q_a\epsilon}{1 + \epsilon^2}\right), \quad \epsilon = \frac{E - E_a}{\frac{1}{2}\Gamma_a} \quad (5.9)$$

where d_{gf} is the dipole transition matrix element in Equation (5.6). d_{gc} is the dipole transition matrix element from the ground state to the $|c\rangle$ state and ϵ is the normalized photon energy. It was already seen in Eq. (4.33) of the previous chapter that q_a represents the strength of interference between the two channels of ionization and hence the degree of asymmetry in the lineshape. Following the expression as given in Eq. (4.33) and noting that \bar{E} is evaluated at E_a (very low detuning)

$$q_a = \frac{d_{ga}}{\pi d_{gc} V_{ca}}, \quad (5.10)$$

Eq (5.9) suggests that there is a maximum and a minimum for the lineshape, given by the expressions

$$E_c^{(max)} = E_a + \frac{\Gamma_a}{2q_a}, \quad E_c^{(min)} = E_a - \frac{1}{2}\Gamma_a q_a. \quad (5.11)$$

Because the pair (E_a, Γ_a) is already known, from either of the above expressions, the value of q_a can be found. If there is an uncertainty in the AIS position, then the knowledge of Γ_a alone is sufficient:

$$\begin{aligned} E_c^{(max)} - E_c^{(min)} &= \frac{\Gamma_a}{2} \left(\frac{1}{q_a} + q_a \right) \\ \implies q_a &= \frac{E_c^{(max)} - E_c^{(min)}}{\Gamma_a} \pm \sqrt{\left(\frac{E_c^{(max)} - E_c^{(min)}}{\Gamma_a} \right)^2 - 1} \end{aligned} \quad (5.12)$$

Thus q_a is obtained either from the first approach of the previous section or the approach given in this section, which is crucial to calculate the other parameters. To proceed with the calculation of the parameter d_{ga} it is seen from Eq. (5.9) that there is an energy \bar{E} where,

$$q_a^2 + 2q_a\bar{\epsilon} - 1 = 0 \quad \rightarrow \quad \bar{E} = E_a + \frac{\Gamma_a}{2} \frac{1 - q_a^2}{2q_a} \quad \rightarrow \quad |d_{gc}|^2 \Big|_{E=\bar{E}} = |d_{gf}|^2 \Big|_{E=\bar{E}}. \quad (5.13)$$

As the values of E_a, q_a, Γ_a are already known, one can calculate the value of d_{gc} from the above expression. Then substitute this in Eq. (5.10) to get the value of d_{ga} . Remember that V_{ca} is known via Eq. (4.39) i.e., $\Gamma_a = 2\pi|V_{ca}|^2$. The relative signs can be confirmed from the profile shape.

The previously derived DM-EOMs are expressed in terms of ionization widths rather than photoionization cross sections. So, a brief note needs to be given which shows their relationship. Assume the photoionization is caused by a monochromatic field of amplitude E_0 and frequency, ω . It is the intensity that is measured in an experiment and not the field (usually this is complex) and hence a relation between them needs to be established before proceeding. Take a time average of the Poynting vector magnitude, S . Then, the peak intensity is given by $I_0 = \langle S \rangle_t = c\epsilon_0 E_0^2/2$, where ϵ_0 is the vacuum's dielectric constant given by $\epsilon_0 = 1/4\pi$ (in a.u.). This gives $I_0 = cE_0^2/8\pi$. Applying standard perturbation theory, the ionization yield is related with the photoionization cross section (from initial state 'i' to final state 'f') via (all quantities in a.u.):

$$\bar{\gamma}_{if} = \sigma_1 \frac{I_0}{\omega} = \frac{4\pi^2}{c} \omega |d_{if}|^2 \frac{cE_0^2/8\pi}{\omega} = 2\pi |d_{if}|^2 \frac{E_0^2}{4} = \gamma_{if} \mathcal{I}, \quad (5.14)$$

The bar over LHS denotes a time averaged rate of ionization and $\mathcal{I} = E_0^2/4$ denotes time averaged intensity. It can be inferred that γ_{if} represents the average ionization rate when $\mathcal{I} = 1$. Thus, when the cross sections are known, the widths can be deduced and when the widths are known, the cross sections can be deduced.

By knowing d_{gc} the unit rate of photoionization is known from the above relation as

$$\gamma_g \text{ (of DM-EOMs)} = \gamma_{gc} = 2\pi |d_{gc}|^2 \quad (5.15)$$

Using Eq. (5.15), Eq. (4.39) and Eq. (4.33), the following useful relation is obtained

$$d_{ga} = \frac{1}{2} |q_a| \sqrt{\gamma_g \Gamma_a} \quad (5.16)$$

from which the d_{ga} is finally obtained.

This shows how to obtain the set of parameters: $\gamma_g, \Gamma_a, d_{ga}, q_a$. To summarize, the order of numerical calculation is as follows

- i From the cross section lineshape and Fano-fit in Fig. 5.2, one obtains $E_a = 60.16$ eV (2.211 a.u.), $q_a = -2.733$ and $\Gamma_a = 0.0373$ eV (0.00137 a.u.).
- ii From Eq. (4.39) Γ_a value gives $V_{ca} = \sqrt{\Gamma_a/2\pi} = 0.01477$ a.u.

iii The energy \bar{E} of Eq. (5.13), where $|d_{gc}|^2 = |d_{gf}|^2$, is $\bar{E} = E_a + \frac{\Gamma_a}{2} \frac{1-q_a^2}{2q_a} = 60.19$ eV (2.2118 a.u.).

iv At the above energy value of \bar{E} , the cross section value obtained is 1.40 Mb. Using Eq. (5.14), one obtains $\gamma_{gc} = \sigma_1 \frac{I_0}{\omega}$, when $\mathcal{I} = 1$. But $\mathcal{I} = 1$ implies that $E_0^2 = 4$ and hence $I_0 = \frac{c}{8\pi} E_0^2 = \frac{c}{2\pi}$. In atomic units, value of $c \approx 137$. Therefore, $\gamma_{gc} = \sigma_1 \frac{137}{2\pi} = 0.494$ a.u. Also, one can start with Eq. (5.6) and obtain $d_{gc} = 0.2805$ a.u. and then insert in Eq. (5.15) to calculate the value of $\gamma_g = 0.494$ a.u.

v Using Eq. (5.16) the value of d_{ga} is obtained as $d_{ga} = 0.5 \times 2.733 \times \sqrt{0.494 \times 0.00137} = 0.0355$ a.u.

5.3.2 Extra channel

In the later chapters, an extra channel of ionization is also considered from the ground state of the hydrogenic state to the doubly ionized state of the helium like atom. So, for completeness, a brief method of calculation of the corresponding rate of its ionization is given below. The photoionization cross sections of the hydrogenic ion, is calculated by,

$$\sigma_1(\epsilon_{np}) = \frac{4\pi^2}{c} \omega |\langle \phi_{1s} | z | \phi_{np} \rangle|^2 = \frac{4\pi^2}{c} \omega |d_{1s;np}|^2, \quad \epsilon_{np} = \epsilon_{1s} + \omega, \quad (5.17)$$

where $\phi_{1s}(\mathbf{r})$ and $\phi_{np}(\mathbf{r})$ are the common eigenstates of the hydrogenic ion's Hamiltonian, angular momentum and its z-projection. The energies, $\epsilon_{1s}, \epsilon_{np}$ are obtained from the solution of the radial eigenvalue equation (5.4). The matrix elements $d_{1s;np}$ have been calculated earlier [68, 69]. One eventually obtains the value of $\gamma_c = 0.426$ a.u. for helium. All these parameters are summarised in the Table 5.1.

5.4 Conclusion

An ab-initio methodology developed and utilised in the references [67–69], was followed in this chapter to show how to obtain the atomic parameters needed to be inserted in the DM-EOMs. This was achieved by first calculating the single electron and two electron wavefunctions after which the dipole matrix elements are evaluated. This helped in obtaining of the one photon cross sections (CS). From the resonance profile of the CS shape, the Fano parameters q_a, Γ_a, E_a were estimated. Using these and the relation of CS with the ionization widths, the other parameters was evaluated. These values were shown to be in good agreement with the experimentally evaluated ones. With the parametric values available, one can now enter into the main subject of the thesis - stochastic averaging of the DM-EOMs.

Chapter 6

Simple theory of averaging

Previous chapters described the necessary DM-EOMs that help in the analysis of light-matter interactions. If the laser were fully coherent, a direct solution of the DM-EOMs would result in the knowledge of the states populations and coherences. But when the laser source is chaotic, like a FEL source, the equations turn into stochastic differential equations (SDEs), due to the field dependent parameters that are involved, which means a direct solution is impossible as the result will differ every time one attempts to solve the EOMs. This requires sophisticated approaches that can solve the new DM SDEs. The present chapter aims to present two simple approaches that can help in turning the SDEs into deterministic equations. The approaches are named ‘simple’ not because of the level of mathematical complexity, but because of the details of the statistical nature of FEL that is considered. Only the ensemble average of the field and its first order correlation are utilised. A rigorous and all-encompassing theory is given in Chapter 7.

6.1 Stochastic field modelling

Before entering into the averaging of the equations, a compact model of the fluctuating field, that is used in the EOMs, is given here. The radiation field is generally modelled as

$$E(t) = E_{0R}(t) \cos(\omega t + \phi(t)). \quad (6.1)$$

with the envelope $E_{0R}(t)$ and the phase $\phi(t)$ considered as real random processes having known statistical properties. But, it is rather more convenient to use a complex analytical field envelope modelled as

$$\mathcal{E}(t) = \frac{1}{2} E_{0R}(t) e^{i\phi(t)} = \mathcal{E}_0(t) \epsilon(t), \quad (6.2)$$

Here, $\mathcal{E}_0(t)$ is complex slowly varying deterministic envelope and all the fluctuations are modeled by the $\epsilon(t)$ which is a complex random processes, fully characterized via its statistical multitime moment functions. As pointed earlier, this chapter only includes first

order multi-time moment function of the field. Two types of correlations are considered

$$\langle \epsilon(t)\epsilon^*(t-\tau) \rangle = \begin{cases} e^{-\frac{|\tau|}{2\tau_c}}, & \text{Lorentzian correlation} \\ e^{-\frac{\tau^2}{2\tau_c^2}}, & \text{Gaussian correlation} \end{cases} \quad (6.3)$$

Using Eq. (6.3) for the value of $\tau = 0$, one obtains $\langle |\mathcal{E}(t)|^2 \rangle = \langle \mathcal{E}_0(t)\mathcal{E}_0^*(t)\epsilon(t)\epsilon^*(t) \rangle = |\mathcal{E}_0(t)|^2 \langle \epsilon(t)\epsilon^*(t) \rangle^1 = |\mathcal{E}_0(t)|^2$. Then, the ensemble average of the intensity would be

$$\langle \mathcal{I}(t) \rangle = \langle |\mathcal{E}(t)|^2 \rangle = |\mathcal{E}_0(t)|^2 \quad (6.4)$$

One can choose many analytical shapes for the complex envelope $\mathcal{E}_0(t)$ such as a square shape or sinusoidal shape or Gaussian shape, etc. In this work, the form of the envelope is chosen to be a Gaussian one

$$\mathcal{E}_0(t) = \mathcal{E}_0 e^{-\chi t^2/2\tau_p^2}, \quad (6.5)$$

with complex χ indicating the chirp of the pulses [35, 37] and amplitude of \mathcal{E}_0 . This choice gives the averaged intensity, via Eq. (6.4) as,

$$\langle \mathcal{I}(t) \rangle = \langle |\mathcal{E}(t)|^2 \rangle = \mathcal{E}_0^2 e^{-t^2/\tau_p^2} = \mathcal{I}_0 e^{-t^2/\tau_p^2}. \quad (6.6)$$

Note that the full width at half maximum FWHM, given by τ_{FWHM} , of the averaged intensity is related with τ_p by $\tau_{fwhm} = \tau_p \sqrt{4 \ln 2}$.

6.2 Approach-1: Retaining the form of EOMs

The goal of the first approach is to show the agility of DM methodology developed in this work and see how the introduction of field fluctuations affect the observables by using a stochastic averaging method which retains the form of the EOMs. To this end this section considers resonant Auger effect of Neon as explored by the authors of the reference [29]. They consider amplitude EOMs whereas in the following averaged DM-EOMs will be developed. It will be shown that the developed averaged EOMs can incorporate fluctuations of the field on demand i.e., one can control the parameter τ_c and either switch on or off the field fluctuations (theoretically). The scenario presented in reference [29], in relation to the DM-EOMs derived earlier, boils down to effectively choosing $q_a \rightarrow \infty$, $\gamma_g(t) \rightarrow 0$, and $\mathcal{E}(t) \rightarrow$ real Gaussian envelope (and hence $\Omega(t) = d_{ga}\mathcal{E}(t)$ is real). Because it is a resonant process, the knowledge of the bound state dynamics is sufficient i.e., just the first three equations of Eqs. (4.45) need to be considered in the following.

The schematic is given in the Fig. 6.1. The final density matrix equations of motion

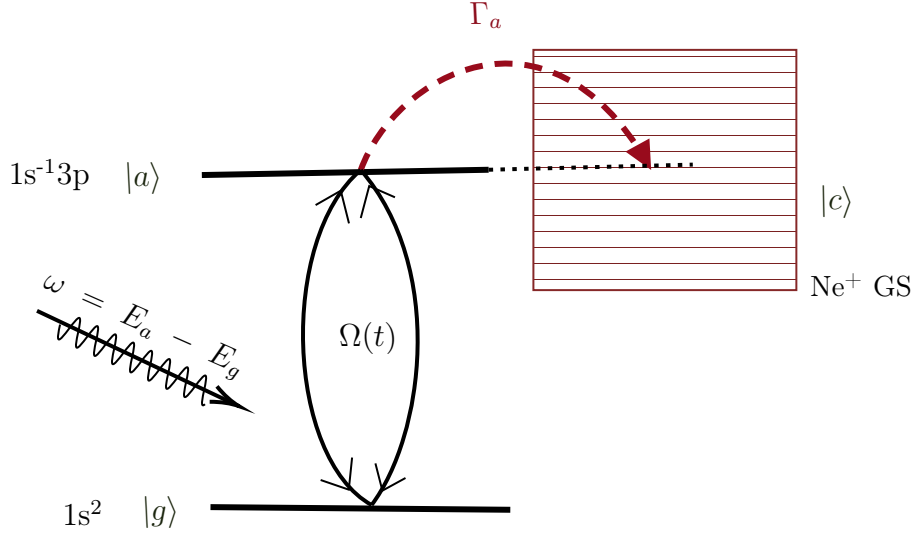


Figure 6.1: Schematic of the interaction of a near resonant FEL field with neon atom. ω is the tunable resonance frequency, $|c\rangle$ is the continuum Γ_a is the Auger-decay width and $\Omega(t)$ denotes the Rabi oscillations.

for this schematic are given below.

$$\dot{\sigma}_{gg}(t) = 2\text{Im}[\Omega(t)\sigma_{ag}(t)] = -2\text{Im}[\Omega(t)\sigma_{ga}(t)] \quad (6.7a)$$

$$\dot{\sigma}_{aa}(t) = -\Gamma_a\sigma_{aa}(t) - 2\text{Im}[\Omega(t)\sigma_{ag}(t)] = -\Gamma_a\sigma_{aa}(t) + 2\text{Im}[\Omega(t)\sigma_{ga}(t)] \quad (6.7b)$$

$$\dot{\sigma}_{ga}(t) = \sigma_{ga}(t)\left[-i\Delta - \frac{\Gamma_a}{2}\right] + i\Omega(t)[\sigma_{gg}(t) - \sigma_{aa}(t)] \quad (6.7c)$$

When the field is stochastic, it renders the above set stochastic. Therefore, an averaging method is required. Before proceeding, the following simplification of the representation of few terms, for ease of calculation, is made: $k = \Delta - i\frac{\Gamma_a}{2}$ and $n_{ga}(t) = \sigma_{gg}(t) - \sigma_{aa}(t)$.

Now, start from Eq. (6.7c),

$$\begin{aligned}
\dot{\sigma}_{ga}(t) &= -\imath k \sigma_{ga}(t) + \imath \Omega(t) n_{ga}(t) \\
\implies \dot{\sigma}_{ga}(t) + \imath k \sigma_{ga}(t) &= \imath \Omega(t) n_{ga}(t) \\
\implies \dot{\sigma}_{ga}(t) e^{\imath \int_{t_i}^t k dt} + \imath k \sigma_{ga}(t) e^{\imath \int_{t_i}^t k dt} &= \imath \Omega(t) n_{ga}(t) e^{\imath \int_{t_i}^t k dt} \\
\implies \frac{d}{dt} (\sigma_{ga}(t) e^{\imath \int_{t_i}^t k dt}) &= \imath \Omega(t) n_{ga}(t) e^{\imath \int_{t_i}^t k dt} \\
\implies \sigma_{ga}(t) e^{\imath \int_{t_i}^t k dt} &= \imath \int_{t_i}^t \Omega(t') n_{ga}(t') e^{\imath \int_{t_i}^{t'} k dt''} dt' \\
\implies \sigma_{ga}(t) &= \imath \int_{t_i}^t \Omega(t') n_{ga}(t') e^{-\imath \int_{t_i}^t k dt''} e^{\imath \int_{t_i}^{t'} k dt''} dt' \\
\implies \sigma_{ga}(t) &= \imath \int_{t_i}^t \Omega(t') n_{ga}(t') e^{-\imath \int_{t_i}^t k dt''} e^{-\imath \int_{t'}^t k dt''} dt' \\
\implies \sigma_{ga}(t) &= \imath \int_{t_i}^t \Omega(t') n_{ga}(t') e^{-\imath \int_{t'}^t k dt''} dt' \\
\implies \sigma_{ga}(t) &= \imath \int_{t_i}^t \Omega(t') n_{ga}(t') e^{-\imath k(t-t')} dt' \\
\implies \Omega(t) \sigma_{ga}(t) &= \imath \int_{t_i}^t \Omega(t) \Omega(t') n_{ga}(t') e^{-\imath k(t-t')} dt' \\
\implies \langle \Omega(t) \sigma_{ga}(t) \rangle &= \imath \int_{t_i}^t \underline{\langle \Omega(t) \Omega(t') n_{ga}(t') \rangle} e^{-\imath k(t-t')} dt'
\end{aligned}$$

To proceed further, an approximation needs to be invoked without which it is not possible to analyse the integral on the right hand side of the above equation due to the underlined term. The approximation is called decorrelation-approximation (DA) (see section 6.3.1). It entails separating the underlined term, i.e.,

$$\underline{\langle \Omega(t) \Omega(t') n_{ga}(t') \rangle} = \underline{\langle \Omega(t) \Omega(t') \rangle} \underline{\langle n_{ga}(t') \rangle}$$

Physically, it implies that the rate of evolution of the field and the atomic states are different which allows for this separate evaluation of the averages. The terms after the DA application are known i.e, one is first order field correlation function and the other is the evolution of the coherence term. The first order field correlation function is modeled as Lorentzian in this approach.

$$\langle \Omega(t) \Omega(t') \rangle = \tilde{\Omega}(t) \tilde{\Omega}(t') e^{-\frac{|t-t'|}{2\tau_c}}$$

where, $\tilde{\Omega}(t) = d_{ag} \mathcal{E}_0(t)$ represents the averaged envelope of the stochastic function $\Omega(t)$. τ_c is the coherence time of the field ($\tau_c \rightarrow \infty$ when the field is completely coherent). Continuing with the derivation

$$\langle \Omega(t) \sigma_{ga}(t) \rangle = \imath \int_{t_i}^t \tilde{\Omega}(t) \tilde{\Omega}(t') e^{-\frac{|t-t'|}{2\tau_c}} e^{-\imath k(t-t')} \langle n_{ga}(t') \rangle dt'$$

because $t > t'$ in the above integral, $|t - t'| = (t - t')$

$$\begin{aligned}\langle \Omega(t)\sigma_{ga}(t) \rangle &= \imath \int_{t_i}^t \tilde{\Omega}(t)\tilde{\Omega}(t')e^{-\frac{t-t'}{2\tau_c}}e^{-\imath k(t-t')}\langle n_{ga}(t') \rangle dt' \\ \implies \langle \Omega(t)\sigma_{ga}(t) \rangle &= \imath \int_{t_i}^t \tilde{\Omega}(t)\tilde{\Omega}(t')e^{-\imath \bar{k}(t-t')}\langle n_{ga}(t') \rangle dt'\end{aligned}$$

where, $\imath \bar{k} = \imath k + \frac{1}{2\tau_c}$ or $\bar{k} = k - \imath \frac{1}{2\tau_c}$

$$\begin{aligned}\implies \frac{\langle \Omega(t)\sigma_{ga}(t) \rangle}{\tilde{\Omega}(t)} &= \imath \int_{t_i}^t \tilde{\Omega}(t')e^{-\imath \bar{k}(t-t')}\langle n_{ga}(t') \rangle dt' \\ \implies \frac{\langle \Omega(t)\sigma_{ga}(t) \rangle}{\tilde{\Omega}(t)} &= \imath \int_{t_i}^t \tilde{\Omega}(t')e^{-\imath \bar{k}t}e^{\imath \bar{k}t'}\langle n_{ga}(t') \rangle dt' \\ \implies \frac{\langle \Omega(t)\sigma_{ga}(t) \rangle}{\tilde{\Omega}(t)}e^{\imath \bar{k}t} &= \imath \int_{t_i}^t \tilde{\Omega}(t')e^{\imath \bar{k}t'}\langle n_{ga}(t') \rangle dt'\end{aligned}$$

Using the first fundamental theorem of calculus (see the footnote on page 87), and *wlog* taking $t_i = 0$,

$$\begin{aligned}\implies \frac{d}{dt} \left[\frac{\langle \Omega(t)\sigma_{ga}(t) \rangle}{\tilde{\Omega}(t)} e^{\imath \bar{k}t} \right] &= \imath \tilde{\Omega}(t) e^{\imath \bar{k}t} \langle n_{ga}(t) \rangle \\ \implies \frac{d}{dt} \left[\frac{\langle \Omega(t)\sigma_{ga}(t) \rangle}{\tilde{\Omega}(t)} \right] e^{\imath \bar{k}t} &+ \frac{\langle \Omega(t)\sigma_{ga}(t) \rangle}{\tilde{\Omega}(t)} (\imath \bar{k} e^{\imath \bar{k}t}) = \imath \tilde{\Omega}(t) e^{\imath \bar{k}t} \langle n_{ga}(t) \rangle\end{aligned}$$

Introducing new notation P_{ga} given by:

$$\begin{aligned}\langle \bar{P}_{ga}(t) \rangle &= \frac{\langle \Omega(t)\sigma_{ga}(t) \rangle}{\tilde{\Omega}(t)} \\ \implies \langle \dot{\bar{P}}_{ga}(t) \rangle &= -\imath \bar{k} \langle \bar{P}_{ga}(t) \rangle + \imath \tilde{\Omega}(t) \langle n_{ga}(t) \rangle \\ \implies \imath \langle \dot{\bar{P}}_{ga}(t) \rangle &= \bar{k} \langle \bar{P}_{ga}(t) \rangle - \tilde{\Omega}(t) \langle n_{ga}(t) \rangle\end{aligned}$$

Going back to the former equations:

$$\begin{aligned}\dot{\sigma}_{gg}(t) &= -2\text{Im}[\Omega(t)\sigma_{ga}(t)] \\ \implies \langle \dot{\sigma}_{gg}(t) \rangle &= -2\text{Im}[\langle \Omega(t)\sigma_{ga}(t) \rangle] \\ \langle \Omega(t)\sigma_{ga}(t) \rangle &= \langle \bar{P}_{ga}(t) \rangle \tilde{\Omega}(t) \\ \implies \langle \dot{\sigma}_{gg}(t) \rangle &= -2\text{Im}[\langle \bar{P}_{ga}(t) \rangle \tilde{\Omega}(t)]\end{aligned}\tag{6.8}$$

$$\begin{aligned}\dot{\sigma}_{aa}(t) &= -\Gamma_a \sigma_{aa}(t) + 2\text{Im}[\Omega(t)\sigma_{ga}(t)] \\ \implies \langle \dot{\sigma}_{aa}(t) \rangle &= -\Gamma_a \sigma_{aa}(t) + 2\text{Im}[\langle \bar{P}_{ga}(t) \rangle \tilde{\Omega}(t)]\end{aligned}\tag{6.9}$$

$$\langle \dot{\bar{P}}_{ga}(t) \rangle = \left(-\imath \Delta - \left[\frac{1}{2\tau_c} + \frac{\Gamma_a}{2} \right] \right) \langle \bar{P}_{ga}(t) \rangle + \imath \tilde{\Omega}(t) \left(\langle \sigma_{gg}(t) \rangle - \langle \sigma_{aa}(t) \rangle \right)\tag{6.10}$$

$$\langle \dot{\bar{P}}_{ag}(t) \rangle = \left(\imath \Delta - \left[\frac{1}{2\tau_c} + \frac{\Gamma_a}{2} \right] \right) \langle \bar{P}_{ga}(t) \rangle + \imath \tilde{\Omega}(t) \left(\langle \sigma_{gg}(t) \rangle - \langle \sigma_{aa}(t) \rangle \right)\tag{6.11}$$

Parameters	Values (a.u.)
Δ	0 (resonance condition)
$1/q_a$	0
d_{ga}	0.0096
γ_g	0
Γ_a	0.0099

Table 6.1: Atomic parameters in a.u. used for the neon resonant Auger decay.

where recollecting that $\tilde{\Omega}(t) = d_{ag}\mathcal{E}_0(t)$ with $\mathcal{E}_0(t)$ the slowly varying envelope of the real field. The last four boxed equations Eq. (6.8) - Eq. (6.11) are the averaged coupled deterministic differential equations of the earlier SDEs and can be solved using Runge–Kutta methods to obtain the required observables.

6.2.1 Results and discussions: Neon

First, consider the dashed curves of Fig. 6.2 which were adapted from reference [29]. These curves represent the ground state population of Neon and the average pulse that had been computed by repeated averages over 10000 chaotic pulses. The Monte Carlo approach that is followed in the aforementioned reference is time consuming and computationally demanding. The immediate thought would be to see if the averaged EOMs derived in Eq. (6.8) - Eq. (6.11) be utilised to achieve the same goal. One of the best features of the averaged DM-EOMs is their fast computational capabilities (due to reduction in the nature of repetitiveness). In order to use the said EOMs in the present context, atomic parameters from Table 6.1 are inserted and the averaged field envelope is chosen to have a slowly rising square shape (shown as the red/black curves of Fig. 6.2). The coherence time of pulse is 3.3 fs. In Fig. 6.2 the averaged intensity used and the evaluated ground-state population of Neon ($\langle\sigma_{gg}(t)\rangle$) are plotted after solving the averaged DM-EOMs. When these are compared against the adapted graphs from [29], it can be seen that both the sets of plots are in close agreement. This suggests the accuracy and efficiency of the present approach. This is a promising start to the averaging approach.

The next part concentrates on the double-dot-dashed curves of Fig. 6.3 which were adapted from the aforementioned reference [29]. These curves represent the Auger-electron yield as a function of the peak intensity of the pulse. A real Gaussian envelope and purely coherent field were used. Though the averaged equations are more useful when field fluctuations are present, one needs to first check if the coherent case is regained or not by removing the factor that controls the stochasticity. Coherent case is but a particular case of stochastic case i.e., $\frac{1}{\tau_c} \rightarrow 0$. Therefore in Fig. 6.3, along with the adapted curves, the Auger-yield profiles obtained by solving the averaged DM-EOMs (Eq. (6.8) - Eq. (6.11)) are plotted. The pulse shape is modeled to have a slowly varying Gaussian shape. Different root-mean-square widths (RMSW), denoted by τ_{rmsw} , were utilised. With the model of the field given in Eq. (6.6), the relation between different widths is given by $\tau_p = \sqrt{2}\tau_{rmsw}$. It can be seen from Fig. 6.3 that for all these pulse durations, the Auger-electron yield profile generated from the averaged DM-EOMs matches that of the curves adapted from

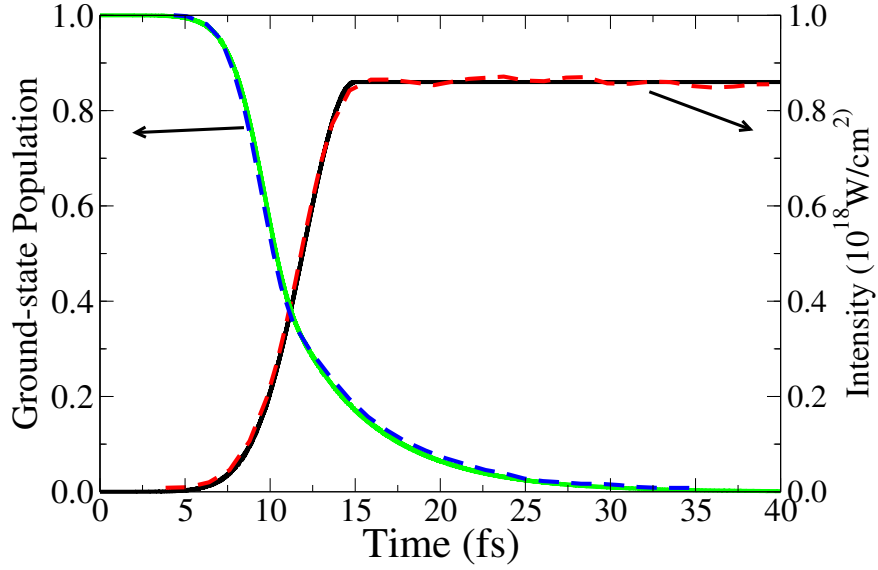


Figure 6.2: Ground-state population of neon after interacting with an ensemble of fluctuating pulses whose average form is slowly varying square shape. The solid curves are obtained by solving the averaged DM-EOMs Eq. (6.8) - Eq. (6.11) whereas the dashed curves mimic the data from the reference [29]. The green and blue curves represent the ground-state population of Neon whereas the red and the black ones represent the averaged intensity profile.

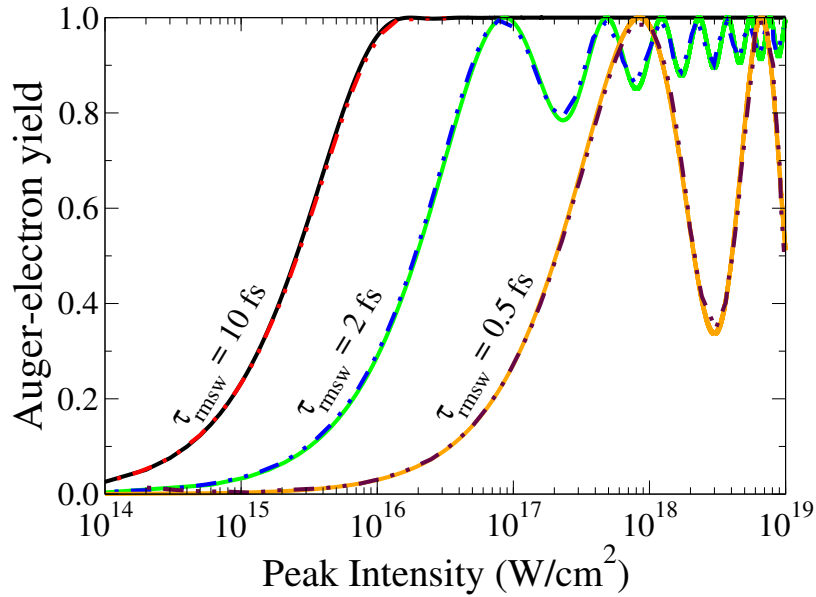


Figure 6.3: Auger-electron yield of Neon after interacting with a coherent pulse of Gaussian shaped envelope. The solid curves are obtained by solving the averaged DM-EOMs Eq. (6.8) - Eq. (6.11) when $\frac{1}{\tau_c} \rightarrow 0$ whereas the double-dot-dashed curves mimic the data from the reference [29].

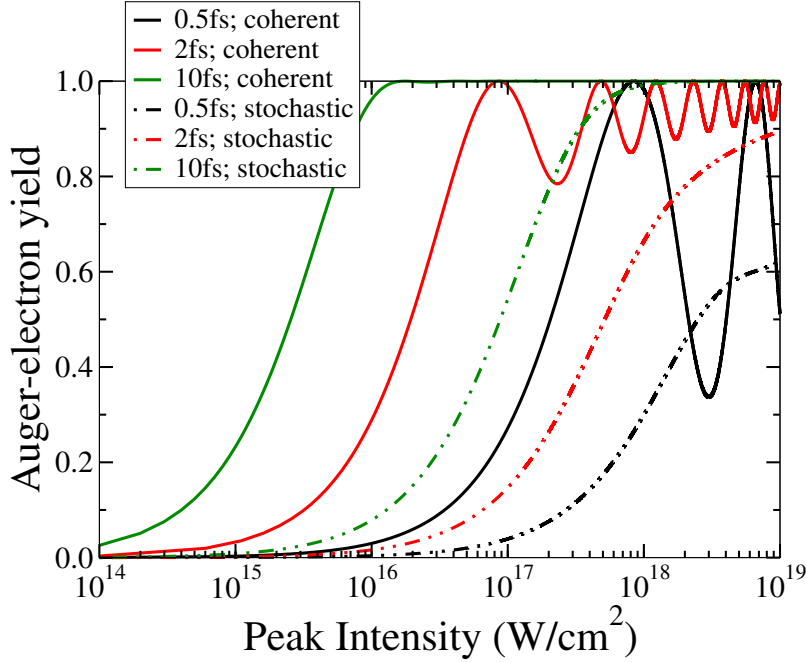


Figure 6.4: Comparison of the Auger-yields for coherent pulse (solid curves) with that of stochastic pulse (double-dot-dashed curves) of $\tau_c = 0.15$ fs. The τ_{rmsw} for the black curves is 0.5 fs, for the red curves is 2 fs and for the green curves is 10 fs.

the reference [29]. This further strengthens the accuracy and efficiency of the averaged DM approach.

Now that the coherent case is explored, one can switch on the stochasticity for the same pulse envelope and see how the Auger-yield changes. The stochastic pulse scenario considered here is of the Lorentzian correlation for the field's first order correlation, as in Eq. (2.12). Fig. 6.4 and Fig. 6.5 show how the parameters like coherence time τ_c , τ_{rmsw} and phenomena like Rabi oscillations affect the observed yield pattern as a function of peak intensity of the pulse.

In Fig. 6.4, the coherence time $\tau_c = 0.15$ fs is less than τ_{rmsw} used for different pulses, whereas in Fig. 6.5, the coherence time 3.3fs is greater than the τ_{rmsw} of some of the pulses. A significant change in the profile of the Auger-electron yield can be seen with this choice. When one compares the yield profile of a stochastic pulse with that of a coherent pulse, the oscillatory behavior prevails in the case of $\tau_c > \tau_{rmsw}$ and the oscillatory behavior totally vanishes for the case of $\tau_c < \tau_{rmsw}$. Physically, the oscillatory behavior of the yield pattern is the manifestation of Rabi oscillations [29]. So, when coherence time is sufficiently large or at least comparable to the RMSW, the Rabi oscillations, as they change with intensity, changes the yield-profiles. But when pulse is sufficiently large, i.e. RMSW is greater than the coherence time, the system ionizes faster & sooner and hence the Rabi oscillations have negligible effect on the oscillatory behavior of the yield-profiles even with increasing intensity.

In summary, it was shown how DM-EOMs could closely reproduce the populations or Auger yield profiles obtained from coherent/stochastic pulses to those obtained in Ref [29], as well as how powerful they are in enabling the incorporation of the field fluctuations.

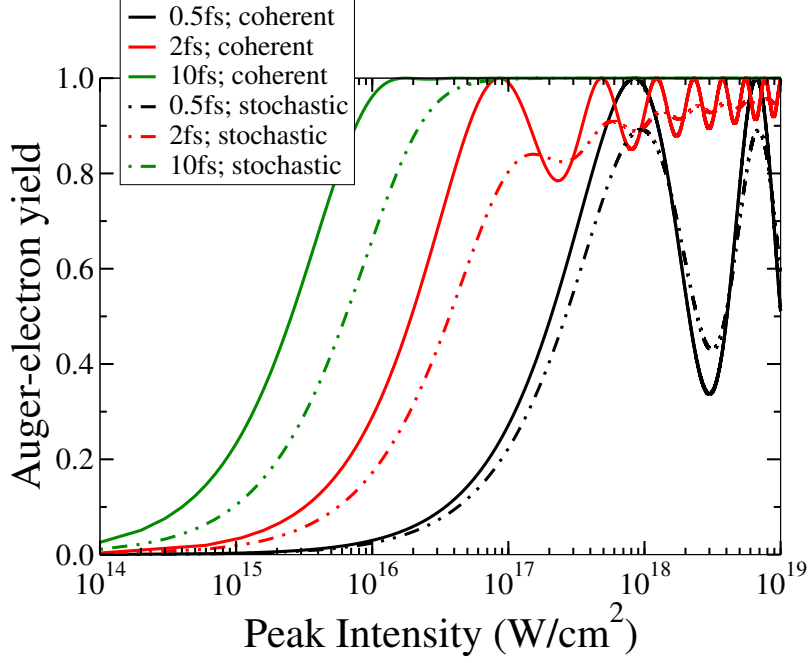


Figure 6.5: Comparison of the Auger-yields for coherent pulse (solid curves) with that of stochastic pulse (double-dot-dashed curves) of $\tau_c = 3.3$ fs. The τ_{rmsw} for the black curves is 0.5 fs, for the red curves is 2 fs and for the green curves is 10 fs.

Through this, a study of the effects of coherence time and pulse duration on the Auger yield in the context of presence of Rabi oscillations has been made. The present method had been confined to Lorentzian correlated fields. In the next approach, though the form of averaged equations is not maintained, there will be provision to include Gaussian correlation for the field fluctuations which implies, it is relatively suitable for FELs.

6.3 Approach - 2: Eliminating the coherence equation

In this approach, a second channel of direct photoionization is also included and hence the interaction is near resonant in contrast to the previous case of pure resonance. Here, the case of Helium autoionization via 2s2p AIS is considered. Fig. 6.6 shows the schematic. Corresponding DM-EOMs are borrowed from the previous chapter.

$$\dot{\sigma}_{gg}(t) = -\left(\gamma_g(t)\right)\sigma_{gg}(t) + 2\text{Im}\left[\left(\Omega(t)\right)\left(1 - \frac{\imath}{q_a}\right)\sigma_{ag}(t)\right] \quad (6.12a)$$

$$\dot{\sigma}_{aa}(t) = -\Gamma_a\sigma_{aa}(t) - 2\text{Im}\left[\left(\Omega(t)\right)\left(1 + \frac{\imath}{q_a}\right)\sigma_{ag}(t)\right] \quad (6.12b)$$

$$\begin{aligned} \dot{\sigma}_{ag}(t) = & \left(i\Delta - \frac{1}{2}\left(\gamma_g(t)\right) + \Gamma_a\right)\sigma_{ag}(t) - \left(\Omega^*(t)\right)\left(1 - \frac{\imath}{q_a}\right)\sigma_{gg}(t) \\ & + \left(\Omega^*(t)\right)\left(1 + \frac{\imath}{q_a}\right)\sigma_{aa}(t) \end{aligned} \quad (6.12c)$$

These circled terms render the EOMs stochastic when the field is stochastic. In contrast to the previous section, the field envelope here is allowed to be complex as well as $\gamma_g \neq 0$

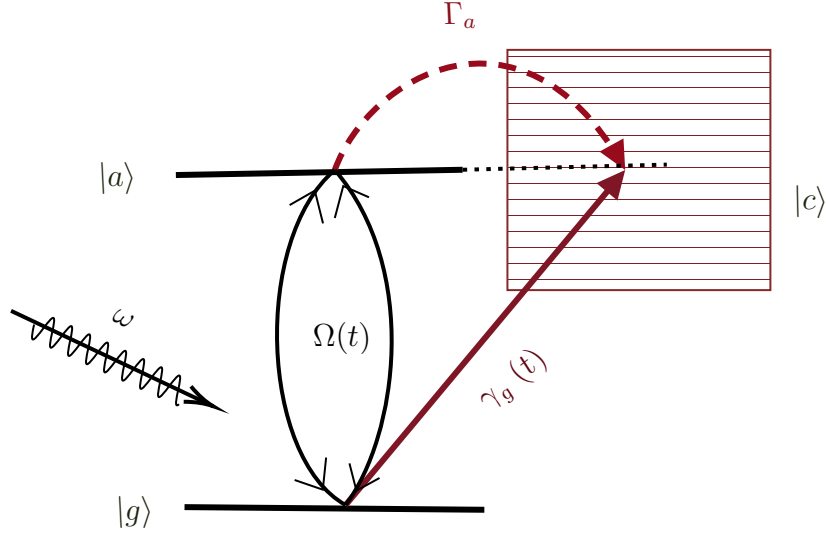


Figure 6.6: Schematic of the interaction of a near resonant FEL field with helium atom. ω is the tunable resonance frequency, $|c\rangle$ is the continuum, $\gamma_g(t)$ is the photoionization width, Γ_a is the autoionization width and $\Omega(t)$ denotes the Rabi oscillations.

and q_a is finite. Hence a different approach is to be sought. To start with the second approach, take the coupled set of SDEs given by Eq. (6.12a)-Eq. (6.12c). The goal is to eliminate the coherence equation Eq. (6.12c), apply the ensemble averages and use some simplifying approximations. Eq. (6.12c) can be viewed as a general ordinary differential equation (ODE) of the form

$$\frac{d}{dt}y(t) + P(t)y(t) = Q(t) \quad (6.13)$$

where,

$$\begin{aligned} y(t) &= \sigma_{ag}(t) \\ P(t) &= -i\Delta + \frac{1}{2}(\gamma_g(t) + \Gamma_a) \\ Q(t) &= -i\Omega^*(t) \left[\left(1 - \frac{i}{q_a}\right) \sigma_{gg}(t) - \left(1 + \frac{i}{q_a}\right) \sigma_{aa}(t) \right] \end{aligned}$$

The ordinary differential (6.13) has a solution of the form [83]

$$y(t) = \frac{1}{u(t)} \int u(t)Q(t)dt \quad (6.14)$$

with $u(t) = e^{\int P(t)dt}$. Substituting the actual forms of the functions into above solution Eq. (6.14) of the ODE, the required expression for $\sigma_{ag}(t)$ takes the following form:

$$\begin{aligned}
\sigma_{ag}(t) &= \frac{1}{e^{\int_0^t P(\tau)d\tau}} \int_0^t e^{\int_0^{t'} P(t'')dt''} Q(t')dt' \\
&= e^{-Pt} \int_0^t e^{Pt'} Q(t')dt' \\
&= \int_0^t e^{-P(t-t')} Q(t')dt' \\
&= \int_0^t e^{-(\imath\Delta + \frac{1}{2}(\gamma + \Gamma_a))(t-t')} \left[-\imath\Omega^*(t') \left[\left(1 - \frac{\imath}{q_a}\right) \sigma_{gg}(t') - \left(1 + \frac{\imath}{q_a}\right) \sigma_{aa}(t') \right] \right] dt'
\end{aligned}$$

6.3.1 Approximations

Approximation-1: For computational simplicity, an approximation is made in deriving the above expression. $P(\tau)$ inside the integral of $e^{-\int_0^t P(\tau)d\tau}$ is assumed to be constant i.e., the time variation of $\gamma_g(t)$, which occurs in $P(t)$, is assumed to not affect the exponential integral value. Now, the above final expression is substituted in Eq. (6.12a) and Eq. (6.12b) to arrive at the following coupled ODEs which are expressed in terms of population states:

$$\begin{aligned}
\dot{\sigma}_{gg}(t) &= -\gamma_g(t)\sigma_{gg}(t) + 2\text{Im} \left[\alpha_1 \int_0^t \left[\Omega(t)\Omega(t')\sigma_{gg}(t')e^{-k(t-t')} \right] dt' \right] \\
&\quad + 2\text{Im} \left[\beta_1 \int_0^t \left[\Omega(t)\Omega^*(t')\sigma_{aa}(t')e^{-k(t-t')} \right] dt' \right] \quad (6.15a)
\end{aligned}$$

$$\begin{aligned}
\dot{\sigma}_{aa}(t) &= -\Gamma_a\sigma_{aa}(t) - 2\text{Im} \left[\alpha_2 \int_0^t \left[\Omega(t)\Omega^*(t')\sigma_{gg}(t')e^{-k(t-t')} \right] dt' \right] \\
&\quad - 2\text{Im} \left[\beta_2 \int_0^t \left[\Omega(t)\Omega^*(t')\sigma_{aa}(t')e^{-k(t-t')} \right] dt' \right] \quad (6.15b)
\end{aligned}$$

Here, $\alpha_1 = (-\imath) \left(1 - \frac{\imath}{q_a}\right)^2$, $\alpha_2 = (\imath) \left(1 + \frac{\imath}{q_a}\right)$, $\beta_1 = (-\imath) \left(1 + \frac{\imath}{q_a}\right)$ and $\beta_2 = (\imath) \left(1 + \frac{\imath}{q_a}\right)^2$; $k = -\imath\Delta + \frac{1}{2}(\gamma_g + \Gamma_a)$. Apply the ensemble average operator $\langle \dots \rangle$ on both sides of the Eqs. (6.15) on the fluctuating quantities. For example, if X fluctuates and c does not, then $\langle cX \rangle = c\langle X \rangle$. In the above equations, $\sigma_{gg}(t)$, $\sigma_{aa}(t)$, $\Omega(t)$, $\Omega^*(t)$ and $\gamma_g(t)$ are the only fluctuating quantities. Thus, the following equations are arrived at

$$\begin{aligned}
\frac{d}{dt}\langle\sigma_{gg}(t)\rangle &= -\langle\gamma_g(t)\sigma_{gg}(t)\rangle + 2\text{Im} \left[\alpha_1 \int_0^t \left[\langle\Omega(t)\Omega^*(t')\sigma_{gg}(t')\rangle e^{-k(t-t')} \right] dt' \right] \\
&\quad + 2\text{Im} \left[\beta_1 \int_0^t \left[\langle\Omega(t)\Omega^*(t')\sigma_{aa}(t')\rangle e^{-k(t-t')} \right] dt' \right] \quad (6.16a)
\end{aligned}$$

$$\begin{aligned}
\frac{d}{dt}\langle\sigma_{aa}(t)\rangle &= -\Gamma_a\langle\sigma_{aa}(t)\rangle - 2\text{Im} \left[\alpha_2 \int_0^t \left[\langle\Omega(t)\Omega^*(t')\sigma_{gg}(t')\rangle e^{-k(t-t')} \right] dt' \right] \\
&\quad - 2\text{Im} \left[\beta_2 \int_0^t \left[\langle\Omega^*(t)\Omega(t')\sigma_{aa}(t')\rangle e^{-k(t-t')} \right] dt' \right] \quad (6.16b)
\end{aligned}$$

Approximation-2 Decorrelation Approximation (DA) : In the above integrals, there are terms of products of populations with photoionization width and populations with Rabi oscillations inside of the averaging operator. Photoionization and Rabi oscillations are dependent on the field intensity or the field amplitude. In general, the evolution of populations are directly related to these parameters. But, under certain conditions, if one is able to assume that the populations vary much slowly than the Rabi oscillations or photoionization widths, then the decorrelation approximation (DA) of Refs [27, 84] can be applied. This significantly simplifies the problem at hand. The validity of this approximation depends on how different their rates of variations are. In general, this approximation is valid for low intensities. For higher intensities, the approximation loses its validity. Applying the DA for the present scenario implies to replace the following LHS quantities with the RHS quantities in the averaged DM-EOMs.

$$\begin{aligned}\langle \gamma_g(t) \sigma_{gg}(t) \rangle &= \langle \gamma_g(t) \rangle \langle \sigma_{gg}(t) \rangle \\ \langle \Omega(t) \Omega^*(t') \sigma_{ii}(t') \rangle &= \langle \Omega(t) \Omega^*(t') \rangle \langle \sigma_{ii}(t') \rangle ; \text{ for } i = g \text{ or } a\end{aligned}$$

After the application of this DA, the averaged DM-EOMs take the form of

$$\begin{aligned}\frac{d}{dt} \langle \sigma_{gg}(t) \rangle &= -\langle \gamma_g(t) \rangle \langle \sigma_{gg}(t) \rangle + 2\text{Im} \left[\alpha_1 \int_0^t \left[\langle \Omega(t) \Omega^*(t') \rangle \langle \sigma_{gg}(t') \rangle e^{-k(t-t')} \right] dt' \right] \\ &\quad + 2\text{Im} \left[\beta_1 \int_0^t \left[\langle \Omega(t) \Omega^*(t') \rangle \langle \sigma_{aa}(t') \rangle e^{-k(t-t')} \right] dt' \right] \quad (6.17a)\end{aligned}$$

$$\begin{aligned}\frac{d}{dt} \langle \sigma_{aa}(t) \rangle &= -\Gamma_a \langle \sigma_{aa}(t) \rangle - 2\text{Im} \left[\alpha_2 \int_0^t \left[\langle \Omega(t) \Omega^*(t') \rangle \langle \sigma_{gg}(t') \rangle e^{-k(t-t')} \right] dt' \right] \\ &\quad - 2\text{Im} \left[\beta_2 \int_0^t \left[\langle \Omega(t) \Omega^*(t') \rangle \langle \sigma_{aa}(t') \rangle e^{-k(t-t')} \right] dt' \right] \quad (6.17b)\end{aligned}$$

It can be seen that, the equations now include explicitly *ensemble average* of the field intensity and *autocorrelation* of the field amplitude, via

$$\langle \gamma_g(t) \rangle = \gamma_g \langle \mathcal{I}(t) \rangle \quad (6.18)$$

$$\langle \Omega(t) \Omega^*(t') \rangle = d_{ag}^2 \langle \mathcal{E}(t) \mathcal{E}(t') \rangle \quad (6.19)$$

Substituting these the DM-EOMs take field dependent form as

$$\begin{aligned}\frac{d}{dt} \langle \sigma_{gg}(t) \rangle &= -\gamma_g \langle \mathcal{I}(t) \rangle \langle \sigma_{gg}(t) \rangle + 2d_{ag}^2 \text{Im} \left[\alpha_1 \int_0^t \left[\langle \mathcal{E}(t) \mathcal{E}^*(t') \rangle \langle \sigma_{gg}(t') \rangle e^{-k(t-t')} \right] dt' \right] \\ &\quad + 2d_{ag}^2 \text{Im} \left[\beta_1 \int_0^t \left[\langle \mathcal{E}(t) \mathcal{E}^*(t') \rangle \langle \sigma_{aa}(t') \rangle e^{-k(t-t')} \right] dt' \right] \quad (6.20a)\end{aligned}$$

$$\begin{aligned}\frac{d}{dt} \langle \sigma_{aa}(t) \rangle &= -\Gamma_a \langle \sigma_{aa}(t) \rangle - 2d_{ag}^2 \text{Im} \left[\alpha_2 \int_0^t \left[\langle \mathcal{E}(t) \mathcal{E}^*(t') \rangle \langle \sigma_{gg}(t') \rangle e^{-k(t-t')} \right] dt' \right] \\ &\quad - 2d_{ag}^2 \text{Im} \left[\beta_2 \int_0^t \left[\langle \mathcal{E}(t) \mathcal{E}^*(t') \rangle \langle \sigma_{aa}(t') \rangle e^{-k(t-t')} \right] dt' \right] \quad (6.20b)\end{aligned}$$

At this point, the equations are ready to be solved by using numerical methods. This set of equations can be called the *raw form* of the DM-EOMs.

Observe the integral terms in Eqs. (6.20). There is a population term along with AC function and an exponential. The profile of this population is not known before hand and hence the integrations need to be performed at every time step 't'. Having to compute such integrations and then to solve the coupled ODEs takes a considerable amount of time (because for each t' the $\sigma_{ii}(t')$ needs to be solved and updated in order to be inserted into the integral). But, it would effectively reduce the computational time if the above integrations are simplified into certain analytical forms invoking appropriate approximations. This idea is expanded in the following.

Approximation-3 Population Approximation: Consider the scenario where the populations do not change with respect to the time limits of the integral, in Eq. (6.20a) and Eq. (6.20b), i.e.,

$$\langle \sigma_{ii}(t') \rangle = \langle \sigma_{ii}(t) \rangle ; \forall i = a, g$$

Physically, this is valid when the field is weak and fluctuates the populations at relatively slower rates in comparison to the other terms in the integral. It will be later shown in the results section that as the peak intensity increases, this approximation loses its validity due to the rapid changes manifesting in populations on par with the other terms of the integration. Applying this population approximation simplifies the problem at hand as it entails pulling out the population terms out of the integrals, i.e.,

$$\begin{aligned} \frac{d}{dt} \langle \sigma_{gg}(t) \rangle = & -\gamma_g \langle \mathcal{I}(t) \rangle \langle \sigma_{gg}(t) \rangle + 2d_{ag}^2 \text{Im} \left[\alpha_1 \langle \sigma_{gg}(t) \rangle \int_0^t \left[\langle \mathcal{E}(t) \mathcal{E}^*(t') \rangle e^{-k(t-t')} \right] dt' \right] \\ & + 2d_{ag}^2 \text{Im} \left[\beta_1 \langle \sigma_{aa}(t) \rangle \int_0^t \left[\langle \mathcal{E}(t) \mathcal{E}^*(t') \rangle e^{-k(t-t')} \right] dt' \right] \end{aligned} \quad (6.21a)$$

$$\begin{aligned} \frac{d}{dt} \langle \sigma_{aa}(t) \rangle = & -\Gamma_a \langle \sigma_{aa}(t) \rangle - 2d_{ag}^2 \text{Im} \left[\alpha_2 \langle \sigma_{gg}(t) \rangle \int_0^t \left[\langle \mathcal{E}(t) \mathcal{E}^*(t') \rangle e^{-k(t-t')} \right] dt' \right] \\ & - 2d_{ag}^2 \text{Im} \left[\beta_2 \langle \sigma_{aa}(t) \rangle \int_0^t \left[\langle \mathcal{E}(t) \mathcal{E}^*(t') \rangle e^{-k(t-t')} \right] dt' \right] \end{aligned} \quad (6.21b)$$

Based on the type of autocorrelation present in the interacting field, as discussed in section 2.2.4 and section 2.2.5 of Chapter 2 the problem of solving the averaged DM-EOMs Eq. (6.21a)-Eq. (6.21b) can be further studied as below.

6.3.2 Different Scenarios of AC function

In the AC function $\langle \mathcal{E}(t) \mathcal{E}^*(t - \tau) \rangle$, when the shortness of correlation time τ_c with respect to the slow variation of the field envelope is invoked, one eventually limits the range of τ , which represents the time-shift of the field with itself, to have a length of τ_c . This allows

one to approximate,

$$\begin{aligned}
\mathcal{E}_0^*(t - \tau) &\approx \mathcal{E}_0^*(t) + ((t - \tau) - t) \frac{d}{d\tau} \mathcal{E}_0^*(\tau) \Big|_t + ((t - \tau) - t)^2 \frac{d^2}{d\tau^2} \mathcal{E}_0^*(\tau) \Big|_t + \dots \\
&\approx \mathcal{E}_0^*(t) - \tau \frac{d}{d\tau} \mathcal{E}_0^*(\tau) \Big|_t + \tau^2 \frac{d^2}{d\tau^2} \mathcal{E}_0^*(\tau) \Big|_t + \dots \\
&\approx \mathcal{E}_0^*(t) - \mathcal{O}(\tau_c \dot{\mathcal{E}}_0^*(t)) + \dots \\
&\approx \mathcal{E}_0^*(t) ; \text{ given that } |\tau_c \dot{\mathcal{E}}_0^*(t)| \ll 1
\end{aligned}$$

Using Eq. (6.2), Eqs. (6.3) and the above approximation, one can arrive at the following approximate expressions for the first order field correlation function in terms of normalised first order field coherence function (as explored in Chapter 2) and ensemble averaged intensity,

$$\langle \mathcal{E}(t) \mathcal{E}^*(t') \rangle = \mathcal{E}_0(t) \mathcal{E}_0^*(t') \langle \epsilon(t) \epsilon^*(t') \rangle = \begin{cases} \langle \mathcal{I}(t) \rangle e^{-\frac{|t-t'|}{2\tau_c}}, & \text{Lorentzian correlation} \\ \langle \mathcal{I}(t) \rangle e^{-\frac{(t-t')^2}{2\tau_c^2}}, & \text{Gaussian correlation} \end{cases} \quad (6.22)$$

Lorentzian correlation When the AC function $\langle \mathcal{E}(t) \mathcal{E}^*(t') \rangle$ takes the form of

$$\langle \mathcal{E}(t) \mathcal{E}^*(t') \rangle = \langle \mathcal{I}(t) \rangle e^{-\frac{|t-t'|}{2\tau_c}}$$

were $\langle \mathcal{I}(t) \rangle = \mathcal{E}_0(t) \mathcal{E}_0^*(t)$ is the peak intensity of the field. Now, the DM-EOMs can be solved analytically. This is because the integral becomes just a function of the exponential term. Noting a new term $\tilde{k} = k + \frac{1}{2\tau_c} = -i\Delta + \frac{1}{2}(\gamma_g + \Gamma_a + \frac{1}{\tau_c})$

$$\begin{aligned}
\frac{d}{dt} \langle \sigma_{gg}(t) \rangle &= -\gamma_g \langle \mathcal{I}(t) \rangle \langle \sigma_{gg}(t) \rangle + 2d_{ag}^2 \langle \mathcal{I}(t) \rangle \text{Im} \left[\alpha_1 \langle \sigma_{gg}(t) \rangle \int_0^t [e^{-\tilde{k}(t-t')}] dt' \right] \\
&\quad + 2d_{ag}^2 \langle \mathcal{I}(t) \rangle \text{Im} \left[\beta_1 \langle \sigma_{aa}(t) \rangle \int_0^t [e^{-\tilde{k}(t-t')}] dt' \right] \\
\frac{d}{dt} \langle \sigma_{aa}(t) \rangle &= -\Gamma_a \langle \sigma_{aa}(t) \rangle - 2d_{ag}^2 \langle \mathcal{I}(t) \rangle \text{Im} \left[\alpha_2 \langle \sigma_{gg}(t) \rangle \int_0^t [e^{-\tilde{k}(t-t')}] dt' \right] \\
&\quad - 2d_{ag}^2 \langle \mathcal{I}(t) \rangle \text{Im} \left[\beta_2 \langle \sigma_{aa}(t) \rangle \int_0^t [e^{-\tilde{k}(t-t')}] dt' \right]
\end{aligned}$$

which result in easily solvable coupled differential equations

$$\frac{d}{dt} \langle \sigma_{gg}(t) \rangle = -\gamma_g \langle \mathcal{I}(t) \rangle \langle \sigma_{gg}(t) \rangle + 2d_{ag}^2 \langle \mathcal{I}(t) \rangle \text{Im} \left[\frac{(1 - e^{-\tilde{k}t})}{\tilde{k}} [\alpha_1 \langle \sigma_{gg}(t) \rangle + \beta_1 \langle \sigma_{aa}(t) \rangle] \right] \quad (6.23a)$$

$$\frac{d}{dt} \langle \sigma_{aa}(t) \rangle = -\Gamma_a \langle \sigma_{aa}(t) \rangle - 2d_{ag}^2 \langle \mathcal{I}(t) \rangle \text{Im} \left[\frac{(1 - e^{-\tilde{k}t})}{\tilde{k}} [\alpha_2 \langle \sigma_{gg}(t) \rangle + \beta_2 \langle \sigma_{aa}(t) \rangle] \right] \quad (6.23b)$$

Parameters	Values (a.u.)
E_a	2.211 a.u.
q_a	-2.733 a.u.
d_{ga}	0.0358 a.u.
γ_g	0.494 a.u.
Γ_a	0.00137 a.u.
τ_p	289.38
τ_c	20.67

Table 6.2: Atomic parameters for the He(2s2p) AIS resonance and field parameters in a.u.; The values for the effective matrix element d_{ga} is calculated by $4|d_{ga}|^2 = q_a^2 \Gamma_a \gamma_g$

It should be noted that $|t - t'| = (t - t')$ for the limits of integration of t' varying from $0 \rightarrow t$.

Gaussian correlation When the AC function $\langle \mathcal{E}(t)\mathcal{E}^*(t') \rangle$ takes the form of

$$\langle \mathcal{E}(t)\mathcal{E}^*(t') \rangle = \langle \mathcal{I}(t) \rangle e^{-\frac{(t-t')^2}{2\tau_c^2}}$$

it introduces square exponential into the integrals as,

$$\begin{aligned} \frac{d}{dt} \langle \sigma_{gg}(t) \rangle &= -\gamma_g \langle \mathcal{I}(t) \rangle \langle \sigma_{gg}(t) \rangle + 2d_{ag}^2 \langle \mathcal{I}(t) \rangle \text{Im} \left[\alpha_1 \langle \sigma_{gg}(t) \rangle \int_0^t \left[e^{-\frac{(t-t')^2}{2\tau_c^2}} e^{-k(t-t')} \right] dt' \right] \\ &\quad + 2d_{ag}^2 \langle \mathcal{I}(t) \rangle \text{Im} \left[\beta_1 \langle \sigma_{aa}(t) \rangle \int_0^t \left[e^{-\frac{(t-t')^2}{2\tau_c^2}} e^{-k(t-t')} \right] dt' \right] \\ \frac{d}{dt} \langle \sigma_{aa}(t) \rangle &= -\Gamma_a \langle \sigma_{aa}(t) \rangle - 2d_{ag}^2 \langle \mathcal{I}(t) \rangle \text{Im} \left[\alpha_2 \langle \sigma_{gg}(t) \rangle \int_0^t \left[e^{-\frac{(t-t')^2}{2\tau_c^2}} e^{-k(t-t')} \right] dt' \right] \\ &\quad - 2d_{ag}^2 \langle \mathcal{I}(t) \rangle \text{Im} \left[\beta_2 \langle \sigma_{aa}(t) \rangle \int_0^t \left[e^{-\frac{(t-t')^2}{2\tau_c^2}} e^{-k(t-t')} \right] dt' \right] \end{aligned}$$

which results in analytical form consisting of error functions (erf) when the Gaussian integral is calculated, by changing the variable of integration from $(t - t') \rightarrow \tau$

$$\frac{d}{dt} \langle \sigma_{gg}(t) \rangle = -\gamma_g \langle \mathcal{I}(t) \rangle \langle \sigma_{gg}(t) \rangle + 2d_{ag}^2 \langle \mathcal{I}(t) \rangle \text{Im} [\mathcal{Q}(t) [\alpha_1 \langle \sigma_{gg}(t) \rangle + \beta_1 \langle \sigma_{aa}(t) \rangle]] \quad (6.24a)$$

$$\frac{d}{dt} \langle \sigma_{aa}(t) \rangle = -\Gamma_a \langle \sigma_{aa}(t) \rangle - 2d_{ag}^2 \langle \mathcal{I}(t) \rangle \text{Im} [\mathcal{Q}(t) [\alpha_2 \langle \sigma_{gg}(t) \rangle + \beta_2 \langle \sigma_{aa}(t) \rangle]] \quad (6.24b)$$

where, using $a = 1/2\tau_c^2$ and $b = k$, $\mathcal{Q}(t)$ is given by

$$\mathcal{Q}(t) = \int_0^t e^{-a\tau^2 - b\tau} d\tau = \frac{\sqrt{\pi} e^{\frac{b^2}{4a}} \left(\text{erf}\left(\frac{2at+b}{2\sqrt{a}}\right) - \text{erf}\left(\frac{b}{2\sqrt{a}}\right) \right)}{2\sqrt{a}}$$

6.3.3 Results and discussions: helium

Here, the focus of study is the effects of stochastic fluctuations on the helium 2s2p 1P ionization yield lineshape. Using the previously derived sets of EOMs one can obtain the

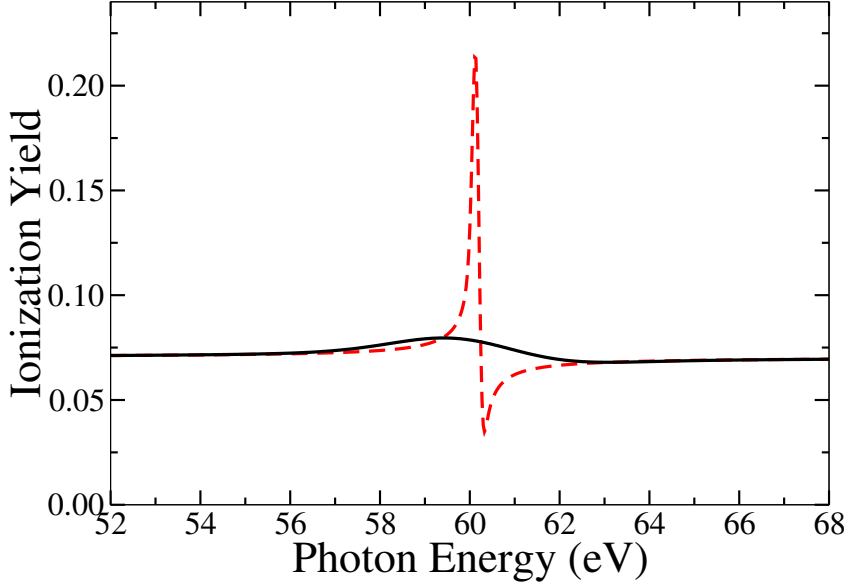


Figure 6.7: The effect of smoothing the familiar Fano-lineshape, caused by averaging the fluctuations can be clearly seen in this figure. The red-dashed curve with highest peak is obtained for a deterministic pulse whereas the black-solid curve is obtained for a stochastic pulse. A Gaussian correlation is attributed to the field having a coherence time of $\tau_c = 0.5$ fs (20.67 a.u.). For both the coherent and chaotic pulses the peak intensity is 10^{13} W/cm² and the pulse duration is $\tau_p = 7$ fs (289.38 a.u.).

average ionization yield $\langle Y \rangle$ by using the formula

$$\langle Y \rangle = 1 - \langle \sigma_{gg}(t) \rangle - \langle \sigma_{aa}(t) \rangle \quad (6.25)$$

Let the laser be tuned around the resonance frequency of $2s2p \ ^1P$ state, which is circa 60.16 eV. Using a traditional fully coherent laser, one expects an asymmetric lineshape which is the famous Fano lineshape. So, curiosity drives one to see what kind of yield profile is obtained when a chaotic laser pulse, having a Gaussian correlation, is utilised. Does the Fano lineshape stays intact or is it distorted? This comparison is plotted in Fig. 6.7 where the red-dashed curve is obtained by solving Eqs. (6.12a)-(6.12c) for a deterministic pulse and the black-solid curve is obtained by solving Eq. (6.24a)-Eq. (6.24b) for a chaotic pulse. The atomic and field parameters, that were calculated according to the methodology presented in Chapter 5 are given in Table 6.2. It can be seen that the coherent pulse results in a Fano-lineshape having a sharp peak and an asymmetric profile around resonance. But the chaotic pulse results in a smooth curve. Around the resonance frequency it can be found that the ionization yield values are drastically different whereas away from the resonance the yield values are identical. This suggests that the fluctuations of a laser pulse manifest and affect the lineshape only around a resonance.

The next point of interest is to check how the population approximation fares. In order to proceed with this task, one needs to solve the set of Eqs. (6.20a)-(6.20b) and compare

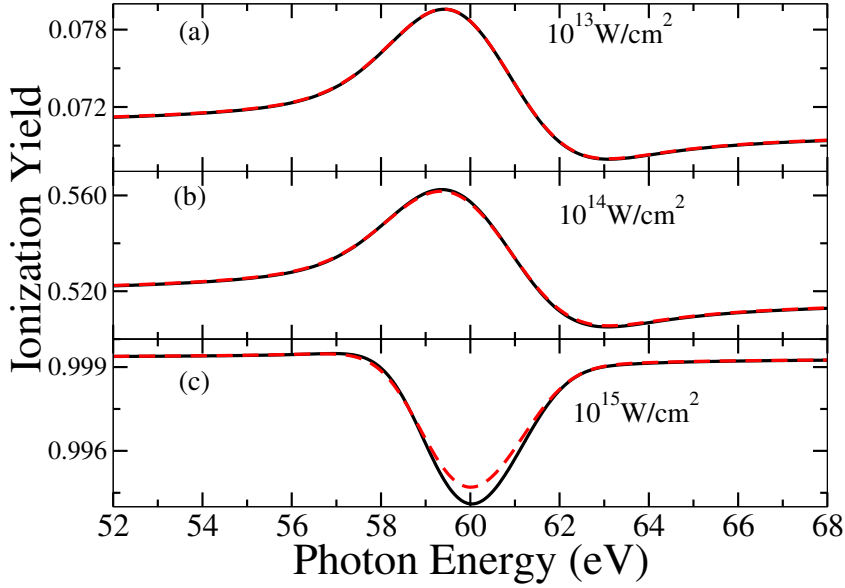


Figure 6.8: Validity of population approximation relative to the raw form of the averaged DM-EOMs. The black solid curve represents the yield profile obtained from the raw form of EOMs whereas the red-dashed curve represents the yield profile obtained after the invocation of population approximation. A Gaussian correlation is attributed to the field having a coherence time of $\tau_c = 0.5$ fs (20.67 a.u.) and a pulse duration of $\tau_p = 7$ fs (289.38 a.u.).

the yield profiles that are obtained by solving the set of Eqs. (6.21a)-(6.21b). Let the stochastic pulse be modeled by a Gaussian correlation for now.

In Fig. 6.8 the ionization yield lineshapes are plotted. The black solid curve is obtained from solving the DM-EOMs before and after the utilization of the population approximation. It can be clearly seen that for almost all peak intensities, the approximation gives the same results as that of the raw forms. But towards the highest peak intensity, the approximation slightly loses its validity. This can be attributed to the strong influence of fields fluctuations on the rates of change of populations being comparable to the other terms of the integration.

The last remaining task is to see how different correlation types affect the lineshape. The correlation shape indicates the nature of the underlying statistics of the fluctuations in a laser. Therefore for a same peak intensity, pulse duration and coherence time, different statistics of a field implies that the affects on the lineshape are going to be different. To see this, one can use the Eqs. (6.24a)-(6.24b) which includes Gaussian correlation of the field or use the Eqs. (6.23a)-(6.23b) which includes Lorentzian correlation of the field.

In Fig. 6.9 the ionization yield obtained by using Gaussian correlation, represented by the solid black curve and Lorentzian correlation, represented by the red dashed curve, are plotted. The field parameters are as in Table 6.2 for both the types of fields. It was earlier seen that the fluctuations manifest around resonance and away from resonance they have almost a nil affect. A correlation shape is a resultant of the nature of fluctuations.

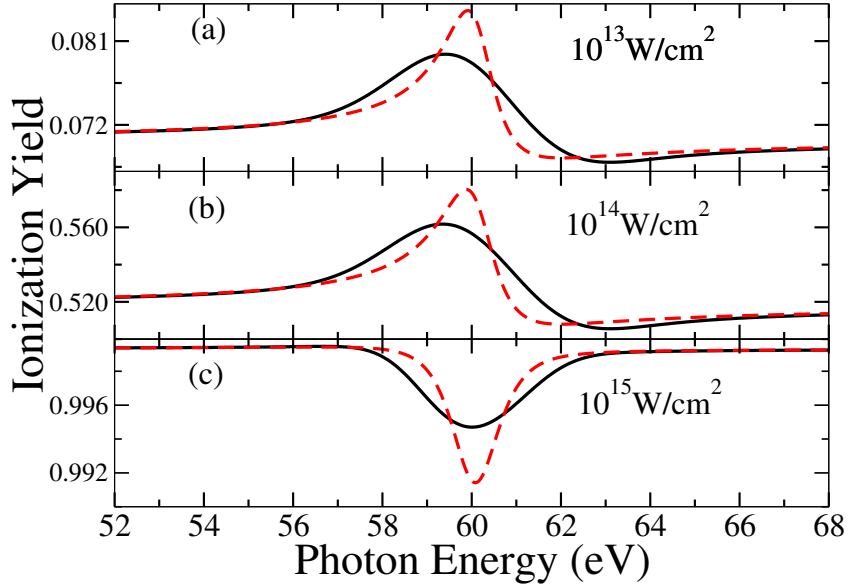


Figure 6.9: Influence of different correlation types on the ionization yield lineshape. The black solid curve utilises a Gaussian correlation whereas the red dashed curve utilises a Lorentzian correlation. Both the correlation types have a coherence time of $\tau_c = 0.5$ fs (20.67 a.u.) and a pulse duration of $\tau_p = 7$ fs (289.38 a.u.). It can be seen how distinct each lineshape is.

Therefore, it is seen in the said figure that the lineshapes differ from each other drastically only around resonance. Towards the tail ends, i.e., away from the resonance, they are almost identical. The Gaussian correlation is wider whereas the Lorentzian correlation is more narrower.

6.4 Conclusions and limitations

- **Conclusions:** The following points can be concluded by observing the averaging approaches developed in this chapter.
 - Two approaches to arrive at the averaged form of DM-EOMs have been explored in this chapter. The aim in these two approaches was to transform a set of stochastic coupled differential equations into a set of deterministic coupled differential equations.
 - Approach-1 retains the form of the EOMs whereas Approach-2 removes the coherence equation from the picture.
 - Even though both the approaches utilise the decorrelation approximation (DA), Approach-2 further utilises another approximation by the name population approximation, which simplifies the computational demand.
 - Approach-1 does not allow for the use of a Gaussian correlated field. When Lorentz correlation is used, it facilitates the exponential to be separated into

two parts i.e., $e^{-i\bar{k}(t-t')} = e^{-i\bar{k}t}e^{i\bar{k}t'}$. This step, in the process of its averaging, becomes an obstacle when a Gaussian correlation is used. So in this case it will be impossible to proceed with. Hence, Approach-1 is restricted to only long wavelength lasers or exponentially correlated fields. Approach-2 has space in its derivation for both types of correlation shapes and thus can be applied to wider types of stochastic fields such as those including FELs.

- In the case of neon, the effects of correlation time of a Lorentzian correlated stochastic field on the Auger electron yield were observed in relation to the pulse duration and peak intensity.
- In the case of helium, the smoothing effect of the fluctuations on the Fano lineshape was shown. The effects of different first order field correlation types on the lineshape were also discussed. The suitability of the population approximation was also suggested.

• **Limitations:** Both these approaches are limited in the way of the details they provide, such as:

- Neither of the two approaches is rigorous i.e, they do not encompass the full statistical properties of a stochastic field. They only consist of either the first order field correlation and the ensemble average of the intensity.
- There are inherent approximations such as Approximation-1, Approximation-2 (DA), etc., which implies that some specified conditions are needed for these approaches to be valid. This restricts the domain of applicability.
- The dynamics of the problem are not completely visible in the form of equations obtained in the two approaches. For example, why is the lineshape the way it is? Can one associate a well-known shape to the obtained lineshape? Is it possible to predict a change in the lineshape with respect to a change in the field parameter such as τ_c or τ_p ? Can one utilise the equations directly with available experimentally measurable entities such as field's autocorrelation or power spectrum, etc., ? No! With the present formulation, it is not possible.
- The dynamics of the continuum states is completely hidden. At stronger field strengths and higher pulse duration, there is a possibility of manifestation of extra channels of ionization from the continua of He^+ or Ne^+ or their corresponding autoionizing states. This is not catered for in these approaches.
- In a way, the approaches are very much limited in their validity (due to many approximations) and applicability. But, it will be later shown in next chapter that in-spite of these drawbacks, the two approaches explored in this chapter give fairly good results at lower field strengths. That means, they can be quickly utilised to anticipate the outcome. But, a rigorous and all-encompassing method needs to be developed for a proper understanding of the stochastic interaction dynamics. This is the subject of Chapter 7.

Chapter 7

Perturbative theory of ensemble averaging

The averaging methods given in the previous chapter are elementary and do not consider the full statistics of the FEL. Therefore, there is a loss of information input to the set of EOMs which would result in inaccurate results. To seek a new all-encompassing approach is necessary. This chapter aims to arrive at an exact differential deterministic equation for the ensemble-averaged density matrix driven by a time-dependent perturbation expansion in terms of cumulants. One may wonder why not use moment expansion? As is shown later, the moment expansion the perturbative series may not always converge and hence the more sophisticated cumulant expansion (see ref [85]), is used in this work.

Such a perturbative formulation, theoretically speaking, requires one to infinitely expand the perturbation series. As this is not practical, one is forced to truncate at a certain order. The validity and range of such a truncation is explicitly derived. One of the outcomes of the present procedure is that the lowest-order term of the truncated expansion is expressed in terms of the autocorrelation (AC) functions of the time-integrated electric field amplitude and intensity, $\langle \mathcal{E}(t)\mathcal{E}^*(t') \rangle$ and $\langle \mathcal{I}(t)\mathcal{I}(t') \rangle$, respectively, which are experimentally accessible quantities (see references [86–91]). The striking difference from the other averaging methods previously discussed is the inclusion of the intensity (or higher order) correlation term(s) whose influence on the observables manifest itself as the peak intensity increases. Statistically speaking, different random fields may have same first order AC function but not the second or higher. This dependence of the dynamics on these AC functions becomes stronger for FEL fields obeying Gaussian statistics and at conditions where the stationarity of the averages may be assumed (long pulse lengths in comparison to the field coherence time) [92].

The present method uses a Fano-representation of the essential states. This is one of the desirable frameworks for the reason that, often the experimental data is conveniently available in terms of the q_a -Fano parameter and the width of the autoionizing states. Also, it can be noted that the only assumption for the method to be valid is the shortness of the field correlation time (condition given in Eq. (7.27)). Therefore the method is valid for wide variety of fields, though the focus here is on the Gaussian FELs. The equations (7.43)

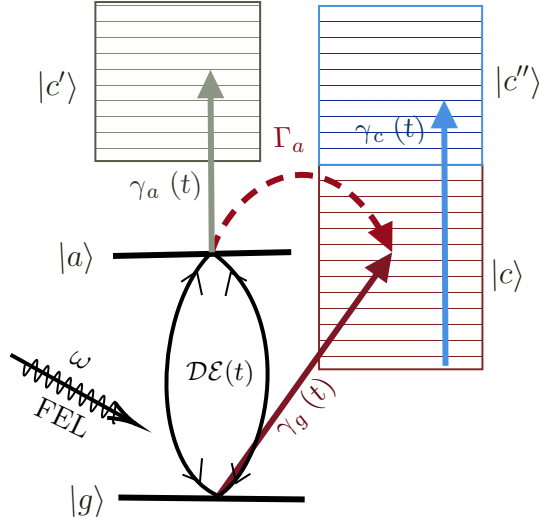


Figure 7.1: Sketch of the near-resonant excitation or ionization scheme, which includes the depiction of further channels of ionization, with a FEL field .

and (7.51) are the main results of this chapter which correspond to the bound and the singly ionized states of the system. These are obtained by evaluation of the first two non-vanishing terms of the series expansion (which is sufficient for the scenario under consideration).

As pointed in Chapter 1, most of the existing theoretical works consider an exponential AC function for the field. But AC of FELs obey square-exponential form. The present method is tailored to both these AC forms, where $AC \sim e^{-(t_1-t_2)^2/2\tau_c^2}$ is more suited for the FELs [35, 40] whereas $AC \sim e^{-|t_1-t_2|/2\tau_c}$ is more suited for the long-wavelength lasers [93, 94]. The affects of these AC shapes on the observables is shown in order to suggest that one can not just replace one with the other, for computational simplicity sake, without affecting the results.

7.1 Extended DM-EOMs

The DM-EOMs derived in Chapter 4 constitute only for the system depicted in Fig. 4.4 i.e., there exists only one channel for the photoionization. But in the real experiment there may also occur further photoionization from the singly ionized state - depicted by $\gamma_c(t) = 2\pi|d_{cc''}|^2$ or from the doubly excited state - depicted by $\gamma_a(t) = 2\pi|d_{ac'}|^2$, for the frequency range and peak-intensities under consideration. This requires one to extend the DM-EOMs to include these processes as well. One can follow the methodology given in the section 4.3 with the physical scheme given in Fig. 7.1.

To recapitulate the fundamentals, assume a Fano representation of the ionization scheme [42, 95, 96], as in Fig. 7.1 . $\rho(t)$ are the atomic density matrix states. $|g\rangle$ is the ground state with energy E_g and $|a\rangle$ is the doubly excited states with energies E_a . The different continuum states are denoted by $|c\rangle$, $|c'\rangle$ and $|c''\rangle$. $\gamma_i \forall i = g, a, c$ denotes the static part of the photoionization from the ground state $|g\rangle$, resonant state $|a\rangle$ and the continuum $|c\rangle$ into the continua $|c\rangle$, $|c'\rangle$ and $|c''\rangle$ respectively. Γ_a denotes the autoionization

width from $|a\rangle$ into the $|c\rangle$ continuum.

The static part of the corresponding ionization widths, $\gamma_g, \gamma_a, \gamma_c$ and the autoionization decay width, Γ_a , are defined in the following way: γ_g is associated with photoionization from the $|g\rangle$ in the $|c\rangle$ continuum, γ_a with photoionization from the resonant state $|a\rangle$ in the $|c'\rangle$ continuum states while Γ_a represents the autoionization width from $|a\rangle$ in the $|c\rangle$ continuum. Finally $|c''\rangle$ represents the continuum states reached from the $|c\rangle$ states, following one-photon absorption; the associated static part of the ionization width is the γ_c .

The external field interacts with the atom via the operator $\hat{D}(t)$. This is given by $\hat{D}(t) = -\hat{d}E(t)$, where \hat{d} characterises the atomic dipole operator and the interacting linearly polarised laser field (including its complex envelope form) is modelled as in the section 6.1. Hypothetically if there are no random fluctuations, for a near-resonant situation, the field-free evolution of the non-diagonal density matrix elements vary sinusoidally as $(E_a - E_g)t \sim \omega t$. The time-scale here is comparable to the periodic part of the external field. But when the random field fluctuations are present, a lot slower timescales are superimposed onto the system's evolution $\sim |D_{ag}| \ll \omega$. For example consider a FEL field interacting with helium atom having a central frequency in near-resonance condition with 2s2p AIS. From Table 5.1, the $|E_a - E_g| \sim 2.211$ a.u. and $d_{ga} = 0.0355$ a.u. This implies, the field-free evolution of the non-diagonal DM elements follow $|E_a - E_g| \sim \omega \sim 2.211$ a.u. If the maximum peak intensity of the interacting FEL field is considered to be 10^{15} W/cm², the system's evolution in the presence of the field follows $\sim |D_{ag}| = d_{ga}|E(t)| = 0.0355 \times \sqrt{\frac{10^{15}}{3.509 \times 10^{16}}} \approx 0.006$ a.u. Therefore $|D_{ag}| \ll \omega$. Taking advantage of this one can effectively removing the fast oscillating terms. This is the fundamental concept behind moving to IP and applying the RWA as explored in 4.2.4. This helps in dealing with only the slow temporal variations of the field envelope ($\sim \tau_p \gg 2\pi/\omega$).

A small recapitulation is needed in regard to the process of arriving at DM-EOMs. After solving the field-free eigenvalue problem, the energies and the dipole transition matrix elements between the eigenstates can be calculated as in Chapter 5. The density matrix $\rho(t)$ can now be expanded on the eigenstate basis of the system. This gives diagonal elements $\rho_{ii}(t)$, $\forall i = g, a, c, c'$ the populations of corresponding states and the off diagonal elements (called atomic coherences) $i \neq j$ $\rho_{ij}(t)$ store the information regarding the phase relations. As the focus is on near resonant situations, the off-resonant continuum states i.e, those states that are off-resonant to $E_g + \omega$ and $E_a + \omega$ are not considered. One can move to IP and apply RWA in order to transform to slowly varying DM variables, where the diagonal terms are kept intact but the off-diagonal terms are changed by $\sigma_{ag} = \rho_{ag}e^{i(E_a - E_g)t}$ [56, 58]. This is the procedure followed in Chapter 4. But now, including the extra channels of ionization, the final set of DM-EOMs in terms of the slowly-varying Rabi transition matrix element, ac-Stark shifts and ionization widths to the respective continua,

are given by

$$\dot{\sigma}_{gg}(t) = -\gamma_g \mathcal{I}(t) \sigma_{gg}(t) + 2\text{Im}[\mathcal{D}\mathcal{E}(t)\sigma_{ag}(t)], \quad (7.1a)$$

$$\dot{\sigma}_{aa}(t) = -[\Gamma_a + \gamma_a \mathcal{I}(t)] \sigma_{aa}(t) - 2\text{Im}[\mathcal{D}^* \mathcal{E}(t)\sigma_{ag}(t)] \quad (7.1b)$$

$$\dot{\sigma}_{ag}(t) = -[\delta + \Delta \mathcal{I}(t)] \sigma_{ag}(t) + \imath \mathcal{D}^* \mathcal{E}^*(t) \sigma_{aa}(t) - \imath \mathcal{D} \mathcal{E}^*(t) \sigma_{gg}(t) \quad (7.1c)$$

$$\dot{\sigma}_{cc}(t) = -\gamma_c \mathcal{I}(t) \sigma_{cc}(t) - \dot{\sigma}_{gg}(t) - \dot{\sigma}_{aa}(t) \quad (7.1d)$$

$$\dot{\sigma}_{c'c'}(t) = \gamma_a \mathcal{I}(t) \sigma_{aa}(t) \quad (7.1e)$$

$$\imath \dot{\sigma}_{gc}(t) = -[\delta_{cg} + \Delta_{cg} \mathcal{I}(t)] \sigma_{gc}(t) + \mathcal{E}(t) \mathcal{D} \sigma_{ac}(t) - V_{ca} \sigma_{ga}(t) - \mathcal{D}_{cg} \sigma_{gg}(t) \quad (7.1f)$$

$$\imath \dot{\sigma}_{ac}(t) = -[\delta_{ca} + \Delta_{ca} \mathcal{I}(t)] \sigma_{ac}(t) + \mathcal{E}^*(t) \mathcal{D} \sigma_{gc}(t) - \mathcal{D}_{cg} \sigma_{ag}(t) - V_{ca} \sigma_{aa}(t), \quad (7.1g)$$

$$\imath \dot{\sigma}_{ac'}(t) = -[\delta_{c'a} + \Delta_{c'a} \mathcal{I}(t)] \sigma_{ac'}(t) - \mathcal{D}_{c'a} \sigma_{aa}(t) \quad (7.1h)$$

δ_0 is the near-resonant detuning ¹ which is given by

$$\delta_0 = E_a - E_g - \omega, \quad (7.2)$$

and Δ , δ are the complex detunings given by,

$$\delta = \imath \delta_0 + \frac{\Gamma_a}{2}, \quad \Delta = \imath(s_a - s_g) + \frac{\gamma_g + \gamma_a}{2}, \quad (7.3)$$

s_g , s_a denote the peak intensity of the ac-Stark shifts for the respective states. The interference matrix element is given by

$$\mathcal{D} = d_{ga} \left(1 - \frac{\imath}{q_a}\right) \quad (7.4)$$

where d_{ga} denotes the real part of the transition matrix element between the ground state $|g\rangle$ and the excited $|a\rangle$ state. q_a is the Fano q parameter. $\mathcal{E}(t)$ is the complex field envelope defined previously. The remaining dynamic detunings are accordingly defined as $\delta_{cg} = E_c - (E_g + \omega)$, $\Delta_{cg} = -s_g + \imath\gamma_g/2$ and $\delta_{ca} = E_c - E_a + \Gamma_a/2$, $\Delta_{ca} = -s_a$, $\delta_{c'a} = E_{c'} - (E_a + \omega)$, $\Delta_{c'a} = -s_a + \imath\gamma_a/2$, $\mathcal{D}_{cg} = d_{cg}\mathcal{E}(t)$ and $\mathcal{D}_{c'a} = d_{c'a}\mathcal{E}(t)$.

It was already seen in Chapter 4 that for near-resonant interactions, there exists an interference between the inter-electronic ionization channel, characterised by Γ_a , and the direct photoionization channel from the $|g\rangle$ state (γ_g). This interference is strongly dependent on the laser and atomic particulars and is encoded in the experimental observables such as ionization yield, photoelectron spectrum, etc. Mathematically, this interference is represented in the above equations via the complex interference matrix element, \mathcal{D} and the complex peak detunings, Δ , δ .

The following establishes the conservation relations

$$\sigma_{gg} + \sigma_{aa} + \sum_c \sigma_{cc} = 1, \quad \text{or} \quad \dot{\sigma}_{gg} + \dot{\sigma}_{aa} + \sum_c \dot{\sigma}_{cc} = 0. \quad (7.5)$$

¹It should be noted that until previous chapter Δ represented the quantity $\omega - (E_a - E_g)$. But this notation changes in this chapter such that $\delta_0 = (E_a - E_g) - \omega$ and $\Delta = \imath(s_a - s_g) + \frac{\gamma_g + \gamma_a}{2}$.

From the population equations it is not difficult to show that [60],

$$\sum_c \dot{\sigma}_{cc} = \gamma_a \sigma_{gg} + \Gamma_a \sigma_{aa} + 4\text{Re}\left[\frac{\Omega_{ga}}{q_a} \sigma_{ag}\right] \quad (7.6)$$

7.2 The Formalism

The time evolution of the density matrix elements $\rho(t)$ is governed by the Liouville equation [59],

$$i\dot{\rho}(t) = [\hat{\mathcal{H}}^a + \hat{D}(t), \rho(t)] \quad (7.7)$$

where $\hat{\mathcal{H}}^a$ is the time-independent field-free atomic Hamiltonian operator and $\hat{D}(t)$ the atom-field interaction operator. Looking at the previous set of DM-EOMs, it can be seen that the equations which govern the bound-state dynamics (Eq. (7.1a)-Eq. (7.1c)) are not directly coupled to the equations which govern the continuum state dynamics (Eq. (7.1d)-Eq. (7.1e)). The procedure which entails to the replacement of the full DM-EOM's with an effective set of DM-EOMs, with a non-conserved trace, is known as continuum elimination (see Refs [58, 97, 98]). It is understood that there is no direct coupling to the continuum density matrix elements $\sigma_{cc}(t), \sigma_{c'c'}(t)$ but there exists the coupling to the continuum states in an indirect fashion via the ac-Stark shifts and the ionization widths. This is the reason why the continuum state dynamics does not affect the bound-state dynamics i.e., the continuum elimination is feasible. But the opposite is not true, because the form of the equations involving $\sigma_{cc}(t), \sigma_{c'c'}(t)$ suggest that they are dependent on the knowledge of bound-state dynamics.

A similar break-up of the analyses is followed in the following sections. First the bound-state dynamics is dealt with exclusively. Only then the developed method is applied to the continuum part. Therefore, (Eq. (7.1a)-Eq. (7.1c)) are first dealt with followed by (Eq. (7.1d)-Eq. (7.1e)). The bound part is denoted by a subscript of 'b' and the continuum part by 'c'.

7.2.1 Liouville - Equation, Matrices and Operators

The set of bound part of the Eqs. (7.1), including the complex conjugate of Eq. (7.1c), can be compactly represented as:

$$\dot{\sigma}_b(t) = L_b(t)\sigma(t) \quad (7.8)$$

where $\sigma_b(t) \equiv (\sigma_{gg}(t), \sigma_{aa}(t), \sigma_{ag}(t), \sigma_{ga}(t))$ and $L_b(t)$ is a 4×4 bound-part Liouville operator.

$$L_b(t) = \begin{pmatrix} -\gamma_g \mathcal{I}(t) & 0 & -i\mathcal{E}(t)\mathcal{D} & i\mathcal{E}^*(t)\mathcal{D}^* \\ 0 & -\gamma_a \mathcal{I}(t) & i\mathcal{E}(t)\mathcal{D}^* & -i\mathcal{E}^*(t)\mathcal{D} \\ -i\mathcal{E}^*(t)\mathcal{D} & i\mathcal{E}^*(t)\mathcal{D}^* & -\delta - \Delta \mathcal{I}(t) & 0 \\ i\mathcal{E}(t)\mathcal{D}^* & -i\mathcal{E}(t)\mathcal{D} & 0 & -\delta^* - \Delta^* \mathcal{I}(t) \end{pmatrix}. \quad (7.9)$$

Useful Symbols

At this juncture, it is beneficial to introduce two complementary operators: \hat{P} and \hat{Q} such that $\hat{P} + \hat{Q} = \mathbb{1}$. Let \hat{P} be the averaging operator i.e., $\hat{P}X = \langle X \rangle = \overline{X}$ where the angular brackets or the overline denote ensemble average. The other operator naturally produces the residual fluctuations as it subtracts the average part out of the original quantity i.e., $\hat{Q}X = (\mathbb{1} - \hat{P})X = X - \langle X \rangle = \tilde{X}$, i.e., the tilde over X denotes the fluctuation or random part.

This implies that the field, intensity, Liouville operator and the density matrices can be explicitly separated as follows:

$$(\hat{P} + \hat{Q})\mathcal{E}(t) = \tilde{\mathcal{E}}(t); \quad \langle \mathcal{E}(t) \rangle = 0 \quad (7.10a)$$

$$(\hat{P} + \hat{Q})\mathcal{I}(t) = \langle \mathcal{I}(t) \rangle + \tilde{\mathcal{I}}(t) = \overline{\mathcal{I}}(t) + \tilde{\mathcal{I}}(t) \quad (7.10b)$$

$$(\hat{P} + \hat{Q})L_b(t) = \langle L_b(t) \rangle + \tilde{L}_b(t) = \overline{L}_b(t) + \tilde{L}_b(t) \quad (7.10c)$$

$$(\hat{P} + \hat{Q})\sigma_b(t) = \langle \sigma_b(t) \rangle + \tilde{\sigma}_b(t) \quad (7.10d)$$

Using the above notation, the bound part of the Liouville equation can be expressed as

$$\dot{\sigma}_b(t) = [\overline{L}_b(t) + \tilde{L}_b(t)]\sigma_b(t), \quad (7.11)$$

with the initial conditions given by $\sigma_b(t_i) = (1, 0, 0, 0)$ at initial time t_i . The mean-averaged part of the Liouville operator is a diagonal-matrix

$$\overline{L}_b(t) = \begin{pmatrix} -\gamma_g \overline{\mathcal{I}}(t) & 0 & 0 & 0 \\ 0 & -(\Gamma_a + \gamma_a \overline{\mathcal{I}}(t)) & 0 & 0 \\ 0 & 0 & -\delta - \Delta \overline{\mathcal{I}}(t) & 0 \\ 0 & 0 & 0 & -\delta^* - \Delta^* \overline{\mathcal{I}}(t) \end{pmatrix} \quad (7.12)$$

and the fluctuating part is given by the matrix

$$\tilde{L}_b(t) = \begin{pmatrix} -\gamma_g \tilde{\mathcal{I}}(t) & 0 & -i\tilde{\mathcal{E}}(t)\mathcal{D} & i\tilde{\mathcal{E}}^*(t)\mathcal{D}^* \\ 0 & -\gamma_a \tilde{\mathcal{I}}(t) & i\tilde{\mathcal{E}}(t)\mathcal{D}^* & -i\tilde{\mathcal{E}}^*(t)\mathcal{D} \\ -i\tilde{\mathcal{E}}^*(t)\mathcal{D} & i\tilde{\mathcal{E}}^*(t)\mathcal{D}^* & -\Delta \tilde{\mathcal{I}}(t) & 0 \\ i\tilde{\mathcal{E}}(t)\mathcal{D}^* & -i\tilde{\mathcal{E}}(t)\mathcal{D} & 0 & -\Delta^* \tilde{\mathcal{I}}(t) \end{pmatrix} \quad (7.13)$$

In compact form, the matrices (7.12) and (7.13) can be written as

$$\overline{L}_b(t) = L_0 + L_2 \overline{\mathcal{I}}(t), \quad (7.14a)$$

$$\tilde{L}_b(t) = L_1 \mathcal{E}(t) + L_1^T \mathcal{E}^*(t) + L_2 \tilde{\mathcal{I}}(t). \quad (7.14b)$$

with the individual matrices given by

$$L_0 = - \begin{pmatrix} 0 & 0 & 0 & 0 \\ 0 & \Gamma_a & 0 & 0 \\ 0 & 0 & \delta & 0 \\ 0 & 0 & 0 & \delta^* \end{pmatrix}, \quad L_2 = - \begin{pmatrix} \gamma_g & 0 & 0 & 0 \\ 0 & \gamma_a & 0 & 0 \\ 0 & 0 & \Delta & 0 \\ 0 & 0 & 0 & \Delta^* \end{pmatrix} \quad (7.15)$$

and

$$L_1 = \iota \begin{pmatrix} 0 & 0 & -\mathcal{D} & 0 \\ 0 & 0 & \mathcal{D}^* & 0 \\ 0 & 0 & 0 & 0 \\ \mathcal{D}^* & -\mathcal{D} & 0 & 0 \end{pmatrix}. \quad (7.16)$$

7.2.2 Infinite expansion of Evolution operator

Eq. (7.11) the mean average deterministic part of the dynamics is absorbed into a newly defined density matrix, via the transformation,

$$\sigma(t) = e^{-\int_{t_i}^t d\tau' \bar{L}_b(\tau')} \sigma_b(t) = \bar{U}_b(t, t_i) \sigma_b(t), \quad (7.17)$$

with $\bar{U}_b(t, t_i)$ as the deterministic time-evolution unitary operator whose complex conjugate is $\bar{U}_b^\dagger(t, t_i)$. Starting from the Eq. (7.17) and using $\bar{U}_b(t, t_i) \bar{U}_b^\dagger(t, t_i) = \mathbf{1}$,

$$\dot{\sigma}_b(t) = [\bar{L}_b(t) + \tilde{L}_b(t)] \sigma_b(t); \quad \sigma_b(t) = \bar{U}_b^\dagger(t, t_i) \sigma(t) \quad (7.18a)$$

$$\begin{aligned} &\implies \frac{d}{dt} [\bar{U}_b^\dagger(t, t_i) \sigma(t)] = \bar{L}_b(t) \bar{U}_b^\dagger(t, t_i) \sigma(t) + \tilde{L}_b(t) \bar{U}_b^\dagger(t, t_i) \sigma(t) \\ \implies &\cancel{[\bar{L}_b \bar{U}_b^\dagger(t, t_i) \sigma(t)]} + \bar{U}_b^\dagger(t, t_i) \dot{\sigma}(t) = \cancel{[\bar{L}_b(t) \bar{U}_b^\dagger(t, t_i) \sigma(t)]} + \tilde{L}_b(t) \bar{U}_b^\dagger(t, t_i) \sigma(t) \\ &\implies \bar{U}_b^\dagger(t, t_i) \dot{\sigma}(t) = \tilde{L}_b(t) \bar{U}_b^\dagger(t, t_i) \sigma(t) \\ &\implies \dot{\sigma}(t) = \boxed{\bar{U}_b(t, t_i) \tilde{L}_b(t) \bar{U}_b^\dagger(t, t_i)} \sigma(t) \quad (7.18b) \end{aligned}$$

In the above derivation, the fact that the operators $\bar{U}_b^\dagger(t, t_i)$ and $\bar{L}_b(t)$ commute with each other was used. Also, the first fundamental theorem of calculus² [99] has been utilised while applying the time derivative to the evolution operator. Looking at Eq. (7.18b), the effective (interaction-picture) time-evolution for the $\sigma(t)$ can be written as,

$$\dot{\sigma}(t) = \tilde{L}(t) \sigma(t), \quad \sigma(t_i) = \sigma_b(t_i), \quad (7.19)$$

where the newly introduced fluctuating interaction matrix $\tilde{L}(t)$ is given by,

$$\tilde{L}(t) = \bar{U}_b(t) \tilde{L}_b(t) \bar{U}_b^\dagger(t). \quad (7.20)$$

² The first fundamental theorem of calculus suggests that for a constant t'

$$\frac{d}{dt} \int_{t'}^t d\tau' \bar{L}_b(\tau') = \bar{L}_b(t)$$

where t' is a constant

Eq. (7.19) represents a typical multiplicative system of SDEs, which were heavily studied over the years in various contexts (see Ref [19]). There are quite a few methods suited to solving such systems, some of which have been used in references [84, 100]. Here, as the title of the chapter suggests, a perturbative approach is utilised which constitutes an infinite expansion solution of Eq. (7.19).

$$\begin{aligned}
\dot{\sigma}(t) &= \tilde{L}(t)\sigma(t) & (7.21a) \\
\implies d\sigma(t) &= \tilde{L}(t)\sigma(t)dt \\
\implies \sigma(t) \Big|_{t_i}^t &= \int_{t_i}^t \tilde{L}(t_1)\sigma(t_1)dt_1 \\
\implies \sigma(t) &= \sigma(t_i) + \int_{t_i}^t \tilde{L}(t_1)\sigma(t_1)dt_1 & (7.21b)
\end{aligned}$$

After the above step, one will have to recursively expand the integral on the right hand side of Eq. (7.21b), as in, expand the boxed $\sigma(t)$.

$$\begin{aligned}
\implies \sigma(t) &= \sigma(t_i) + \int_{t_i}^t \tilde{L}(t_1) \boxed{\sigma(t_1)} dt_1 \\
\implies \sigma(t) &= \sigma(t_i) + \int_{t_i}^t \tilde{L}(t_1) \left[\sigma(t_i) + \int_{t_i}^{t_1} \tilde{L}(t_2)\sigma(t_2)dt_2 \right] dt_1 \\
&= \sigma(t_i) + \int_{t_i}^t \tilde{L}(t_1)\sigma(t_i)dt_1 + \int_{t_i}^t dt_1 \int_{t_i}^{t_1} dt_2 \tilde{L}(t_1)\tilde{L}(t_2) \boxed{\sigma(t_2)} \\
\implies \sigma(t) &= \sigma(t_i) + \int_{t_i}^t \tilde{L}(t_1)\sigma(t_i)dt_1 \\
&+ \int_{t_i}^t dt_1 \int_{t_i}^{t_1} dt_2 \tilde{L}(t_1)\tilde{L}(t_2) \left[\sigma(t_i) + \int_{t_i}^{t_2} \tilde{L}(t_3)\sigma(t_3)dt_3 \right] \\
&= \sigma(t_i) + \int_{t_i}^t \tilde{L}(t_1)\sigma(t_i)dt_1 \\
&+ \int_{t_i}^t dt_1 \int_{t_i}^{t_1} dt_2 \tilde{L}(t_1)\tilde{L}(t_2)\sigma(t_i) + \int_{t_i}^t dt_1 \int_{t_i}^{t_1} dt_2 \int_{t_i}^{t_2} \tilde{L}(t_1)\tilde{L}(t_2)\tilde{L}(t_3) \boxed{\sigma(t_3)} dt_3 \\
&\dots\dots
\end{aligned}$$

In this way, when one infinitely expands the integral on the right hand side by recursive substitution, one arrives at the following solution

$$\sigma(t) = \tilde{U}(t)\sigma(t_i), \quad (7.23)$$

with the evolution operator, $\tilde{U}(t)$, expressed in a chronologically ordered format, $t > t_1 > t_2 > \dots > t_n$:

$$\tilde{U}(t) = \mathbb{1} + \sum_{n=1}^{\infty} \tilde{U}_n(t) = \mathbb{1} + \sum_{n=1}^{\infty} \int_{t_i}^t dt_1 \int_{t_i}^{t_1} dt_2 \dots \int_{t_i}^{t_{n-1}} dt_n \tilde{L}(t_1)\tilde{L}(t_2)\dots\tilde{L}(t_n), \quad (7.24)$$

where, the $\tilde{U}_n(t)$ terms can be understood by inspection. The chronological ordering is important because generally the individual integrands do not commute with each other

i.e., $[\tilde{L}(t), \tilde{L}(t')] \neq 0$.

Applying the averaging operator on the Eq. (7.23) $\langle \sigma(t) \rangle = \langle \tilde{U}(t) \sigma(t_i) \rangle = \langle \tilde{U}(t) \rangle \sigma(t_i)$, as $\sigma(t_i)$ is a constant matrix. Then, the average of the evolution operator is:

$$\langle \tilde{U}(t) \rangle = \mathbb{1} + \sum_{n=1} \int_{t_i}^t dt_1 \int_{t_i}^{t_1} dt_2 \cdots \int_{t_i}^{t_{n-1}} dt_n \langle \tilde{L}(t_1) \tilde{L}(t_2), \cdots, \tilde{L}(t_n) \rangle \quad (7.25)$$

In the introductory chapters, the concept of moments was introduced. The integrand of the Eq. (7.25) is nothing but n^{th} moment in terms of $\tilde{L}(t)$, which in turn implies that it is an n^{th} moment of the field or intensity. Let this n^{th} order moment be denoted by $M_n(t_1, t_2, \cdots, t_n)$. Thus, the averaging of the evolution operator, in terms of moments, is given by

$$\langle \tilde{U}(t) \rangle = \mathbb{1} + \sum_{n=1} U_n(t) \quad (7.26a)$$

$$U_n(t) = \int_{t_i}^t dt_1 \int_{t_i}^{t_1} dt_2 \cdots \int_{t_i}^{t_{n-1}} dt_n M_n(t_1, t_2, \cdots, t_n) \quad (7.26b)$$

$$M_n(t_1, t_2, \cdots, t_n) = \langle \tilde{L}(t_1) \tilde{L}(t_2), \cdots, \tilde{L}(t_n) \rangle \quad (7.26c)$$

By inspecting the Eq. (7.20), Eq. (7.13) and $M_n(t_1, t_2, \cdots, t_n)$, it is easy to conclude that one now has the time evolution of the transformed density-matrices in terms of field coherence functions.

Limitations of the moment-expansion approach

As the goal is to use a perturbative expansion, each successive term of the expansion should reduce in its magnitude for the series to converge. A check needs to be performed at this junction to see if the moment-expansion satisfies this criteria. Looking at matrix in Eq. (7.13), it can be easily seen that $\tilde{L}(t)$ is dependent on field and intensity terms. So, it has the peak value (say $L_0 \sim |\mathcal{D}| \mathcal{E}_0, \gamma_g \mathcal{I}_0 a, \Gamma_a$ and $\gamma_a \mathcal{I}_0$ (where \mathcal{I}_0 is the peak value of instantaneous intensity envelope)). Keeping this point in mind, one can now proceed to see how each term of Eq. (7.26b) expands. The first term expands by the order of tL_0 ($\int_{t_i}^t dt_1 \langle L(t_1) \rangle$) whereas the second by $t^2 L_0^2$ ($\int_{t_i}^t dt_1 \int_{t_i}^{t_1} dt_2 \langle L(t_1) L(t_2) \rangle$) and so on and so forth. Thus, the n -th terms expands by the order of $(tL_0)^n$. For a proper perturbative expansion one requires the constraint of $tL_0 \ll 1$. For example, taking the peak value of $L_0 \sim 1$ a.u., one enforces the constraint that the expansion is well behaved only within the limits of $t \ll 1$ a.u. So, for $t \gg 1$ a.u. , the said expansion may be invalidated. The times duration of $t \gg 1$ a.u. ($\gg 0.025$ fs) are within the typical range of FEL-pulse duration available nowadays. That means, within the typical duration in which the pulse is present, the moment-expansion may not yield proper results.

7.2.3 Cumulant-expansion vs moment-expansion

In Appendix B it has been seen how cumulants have certain nicer properties than moments and how they can be more useful for certain problems. The above observations call in

for such situations where cumulant-expansion is favoured over moment-expansion. Before going into the derivation of the cumulants, the validity may be established here by contrast with the method of the moments. For the Gaussian fields with a zero-mean, only the first two cumulant remains.

In the cumulant-expansion, the only term remaining is $\kappa_2(t)$ which depends on time integral of field coherence functions i.e., $\langle \mathcal{E}(t)\mathcal{E}^*(t') \rangle$, $\langle \mathcal{E}^*(t)\mathcal{E}(t') \rangle$ or $\langle \mathcal{I}(t)\mathcal{I}(t') \rangle$. For times larger than the coherence time (refer chapter-2) $|t - t'| \gg \tau_c$, the contributing terms bifurcate into $\langle \mathcal{E}(t)\mathcal{E}^*(t') \rangle \sim \langle \mathcal{E}(t) \rangle \langle \mathcal{E}^*(t') \rangle \sim 0$, $\langle \mathcal{E}^*(t)\mathcal{E}(t') \rangle \sim \langle \mathcal{E}^*(t) \rangle \langle \mathcal{E}(t') \rangle \sim 0$ and $\langle \mathcal{I}(t)\mathcal{I}(t') \rangle \sim \langle \mathcal{I}(t) \rangle \langle \mathcal{I}(t') \rangle$. That means, with the time-integrals having a short lifetime of around τ_c , one obtains the peak value for $\kappa_2(t) \sim \gamma_g^2 \mathcal{I}_0^2 \tau_c$, $\gamma_a^2 \mathcal{I}_0^2 \tau_c$ and $\Gamma_a^2 \tau_c$. This immediately necessitates a general condition for cumulant-expansion:

$$\gamma_i \mathcal{I}_0 \tau_c < 1, \quad i = g, a \quad \text{and} \quad \Gamma_a \tau_c < 1, \quad (7.27)$$

This is what is meant by the shorter coherence (or correlation) times. The evolution time did not matter anymore in this case as it is replaced by the coherence time due to the short-lived time integrals of coherences. Therefore, the only conditions for the cumulant-expansion to be valid are given by the above Eq. (7.27). To contrast this with the moment-expansion, note that the higher order moments need not vanish nor the magnitude of their time integrals reduce which made the successive terms in time evolution expand rather than decay. This clearly puts the cumulant-expansion at an advantage. Is this condition meaningful? The present FELs have short-coherence time and hence the cumulant approach of the perturbative expansion should help in the theoretical study of the photoionization processes with FELs.

7.2.4 The cumulant-expansion

The previous section would have definitely established a preference of utilising cumulant-expansion in the perturbative method which would be valid for arbitrarily long times. Eqs. (7.26) suggest a generalised moment expansion. The concept of cumulant arises when one desires to find a solution of

$$\langle \tilde{U}(t) \rangle = e^{K(t)} \quad (7.28)$$

This $K(t)$ is then called generalised cumulant [101]. It can be expressed as the sum of n^{th} order cumulants $C_n(t_1, t_2, \dots, t_n)$ similar to $U_n(t)$ which is a sum of n^{th} order moments [85, 101]. Therefore, to obtain the cumulant expansion, one takes the natural logarithm of Eq. (7.26a) i.e.,

$$K(t) = \ln \langle \tilde{U}(t) \rangle = \sum_{n=1}^{\infty} \kappa_n(t) \quad (7.29a)$$

$$\kappa_n(t) = \int_{t_i}^t dt_1 \int_{t_i}^{t_1} dt_2 \cdots \int_{t_i}^{t_{n-1}} dt_n C_n(t_1, t_2, \dots, t_n). \quad (7.29b)$$

The nature of these cumulants is well understood from Appendices B and C. Kubo in his seminal work [85] elaborately applied the concept of these cumulants to many physics

problems and has shown their seamless advantage.

At any rate, in the present context, the cumulants enter into the problem when a time derivative is taken for the averaged Eq. (7.23), i.e.,

$$\langle \sigma(t) \rangle = \langle \tilde{U}(t) \rangle \sigma(t_i) = e^{K(t)} \sigma(t_i), \quad (7.30)$$

$$\implies \frac{d}{dt} \langle \sigma(t) \rangle = \frac{d}{dt} \left(e^{K(t)} \sigma(t_i) \right) = \dot{K}(t) \boxed{e^{K(t)} \sigma(t_i)} = \dot{K}(t) \langle \sigma(t) \rangle, \quad (7.31)$$

Eq. (7.30) was used to replace the $\sigma(t_i)$, where t_i is the initial time where the field is assumed to be zero, so as to get back the equation in terms of $\langle \sigma(t) \rangle$. It must always be kept in mind that the above expressions are time-ordered i.e., the strict inequalities $t > t_1 > t_2 > \dots > t_n > t_i$ must be verified.

To obtain $\dot{K}(t)$ use Eqs. (7.29)

$$\begin{aligned} \dot{K}(t) &= \sum_{n=1}^{\infty} \dot{\kappa}_n(t) \\ &= \sum_{n=1}^{\infty} \frac{d}{dt} \int_{t_i}^t dt_1 \boxed{\int_{t_i}^{t_1} dt_2 \dots \int_{t_i}^{t_{n-1}} dt_n C_n(t_1, t_2, \dots, t_n)} \rightarrow C_n(t_1, \lambda) \\ &= \sum_{n=1}^{\infty} \frac{d}{dt} \int_{t_i}^t dt_1 C_n(t_1, \lambda); \lambda = t_2, t_3, \dots, t_n \\ &= \sum_{n=1}^{\infty} C_n(t, \lambda) \text{ (using the first fundamental theorem of calculus)} \\ &= \sum_{n=1}^{\infty} C_n(t, t_2, t_3, \dots, t_n) \\ &= \sum_{n=1}^{\infty} C_n(t, t_1, t_2, \dots, t_{n-1}); \text{ (change of variable names)} \\ \implies \dot{K}(t) &= \sum_{n=1}^{\infty} \dot{\kappa}_n(t) = C_1(t) + \sum_{n=2}^{\infty} \int_{t_i}^t dt_1 \int_{t_i}^{t_1} dt_2 \dots \int_{t_i}^{t_{n-2}} dt_{n-1} C_n(t, t_1, t_2, \dots, t_{n-1}) \end{aligned} \quad (7.32)$$

In the above, $t_0 = t$. Inserting Eq. (7.32) into Eq. (7.31) the time derivative of the averaged $\sigma(t)$ is given by the following

$$\frac{d}{dt} \langle \sigma(t) \rangle = \sum_{n=1}^{\infty} \dot{\kappa}_n(t) \langle \sigma(t) \rangle, \quad (7.33)$$

where the time-derivatives of $\kappa_n(t)$ are obtained from Eq. (7.32):

$$\dot{\kappa}_n(t) = \begin{cases} C_1(t), & \text{if } n = 1 \\ \int_{t_i}^t dt_1 \int_{t_i}^{t_1} dt_2 \dots \int_{t_i}^{t_{n-2}} dt_{n-1} C_n(t, t_1, \dots, t_{n-1}), & \forall n \geq 2 \end{cases} \quad (7.34)$$

For a general expansion $\dot{\kappa}_n(t)$ up to $n = 4$ refer to Appendix C: Eqs. (C.3), (C.4), (C.5) and (C.9). Eq. (7.33) is the starting master averaged equation which can be solved, maybe

after certain transformations, to obtain the dynamical averaged observables such as the state populations, etc. Note that in Eq. (7.33) the population part $\sigma(t)$ and the field part, which is absorbed into the cumulant averages $C_n(t)$, are decorrelated naturally i.e., their averages evolve independently without any artificial decorrelation approximation (DA) such as the ones used in [27, 84]. Also, in the derivation of Eq. (7.33) no assumptions were made as to the Gaussian character of the multi-time correlations or stationarity of the involved random processes. Therefore, Eq. (7.33) is valid for general random fields with the only constraint being that the correlation time τ_c should satisfy Eq. (7.27).

7.2.5 The first two non-vanishing terms

Eq. (7.33) has infinite terms. As pointed earlier, the successive terms decrease in magnitude. So, for all practical purposes, one may truncate this expansion up to certain terms of $\dot{\kappa}_n(t)$ resulting in an approximated form of the density matrix equations. In this section, the first two terms of the expansion are retained and the equations of motion are obtained. Appendix C shows the first four terms for a scalar and multi-time commutative field to give an idea as to how to proceed with higher terms.

$$\begin{aligned}
\dot{\kappa}_2(t) &= \int_{t_i}^t dt_1 \langle \tilde{L}(t) \tilde{L}(t_1) \rangle \\
&= \int_{t_i}^t dt_1 \langle \bar{U}_b(t, t_i) \tilde{L}_b(t) \bar{U}_b^\dagger(t, t_i) \bar{U}_b(t_1, t_i) \tilde{L}_b(t_1) \bar{U}_b^\dagger(t_1, t_i) \rangle \\
&= \bar{U}_b(t) \int_{t_i}^t dt_1 \langle \tilde{L}_b(t) \bar{U}_b^\dagger(t) \bar{U}_b(t_1) \tilde{L}_b(t_1) \rangle \bar{U}_b^\dagger(t_1) \\
&= \bar{U}_b(t) \int_{t_i}^t dt_1 \langle \tilde{L}_b(t) e^{\int_{t_i}^t d\tau' \bar{L}_b(\tau')} e^{-\int_{t_i}^{t_1} d\tau' \bar{L}_b(\tau')} \tilde{L}_b(t_1) \rangle e^{\int_{t_i}^{t_1} d\tau' \bar{L}_b(\tau')} \\
&= \bar{U}_b(t) \int_{t_i}^t dt_1 \langle \tilde{L}_b(t) e^{\int_{t_1}^t d\tau' \bar{L}_b(\tau')} \tilde{L}_b(t_1) \rangle e^{\int_{t_i}^{t_1} d\tau' \bar{L}_b(\tau')} \\
&\quad \text{Now changing the variable } \tau_1 = t - t_1 \text{ and making } t_i = -\infty \\
&= \bar{U}_b(t) \int_0^\infty d\tau_1 \langle \tilde{L}_b(t) e^{\int_{t-\tau_1}^t d\tau' \bar{L}_b(\tau')} \tilde{L}_b(t - \tau_1) \rangle e^{\int_{t_i}^{t-\tau_1} d\tau' \bar{L}_b(\tau')} \\
&\quad \text{and observing the integral } \int_{t_i}^{t-\tau_1} = \int_{t_i}^t - \int_{t-\tau_1}^t \\
&= \bar{U}_b(t) \int_0^\infty d\tau_1 \langle \tilde{L}_b(t) e^{\int_{t-\tau_1}^t d\tau' \bar{L}_b(\tau')} \tilde{L}_b(t - \tau_1) \rangle e^{-\int_{t-\tau_1}^t d\tau' \bar{L}_b(\tau')} \bar{U}_b^\dagger(t) \\
\implies \dot{\kappa}_2(t) &= \bar{U}_b(t) \int_0^\infty d\tau_1 \langle \tilde{L}_b(t) e^{\int_{t-\tau_1}^t d\tau' \bar{L}_b(\tau')} \tilde{L}_b(t - \tau_1) \rangle e^{-\int_{t-\tau_1}^t d\tau' \bar{L}_b(\tau')} \bar{U}_b^\dagger(t) \quad (7.35)
\end{aligned}$$

For zero-mean fields, both first cumulant and moment are 0 i.e., $C_1(t) = M_1(t) = 0$. Therefore $\dot{\kappa}_1(t) = 0$, and what remains is the $\dot{\kappa}_2(t)$ term. By using Eqs. (7.17) and (7.20) it is calculated as above. A meaningful average law should lose any memory at times much longer than the fluctuation correlation time [19]. The change of variable in Eq. (7.35) has effectively removed the dependence on the initial time, as desired. At this point, one should take advantage of the shortness of the correlation time relative to the average intensity

slow variation. This helps in expressing the integral over $\bar{L}_b(\tau')$ more conveniently as:

$$\int_{t-\tau_1}^t d\tau' \bar{L}_b(\tau') = L_0 \tau_1 + \langle W(t, \tau_1) \rangle L_2 \approx \bar{L}_b(t) \tau_1 \quad (7.36)$$

where $\langle W(t, t') \rangle$ is the mean energy contained in the time interval $|t - t'|$:

$$\langle W(t, t') \rangle = \int_{t'}^t d\tau' \langle \mathcal{I}(\tau') \rangle \quad (7.37)$$

$$\begin{aligned} \int_{t-\tau_1}^t dt'' \langle \mathcal{I}(t'') \rangle &= \int_0^{\tau_1} d\tau (\langle \mathcal{I}(t) \rangle \tau - \tau \langle \dot{\mathcal{I}}(t) \rangle + \dots) \\ &\simeq \langle \mathcal{I}(t) \rangle \tau_1 - \mathcal{O}(\tau_c \langle \dot{\mathcal{I}}(t) \rangle) \tau_1 / 2, \end{aligned}$$

with the leading error term replaced by $\tau_1 \langle \dot{\mathcal{I}}(t) \rangle \simeq \tau_c \langle \dot{\mathcal{I}}(t) \rangle \ll 1$.

7.2.6 Equations for the bound-part

Using Eq. (7.17) and Eq. (7.33), one can revert back to the equations in terms of original density matrices.

$$\begin{aligned} \frac{d}{dt} \langle \sigma(t) \rangle &= \sum_{n=1}^{\infty} \dot{\kappa}_n(t) \langle \sigma(t) \rangle \implies \frac{d}{dt} \langle \bar{U}_b(t) \sigma_b(t) \rangle = \sum_{n=1}^{\infty} \dot{\kappa}_n(t) \langle \bar{U}_b(t) \sigma_b(t) \rangle \\ &\implies \langle -\bar{U}_b(t) \bar{L}_b(t) \sigma_b(t) + \bar{U}_b(t) \sigma_b(t) \rangle = \sum_{n=1}^{\infty} \dot{\kappa}_n(t) \langle \bar{U}_b(t) \sigma_b(t) \rangle \\ &\implies \bar{U}_b(t) \langle \dot{\sigma}_b(t) \rangle = \bar{U}_b(t) \bar{L}_b(t) \langle \sigma_b(t) \rangle + \sum_{n=1}^{\infty} \dot{\kappa}_n(t) \bar{U}_b(t) \langle \sigma_b(t) \rangle \\ &\implies \langle \dot{\sigma}_b(t) \rangle = \cancel{\bar{U}_b^\dagger(t) \bar{U}_b(t)} \bar{L}_b(t) \langle \sigma_b(t) \rangle + \bar{U}_b^\dagger(t) \sum_{n=1}^{\infty} \dot{\kappa}_n(t) \bar{U}_b(t) \langle \sigma_b(t) \rangle \quad (7.38) \end{aligned}$$

The above Eq. (7.38) is valid for general cumulant expansion. But, for the specific case of the Gaussian fields, with only $\dot{\kappa}_2(t)$ remaining, one can insert Eq. (7.36) in Eq. (7.35) and complete the above transformation as

$$\langle \dot{\sigma}_b(t) \rangle = \bar{L}_b(t) \langle \sigma_b(t) \rangle + \bar{U}_b^\dagger(t) \dot{\kappa}_2(t) \bar{U}_b(t) \langle \sigma_b(t) \rangle \quad (7.39)$$

$$= \bar{L}_b(t) \langle \sigma_b(t) \rangle + \cancel{\bar{U}_b^\dagger(t) \bar{U}_b(t)} \int_0^\infty d\tau_1 \boxed{\langle \tilde{L}_b(t) e^{\bar{L}_b(t)\tau_1} \tilde{L}_b(t-\tau_1) \rangle e^{-\bar{L}_b(t)\tau_1}} \cancel{\bar{U}_b^\dagger(t) \bar{U}_b(t)} \langle \sigma_b(t) \rangle \quad (7.40)$$

$$\implies \langle \dot{\sigma}_b(t) \rangle = \left[\bar{L}_b(t) + \int_0^\infty d\tau_1 \mathcal{K}_2(t, t-\tau_1) \right] \langle \sigma_b(t) \rangle \quad (7.41)$$

$\mathcal{K}_2(t, t - \tau_1)$ in Eq. (7.41) is the new term generated by the averaging process. It can be evaluated by considering the matrices of L_i that were considered previously.

$$\begin{aligned}
\mathcal{K}_2(t, t - \tau_1) &= \langle \tilde{L}(t) e^{\bar{L}_b(t)\tau_1} \tilde{L}(t - \tau_1) \rangle e^{-\bar{L}_b(t)\tau_1} \\
&= \langle (L_1 \mathcal{E}(t) + L_1^T \mathcal{E}^*(t) + L_2 \tilde{\mathcal{I}}(t)) e^{\bar{L}_b(t)\tau_1} \\
&\quad (L_1 \mathcal{E}(t - \tau_1) + L_1^T \mathcal{E}^*(t - \tau_1) + L_2 \tilde{\mathcal{I}}(t - \tau_1)) \rangle e^{-\bar{L}_b(t)\tau_1} \\
&= \langle \mathcal{E}(t) \mathcal{E}^*(t - \tau_1) \rangle L_1 e^{\bar{L}_b(t)\tau_1} L_1^T e^{-\bar{L}_b(t)\tau_1} \\
&\quad + \langle \mathcal{E}^*(t) \mathcal{E}(t - \tau_1) \rangle L_1^T e^{\bar{L}_b(t)\tau_1} L_1 e^{-\bar{L}_b(t)\tau_1} \\
&\quad + \langle \tilde{\mathcal{I}}(t) \tilde{\mathcal{I}}(t - \tau_1) \rangle L_2 e^{\bar{L}_b(t)\tau_1} L_2 e^{-\bar{L}_b(t)\tau_1} \\
\implies \mathcal{K}_2(t, t - \tau_1) &= 2 \operatorname{Re}[\langle \mathcal{E}(t) \mathcal{E}^*(t - \tau_1) \rangle L_1 e^{\bar{L}_b(t)\tau_1} L_1^T] e^{-\bar{L}_b(t)\tau_1} \\
&\quad + \langle \tilde{\mathcal{I}}(t) \tilde{\mathcal{I}}(t - \tau_1) \rangle L_2 e^{\bar{L}_b(t)\tau_1} L_2 e^{-\bar{L}_b(t)\tau_1} \\
\text{using } \tilde{\mathcal{I}}(t) &= \mathcal{I}(t) - \bar{\mathcal{I}}(t) \implies \langle \tilde{\mathcal{I}}(t) \tilde{\mathcal{I}}(t - \tau_1) \rangle = \langle \mathcal{I}(t) \mathcal{I}(t - \tau_1) \rangle - \langle \mathcal{I}(t) \rangle \langle \mathcal{I}(t - \tau_1) \rangle \\
\implies \mathcal{K}_2(t, t - \tau_1) &= 2 \operatorname{Re}[\langle \mathcal{E}(t) \mathcal{E}^*(t - \tau_1) \rangle L_1 e^{\bar{L}_b(t)\tau_1} L_1^T] e^{-\bar{L}_b(t)\tau_1} \\
&\quad + \langle \mathcal{I}(t) \mathcal{I}(t - \tau_1) \rangle - \langle \mathcal{I}(t) \rangle \langle \mathcal{I}(t - \tau_1) \rangle L_2 e^{\bar{L}_b(t)\tau_1} L_2 e^{-\bar{L}_b(t)\tau_1}
\end{aligned} \tag{7.42}$$

It can be clearly seen that $\mathcal{K}_2(t, t - \tau_1)$ is structured upon the field and intensity first order coherence functions which are known i.e., the statistics of the stochastic field are assumed to be known. Using Eqs (7.12), (7.15), (7.16) and the fact that the exponential of a diagonal matrix is obtained by exponentiating each of the diagonal elements, the following set of main expressions for the averaged EOMs of the bound states are obtained:

$$\begin{aligned}
\frac{d}{dt} \langle \sigma_{gg}(t) \rangle &= - [\gamma_g \langle \mathcal{I}(t) \rangle - \gamma_g^2 S_{2t}(0) + 2 \operatorname{Re}\{\mathcal{D}^2 S_{1t}(\delta_+)\}] \langle \sigma_{gg}(t) \rangle \\
&\quad + 2 |\mathcal{D}|^2 \operatorname{Re}\{S_{1t}(\delta_-)\} \langle \sigma_{aa}(t) \rangle
\end{aligned} \tag{7.43a}$$

$$\begin{aligned}
\frac{d}{dt} \langle \sigma_{aa}(t) \rangle &= - [\Gamma_a + \gamma_a \langle \mathcal{I}(t) \rangle - \gamma_a^2 S_{2t}(0) + 2 \operatorname{Re}\{\mathcal{D}^{*2} S_{1t}(\delta_-)\}] \langle \sigma_{aa}(t) \rangle \\
&\quad + 2 |\mathcal{D}|^2 \operatorname{Re}\{S_{1t}(\delta_+)\} \langle \sigma_{gg}(t) \rangle
\end{aligned} \tag{7.43b}$$

$$\begin{aligned}
\frac{d}{dt} \langle \sigma_{ag}(t) \rangle &= - [\delta + \Delta \langle \mathcal{I}(t) \rangle - \Delta^2 S_{2t}(0) + \{\mathcal{D}^2 S_{1t}(-\delta_+) + \mathcal{D}^{*2} S_{1t}(-\delta_-)\}] \langle \sigma_{ag}(t) \rangle
\end{aligned} \tag{7.43c}$$

In the above, $\delta_{\pm} \equiv \delta_{\pm}(t)$ are the averaged dynamic detunings, defined by,

$$\delta_{\pm}(t) = \iota [\delta_0 + (s_a - s_g) \langle \mathcal{I}(t) \rangle] \pm \frac{\Gamma_a + (\gamma_a - \gamma_g) \langle \mathcal{I}(t) \rangle}{2} \tag{7.44}$$

The coefficients in Eqs. (7.43) are expressed as the Laplace transforms of the coherence

functions of the field and the intensity, respectively:

$$S_{1t}(\delta) = \int_0^\infty d\tau \langle \mathcal{E}(t) \mathcal{E}^*(t - \tau) \rangle e^{-\delta\tau}, \quad (7.45)$$

$$S_{2t}(0) = \int_0^\infty d\tau (\langle \mathcal{I}(t) \mathcal{I}(t - \tau) \rangle - \langle \mathcal{I}(t) \rangle \langle \mathcal{I}(t - \tau) \rangle). \quad (7.46)$$

The complex quantity $S_{1t}(\delta)$ is closely related with a time-dependent frequency spectrum and for such long pulses, where stationarity conditions of the field statistical properties are reached, approaches the field power spectrum via the Wiener–Khinchin theorem [35]. Under the later (stationarity) assumption it can also be shown that $S_{2t}(0)$ in Eq. (7.46) is proportional to the field average energy standard deviation, $\langle \Delta W^2(t) \rangle$. Eqs. (7.43) are the result of the lowest-order non-vanishing approximation of an infinite term expansion and have general applicability with respect to the field fluctuations on proviso of the conditions set by Eq. (7.27); as such there is an associated upper limit in the intensity for the condition to be fulfilled. Explicit, analytical, expressions for S_{1t} , S_{2t} are given later for the case where the field is considered non-stationary, Gaussian and square-exponentially time correlated coherence functions.

7.2.7 Equations for the continuum populations

The next part of the formalism includes a derivation of the EOMs for the continuum part of the density matrix i.e., the time evolution of $\langle \sigma_{cc}(t) \rangle$ and $\langle \sigma_{c'c'}(t) \rangle$. The starting point would be the following set of stochastic equations borrowed from Eqs. (7.1)

$$\dot{\sigma}_{cc}(t) = -\gamma_c \mathcal{I}(t) \sigma_{cc}(t) - \dot{\sigma}_{gg}(t) - \dot{\sigma}_{aa}(t) \quad (7.47a)$$

$$\dot{\sigma}_{c'c'}(t) = \gamma_a \mathcal{I}(t) \sigma_{aa}(t) \quad (7.47b)$$

The method applied for the bound part of the density matrix can be repeated in the present case. For this, the first task is to bring the continuum equations in the form of Eq. (7.11). To achieve this, one needs to augment the set of the continuum equations to include the $\dot{\sigma}_{gg}(t)$, $\dot{\sigma}_{aa}(t)$ and define $\sigma_c(t) = (\sigma_{cc}(t), \sigma_{c'c'}(t), 1)$ with $p_b(t) = \sigma_{gg}(t) + \sigma_{aa}(t)$. Thus, the reformulated equations get the desired form as

$$\dot{\sigma}_c(t) = [\bar{L}_c(t) + \tilde{L}_c(t)] \sigma_c(t), \quad (7.48)$$

with $\sigma_c(t_i) = (0, 0, 1)$. The mean-average and the random parts of the new continuum Liouville operator ($L_c(t)$) i.e., $\bar{L}_c(t)$ and $\tilde{L}_c(t)$, are given by ,

$$\bar{L}_c(t) = \begin{pmatrix} -\gamma_c \langle \mathcal{I}(t) \rangle & 0 & 0 \\ 0 & \gamma_a \langle \mathcal{I}(t) \rangle & 0 \\ 0 & 0 & 0 \end{pmatrix}, \quad (7.49)$$

$$\tilde{L}_c(t) = \begin{pmatrix} -\gamma_c \tilde{\mathcal{I}}(t) & 0 & \dot{p}_b(t) \\ 0 & \gamma_a \tilde{\mathcal{I}}(t) & 0 \\ 0 & 0 & 0 \end{pmatrix}. \quad (7.50)$$

Repeating the steps described in the previous sections and keeping only the first two terms of the perturbative expansion one arrives at equations analogous to Eq. (7.41). The end result for the averaged populations is,

$$\begin{aligned} \langle \dot{\sigma}_{cc}(t) \rangle &= -\gamma_c \langle \mathcal{I}(t) \rangle \langle \sigma_{cc}(t) \rangle - \langle \dot{\sigma}_{gg}(t) \rangle - \langle \dot{\sigma}_{aa}(t) \rangle \\ &\quad + \gamma_c S_{2t}(0) [\gamma_c \langle \sigma_{cc}(t) \rangle - \gamma_g \langle \sigma_{gg}(t) \rangle - \gamma_a \langle \sigma_{aa}(t) \rangle] \end{aligned} \quad (7.51a)$$

$$\langle \dot{\sigma}_{c'c'}(t) \rangle = + [\gamma_a \bar{\mathcal{I}}(t) + \gamma_a^2 S_{2t}(0)] \langle \sigma_{aa}(t) \rangle \quad (7.51b)$$

7.3 The case of a Gaussian random field

Until now, the discussion had been with general zero mean stochastic fields. But a particular class of statistics takes prominence in many physical processes. They are the famous Gaussian processes which have a bell-shaped probability distribution function of the random variables. The random FEL field which was discussed in Chapter 3 was modelled as a Gaussian field. In order to study the interaction of the FEL field with atomic systems, the previously derived EOMs will have to be tailored to fit the Gaussian statistics. The present section is dedicated to achieving this goal.

For the particular form of the modeled radiation, see section 6.1. For the sake of continuity, it is given as $\mathcal{E}(t) = \mathcal{E}_0(t)\epsilon(t)$ where all the fluctuations are now included in $\epsilon(t)$. Using Eq. (6.2), the non-stationary first-order field coherence function, as it appears in the EOMs derived earlier, now takes the form

$$\langle \mathcal{E}(t)\mathcal{E}^*(t') \rangle = \mathcal{E}_0(t)\mathcal{E}_0^*(t') \langle \epsilon(t)\epsilon^*(t') \rangle. \quad (7.52)$$

Krinsky and Li suggest [35] that for a Gaussian random field $|\langle \mathcal{E}(t)\mathcal{E}^*(t') \rangle|^2 = \langle |\mathcal{E}(t)|^2 |\mathcal{E}(t')|^2 \rangle - \langle |\mathcal{E}(t)|^2 \rangle \langle |\mathcal{E}(t')|^2 \rangle$. This, written in terms of intensity $\mathcal{I}(t) = |\mathcal{E}(t)|^2$ gives $|\langle \mathcal{E}(t)\mathcal{E}^*(t') \rangle|^2 = \langle \mathcal{I}(t)\mathcal{I}(t') \rangle - \langle \mathcal{I}^2(t) \rangle$. This can be used in the formulation to evaluate the expression of the first order coherence function of intensity as

$$\langle \tilde{\mathcal{I}}(t)\tilde{\mathcal{I}}(t') \rangle = |\langle \mathcal{E}(t)\mathcal{E}^*(t') \rangle|^2 \quad (7.53)$$

That means, the expressions concerning the Laplace transforms, $S_{1t}(\pm\delta_{\pm})$ and $S_{2t}(0)$, can now be expressed in terms of only the first-order field coherence function $\langle \mathcal{E}(t)\mathcal{E}^*(t') \rangle$. With these initial steps, one can now choose the specific form of the first order coherence function. This choice is dependent on the type of the interacting laser field. For FELs, it is square exponential or Gaussian whereas for the long wavelength lasers, it is exponential or Lorentzian. The particular expressions of $S_{1t}(\pm\delta_{\pm})$ and $S_{2t}(0)$ for these two types of shapes of the coherence function are obtained below.

Square exponential correlated 1st-order coherence: This entails assigning the below form:

$$\langle \epsilon(t)\epsilon^*(t') \rangle = e^{-(t-t')^2/2\tau_c^2} \quad (7.54)$$

where τ_c is the coherence time as defined in section 2.2.2. This form is regarded as a sufficiently good approximation for the nature of the fluctuations present in actual FELs [35, 38]. Using Eq. (7.54), the exact integrals for the expressions of $S_{1t}(\pm\delta_{\pm})$ and $S_{2t}(0)$ are evaluated in Appendix D.1 and given below

$$S_{1t}(\delta) = \tau_{coh} \sqrt{\pi} \langle I(t) \rangle \lambda w\left(\lambda \left(\frac{\chi^* t}{M\tau_p} - \delta\tau_{coh}\right)\right) \quad (7.55a)$$

$$S_{2t}(0) = \tau_{coh} \sqrt{\pi} \frac{\langle I(t) \rangle^2}{2} w\left(\frac{t}{M\tau_p}\right) \quad (7.55b)$$

$$M = \frac{\tau_p}{\tau_{coh}}, \quad \tau_{coh} = \frac{\tau_p \tau_c}{\sqrt{\tau_p^2 + \tau_c^2}} \quad (7.55c)$$

$$\chi = 1 - ik, \quad \lambda = \frac{1}{\sqrt{2(1 + ik/M^2)}} \quad (7.55d)$$

Here $w(z) = e^{z^2}(1 + \text{erf}(z))$ and $\text{erf}(z)$ is the error function. The parameter k is equal to $\frac{1}{\sqrt{3}}$ for FEL pulses. These expressions are very close to a Voigt profile functions [102] which result from the convolution of a Gaussian and Lorentzian function. The Gaussian character is due to the field properties, namely the envelope mean-value time-dependence ($\sim \tau_p$) as well as the coherence time ($\sim \tau_c$). The Lorentzian character is due to the near-resonant effects which consists in it the information about the atomic system and its response to the atomic field via the mean-average detunings $\delta_{\pm}(t)$. If observed closely, these detunings include information only about the mean intensity, $\langle I(t) \rangle$ which means that the Lorentzian character of the lineshape is not influenced by the field fluctuations at all.

M can be seen as a measure of number of random ‘spikes’ in an FEL pulse [35, 38]. It measures the strength of the fluctuations because the inverse of this M -parameter is proportional to the ratio $\langle (\Delta W)^2 \rangle / \langle W \rangle^2$ as seen from ref [35]. Here, $\langle W \rangle$ and $\langle (\Delta W)^2 \rangle$ are the mean and standard deviation of time integrated intensity $W(t)$ respectively. According to the reference [92], this ratio is related to root mean square signal to noise ratio. The physical meaning of M can be well understood when its limiting values are considered. Using Eq. (7.55c) M can be written as

$$M = \sqrt{1 + \frac{\tau_p^2}{\tau_c^2}} \quad (7.56)$$

Eq. (7.56) suggests that minimum value of M is 1. For a fixed pulse duration this is achieved when $\tau_c \rightarrow \infty$. But this $\tau_c \rightarrow \infty$ is the condition of coherent pulse (as was utilised in section 6.2). Therefore, for a partially coherent pulse with finite τ_c , the value of M is greater than 1 and hence is a measure of the degree of coherence [60] or the strength of fluctuations present in the pulse.

When the pulse duration is relatively long i.e., $M \gg 1$ ($\tau_p \gg \tau_c$), then the expressions given by Eq. (7.55a) and Eq. (7.55b) reduce to a simpler form. It can be understood from the form of the mean intensity $e^{-(t/\tau_p)^2}$ that it attains negligible values when $t \sim M\tau_p$. Therefore, one may consider the times of the order of $t \sim \tau_p$ only. Looking at the Eqs. (7.55), the argument of $w(z)$ is $t/M\tau_p + b$, the term $t/M\tau_p \rightarrow 0$ and, hence,

$w(t/M\tau_p + b) \rightarrow w(b)$. This allows a kind of time and frequency factorization in the simplified or approximated expressions for the $S_{1t}(\pm\delta_{\pm})$ and $S_{2t}(0)$ as in:

$$S_{1t}(\delta) \simeq \tau_{coh} \sqrt{\pi} \frac{\langle \mathcal{I}(t) \rangle}{\sqrt{2}} w\left(\frac{-\delta\tau_{coh}}{\sqrt{2}}\right) \quad (7.57a)$$

$$S_{2t}(0) \simeq \tau_{coh} \sqrt{\pi} \frac{\langle \mathcal{I}(t) \rangle^2}{2} . \quad (7.57b)$$

From Eq. (7.57a) it is easier to see the role of the various parameters in the line-shape profile. In the argument of Eq. (7.57a) the smooth time-dependence on the mean intensity is present as seen from Eq. (7.44). So S_{1t} depends on the atomic parameters as well as the smooth mean intensity envelope and the field coherence time τ_{coh} . It should be noted that for $M \gg 1$, $\tau_{coh} \rightarrow \tau_c$. With decreasing τ_{coh} the lineshape takes a Lorentzian shape regardless of the field intensity. In such conditions, the shape of the Lorentzian profile will not contain any direct influence of the field fluctuations statistics; this will depend on the parameters included in the δ_{\pm} mean detunings.

Lorentzian correlated 1st-order coherence. Here, the AC function shape is assumed to be of the form:

$$\langle \epsilon(t)\epsilon^*(t') \rangle = e^{-|t-t'|/2\tau_c} \quad (7.58)$$

For simplicity consider the case of non-chirped pulses i.e., $\chi = 1$ in Eq. (6.5) (chirp can be incorporated, if needed). The corresponding expressions for S_{1t} and S_{2t} are derived in Appendix D.2 and given below:

$$S_{1t}(\delta) = \tau_p \sqrt{\pi} \frac{\langle \mathcal{I}(t) \rangle}{\sqrt{2}} w\left(\frac{\tau_{\delta}}{\sqrt{2}}\right), \quad (7.59a)$$

$$S_{2t}(0) = \tau_p \sqrt{\pi} \frac{\langle \mathcal{I}(t) \rangle^2}{2} w(\tau(0)), \quad (7.59b)$$

$$\tau_{\delta} = \frac{t}{\tau_p} - \left(\frac{1}{2\tau_c} + \delta\right)\tau_p . \quad (7.59c)$$

These also show a Voigt profile shape. Using the asymptotic value of $w(z \gg 1) \rightarrow 1/z\sqrt{\pi}$, the corresponding approximate expressions for longer pulses ($\tau_p \gg \tau_c$) are:

$$S_{1t}(\delta) = \langle \mathcal{I}(t) \rangle \frac{2\tau_c}{1 + 2\delta\tau_c} \quad (7.60a)$$

$$S_{2t}(0) = \langle \mathcal{I}(t) \rangle^2 \tau_c . \quad (7.60b)$$

7.4 Conclusion

A perturbative ensemble averaging method was developed and applied to the stochastic density matrix equations of motion (Eqs. (7.1)) in the Fano picture. For all practical purposes, the resultant deterministic averaged DM-EOMs were obtained after truncating the perturbative cumulant expansion to its second order term. This comprised the inclusion of the intensity correlation term (S_{2t}) along with the field correlation term (S_{1t}). Later

these terms were specified for two kinds of field first order correlation shapes: square exponential and Lorentzian. Approximate forms of these expressions were also derived in the conditions of long-pulses ($\tau_p \gg \tau_c$). These terms were explained as Voigt profiles whose Gaussian character belongs to the field-part and whose Lorentzian character belongs to the atomic-part. This knowledge was established only because of the structure of equations. In contrast, if one considers the averaging methods of the previous chapter, no knowledge was obtained which would help one to either predict the lineshape or understand the role of different atomic/field characteristics. This is one of the important results of the method presented here. Also, it must be noted that unlike in the methods of Chapter 6, the present derivations did not need any decorrelation approximation (DA). In fact, the only constraint for the perturbative averaging is the condition laid on the coherence time by Eq. (7.27). Other than that, the method is valid for any kind of statistical field. Appendix C suggests a way to obtain higher order terms in the perturbative expansion. Depending on the context, one can tailor the approach and even extend it, though mathematically cumbersome, to incorporate the higher orders of statistics of the field into the averaging. In a way the method presented in this chapter is most versatile.

Chapter 8

Helium in 60.16 eV FEL radiation

The previous chapter has, in detail, given a perturbative ensemble averaging theory involving cumulants of the FEL field. An immediate task then would be to apply it to a specific system. The atomic system considered in this chapter is the helium atom. In the following sections, the previously derived deterministic averaged DM-EOMs (Eqs. (7.43) and Eqs. (7.51)) are used to explore the near resonant ionization of helium, via the $2s2p\ ^1P_1$ AIS located around 60.16 eV (above the $1s^2\ ^1S_0$ ground state), by a near resonant FEL radiation.

The set of the atomic parameters used in the calculations, that were obtained in Chapter 5, are given in Table 8.1. The corresponding schematic of the atomic processes is given in Fig. 8.1. The different states and transitions involved are: $|g\rangle$ is the ground state $|1s^2\rangle$, $|a\rangle$ is the bound autoionization state $|2s2p\ ^1P\rangle$, $|c\rangle$ are the $\text{He}^+(1s) + e^-$ continuum states and finally $|c''\rangle$ are the doubly ionized helium states reached by ionization of the $\text{He}^+(1s)$ ground states. From the calculations it was estimated that the ac-Stark shifts of the bound states have negligible contribution into the dynamics compared to the parameters finally kept in the averaged EOMs.

The next part of the chapter is structured as follows:

- Though computationally demanding, the Monte Carlo (MC) method can emulate an experimental scenario. It constitutes a test of accuracy of the averaging method developed in this work. So, first a comparison of the ionization yields obtained via MC and perturbative averaging methods is made.

Parameters	Description	Values
E_g	ground state energy position	0
E_a	resonance energy position	2.211
q_a	Fano-asymmetry parameter	-2.733
d_{ga}	dipole matrix element between $ g\rangle$ and $ a\rangle$	0.0355
Γ_a	autoionization width from $ a\rangle$ to $ c\rangle$	0.00137
γ_g	photoionization width from $ g\rangle$ to $ c\rangle$	0.494
γ_c	photoionization width from $ c\rangle$ to $ c''\rangle$	0.426

Table 8.1: Atomic structure parameters for the He system in a.u.

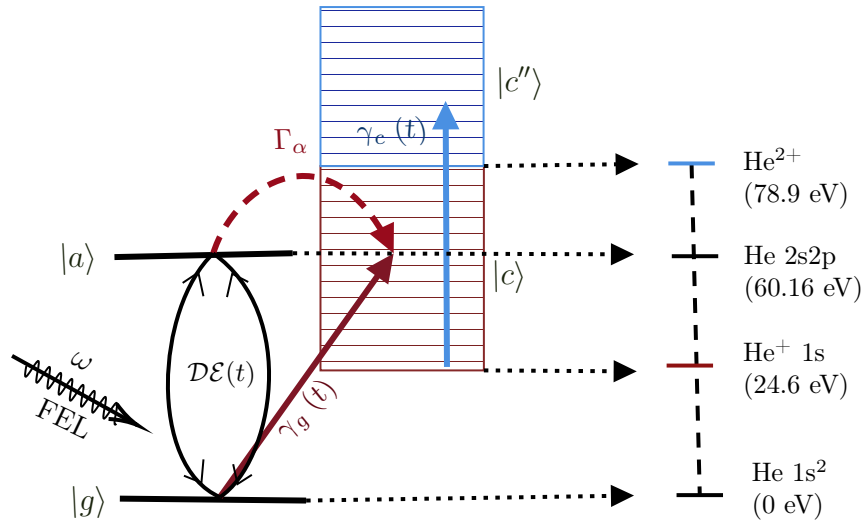


Figure 8.1: Ionization scheme of He in a 60.16 eV FEL radiation. $|g\rangle$ 1s² is the ground state, $|a\rangle$ 2s2p is the auto-ionizing state, $|c\rangle$ is the continuum above the ionized state of He⁺ 1s and the $|c''\rangle$ is the continuum above the ionized state He²⁺. The energies depicted on the right are not to scale but only give an idea of the values of the levels.

- After establishing the strengths and accuracy of the perturbative averaging method, the same is done with the method of Fano-convolution. Though the latter is often used in the weak field excitation case, this comparison shows the averaging method superiority.
- Next, a comparison is made between the approximate and non approximate forms of the $S_{1t}(\pm\delta_\pm)$ and $S_{2t}(0)$ and the former closeness to the latter is also shown. The approximate forms are computationally simpler and hence help reduce the time of calculations.
- The importance of intensity correlation term in the derived averaged DM-EOMs is discussed.
- Given the above comparisons, it is fitting to compare how the perturbative averaging method with the simple averaging method of the previous chapter. This helps in understanding the limitations of the latter and the importance of the former methods.
- This is followed by a comparison of the effects of shapes of AC where it is concluded that a square exponential AC form of a FEL pulse can not be replaced by an exponential AC function.
- Finally, a practical set of parameters are borrowed from a recent FEL experiment and the role of coherence time in affecting the ionization yield lineshape is explored.

8.1 Comparison with the Monte Carlo calculations

8.1.1 Monte Carlo method

Whenever a quantity undergoes random fluctuations, it is often recommended to utilize the *law of Large Numbers* [103]. It states that a repeated estimation of a randomly fluctuating quantity will give close results to the expectation value. This is the fundamental basis of the Monte Carlo approach, which utilizes computers to solve for the expected values of random quantities [104]. In this approach, one generates repeated simulation of the random yield by solving the Eqs. (7.1) and estimating the value of the ion yield via the following, for every shot.

$$Y = 1 - \sigma_{gg}(t) - \sigma_{aa}(t) \quad \text{or} \quad Y = \sigma_{cc}(t) \quad (8.1)$$

The yield thus obtained is averaged over the number of repetitions (N) of pulse shots. Larger N gives better estimate of the effective yield. The final Monte Carlo averaged yield is given by

$$Y_{MC} = \lim_{N \rightarrow \infty} \frac{\sum_{i=1}^N Y_i}{N} \quad (8.2)$$

8.1.2 Comparison

Using the averaging method, not only the computational demands are significantly reduced but a clearer insight of the ionization dynamics under stochastic fields may be obtained. To investigate the validity of the equations, the ionization yields obtained with the perturbatively averaged DM-EOMs are compared against those obtained via the above Monte Carlo (MC) approach. In principle, when the number of the MC trials goes to infinity (in practice this number depends on the problem) one should expect the results between the two calculational methods (MC and averaged equations) to match to a high degree.

When a single FEL pulse, as given in Eq. (3.2b) is used in the aforementioned stochastic DM-EOMs, the obtained yield shape resembles the fluctuating red-solid curve of Fig. 8.2. This noisy shape is due to the FEL fluctuations as depicted in Fig. 3.5 and Fig. 3.6. After an average over $N = 300$ pulse realizations, using Eq. (8.2), the yield profile takes a less noisy shape, resembling the blue-dashed curve of Fig. 8.2. The larger N increases the computational time. For $N = 300$, the trend of the average lineshape is clearly visible. Therefore, $N = 300$ is chosen for the MC calculations. In the same Fig. 8.2, the yield obtained by the rigorously averaged deterministic DM-EOMs is shown which identically fits the average of the MC yield. This is shown as the black-dashed curve. This plot was for a peak intensity of 10^{13} W/cm².

In Fig. 8.3 and Fig. 8.4, the ionization yields obtained from both these methods, for different peak intensities of the pulse are plotted. Figs. 8.3 (a),(b) and (c) show the single ionization yield without including the subsequent ionization step from He⁺ and without considering ionization directly from the AIS state. For this, $\gamma_c = \gamma_a = 0$ have been assumed and calculated for three different peak intensities, 10^{13} W/cm², 10^{14} W/cm²

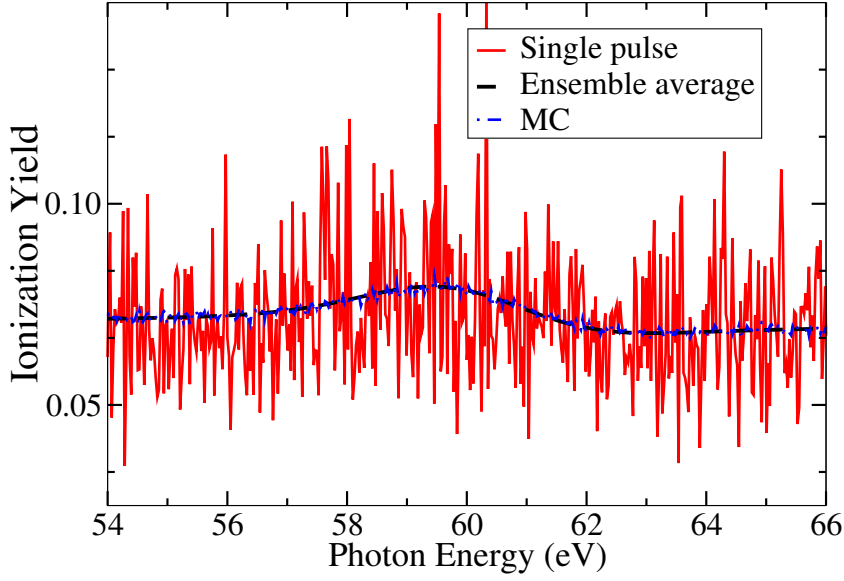


Figure 8.2: Single-ionization yield for one realization of the random pulse (red-solid curve), and its corresponding ensemble average obtained from the averaged EOMs (black-dashed curve) and the MC method (blue-dashed curve and is calculated over 300 pulse realizations). The yields were obtained at the resonance frequency 60.16 eV and for $\tau_p = 7$ fs, $\tau_c = 0.5$ and peak intensity 10^{13} W/cm².

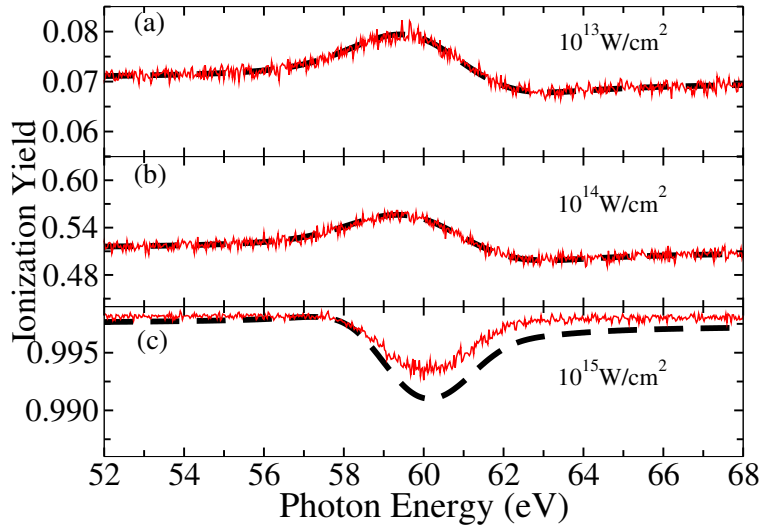


Figure 8.3: Comparison of ionization yields obtained from the Monte Carlo method (red solid curve) and averaged density matrix equations (black dashed curve) for peak intensities of 10^{13} W/cm², 10^{14} W/cm² and 10^{15} W/cm² (top to bottom respectively). $\gamma_c = 0$ a.u. Other parameters are $\tau_p = 7$ fs, $\tau_c = 0.5$ fs ($M = 14$).

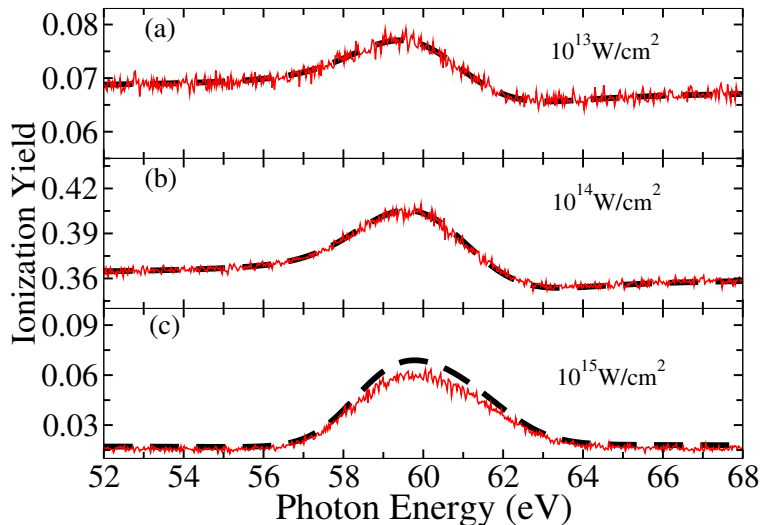


Figure 8.4: Comparison of ionization yields obtained from the Monte Carlo method (red solid curve) and averaged density matrix equations (black dashed curve) for peak intensities of 10^{13} W/cm², 10^{14} W/cm² and 10^{15} W/cm² (top to bottom respectively). $\gamma_c = 0.426$ a.u. Other parameters are $\tau_p = 7$ fs, $\tau_c = 0.5$ fs ($M = 14$).

and 10^{15} W/cm². Simple inspection of the plots shows that for the higher intensity the agreement between the two methods is less satisfactory, especially in the proximity of the resonance. For this highest peak intensity the perturbative terms due to the intensity correlation take the peak values $\gamma_g I_0 \tau_c \sim 0.3$ ($\Gamma_a \tau_c \sim 0.028$) in fair consistency with the conditions of Eq. (7.27). The cumulant perturbative expansion was truncated in the second order which includes the first two coherences functions of the field. So, at this peak intensity the next perturbative term should be included in the averaged equations, but for the intensities currently available at this wavelength and the current purposes of this work it is not vital to include the next term of the expansion.

In an actual experiment, further ionization of the singly-ionized He takes place and a proper treatment requires to take into account the complete set of the density matrix equations. The plots (a), (b) and (c) of the Fig. (8.4) include the ionization channel from He⁺ to He²⁺ ($\gamma_c = 0.436$ a.u. but $\gamma_a = 0$). The first thing to note is the broadened yield around resonance. In contrast, a deterministic (and Fourier-limited) pulse would have developed a sharp asymmetric peak near the resonance energy of 2s2p i.e., 60.16 eV (2.211 a.u.), typical of an AIS resonance with $q = -2.733$ Fano parameter i.e., a lineshape similar to Fig. 5.2. The width of this resonance would reflect the AIS width, Γ_a . In the present case, the fluctuations of the FEL field have smoothed this sharp resonance resulting to a broadened shape.

On another note, in Fig. 8.3 and Fig. 8.4 it can be seen that for lower peak intensities the He⁺ yields obtained for $\gamma_c = 0$ a.u. are close to those when $\gamma_c = 0.426$ a.u. An increase in the yield value from (a) to (b) can be noticed in both the plots. But the same trend is lost in Fig. 8.4 (c). This is due to the enhanced He⁺ generated at times before the pulse

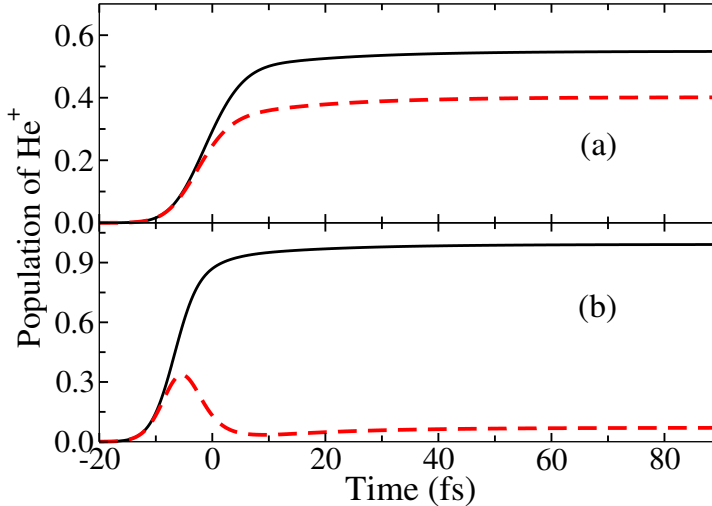


Figure 8.5: Comparison of He^+ yield when its further ionization ($\text{He}^+ \rightarrow \text{He}^{2+}$) is taken into account (red-dashed curves) and when it is not (black-solid curves), for the peak intensities 10^{14} W/cm^2 - (plot (a)) and 10^{15} W/cm^2 - (plot (b)). The yields were obtained at the resonance frequency 60.16 eV and for $\tau_p = 7$ fs, $\tau_c = 0.5$ fs ($M = 14$).

reached its peak value, followed by its quick ionization to He^{2+} . Obviously this is not the case for lower peak intensities where He^+ is generated past the pulse peak. This is shown clearly at the bottom panel of Fig. 8.5 where as soon as the population of He^+ reaches a maximum, it decays rapidly into He^{2+} for the highest peak intensity ($\sim 10^{15}$ W/cm^2); in contrast with what is observed at the upper panel of the same figure, where the He^+ populations develop post the pulse peak value (assumed at $t = 0$).

8.2 Comparison with the Fano-convolution method

In Chapter 7 it was shown that the observables obtained through the ensemble averaging acquire Voigt profile shape. Ref [102] suggests that a convolution of a Gaussian profile with a Fano profile can be expressed in terms of Voigt functions. Therefore, one may think that the obtained yield profiles in the present chapter could also be obtained from the convolution of intensity profile (having a Gaussian form) and the Fano profile. But such approach can not guarantee the accuracy nor give much insights into the ionization dynamics. This can be justified as shown below. The convolution ionization profile can be obtained as,

$$Y(\omega) = \int_{-\infty}^{\infty} d\omega' \overline{\mathcal{I}(\omega')} F(\omega - \omega'), \quad (8.3)$$

where the AIS's Fano profile represented by, $F(\omega) \sim [(q_a + \epsilon_\omega)^2 / (1 + \epsilon_\omega^2) - 1] / (q_a^2 \Gamma_a)$ with $\epsilon_\omega = 2(E_g + \omega - E_a) / \Gamma_a$. With this definition, $F(\omega)$ has as limiting case a Lorentzian shape for $q \rightarrow \infty$. $\overline{\mathcal{I}(\omega)} = \langle |\mathcal{E}(\omega')|^2 \rangle$ represents the obtained ensemble-averaged frequency profile. In Fig. 8.6 this ensemble-averaged spectrum of the FEL intensity is plotted for $\tau_c = 0.5$ fs and $\tau_p = 7$ fs. Around 300 pulses were included in the ensemble averaging. It can be seen that the profile tends to a Gaussian shape. Fitting with a Gaussian envelope the pulse's frequency bandwidth is found to be in line with the theoretical values i.e, 1.31

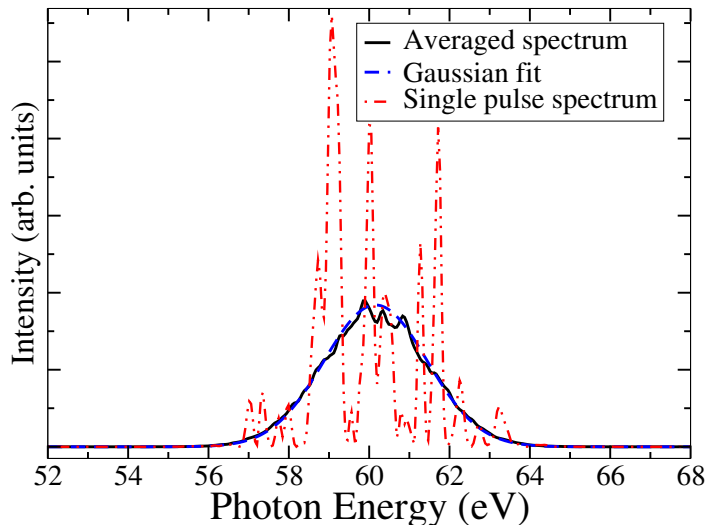


Figure 8.6: Amplitude of intensity profile in frequency domain. The black-solid curve represents the averaged spectrum, blue-dashed curve is its Gaussian fit with a width of ~ 1.31 eV while the red dot-dashed curve is the spectrum corresponding to one of the FEL pulse's single shot realizations.

eV.

In Fig. 8.7 the corresponding MC calculations are shown. The ensemble-averaged profile of the present method is in excellent agreement with the MC calculations while the convolution method leads to a more symmetric profile. It is worth noting here that the convolution profile has been multiplied so as to match the ionization profile produced from the full time-dependent MC and the averaged EOMs equations. For the particular helium AIS where $q_a = -2.733$ the convolution method is expected to produce a peak rather than a dip in the resonance position [102, 105], regardless of the peak intensity. But in Fig. 8.3 (c) a dip was obtained. Therefore, the Fano convolution method is not at all a meaningful one, especially when dealing with fluctuating FELs.

8.3 Validity of the approximate expressions

The next point is about the use of the approximate expressions for the $S_{1t}(\pm\delta_{\pm})$ and $S_{2t}(0)$ quantities, when the correlation time is much shorter than the total pulse duration, $\tau_c \ll \tau_p$ or equivalently $M \gg 1$. However it should be noted beforehand that for practical purposes it was verified that the approximated expressions can be used even for $M > 3$. The approximate forms are simple and give a clear view of the underlying physics as they can be directly related with experimentally measured quantities. Furthermore, unless a very special experimental scheme is studied, the calculated ionization yields are within the current experimental uncertainties compared to those calculated when the exact expressions are used.

In Fig. 8.8, the ionization yields obtained from the full [Eqs. (7.55a),(7.55b)] and approximate [Eqs. (7.57a),(7.57b)] expressions of S_{1t} and S_{2t} , respectively, are shown. The

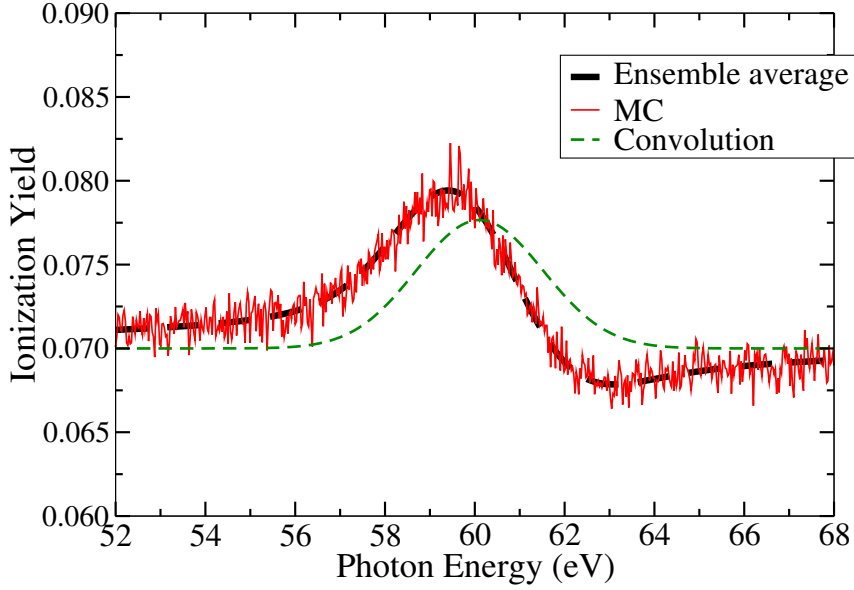


Figure 8.7: He^+ yields using the convolution of the AIS Fano-shape with the averaged pulse profile (green dashed line), Eq. (8.3), the averaged EOMs (black line) and the MC approach (red line). The yields were obtained at the resonance frequency 60.16 eV and for $\tau_p = 7$ fs, $\tau_c = 0.5$ and peak intensity 10^{13} W/cm 2 . The scaling factor for the convolution profile so as to match the other profiles is 80.

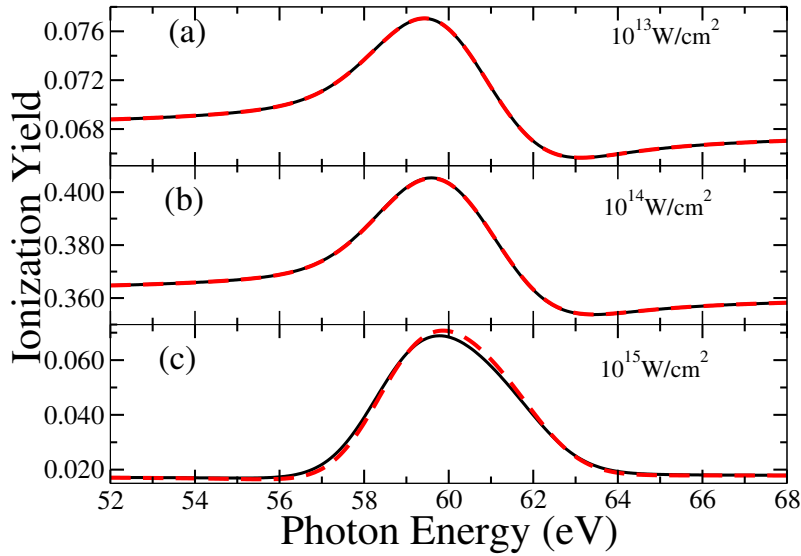


Figure 8.8: Comparison of the ionization yields obtained by approximate (red dashed curve) and non-approximate expressions (black solid curve) for the S_{1t} and S_{2t} terms for the peak intensities of 10^{13} W/cm 2 , 10^{14} W/cm 2 and 10^{15} W/cm 2 from top to bottom, respectively. Gaussian correlation is used and the γ_c channel is included. Other parameters are $\tau_p = 7$ fs, $\tau_c = 0.5$ fs ($M = 14$).

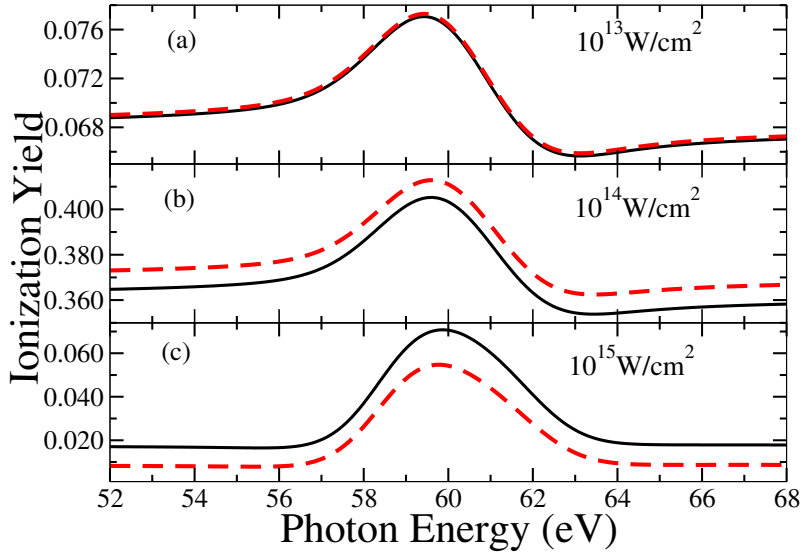


Figure 8.9: Comparison of the ionization yields obtained when the intensity correlation $S_{2t}(0)$ is included (black solid curve) and not included (red dashed curve) in the averaged DM-EOMs equations, for different peak intensities.

plots suggest that for lower intensities, the usage of approximate expressions or non-approximate expressions result in the same yield. For the highest intensity, there is a very slight difference. This clearly shows that, as argued earlier, one can replace the non-approximate expressions of S_{1t} and S_{2t} with the approximated ones, without causing significant disagreement with the experimental data.

8.4 Effects of intensity correlation

The expression $S_{2t}(0)$ shows the effects of intensity correlations. Its effects manifest themselves when the intensity is sufficiently large. In Fig. 8.9 the ionization yield obtained from keeping intact the intensity correlation term $S_{2t}(0)$ and the yield obtained from neglecting the same, for different peak intensities, is plotted. This is achieved by switching the term $S_{2t}(0)$ on and off respectively, in the averaged DM equations. Fig. 8.9 suggests that for lower peak intensity, the intensity correlation has minute effect whereas for medium to higher peak intensities, the intensity correlation term does play a prominent role. This term not only affects the near resonance but the whole line profile.

8.5 Comparison with the simple averaging method

In Chapter 6 a simple averaging method was shown and the case of helium photoionization was explored. It was mentioned in section 6.4 that the method does not include the higher order field correlations and hence may not be suitable for some situations such as those where the intensity fluctuations play a prominent role. Mathematically, the set of

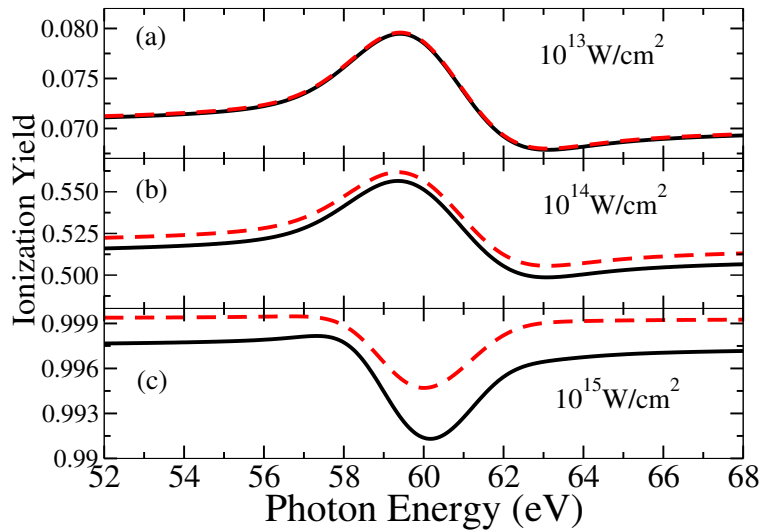


Figure 8.10: Comparison of the ionization yield of helium obtained by perturbative averaging method (black-solid curve) and simple averaging method (red-dashed curve) for the peak intensities of 10^{13} W/cm², 10^{14} W/cm² and 10^{15} W/cm² from top to bottom, respectively. Gaussian correlation is used and the γ_c channel is not included. Other parameters are $\tau_p = 7$ fs, $\tau_c = 0.5$ fs ($M = 14$).

Eqs. (6.21) derived in the Chapter 6 can be derived from the main averaged Eqs. (7.43) of Chapter 7 when in the latter, $S_{2t}(0) \rightarrow 0$ and $S_{1t}(\delta_{\pm}) \rightarrow S_{1t}(\delta_-)$. This clearly shows that the method of averaging of Chapter 6 does not include full statistical information.

To see how differently both the procedures affect the observable, a comparison is made here between the ionization yields obtained from simple averaging approach of the previous chapter and the perturbative averaging approach of this chapter. As the simple method only includes one channel of ionization, the same is maintained for the other method as well i.e., $\gamma_a = \gamma_c = 0$. Rest of the field parameters are kept the same i.e., $\tau_p = 7$ fs and $\tau_c = 0.5$ fs and the AC function of the field is chosen to be square-exponential as the focus of observation is regarding the FEL interactions.

In Fig. 8.10 this comparison is shown. From (a) to (c) peak intensity of the FEL pulse is increased. It can be seen that for lower peak intensity, the difference is minute. But as the peak intensity increases, the difference between the yield profiles obtained from both the methods is vividly different. Not only the peak around resonance is different, but also the whole profile seems to change and shift. This is a direct consequence of the effect of the intensity correlation term explored before along with the structure of the field correlation integral as well.

This shows that the simpler method does not give a complete picture of the photoionization dynamics. Thus, when dealing with high intense FELs it is the perturbative method that needs to be used as it can cater for the higher order fluctuations present in the field which manifest themselves via intensity correlation functions.

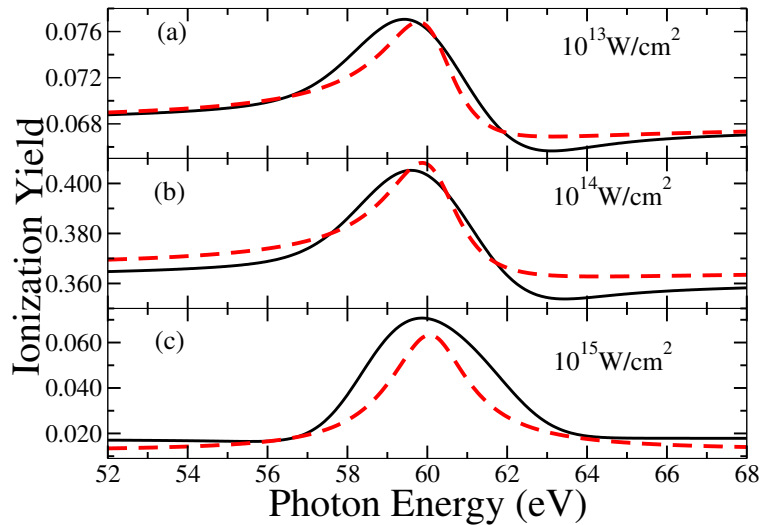


Figure 8.11: Comparison of ionization yields obtained from the Gaussian correlation (black solid curve) and Lorentzian correlation (red dashed curve) for peak intensities of 10^{13} W/cm^2 , 10^{14} W/cm^2 and 10^{15} W/cm^2 (top to bottom respectively). The figures (a), (b) and (c) are obtained when the area under the $g_1(\tau)$ is kept the same for both the correlations. $\tau_{\text{Gauss}} = 0.5 \text{ fs}$ and $\tau_{\text{Lorentz}} = 0.31 \text{ fs}$.

8.6 Effects of the field AC shape:

It is easily shown that a stationary (or nearly stationary) field of an exponentially-correlated coherence function has a Lorentzian-like power spectrum whereas for a square-exponentially dependent coherence function the spectrum is Gaussian. The goal is to see how the field AC function affects the AIS lineshape. Two scenarios are considered here: (i) the area under the $g_1(\tau)$ curve is kept the same for both Lorentz and Gaussian shapes, which results in their correlation times being different and (ii) when their correlation times τ_c are the same. In Figs. 8.11 (a)(b)(c) and 8.12 (a)(b)(c) the yields obtained from scenario-(i) and scenario-(ii) are shown. In both scenarios, the γ_c channel is included and the approximated expressions for the correlation: $S_{1t}(\delta_{\pm})$ and $S_{2t}(0)$, are used. From top to bottom, the peak intensity increases from 10^{13} W/cm^2 to 10^{15} W/cm^2 .

For the plots Fig. 8.11 (a)(b)(c), it is seen that the peaks of yields obtained from both the shapes are of similar order whereas that of the plots Fig. 8.12 (a)(b)(c) have different peak values. There is a notable difference in the yield profile around the resonance region which can be attributed exclusively to the choice of the AC temporal dependence. The Lorentzian correlation gives a narrower shape of the yield whereas the Gaussian correlation gives a relatively broader shape of the yield. The tails almost match or tend to match, but at resonance the difference is strongly seen. In either scenarios, it is clearly observed that the yields do not match. It was earlier seen that a Gaussian correlated field of averaged method matches that of the MC approach. In conjunction with that conclusion, the present mismatch of the different AC-shaped yields suggests that one can not replace a FEL field, which inherently has Gaussian shaped first order coherence function, with a field having

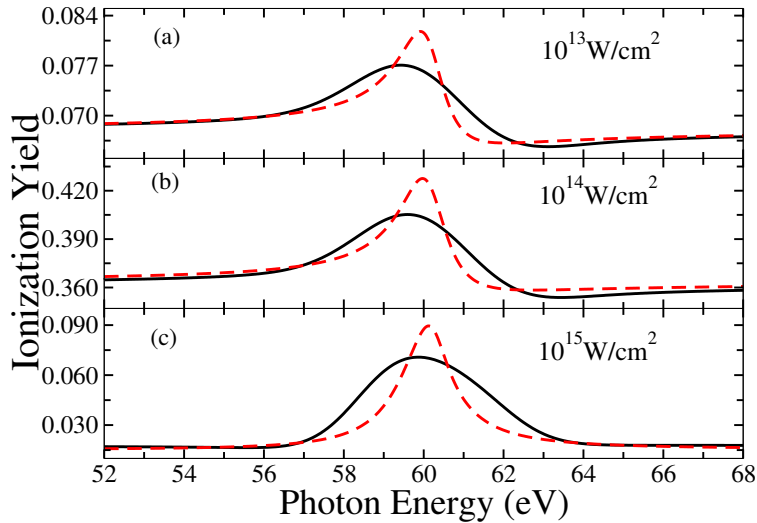


Figure 8.12: Comparison of ionization yields obtained from the Gaussian correlation (black solid curve) and Lorentzian correlation (red dashed curve) for peak intensities of 10^{13} W/cm^2 , 10^{14} W/cm^2 and 10^{15} W/cm^2 (top to bottom respectively). The figures (a), (b) and (c) are obtained when the correlation time $\tau_c = 0.5 \text{ fs}$ is maintained the same.

Lorentzian shaped first order coherence function.

8.7 Effects of τ_c

As the accuracy of the perturbative averaging technique has already been established in the previous sections, one may now consider a practical scenario. Take the parameters utilised in one of the recent experiments performed at Free-Electron Laser in Hamburg (FLASH) on helium atom [49]. The central frequency varied around $\sim 60.10 \text{ eV}$ with a bandwidth of 0.4 eV . The pulse duration was approximately 75 fs (FWHM). Converting these parameters to the present framework, one obtains $\tau_p \approx 45 \text{ fs}$ and $\tau_c \approx 4 \text{ fs}$. The coherence time of the pulse satisfies the criteria for low coherence time ($\tau_c \ll \tau_p$). Incorporating these into the averaged DM-EOMs, the effects of different coherence times of the FEL field on the AIS lineshape are investigated.

In Fig. (8.13), the ionization yield obtained for various correlation times varying around the experimental value and a peak intensity of 10^{13} W/cm^2 is plotted. It is seen that, as the correlation time decreases the yield value at the resonance position drops and the AIS lineshape becomes broader. As τ_c is in indirect proportion to the laser bandwidth, a decrease in the correlation time of the field implies an increase in the laser bandwidth which manifests as the broadening of the AIS lineshape; so the broadening effect is compensated by the drop of the resonance peak. As, at the tails of the yield, the values are quite constant it is concluded that the coherence time effects are manifested mainly around the resonance peak. This behaviour is also consistent with the behaviour of S_{1t} in Eq. (7.57a) where towards smaller τ_c the line-shape gradually broadens at the wings following a Lorentzian-

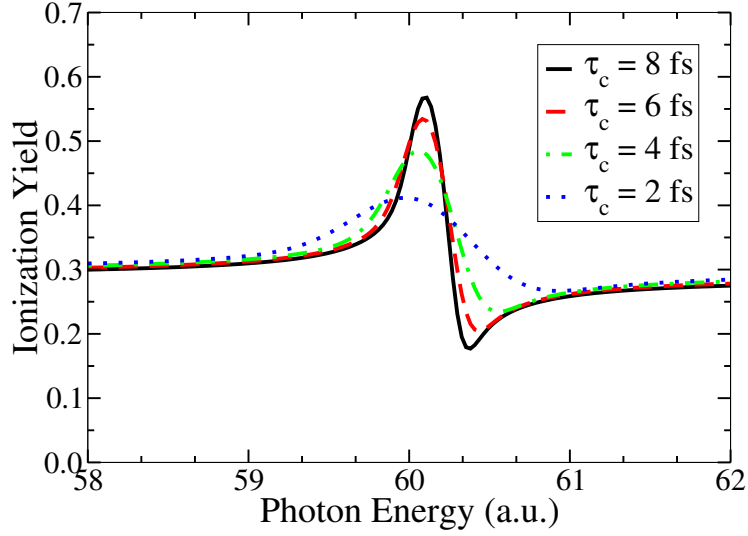


Figure 8.13: Comparison of the ionisation yield obtained by using Gaussian form of the field's autocorrelation function at 10^{13} W/cm^2 for different coherence times τ_c : 2 fs (black-curve), 4 fs (red-curve), 6 fs (green-curve) and 8 fs (blue-curve). At resonance, the yield is highest for the longest coherence time and it gradually decreases as the τ_c is decreased. The pulse duration used is $\tau_p = 45 \text{ fs}$.

like trend.

8.8 Conclusion

In this chapter, the previously derived averaged DM-EOMs were applied to the system of intense FEL interacting with a helium atom near the 2s2p AIS. The perturbative ensemble averaging method's superiority over the Monte Carlo approach and the Fano-convolution method was shown. The accuracy and the validity of the approximate expressions of the S_{1t} and S_{2t} terms were discussed. The vital role of the intensity correlation term (towards higher peak intensities), which is missing from the existing ensemble averaging methods, was discussed. The earlier chapter simple averaging methods being a subset of the previous chapter perturbative ensemble averaging method was also shown. The influence of the statistical part of the FEL i.e., the effects of AC-shape, was investigated. A practical set of parameters were borrowed from a recent FEL experiment and the role of coherence time on the ionization yield was explored.

Chapter 9

Li⁺ in 150.2 eV FEL radiation

In the previous chapter it was established that the approximate form of S_{1t} and S_{2t} is enough to obtain almost accurate results. The approximation also helps in simplifying the mathematical complexity and lets one see clearly the role of different parameters involved. The goal then would be to restructure the derived DM-EOMs by utilising the approximate form of the said terms and explicitly externalise the field parameters.

Slightly changing the definition of the detuning, in reference to Eq. (7.44), as

$$\hat{\delta}_{\pm}(t) = \delta_0 \pm i \frac{\Gamma_a - \gamma_g \langle \mathcal{I}(t) \rangle}{2}. \quad (9.1)$$

and the function $w(z)$ as

$$w(z) = e^{-z^2} [1 - \operatorname{erf}(iz)] = U(x, y) + iV(x, y), \quad z = x - iy, \quad (9.2)$$

where $\operatorname{erf}(z)$ is the error function and $U(z) = U(x, y)$, $V(z) = U(x, y)$ are quantities which are closely related to the Voigt functions i.e., as the real (Re) and imaginary (Im) part of $w(z)$ [106], and utilising the Fano-picture relation $4|d_{ga}|^2 = q_a^2 \Gamma_a \gamma_g$ (Eq. (5.16)), one finally arrives at the following set of averaged density matrix EOMs in the Fano representation,

$$\begin{aligned} \langle \dot{\sigma}_{gg}(t) \rangle = & -\gamma_g \langle \mathcal{I}(t) \rangle \left[1 - \gamma_g \tau_c \sqrt{\pi} \frac{\langle \mathcal{I}(t) \rangle}{2} + \frac{\Gamma_a \tau_c \sqrt{\pi}}{2\sqrt{2}} \left[(q_a^2 - 1) U\left(\frac{\hat{\delta}_- \tau_c}{\sqrt{2}}\right) \right. \right. \\ & \left. \left. + 2q_a V\left(\frac{\hat{\delta}_- \tau_c}{\sqrt{2}}\right) \right] \right] \langle \sigma_{gg}(t) \rangle + (q_a^2 + 1) \frac{\Gamma_a \gamma_g \tau_c \sqrt{\pi} \langle \mathcal{I}(t) \rangle}{2\sqrt{2}} U\left(\frac{\hat{\delta}_+ \tau_c}{\sqrt{2}}\right) \langle \sigma_{aa}(t) \rangle \end{aligned} \quad (9.3a)$$

$$\begin{aligned} \langle \dot{\sigma}_{aa}(t) \rangle = & -\Gamma_a \left[1 + \frac{\gamma_g \tau_c \sqrt{\pi} \langle \mathcal{I}(t) \rangle}{2\sqrt{2}} \left[(q_a^2 - 1) U\left(\frac{\hat{\delta}_+ \tau_c}{\sqrt{2}}\right) - 2q_a V\left(\frac{\hat{\delta}_+ \tau_c}{\sqrt{2}}\right) \right] \right] \langle \sigma_{aa}(t) \rangle \\ & + (q_a^2 + 1) \frac{\Gamma_a \gamma_g \tau_c \sqrt{\pi} \langle \mathcal{I}(t) \rangle}{2\sqrt{2}} U\left(\frac{\hat{\delta}_- \tau_c}{\sqrt{2}}\right) \langle \sigma_{gg}(t) \rangle \end{aligned} \quad (9.3b)$$

$$\begin{aligned} \langle \dot{\sigma}_{cc}(t) \rangle = & -\gamma_c \langle \mathcal{I}(t) \rangle \langle \sigma_{cc}(t) \rangle - \langle \dot{\sigma}_{gg}(t) \rangle - \langle \dot{\sigma}_{aa}(t) \rangle \\ & + \gamma_c \tau_c \sqrt{\pi} \frac{\langle \mathcal{I}(t) \rangle^2}{2} (\gamma_c \langle \sigma_{cc}(t) \rangle - \gamma_g \langle \sigma_{gg}(t) \rangle) \end{aligned} \quad (9.3c)$$

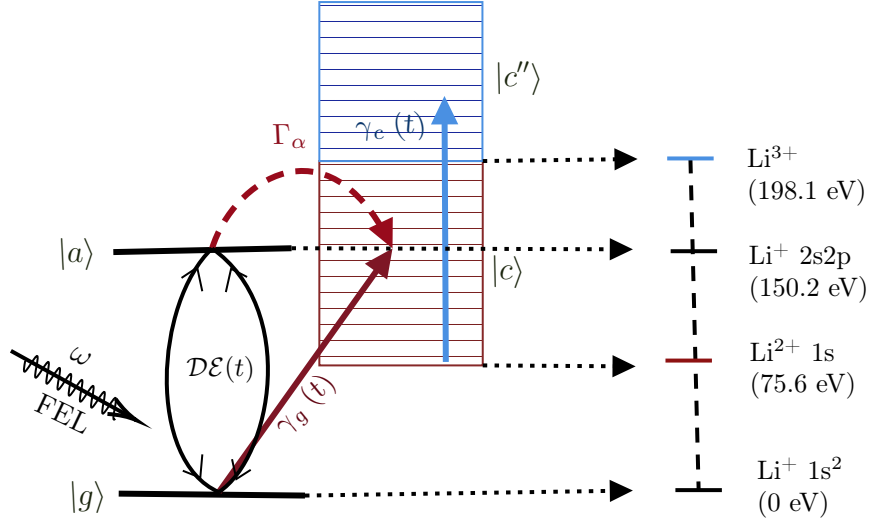


Figure 9.1: Ionization scheme of Li^+ in a 150.2 eV FEL radiation. $|g\rangle$ $1s^2$ is the ground state, $|a\rangle$ $2s2p$ is the auto-ionizing state, $|c\rangle$ is the continuum above the ionized state of Li^{2+} $1s$ and the $|c''\rangle$ is the continuum above the ionized state Li^{3+} . The energies depicted on the right are not to scale but only give an idea of the values of the levels.

After achieving the above restructured equations, they are applied to a new system, namely the lithium ion Li^+ in a 150.2 eV FEL radiation. The schematic of the interaction and atomic levels involved are given in Fig. 9.1. Specifically, the ground-state $|g\rangle$ ($1s^2$) is considered to be at $E_g = 0$ eV (0 a.u.) and the FEL pulse central frequency ω is chosen near the resonance energy of $|a\rangle$ ($2s2p$). The system ionizes into the continuum $|c\rangle$ (ionization potential at 75.6 eV (2.778 a.u.)) characterised by the field-dependent photoionization width $\gamma_g(t)$. After following a photon absorption by the field, the system may also excite to the unstable doubly excited auto-ionizing state $|a\rangle$ ($E_a = 150.2$ eV (5.52 a.u.)) with a rate characterized by the field dependent Rabi matrix element $\mathcal{D}\mathcal{E}(t)$ coupled with continuum $|c\rangle$. The interference between these two ionizing channels is described by the introduction of the Fano-parameter $q_a = -2.2$. Finally, the generated Li^{2+} may further ionize by absorbing one more photon. This ionization width is characterised as $\gamma_c(t)$.

The atomic structure calculations follow the procedure laid in Chapter 5. From the calculations it was estimated that the ac-Stark shifts of the bound states and the direct photoionization from the doubly excited state have negligible contribution into dynamics compared to the parameters finally kept in the averaged EOMs. The atomic structure parameter values are given in the Table 9.1. The calculated atomic parameters are in good agreement with those measured in references [107–109].

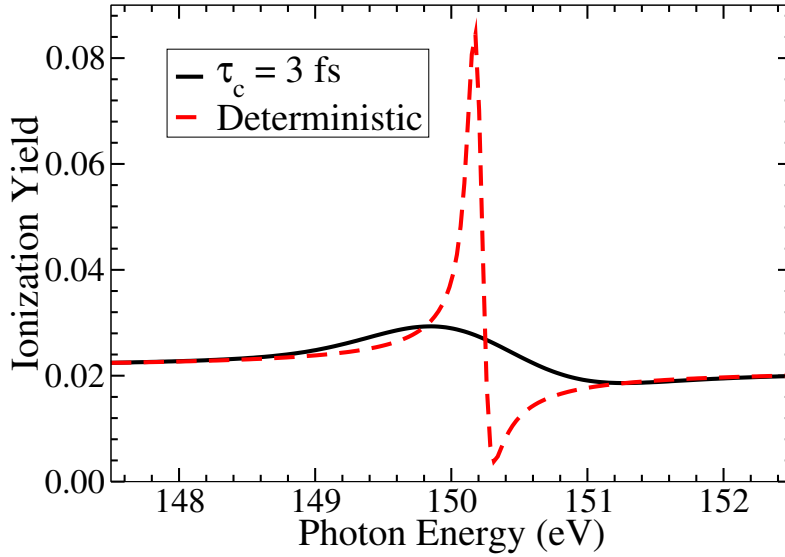


Figure 9.2: The effect of smoothing the familiar Fano-profile, caused by averaging the fluctuations can be clearly seen in this figure. The red-dashed curve with highest peak is obtained for a deterministic pulse whereas the black-solid curve is obtained for a stochastic pulse with coherence time of 1.3 fs (53.74 a.u.). The peak intensity is 10^{13} W/cm² and the pulse duration $\tau_p = 12.7$ fs (525.02 a.u.).

Parameters	Description	Values
E_g	ground state energy position	0
E_a	resonance energy position	5.52
q_a	Fano-asymmetry parameter	-2.2
d_{ga}	dipole matrix element between $ g\rangle$ and $ a\rangle$	0.01527
Γ_a	autoionization width from $ a\rangle$ to $ c\rangle$	0.00235
γ_g	photoionization width from $ g\rangle$ to $ c\rangle$	0.0819
γ_c	photoionization width from $ c\rangle$ to $ c''\rangle$	0.0584

Table 9.1: Atomic structure parameters for the Li^+ system in a.u.

In the previous chapter, for helium, the study was concentrated on the accuracy of the averaging approach and the effects of fluctuations on the ionization yield line shape. In this section, for lithium ion, the focus of observation will be of the effects of the pulse parameters such as pulse duration and coherence time, on the ionization yield profile. Combining the results of the previous and the present chapters, a totality of knowledge is gained as to the way of averaging and the effects of random FELs on AIS lineshapes via the averaging.

9.1 The AIS lineshape

A check is needed if the AIS lineshape is following the trend of the previous chapters. For a pulse of moderate intensity, free of fluctuations in the amplitude and the phase,

the AIS lineshape of $\text{Li}^+ 2s2p$ should also resemble that of the familiar asymmetric Fano profile [42] as in Fig. 5.2. It was earlier seen that the fluctuations cause a smoothing effect of such sharp asymmetric line shape. Solving Equation (7.1) for a deterministic pulse, gives the ionization yield profile depicted by the red-dashed curve of the Figure 9.2, whereas solving Equation (9.3) for a Gaussian correlated stochastic pulse, having a coherence time of $\tau_c = 1.3$ fs (53.74 a.u.), gives the ionization yield profile depicted by the black-solid curve of the Fig 9.2. The peak intensity used is 10^{13} W/cm² and the pulse duration used is $\tau_p = 12.7$ fs (525.02 a.u.).

It can be seen that for the same pulse duration and peak intensity one obtains drastically different yield values and lineshapes. The deterministic pulse gives the profile which has a sharp peak and asymmetry around the resonance energy whereas the stochastic pulse gives a smooth peak. The values of the ionization yield are also very different around the resonance but are identical towards the tail-ends. It can be thus concluded that the effects of fluctuations manifest and smooths the lineshape around the resonance, whereas the tail-ends are relatively unaffected.

9.2 Effects of the coherence time

For the Gaussian pulse the coherence time which is decisive for the ionization dynamics is considered here. In Fig 9.3, a choice of four values for τ_c , 1.3 fs, 3.3 fs, 5.3 fs and 7.3 fs (53.74 a.u., 136.42 a.u., 219.1 a.u. and 301.78 a.u., correspondingly) is made. It can be seen that as coherence time increases, the ionization yield around the resonance increases which is accompanied by a narrowing of the AIS lineshape. Ideally, for very large τ_c , these lineshapes tend towards an asymmetric Fano-shape. This trend can be clearly seen here. It can also be observed that the effects of coherence time manifest itself only around the resonance. Towards the tail ends, the effects are negligible and the yield values are fairly constant.

9.3 Effects of the pulse duration

Since the pulse duration determines the interaction time with the system it is reasonable to expect that the longer the pulse the larger the ionization yield (this might not be the case under special resonance conditions). Here, the role of pulse duration in affecting the ionization yield for different peak intensities is explored.

Figs 9.4, (a)(b)(c) are for intensities of 10^{13} W/cm², 10^{14} W/cm² and 10^{15} W/cm² respectively. For (a) and (b) the trend is that, as pulse duration increases, the yield also increases. But for (c), this trend is reversed. As the peak intensity increases, the yield values decrease. This reversing of the behavior is due to the extra channel of ionization of Li^{2+} from $|c\rangle \rightarrow |c''\rangle$ which is rapidly active at higher peak intensities that is, as peak intensity increases, the population of $|c\rangle$ decreases and the system ionizes into $|c''\rangle$. The same is true with increasing pulse duration as well. That is why, at the highest peak intensity, the ionization yield values are low for the largest pulse duration and high for the

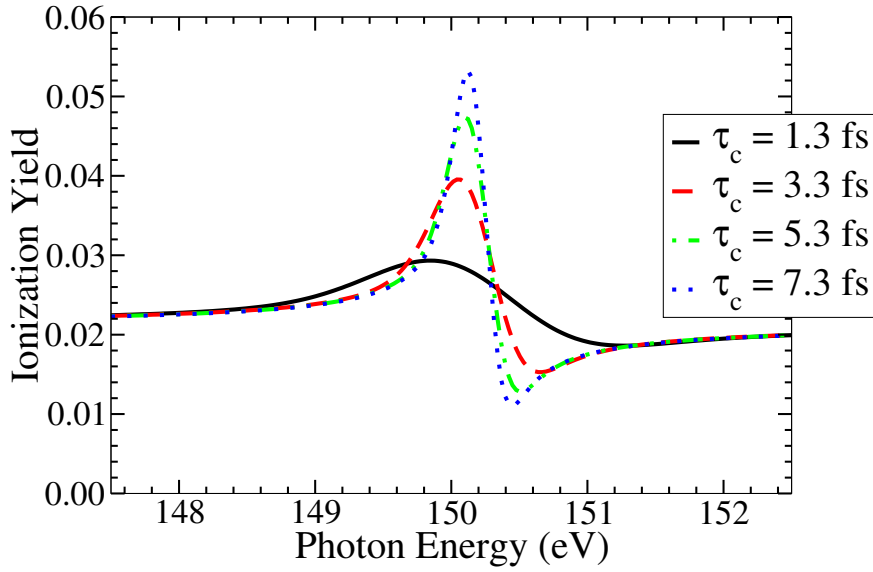


Figure 9.3: Effect of coherence time on the ionization yield. As τ_c increases, the ionization yield also increases, near resonance. The peak intensity is 10^{13} W/cm² and the pulse duration $\tau_p = 12.7$ fs (525.02 a.u.).

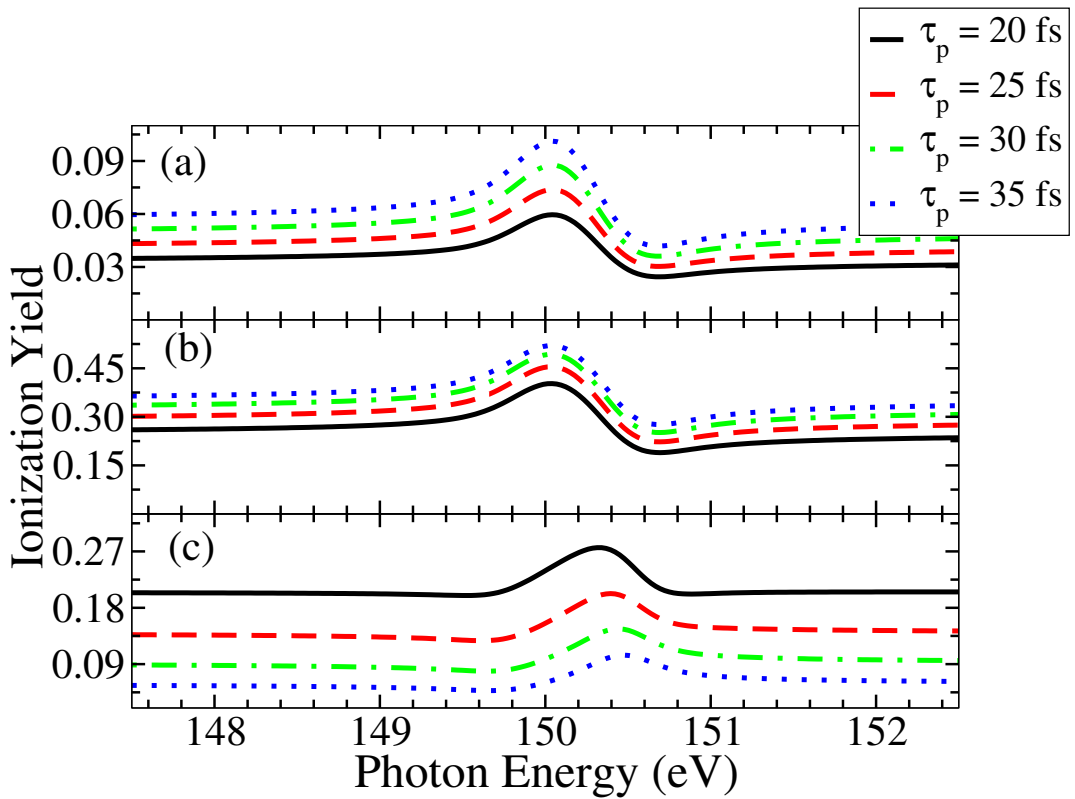


Figure 9.4: Effect of pulse duration on the ionization yield. The coherence time used is $\tau_c = 3$ fs (124.02 a.u.) and the peak intensities are: 10^{13} W/cm² for (a), 10^{14} W/cm² for (b) and 10^{15} W/cm² for (c).

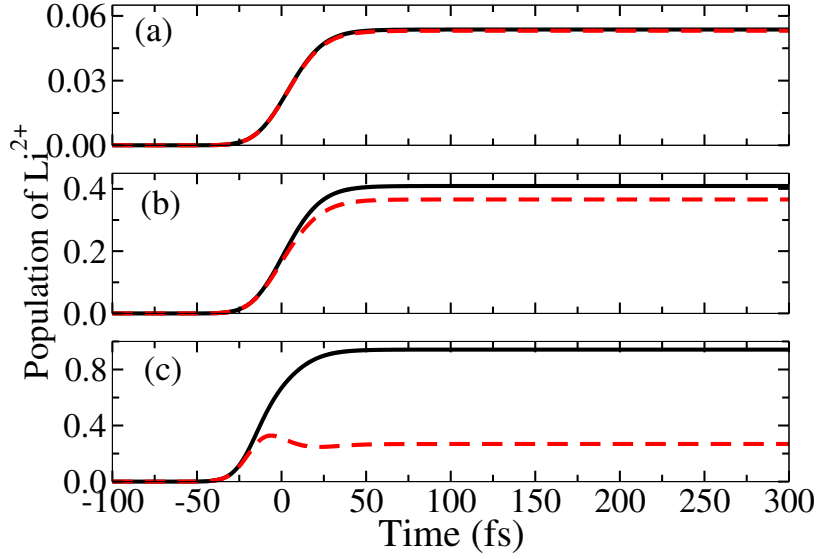


Figure 9.5: Effect of peak intensity on the population of Li^{2+} . The peak intensities used are: 10^{13} W/cm² for (a), 10^{14} W/cm² for (b) and 10^{15} W/cm² for (c). Black-solid curve is when the further ionization channel is ignored ($\gamma_c = 0$) and the red-dashed curve is when the further ionization channel is considered. The pulse duration $\tau_p = 20$ fs (826.8 a.u.) and the coherence time $\tau_c = 3$ fs (124.02 a.u.).

smallest pulse duration.

To understand this behavior, one may have to explore the time-evolution of the population of Li^{2+} . In Fig 9.5, a plot of the population of Li^{2+} in time for various peak intensities is given. The black-solid curve is for the situation when the additional channel of ionization is not considered ($\gamma_c = 0$ a.u.) whereas the red-dashed curve is for the current situation where the said channel is present. In the former case, the expected behaviour, namely that by increasing the τ_p increases the ionization yield applies; the plots (a) and (b) depict the rise of populations even after the peak of the pulse (at $t = 0$ fs) has hit the system. In contrast, for the highest peak intensity, the population of Li^{2+} reaches a maximum before the peak of the pulse and the same population starts to decrease as pulse evolves. This clearly drops the ionization yield values which is the cause for the aforementioned trend-change in Figure 9.4.

9.4 Conclusion

The interaction of intense FEL pulses with lithium ion near 2s2p AIS was explored in this chapter mainly concentrating on the field's parameters such as pulse duration and coherence time. First, the smoothing effects on the resonant Fano asymmetric lineshape by the fluctuating FEL is shown. Later it was shown that the coherence time, which characterises the field's coherence properties, affects the lineshape near the resonance peak. The effects of pulse duration on the yield shape was also discussed. It was shown that the

usual trend of pulse duration increasing the doubly ionized lithium yield is reversed at the highest peak intensity due to an increase in its further photoionization.

Chapter 10

Summary and outlook

10.1 Overall summary

The thesis is aimed at theoretically understanding the near resonant photoionisation processes of atomic/ionic systems when driven by fluctuating XUV FEL fields. The path to achieve this goal was chosen to be stochastic averaging techniques. The widely used Monte Carlo approach is time consuming, computationally demanding and does not offer any perspective into the nature of the dynamics. A new method developed should be able to quickly predict the outcome of an experiment including a set of suggestion in regard of the effects of different experimentally accessible entities. This has been the main driver for the choice of a stochastic averaging approach which fares better than the MC approach in many ways.

To this end, a rigorous cumulant based perturbative method was developed and shown to be of high value. The path leading to this chapter started with a topic on basic terminology related to a statistical field. An example of chaotic light was given to better understand these terms. Later, the model of FEL simulated and used in the MC approach was presented with all the fundamental definitions in line with the statistical terms previously explored. It was shown that the simulated FEL was in line with the theoretical prescriptions. It is this FEL that was input into the MC method and resulted in the fluctuating lineshape. Having laid the foundations on the statistical field part, the next step in the path was to develop an interface that helps one to study the nature of light-matter interaction dynamics. To this end a set of density matrix equations of motion were developed for a simple helium-like system, under Fano-picture, after having explored first a two-level prototype. The developed equations need certain parametric values to be calculated for a meaningful solution to be achieved. Therefore a chapter was dedicated to give a brief account on how the associated parameters, such as matrix elements, widths, resonance position, etc., are calculated. After having tread the steps until now, one is ready to dive into the main problem. One chapter gave a simpler approach of averaging - to primarily estimate the profile shape and the like. But there were many limitations that were pointed out. This lead to the heart of the thesis - the perturbative averaging of DM-EOMs using a cumulant based approach. This chapter developed a set of deterministic DM-EOM which are valid for wide verity of statistical fields with the only constraint of low coherence time.

The method was applied to helium atom and lithium ionic systems in the later chapters to explore the influence of the stochastic field and atomic part on the ionization yield line shape.

Though the Chapter 7 is thorough, there are still some developments needed to get a better insight into the interaction dynamics. The corresponding line of thought is presented below.

10.2 Outlook - Future work

There are a number of other statistical aspects of the atom/FEL radiation interactions which necessitate further study in order to identify more comprehensively the role of the fluctuations in the ionization process. First, possible improvements of the averaging procedure needs to be investigated; one such alternative is based on the atomic physics projection-operator method, but now applied to stochastic problems, also leading to averaged equations for the density matrix elements, known as Nakajima-Zwanzig equation [110, 111]; nevertheless this equation has a non-Markovian structure which implies knowledge of the average density matrix at all previous times is needed, $\langle\sigma(t')\rangle, t' < t$ and not only at one-time, $\langle\sigma(t)\rangle$ as the Markov-type derived equation Eq. (7.33).

Along similar lines it is needed to improve the developed method in order to drop the assumption of τ_c as the shortest characteristic time. Another route would be to provide a method where higher-order terms of the perturbative expansion can be calculated more automatically and efficiently for arbitrary FEL fields without the need to invoke the Gaussian statistics requirement; this will allow to model a larger class of problems than those that can be treated with the present method. Finally, an alternative direction is to deal with problems where the statistics of the system's density matrix itself (beyond its average) is required; this calls for two-time averages of the type $\langle\sigma(t)\sigma(t')\rangle$ to be calculated; the method presented in this work, can be also applied for such averages to be calculated, but within the limitations of the short-correlation time, τ_c .

The exploration of this line of thought can be extended not only to the ionization yield or population calculations, but also to obtain photoelectron spectra, transient absorption spectra, photoelectron angular distributions, etc. Recently Ott et al [49], revealed the effects of FEL fluctuations on the absorption spectra of helium around the resonant frequency of circa 60.10 eV in one of their research articles. In another recent research article, L Aufleger et al [112], reported some of the effects of pulse duration of an intense SASE XUV fields on the transient absorption spectroscopy involving 2s2p AIS of helium atom. The present theory or the to be extended version in the above lines of thought can be used to study the effects of FEL fluctuations and its parameters on the absorption lineshape and see how it fares with the aforementioned findings.

The perturbative theory of averaging can also be extended to other atomic systems such as Argon and so one can compare the simulated electron energy spectra or the angular distributions with the experimental results obtained by S. Augustin et al, [113]. So, there are already some nice experiments performed which the theory can better test its

special status in effectively predicting the associated results as well as with the increasing demand in the future experiments on similar lines of probing an atom with FEL, the theory developed here (including its potential for future developments) can act as a foreground in giving further insights and help shape the experimental design if need be. Being computationally fast, the theory also replaces the widely used MC approaches which has been generally the favoured theoretical approach in the study of FEL interactions up to now [29, 31].

Bibliography

- [1] G. S. Agarwal. “Field-Correlation Effects in Multiphoton Absorption Processes”. In: *Phys. Rev. A* 1 (5 May 1970), pp. 1445–1459. DOI: 10.1103/PhysRevA.1.1445.
- [2] A. T. Georges and P. Lambropoulos. “Saturation and Stark splitting of an atomic transition in a stochastic field”. In: *Phys. Rev. A* 20 (3 Sept. 1979), pp. 991–1004. DOI: 10.1103/PhysRevA.20.991.
- [3] P Zoller. “Stark shifts and resonant multiphoton ionisation in multimode laser fields”. In: *Journal of Physics B: Atomic and Molecular Physics* 15.17 (Sept. 1982), pp. 2911–2933. DOI: 10.1088/0022-3700/15/17/023.
- [4] J. H. Eberly, K. Wódkiewicz, and B. W. Shore. “Noise in strong laser-atom interactions: Phase telegraph noise”. In: *Phys. Rev. A* 30 (5 Nov. 1984), pp. 2381–2389. DOI: 10.1103/PhysRevA.30.2381.
- [5] DAVID ATTWOOD ANNE SAKDINAWAT. *X-Rays and Extreme Ultraviolet Radiation. Principles and Applications*. Cambridge University Press, 2016.
- [6] Peter W. Milonni and Joseph H. Eberly. *Laser Physics*. John Wiley and Sons, Inc., 2010.
- [7] H. Wabnitz et al. “Multiple ionization of atom clusters by intense soft X-rays from a free-electron laser”. In: *Nature* 420.6915 (Dec. 2002), pp. 482–485. ISSN: 1476-4687. DOI: 10.1038/nature01197.
- [8] W. Ackermann et al. “Operation of a free-electron laser from the extreme ultraviolet to the water window”. In: *Nature Photonics* 1.6 (June 2007), pp. 336–342. ISSN: 1749-4893. DOI: 10.1038/nphoton.2007.76.
- [9] L. Young et al. “Femtosecond electronic response of atoms to ultra-intense X-rays”. In: *Nature (London)* 466 (2010), pp. 56–61. DOI: [https://DOI.org/10.1038/nature09177](https://doi.org/10.1038/nature09177).
- [10] E A Seddon et al. “Short-wavelength free-electron laser sources and science: a review”. In: *Reports on Progress in Physics* 80.11 (Oct. 2017), p. 115901. DOI: 10.1088/1361-6633/aa7cca.
- [11] C. Pellegrini. “The history of X-ray free-electron lasers”. In: *The European Physical Journal H* 37.5 (Oct. 2012), pp. 659–708. ISSN: 2102-6467. DOI: 10.1140/epjh/e2012-20064-5.

-
- [12] J Feldhaus. “FLASH—the first soft x-ray free electron laser (FEL) user facility”. In: *Journal of Physics B: Atomic, Molecular and Optical Physics* 43.19 (Sept. 2010), p. 194002. DOI: 10.1088/0953-4075/43/19/194002.
- [13] G Geloni et al. “Coherence properties of the European XFEL”. In: *New Journal of Physics* 12.3 (Mar. 2010), p. 035021. DOI: 10.1088/1367-2630/12/3/035021.
- [14] M.V. Yurkov Evgeny Saldin E.V. Schneidmiller. *The Physics of Free Electron Lasers*. Springer-Verlag Berlin Heidelberg, 2000.
- [15] John Costello, Eugene Kennedy, and Lampros Nikolopoulos. “Short wavelength free electron lasers”. In: *Journal of Modern Optics* 63.4 (2016), pp. 285–287. DOI: 10.1080/09500340.2016.1131431.
- [16] E Allaria et al. “The FERMI free-electron lasers”. In: *Journal of synchrotron radiation* 22.3 (May 2015), pp. 485–491. ISSN: 0909-0495. DOI: 10.1107/S1600577515005366.
- [17] K Tiedtke et al. “The soft x-ray free-electron laser FLASH at DESY: beamlines, diagnostics and end-stations”. In: *New Journal of Physics* 11.2 (Feb. 2009), p. 023029. DOI: 10.1088/1367-2630/11/2/023029.
- [18] L Fang et al. “Probing ultrafast electronic and molecular dynamics with free-electron lasers”. In: *Journal of Physics B: Atomic, Molecular and Optical Physics* 47.12 (June 2014), p. 124006. DOI: 10.1088/0953-4075/47/12/124006. URL: <https://doi.org/10.1088/0953-4075/47/12/124006>.
- [19] N.G Van Kampen. “Stochastic differential equations”. In: *Physics Reports* 24.3 (1976), pp. 171–228. ISSN: 0370-1573. DOI: [https://DOI.org/10.1016/0370-1573\(76\)90029-6](https://DOI.org/10.1016/0370-1573(76)90029-6).
- [20] Athanasios Papoulis and S. UnniKrishna Pilai. *Probability, Random Variables and Stochastic Processes*. McGraw-Hill, 2002.
- [21] M. Lax, W. Cai, and M. Xu. *Random Processes in Physics and Finance*. Oxford University Press, 2006.
- [22] Greg Pavliotis and A. Stuart. *Multiscale Methods*. 53. Springer-Verlag New York, 2008. ISBN: 978-1-4419-2532-9. DOI: 10.1007/978-0-387-73829-1.
- [23] Nina Rohringer and Robin Santra. “Resonant Auger effect at high x-ray intensity”. In: *Phys. Rev. A* 77 (5 May 2008), p. 053404. DOI: 10.1103/PhysRevA.77.053404.
- [24] L. A. A. Nikolopoulos, T. J. Kelly, and J. T. Costello. “Theory of ac Stark splitting in core-resonant Auger decay in strong x-ray fields”. In: *Phys. Rev. A* 84 (6 Dec. 2011), p. 063419. DOI: 10.1103/PhysRevA.84.063419.
- [25] D.P.W. Middleton and L.A.A. Nikolopoulos. “Effects of autoionising states on the single and double ionisation yields of neon with soft X-ray fields”. In: *Journal of Modern Optics* 59.19 (2012), pp. 1650–1663. DOI: 10.1080/09500340.2012.737481. eprint: <https://DOI.org/10.1080/09500340.2012.737481>.
-

-
- [26] G. M. Nikolopoulos and P. Lambropoulos. “Effects of free-electron-laser field fluctuations on the frequency response of driven atomic resonances”. In: *Phys. Rev. A* 86 (3 Sept. 2012), p. 033420. DOI: 10.1103/PhysRevA.86.033420.
- [27] George Mouloudakis and Peter Lambropoulos. “Effects of field fluctuations on driven autoionizing resonances”. In: *The European Physical Journal D* 72.12 (Dec. 2018), p. 226. ISSN: 1434-6079. DOI: 10.1140/epjd/e2018-90303-8.
- [28] E L Saldin, E A Schneidmiller, and M V Yurkov. “Statistical and coherence properties of radiation from x-ray free-electron lasers”. In: *New Journal of Physics* 12.3 (Mar. 2010), p. 035010. DOI: 10.1088/1367-2630/12/3/035010.
- [29] Nina Rohringer and Robin Santra. “Resonant Auger effect at high x-ray intensity”. In: *Phys. Rev. A* 77 (5 May 2008), p. 053404. DOI: 10.1103/PhysRevA.77.053404.
- [30] Sang-Kil Son and Robin Santra. “Monte Carlo calculation of ion, electron, and photon spectra of xenon atoms in x-ray free-electron laser pulses”. In: *Phys. Rev. A* 85 (6 June 2012), p. 063415. DOI: 10.1103/PhysRevA.85.063415. URL: <https://link.aps.org/doi/10.1103/PhysRevA.85.063415>.
- [31] Henry I. B. Banks, Antonis Hadjipittas, and Agapi Emmanouilidou. “Auger cascades leading to higher charged states in xenon driven by an X-ray free-electron-laser pulse”. In: *The European Physical Journal D* 74.5 (May 2020), p. 98. DOI: 10.1140/epjd/e2020-100416-6.
- [32] Russel E. Caflisch. “Monte Carlo and quasi-Monte Carlo methods”. In: *Acta Numerica* 7 (1998), pp. 1–49. DOI: 10.1017/S0962492900002804.
- [33] DANIEL M. TARTAKOVSKY, ALBERTO GUADAGNINI, and MONICA RIVA. “Stochastic averaging of nonlinear flows in heterogeneous porous media”. In: *Journal of Fluid Mechanics* 492 (2003), pp. 47–62. DOI: 10.1017/S002211200300538X.
- [34] N. A. Papadogiannis et al. “On the feasibility of performing non-linear autocorrelation with attosecond pulse trains”. In: *Applied Physics B* 76.7 (July 2003), pp. 721–727. ISSN: 1432-0649. DOI: 10.1007/s00340-003-1179-6.
- [35] S. Krinsky and Y. Li. “Statistical analysis of the chaotic optical field from a self-amplified spontaneous-emission free-electron laser”. In: *Phys. Rev. E* 73 (6 June 2006), p. 066501. DOI: 10.1103/PhysRevE.73.066501.
- [36] S. O. Rice. “Mathematical analysis of random noise”. In: *The Bell System Technical Journal* 23.3 (1944), pp. 282–332. DOI: 10.1002/j.1538-7305.1944.tb00874.x.
- [37] M.V. Yurkov Evgeny Saldin E.V. Schneidmiller. *The Physics of Free Electron Lasers*. Springer-Verlag Berlin Heidelberg, 2000.
- [38] Kwang-Je Kim, Zhirong Huang, and Ryan Lindberg. *Synchrotron Radiation and Free-Electron Lasers*. Cambridge University Press, 1st Ed., 2017.
- [39] William T. Vetterling William H. Press Saul A. Teukolsky and Brian P. Flannery. *Numerical Recipes in C: The Art of Scientific Computing*. Cambridge University Press, 2002.
-

-
- [40] E.L. Saldin, E.A. Schneidmiller, and M.V. Yurkov. “Statistical properties of radiation from VUV and X-ray free electron laser”. In: *Optics Communications* 148.4 (1998), pp. 383–403. ISSN: 0030-4018. DOI: [https://doi.org/10.1016/S0030-4018\(97\)00670-6](https://doi.org/10.1016/S0030-4018(97)00670-6).
- [41] John von Neumann. *Mathematical Foundations of Quantum Mechanics*. Princeton, NJ: Princeton University Press, 2018.
- [42] U. Fano. “Effects of Configuration Interaction on Intensities and Phase Shifts”. In: *Phys. Rev.* 124 (6 Dec. 1961), pp. 1866–1878. DOI: [10.1103/PhysRev.124.1866](https://doi.org/10.1103/PhysRev.124.1866).
- [43] P. Lambropoulos and P. Zoller. “Autoionizing states in strong laser fields”. In: *Phys. Rev. A* 24 (1 July 1981), pp. 379–397. DOI: [10.1103/PhysRevA.24.379](https://doi.org/10.1103/PhysRevA.24.379).
- [44] Emil Wolf. *Introduction to the Theory of Coherence and Polarization of Light*. Cambridge University Press, 2007.
- [45] Rodney Loudon. *The Quantum Theory of Light*. 3rd ed. Oxford University Press, 2000. ISBN: 9780198501763.
- [46] MALVIN CARL TEICH BAHAA E. A. SALEH. *FUNDAMENTALS OF PHOTONICS*. JOHN WILEY and SONS, INC., 1991.
- [47] M. Siano et al. “Characterizing temporal coherence of visible synchrotron radiation with heterodyne near field speckles”. In: *Phys. Rev. Accel. Beams* 20 (11 Nov. 2017), p. 110702. DOI: [10.1103/PhysRevAccelBeams.20.110702](https://doi.org/10.1103/PhysRevAccelBeams.20.110702).
- [48] S. Roling et al. “Temporal and spatial coherence properties of free-electron-laser pulses in the extreme ultraviolet regime”. In: *Phys. Rev. ST Accel. Beams* 14 (8 Aug. 2011), p. 080701. DOI: [10.1103/PhysRevSTAB.14.080701](https://doi.org/10.1103/PhysRevSTAB.14.080701).
- [49] Christian Ott et al. “Strong-Field Extreme-Ultraviolet Dressing of Atomic Double Excitation”. In: *Phys. Rev. Lett.* 123 (16 Oct. 2019), p. 163201. DOI: [10.1103/PhysRevLett.123.163201](https://doi.org/10.1103/PhysRevLett.123.163201).
- [50] Makina Yabashi, Hitoshi Tanaka, and Tetsuya Ishikawa. “Overview of the SACLA facility”. In: *Journal of Synchrotron Radiation* 22.3 (May 2015), pp. 477–484. DOI: [10.1107/S1600577515004658](https://doi.org/10.1107/S1600577515004658).
- [51] Kiyoshi Ueda. “X-ray Free-Electron Laser”. In: *Applied Sciences* 8.6 (May 2018), p. 879. ISSN: 2076-3417. DOI: [10.3390/app8060879](https://doi.org/10.3390/app8060879).
- [52] Marc Gregoire Peter Van Weert. *C++ Standard Library Quick Reference*. Apress, 2016.
- [53] Eduard Prat et al. “A compact and cost-effective hard X-ray free-electron laser driven by a high-brightness and low-energy electron beam”. In: *Nature Photonics* (Nov. 2020). ISSN: 1749-4893. DOI: [10.1038/s41566-020-00712-8](https://doi.org/10.1038/s41566-020-00712-8).
- [54] Christopher Milne et al. “SwissFEL: The Swiss X-ray Free Electron Laser”. In: *Applied Sciences* 7.7 (July 2017), p. 720. ISSN: 2076-3417. DOI: [10.3390/app7070720](https://doi.org/10.3390/app7070720). URL: <http://dx.doi.org/10.3390/app7070720>.
-

-
- [55] Thomas Tschentscher et al. “Photon Beam Transport and Scientific Instruments at the European XFEL”. In: *Applied Sciences* 7.6 (June 2017), p. 592. ISSN: 2076-3417. DOI: 10.3390/app7060592. URL: <http://dx.doi.org/10.3390/app7060592>.
- [56] Shore B W. *Manipulating Quantum Structures Using Laser Pulses*. Cambridge University Press, 2011.
- [57] David Petrosyan Peter Lambropoulos. *Fundamentals of Quantum Optics and Quantum Information*. 1st ed. Springer-Verlag Berlin Heidelberg, 2007.
- [58] Karl Blum. *Density Matrix Theory and Applications*. 3rd ed. Springer-Verlag Berlin Heidelberg, 2012.
- [59] D. Ter Haar. “Theory and applications of the density matrix”. In: *Reports on Progress in Physics* 24 (1961), pp. 304–362.
- [60] Lampros A A Nikolopoulos. *Elements of Photoionization Quantum Dynamics Methods*. 2053-2571. Morgan & Claypool Publishers, 2019. ISBN: 978-1-68174-712-5. DOI: 10.1088/2053-2571/aaf10d.
- [61] Maximilian A. Schlosshauer. *Decoherence and the Quantum-To-Classical Transition*. 1st ed. Springer-Verlag Berlin Heidelberg, 2007.
- [62] A D Bandrauk, F Fillion-Gourdeau, and E Lorin. “Atoms and molecules in intense laser fields: gauge invariance of theory and models”. In: *Journal of Physics B: Atomic, Molecular and Optical Physics* 46.15 (July 2013), p. 153001. DOI: 10.1088/0953-4075/46/15/153001.
- [63] Martin Schechter. *Operator Methods in Quantum Mechanics*. Elsevier North Holland, 1981.
- [64] Robert D. Cowan. *THE THEORY OF ATOMIC STRUCTURE AND SPECTRA*. University of California Press Berkeley and Los Angeles, California, 1981.
- [65] Kenneth M. Watson Marvin L. Goldberger. *Collision Theory*. JOHN WILEY & SONS. Inc., 1964.
- [66] N B Delone and Vladimir P Krainov. “AC Stark shift of atomic energy levels”. In: *Physics-Uspekhi* 42.7 (July 1999), pp. 669–687. DOI: 10.1070/pu1999v042n07abeh000557.
- [67] L.A.A. Nikolopoulos. “A package for the ab-initio calculation of one- and two-photon cross sections of two-electron atoms, using a CI B-splines method”. In: *Computer Physics Communications* 150.2 (2003), pp. 140–165. ISSN: 0010-4655. DOI: [https://doi.org/10.1016/S0010-4655\(02\)00684-7](https://doi.org/10.1016/S0010-4655(02)00684-7).
- [68] William Hanks. “Multi-photon Cross Section of Helium-like Ions Under Soft XUV Fields”. MSc Thesis. Dublin City University: School of Physical Sciences, 2017.
- [69] William Hanks, John Costello, and Lampros Nikolopoulos. “Two- and Three-Photon Partial Photoionization Cross Sections of Li^+ , Ne^{8+} and Ar^{16+} under XUV Radiation”. In: *Applied Sciences* 7.3 (Mar. 2017), p. 294. ISSN: 2076-3417. DOI: 10.3390/app7030294.
-

-
- [70] H Bachau et al. “Applications of B-splines in atomic and molecular physics”. In: *Reports on Progress in Physics* 64.12 (Nov. 2001), pp. 1815–1943. DOI: 10.1088/0034-4885/64/12/205.
- [71] A. Riera. “A simple example to introduce continuum discretization”. In: *American Journal of Physics* 59.1 (1991), pp. 62–64. DOI: 10.1119/1.16688.
- [72] B. H. Bransden and C. J. Joachain. *Physics of Atoms and Molecules*. Longman Scientific and Technical, 1990.
- [73] L.A.A. Nikolopoulos. “A package for the ab-initio calculation of one- and two-photon cross sections of two-electron atoms, using a CI B-splines method”. In: *Computer Physics Communications* 150.2 (2003), pp. 140–165. ISSN: 0010-4655. DOI: [https://doi.org/10.1016/S0010-4655\(02\)00684-7](https://doi.org/10.1016/S0010-4655(02)00684-7).
- [74] Harry D. Morgan and David L. Ederer. “Photoionization cross section of helium for photon energies 59-67 eV: The $(sp, 2n+)^1P^o$ Rydberg series of autoionizing resonances”. In: *Phys. Rev. A* 29 (4 Apr. 1984), pp. 1901–1906. DOI: 10.1103/PhysRevA.29.1901.
- [75] J. B. West, G. V. Marr, and George William Series. “The absolute photoionization cross sections of helium, neon, argon and krypton in the extreme vacuum ultraviolet region of the spectrum”. In: *Proceedings of the Royal Society of London. A. Mathematical and Physical Sciences* 349.1658 (1976), pp. 397–421. DOI: 10.1098/rspa.1976.0081.
- [76] T. N. Chang and X. Tang. “Photoionization of two-electron atoms using a nonvariational configuration-interaction approach with discretized finite basis”. In: *Phys. Rev. A* 44 (1 July 1991), pp. 232–238. DOI: 10.1103/PhysRevA.44.232.
- [77] R. P. Madden and K. Codling. “Two-Electron Excitation States in Helium.” In: *Astrophysical Journal* 141 (Feb. 1965), p. 364. DOI: 10.1086/148132.
- [78] A Bordenave-Montesquieu et al. “Analysis of the 2s21S, 2p21D and 2s2p1P autoionizing levels of helium, in proton-helium collisions”. In: *Journal of Physics B: Atomic and Molecular Physics* 6.10 (Oct. 1973), pp. 1997–2009. DOI: 10.1088/0022-3700/6/10/016.
- [79] Kwong T. Chung and Brian F. Davis. “Helium 2s2p $^1P^o$ energy with relativistic corrections”. In: *Phys. Rev. A* 31 (2 Feb. 1985), pp. 1187–1188. DOI: 10.1103/PhysRevA.31.1187.
- [80] H Kossmann, B Krassig, and V Schmidt. “New determination of Beutler-Fano parameters for the 3s3p1P1resonance in helium”. In: *Journal of Physics B: Atomic, Molecular and Optical Physics* 21.9 (May 1988), pp. 1489–1497. DOI: 10.1088/0953-4075/21/9/009.
- [81] R Gersbacher and J T Broad. “Resonances in helium photoionisation”. In: *Journal of Physics B: Atomic, Molecular and Optical Physics* 23.3 (Feb. 1990), pp. 365–384. DOI: 10.1088/0953-4075/23/3/008.
-

-
- [82] P. Lambropoulos, P. Maragakis, and Jian Zhang. “Two-electron atoms in strong fields”. In: *Physics Reports* 305.5 (1998), pp. 203–293. ISSN: 0370-1573. DOI: [https://doi.org/10.1016/S0370-1573\(98\)00027-1](https://doi.org/10.1016/S0370-1573(98)00027-1).
- [83] Frank E. Harris George B. Arfken and Hans J. Weber. *Mathematical Methods for Physicists*. Academic Press, Elsevier, 2012.
- [84] P Agostini et al. “Saturation effects in resonant three-photon ionisation of sodium with a non-monochromatic field”. In: *Journal of Physics B: Atomic and Molecular Physics* 11.10 (May 1978), pp. 1733–1747. DOI: 10.1088/0022-3700/11/10/011.
- [85] Ryogo Kubo. “Generalized Cumulant Expansion Method”. In: *Journal of the Physical Society of Japan* 17.7 (July 1962), pp. 1100–1120. DOI: 10.1143/JPSJ.17.1100.
- [86] P. Tzallas et al. “Direct observation of attosecond light bunching”. In: *Nature* 426.6964 (Nov. 2003), pp. 267–271. ISSN: 1476-4687. DOI: 10.1038/nature02091.
- [87] P. Tzallas et al. “Second-order autocorrelation measurements of attosecond XUV pulse trains”. In: *Journal of Modern Optics* 52.2-3 (2005), pp. 321–338. DOI: 10.1080/09500340412331301533.
- [88] R. Moshhammer et al. “Second-order autocorrelation of XUV FEL pulses via time resolved two-photon single ionization of He”. In: *Opt. Express* 19.22 (Oct. 2011), pp. 21698–21706. DOI: 10.1364/OE.19.021698.
- [89] Joachim Ullrich, Artem Rudenko, and Robert Moshhammer. “Free-Electron Lasers: New Avenues in Molecular Physics and Photochemistry”. In: *Annual Review of Physical Chemistry* 63.1 (2012). PMID: 22404584, pp. 635–660. DOI: 10.1146/annurev-physchem-032511-143720.
- [90] Andréa Le Marec et al. “Evidence of partial temporal coherence effects in the linear autocorrelation of extreme ultraviolet laser pulses”. In: *Opt. Lett.* 41.14 (July 2016), pp. 3387–3390. DOI: 10.1364/OL.41.003387.
- [91] Armin Azima et al. “Direct measurement of the pulse duration and frequency chirp of seeded XUV free electron laser pulses”. In: *New Journal of Physics* 20.1 (Jan. 2018), p. 013010. DOI: 10.1088/1367-2630/aa9b4c.
- [92] J. W. Goodman. *Statistical Optics*. John Wiley and Sons, 1985. Chap. 6, p. 239.
- [93] M. Schubert and B. Wilhelmi. *Nonlinear optics and quantum electronics*. 1986.
- [94] P Avan and C Cohen-Tannoudji. “Two-level atom saturated by a fluctuating resonant laser beam. Calculation of the fluorescence spectrum”. In: *Journal of Physics B: Atomic and Molecular Physics* 10.2 (Feb. 1977), pp. 155–170. DOI: 10.1088/0022-3700/10/2/006.
- [95] P. Lambropoulos and P. Zoller. “Autoionizing states in strong laser fields”. In: *Phys. Rev. A* 24 (1 July 1981), pp. 379–397. DOI: 10.1103/PhysRevA.24.379.
-

-
- [96] L. A. A. Nikolopoulos, Takashi Nakajima, and P. Lambropoulos. “Influence of the helium autoionization structures on the single/double ionization signal”. In: *The European Physical Journal D - Atomic, Molecular, Optical and Plasma Physics* 20.2 (2002), pp. 297–304. DOI: [10.1140/epjd/e2002-00135-x](https://doi.org/10.1140/epjd/e2002-00135-x).
- [97] A.T. Georges and P. Lambropoulos. “Aspects of Resonant Multiphoton Processes”. In: ed. by L. Marton and C. Marton. Vol. 54. *Advances in Electronics and Electron Physics*. Academic Press, 1980, pp. 191–240. DOI: [https://doi.org/10.1016/S0065-2539\(08\)60099-2](https://doi.org/10.1016/S0065-2539(08)60099-2).
- [98] Claude Cohen-Tannoudji, Jacques Dupont-Roc, and Gylbert Grynberg. *Atom-Photon Interactions, Basic Processes and Applications*. John Wiley and Sons, 1977. ISBN: 0-471-29336-9.
- [99] Tom M. Apostol. *Calculus, Vol. 1: One-Variable Calculus with an Introduction to Linear Algebra*. 2nd ed. New York: John Wiley & Sons, 1967. Chap. 5, p. 202.
- [100] Greg Pavliotis and A. Stuart. *Multiscale Methods*. 53. Springer-Verlag New York, 2008. ISBN: 978-1-4419-2532-9. DOI: [10.1007/978-0-387-73829-1](https://doi.org/10.1007/978-0-387-73829-1).
- [101] Jack H. Freed. “Generalized Cumulant Expansions and Spin-Relaxation Theory”. In: *The Journal of Chemical Physics* 49.1 (1968), pp. 376–391. DOI: [10.1063/1.1669833](https://doi.org/10.1063/1.1669833).
- [102] S. Schippers. “Analytical expression for the convolution of a Fano line profile with a gaussian”. In: *Journal of Quantitative Spectroscopy and Radiative Transfer* 219 (2018), pp. 33–36. ISSN: 0022-4073. DOI: <https://doi.org/10.1016/j.jqsrt.2018.08.003>.
- [103] Sheldon Ross. *A First Course in Probability Theory*. 8th ed. Prentice Hall Press, 2010.
- [104] Taimre T Kroese D Brereton T and Botev Z. “Why the Monte Carlo method is so important today”. In: *WIREs Computational Statistics* 6.6 (June 2014), pp. 386–392. DOI: [0.1002/wics.1314](https://doi.org/10.1002/wics.1314).
- [105] Jan M Rost et al. “Resonance parameters of photo doubly excited helium”. In: *Journal of Physics B: Atomic, Molecular and Optical Physics* 30.21 (Nov. 1997), pp. 4663–4694. DOI: [10.1088/0953-4075/30/21/010](https://doi.org/10.1088/0953-4075/30/21/010). URL: <https://doi.org/10.1088/0953-4075/30/21/010>.
- [106] *NIST Digital Library of Mathematical Functions*. <http://dlmf.nist.gov/>, Release 1.0.27 of 2020-06-15. F. W. J. Olver, A. B. Olde Daalhuis, D. W. Lozier, B. I. Schneider, R. F. Boisvert, C. W. Clark, B. R. Miller, B. V. Saunders, H. S. Cohl, and M. A. McClain, eds.
- [107] S Diehl et al. “New high-resolution measurements of doubly excited states of Li⁺”. In: *Journal of Physics B: Atomic, Molecular and Optical Physics* 32.17 (Aug. 1999), pp. 4193–4207. DOI: [10.1088/0953-4075/32/17/305](https://doi.org/10.1088/0953-4075/32/17/305).
-

-
- [108] Jean-Paul Mosnier et al. “The photoabsorption spectrum of laser-generated Li⁺ in the 60-190 eV photon energy range”. In: *Journal of Physics B: Atomic, Molecular and Optical Physics* 33.22 (Nov. 2000), pp. 5203–5214. DOI: 10.1088/0953-4075/33/22/320.
- [109] S W J Scully et al. “Doubly excited resonances in the photoionization spectrum of Li⁺: experiment and theory”. In: *Journal of Physics B: Atomic, Molecular and Optical Physics* 39.18 (Sept. 2006), pp. 3957–3968. DOI: 10.1088/0953-4075/39/18/024.
- [110] Sadao Nakajima. “On Quantum Theory of Transport Phenomena: Steady Diffusion”. In: *Progress of Theoretical Physics* 20.6 (Dec. 1958), pp. 948–959. ISSN: 0033-068X. DOI: 10.1143/PTP.20.948.
- [111] Robert Zwanzig. “Ensemble Method in the Theory of Irreversibility”. In: *The Journal of Chemical Physics* 33.5 (1960), pp. 1338–1341. DOI: 10.1063/1.1731409.
- [112] L Aufleger et al. “Pulse length effects on autoionizing states under the influence of intense SASE XUV fields”. In: *Journal of Physics B: Atomic, Molecular and Optical Physics* 53.23 (Nov. 2020), p. 234002. DOI: 10.1088/1361-6455/abbe2d.
- [113] S. Augustin et al. “Signatures of autoionization in the angular electron distribution in two-photon double ionization of Ar”. In: *Phys. Rev. A* 98 (3 Sept. 2018), p. 033408. DOI: 10.1103/PhysRevA.98.033408.
- [114] N.G. Van Kampen. *Stochastic Processes in Physics and Chemistry*. Elsevier Science B.V. Amsterdam, 1992.

Appendix A

Laplace transform and pole approximation

A.1 Laplace transform and its inverse

An operator acts on a function and gives another function of same variable whereas a transform acts on a function of one independent variable and gives another function of a different independent variable.

$$\mathbf{Function:} \hat{A}f_1(x) = f_2(x)$$

$$\mathbf{Transform:} \mathcal{T}[f_1(x)] = F(\epsilon)$$

Laplace Transform (LT) of a function $f(t)$, where ‘ t ’ is a real variable (in the context of DM-EOMs it is the time variable), is another function $F(s)$, where ‘ s ’ is in general a complex entity $s = a + \imath b$. Inverse Laplace transform reverts the effects of the former transformation. It involves a complex integration over a line parallel to the imaginary part of s -plane which acts as the boundary to all the singularities of the $F(s)$ i.e., there does not exist any singularity to the right of the line $a = a_0$. These both definitions are given below and the diagrammatic understanding of the inverse transform is given in Fig. A.1.

$$\mathcal{L}[f(t)] = F(s) = \int_0^{\infty} e^{-st} f(t) dt \quad (\text{A.1})$$

$$\mathcal{L}^{-1}[F(s)] = f(t) = \frac{1}{2\pi\imath} \int_{L_1} e^{st} F(s) ds = \frac{1}{2\pi\imath} \lim_{b \rightarrow \infty} \int_{a-\imath b}^{a+\imath b} e^{st} F(s) ds \quad (\text{A.2})$$

A.2 Pole approximation

The goal is to prove the identity of Eq. (4.29). First, let it be written in a simple form with the understanding that the integration is carried out with the limits which contain the relevant pole.

$$\lim_{\eta \rightarrow +0} \int dx \frac{f(x)}{x + \imath\eta} = \mathcal{P} \int dx \frac{f(x)}{x} - \imath\pi \int dx \delta(x) f(x) \quad (\text{A.3})$$

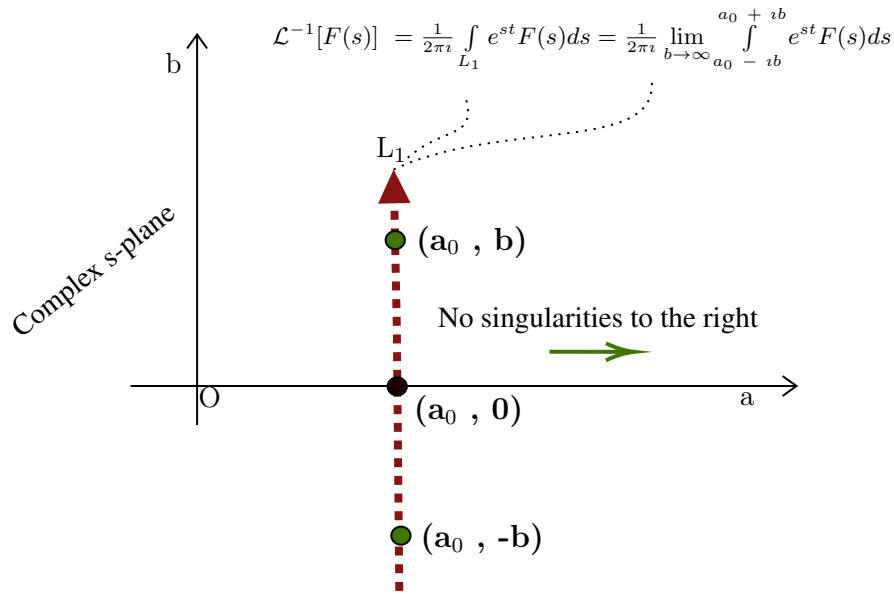


Figure A.1: The scheme of integration of an inverse Laplace transform along the vertical contour line L_1 which has all its singularities strictly to the left of it.

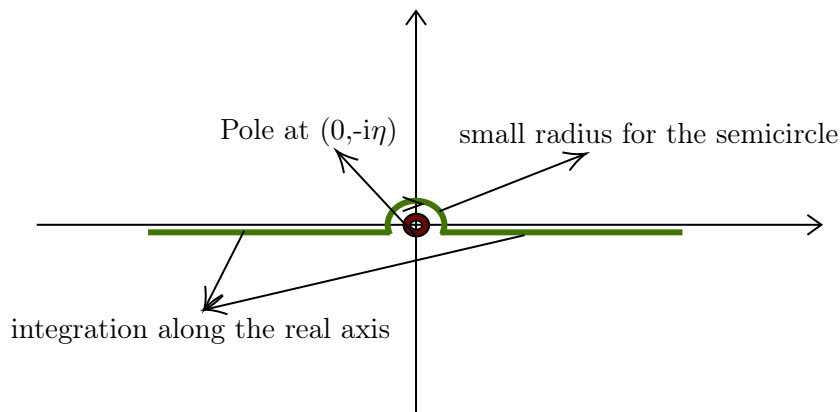


Figure A.2: Integration scheme for pole-approximation.

Let the approach start by taking an object of the form $\frac{f(x)}{x}$ with real x . As one integrates this object through the singularity (here $x = 0$), the function blows up the integral value i.e., it is undefined except when $f(x) = 0$. One of the ways to cope with this is to convert the x into a complex number $x + i\eta$ and then let imaginary part $\eta \rightarrow +0$ (η is always positive and this limit implies that it is taken from the right side of 0). It implies that the pole is below the real axis ($x = -i\eta$).

$$\lim_{\eta \rightarrow +0} \int \frac{f(x)}{x + i\eta} dx \quad (\text{A.4})$$

In Fig. A.2 the way of performing this integration is depicted. It has two parts:

1. First, integration along the real axis escaping the pole symmetrically around the origin. This is achieved by taking Cauchy's principal value of the integral

$$\mathcal{P} \int_{-a}^b dx \frac{f(x)}{x} = \int_{-a}^{-\eta} dx \frac{f(x)}{x} + \int_{\eta}^b dx \frac{f(x)}{x} \quad (\text{A.5})$$

2. Second, the semicircular curve above the pole. When one takes its radius to be super small (this is valid because, the contour shape can be deformed without affecting the integral value as long as one does not hit a pole), the value of $f(x)$ can be assumed to be constant $f(0)$ i.e., the value taken at the pole. This is where the assumption that the $f(x)$ is smoothly and slowly varying function of the variable, around the pole, is imposed. In the main text this relates to the matrix elements being smooth and slowly varying functions of the continuum energies. With this assumption, it can be seen that the integration around the semicircular contour is half of that of a circular contour. A circular contour integration (clockwise) gives $\oint \frac{1}{x} dx = -2\pi i$ [83]. Therefore, along the semicircular path as depicted in Fig. A.2, one obtains a value of $\oint_{\text{semicircle}} \frac{f(0)}{x} dx = -i\pi f(0)$. Using δ -function, one can write this in terms of $f(x)$ as

$$-i\pi f(0) = - \int_{-\eta}^{\eta} i\pi \delta(x) f(x) dx \quad (\text{A.6})$$

Note that in the Eq. (4.29), the delta function's argument is $E'_g - E_c$. But in the above simple treatment, pole of x is at 0. In the Eq. (4.29), the pole is at $E_c = E'_g$ and therefore, the delta function obtains the said argument. This will be clearer if the above LHS is understood as $-i\pi f(x = \text{pole})$.

Therefore, the total integration that involves the pole can be now obtained by clubbing Eq. (A.5) and Eq. (A.6). Thus one obtains the desired identity

$$\lim_{\eta \rightarrow +0} \int dx \frac{f(x)}{x + i\eta} = \underbrace{\int_{-a}^{-\eta} dx \frac{f(x)}{x} + \int_{\eta}^b dx \frac{f(x)}{x}}_{\mathcal{P}} - i\pi \int_{-\eta}^{\eta} dx \delta(x) f(x) \quad (\text{A.7})$$

One can ignore to depict the limits of integration with the relevant understanding of the direction of integration and thus one obtains the identity form as given by Eq. (A.3)

Appendix B

Moments and cumulants

B.1 Overview

Let $x(t)$ be a random process dependent on random times t_i , for $i = 1$ to n . Then, an n^{th} order multitime moment is a kind of averaging defined by the following expression

$$M_n(t_1, t_2 \cdots, t_n) \equiv \langle x(t_1)x(t_2) \cdots x(t_n) \rangle = \int dx_1 dx_2 \cdots dx_n p_n(x_1, x_2 \cdots x_n) x_1 x_2 \cdots x_n \quad (\text{B.1})$$

where $p_n(x_1, x_2, \cdots, x_n)$ is the n -th order joint *probability density distribution* of the $X(t)$ random process and $x_i = x(t_i)$. Very frequently the physical conditions allows the description in terms of an important class of stochastic processes which require the knowledge of only the first and second moments, $\langle x(t_1) \rangle$ and $\langle x(t_1)x(t_2) \rangle$, i.e., the mean and the auto-correlation (AC) functions respectively (for radiation field these are known as statistical 1st- and 2nd- coherence functions). In such cases the process obeys, *Gaussian* statistics.

If $x(t)$ obeys Gaussian statistics the higher order moments factorize into the products of the first two moments: the mean and the AC function. However, despite this reduction in terms of the lowest two moments, the higher-order moments may still strongly contribute in the system's EOMs. It is here, the multitime cumulant averages (or semi-invariants) enter as an alternative statistical machinery [85]. Cumulants are a particular combination of moments with special properties,

$$C_n(t_1, t_2 \cdots, t_n) \equiv \langle x(t_1)x(t_2) \cdots x(t_n) \rangle_c \quad (\text{B.2})$$

The cumulants exhibit what is called a ‘cluster’ behaviour in contrast to a ‘factorization’ property of moments for Gaussian processes [Eq. (C.10)]. Due to this, all cumulants beyond the second, strictly vanish for Gaussian processes whereas for non-Gaussian ones they successively decrease. So, the cumulants have the appropriate behaviour to serve a twofold role: first, as successive terms of a perturbative expansion and second, as a robust measure of the non-Gaussianity of the random field; any cumulant average of higher-order beyond the second is exclusively due to the non-Gaussian statistical properties of the process.

B.2 Moments and cumulants relation:

Let X be the random variable for which moments $M_n \forall n = 1, 2, 3, \dots$ are defined. There exist moment generating function, for some dummy variable λ , defined via the following relation:

$$M(\lambda) = \langle e^{\lambda X} \rangle = \sum_r M_r \frac{\lambda^r}{r!} \quad (\text{B.3})$$

which when derived n-times, at origin, gives nth moment. Cumulant generating function is defined as a natural logarithm of the moment generating function i.e.,

$$C(\lambda) = \ln(M(\lambda)) = \sum_r C_r \frac{\lambda^r}{r!} \quad (\text{B.4})$$

from which cumulants C_n can be extracted by looking at RHS. Explicitly expanding the RHS,

$$C(\lambda) = C_0 + \lambda C_1 + \frac{1}{2!} \lambda^2 C_2 + \frac{1}{3!} \lambda^3 C_3 + \dots \quad (\text{B.5})$$

But Eq. (B.4) suggest that $M(\lambda) = e^{C(\lambda)}$ inserting the above expansion here, one obtains

$$e^{C(\lambda)} = 1 + C(\lambda) + \frac{1}{2!} C^2(\lambda) + \frac{1}{3!} C^3(\lambda) + \dots \quad (\text{B.6})$$

$$\begin{aligned} &= 1 + \left[C_0 + \lambda C_1 + \frac{1}{2} \lambda^2 C_2 + \dots \right] + \frac{1}{2} \left[C_0 + \lambda C_1 + \frac{1}{2!} \lambda^2 C_2 + \dots \right]^2 \\ &+ \frac{1}{3!} \left[C_0 + \lambda C_1 + \frac{1}{2!} \lambda^2 C_2 + \dots \right]^3 + \dots \end{aligned} \quad (\text{B.7})$$

$$\begin{aligned} \Rightarrow e^{C(\lambda)} &= 1 + C_0 + \lambda [C_1] + \lambda^2 \left[\frac{1}{2} C_1^2 + \frac{1}{2} C_2 \right] \\ &+ \lambda^3 \left[\frac{1}{3!} C_3 + \frac{1}{3!} C_1^3 + \frac{1}{2!} (C_1 C_2 + C_2 C_1) \right] + \dots \end{aligned} \quad (\text{B.8})$$

But Eq. (B.8) is same as Eq. (B.3). Therefore, one has

$$\begin{aligned} \sum_r M_r \frac{\lambda^r}{r!} &= M_0 + \lambda M_1 + \frac{1}{2!} \lambda^2 M_2 + \frac{1}{3!} \lambda^3 M_3 + \dots \\ &= 1 + C_0 \lambda [C_1] + \lambda^2 \left[\frac{1}{2} C_1^2 + \frac{1}{2} C_2 \right] \\ &+ \lambda^3 \left[\frac{1}{3!} C_3 + \frac{1}{3!} C_1^3 + \frac{1}{2!} (C_1 C_2 + C_2 C_1) \right] + \dots \end{aligned} \quad (\text{B.9})$$

Comparing Eq. (B.9) and Eq. (B.10a) and extracting the terms having same powers of λ , one obtains the following

$$M_0 = 1 + C_0 \implies C_0 = 0 \quad (\text{B.10a})$$

$$M_1 = C_1 \implies C_1 = M_1 \quad (\text{B.10b})$$

$$M_2 = C_2 + C_1^2 \implies C_2 = M_2 - M_1^2 \quad (\text{B.10c})$$

$$M_3 = C_3 + C_1^3 + \frac{3}{2}(C_1 C_2 + C_2 C_1) \implies C_3 = M_3 - \frac{3}{2}(M_2 M_1 + M_1 M_2) + M_1^3 \quad (\text{B.10d})$$

\vdots

Note that from Eq. (B.3) one has $M_0 = \langle 1 \rangle = 1$ and that is why $C_0 = 0$ in the above equations. So, this gave a brief overview as to how moments and cumulants are generated and related.

B.3 Zero mean - Gaussian case

In relevance to the main text, consider a zero mean value, $\langle x(t) \rangle = 0$. In this situation, the cumulants simplify considerably. For simplicity, assuming $x(t)$ as a scalar random process and using a compact notation for the moments and the cumulants, $M_{ijk..n} = M_n(t_i, t_j, \dots, t_n)$ and $C_{ijk..n} = C_n(t_i, t_j, \dots, t_n)$, respectively, one has:

$$\begin{aligned} C_1 &= 0, & C_{12} &= M_{12}, & C_{123} &= M_{123}, \\ C_{1234} &= M_{1234} - M_{12}M_{34} - M_{13}M_{24} - M_{14}M_{23}. \end{aligned} \quad (\text{B.11})$$

If, in addition, the $x(t)$ has Gaussian probability distribution all the odd moments vanish ($C_{123} = 0$) while the even ones factorize in terms of the second moments (M_{ij}). For the fourth moment,

$$M_{1234} = M_{12}M_{34} + M_{13}M_{24} + M_{14}M_{23},$$

with the immediate result $C_{1234} = 0$. Therefore for scalar Gaussian processes one is left with the cumulants $C_1 = 0$ and $C_{12} = M_{12}$. The higher cumulants vanish whereas the higher moments are expressed in terms of the second moment M_{ij} , but do not vanish.

Appendix C

Cumulant-expansion terms

In this appendix the first four expansion terms of the averaged equation Eq. (7.33) are obtained by explicit calculation of the $\dot{K}(t)$ operator in Eq. (7.31). Consider the average evolution operator, $\tilde{U}(t)$ of Eq. (7.24):

$$\langle \tilde{U}(t) \rangle = \mathbb{1} + \sum_{n=1} U_n(t) \quad (\text{C.1})$$

with the $U_n(t)$ terms defined in Eq. (7.26b). The time-derivative of $U_n(t)$ is given by:

$$\dot{U}_n(t) = \int_{t_i}^t dt_1 \int_{t_i}^{t_1} dt_2 \dots \int_{t_i}^{t_{n-2}} dt_{n-1} M_n(t, t_1, \dots, t_{n-1}). \quad (\text{C.2})$$

with $M_n(t_1, \dots, t_n)$ given in Eq. (B.1). The integral limits are such that the chronological ordering $t > t_1 > t_2 > \dots > t_n > t_i$ is maintained. For non-commutative matrices, the chosen evaluation order in the integral matters and was taken into consideration by introducing the proper Dyson chronological operator in the time derivative of $K(t)$:

$$\begin{aligned} \dot{K}(t) &= \hat{T} \left[\frac{\langle \dot{\tilde{U}}(t) \rangle}{\langle \tilde{U}(t) \rangle} \right] = \hat{T} \left[\frac{\sum_n \dot{U}_n}{\mathbb{1} + \sum_n U_n} \right] \\ &= \hat{T} \left[\left(\sum_n \dot{U}_n \right) \left(\mathbb{1} - \sum_n U_n + \left(\sum_n U_n \right)^2 - \dots \right) \right]. \end{aligned}$$

In the second line of the last equation a Neumann expansion of the denominator was performed. This is a legitimate expansion, provided that $|\sum_n U_n| < 1$; an assumption which should hold if the elements U_n are to be used to make up an evolution operator. Expanding the terms of the last line inside the \hat{T} bracket and gathering together those of

the same order one has (up to 4th power are shown below) :

$$\begin{aligned}
& (\dot{U}_1 + \dot{U}_2 + \dots)(\mathbb{1} - U_1 - U_2 - \dots + U_1^2 + U_2^2 + \dots) \\
&= \dot{U}_1 + \dot{U}_2 + \dot{U}_3 + \dot{U}_4 - \dot{U}_1 U_1 - \dot{U}_1 U_2 - \dot{U}_1 U_3 \\
&\quad - \dot{U}_2 U_1 - \dot{U}_2 U_2 \dots - \dot{U}_3 U_1 - \dots \\
&\quad + \dot{U}_1 U_1^2 + \dot{U}_1 U_1 U_2 + \dot{U}_1 U_2 U_1 + \dots \\
&= \dot{U}_1 + (\dot{U}_2 - \dot{U}_1 U_1) + (\dot{U}_3 - \dot{U}_1 U_2 - \dot{U}_2 U_1 + \dot{U}_1 U_1^2) \\
&\quad + (\dot{U}_4 - \dot{U}_2 U_2 - \dot{U}_1 U_3 - \dot{U}_3 U_1 + \dot{U}_1 U_1 U_2 + \dot{U}_1 U_2 U_1) \\
&\quad + \dots + O(U^5)
\end{aligned}$$

One may now write compactly, $\dot{K}(t) = \sum_{n=1}^{\infty} \dot{\kappa}_n(t)$ with,

$$\dot{\kappa}_1(t) = \hat{T} [\dot{U}_1] = 0 \quad (\text{C.3})$$

$$\begin{aligned}
\dot{\kappa}_2(t) &= \hat{T} [\dot{U}_2 - \dot{U}_1 U_1] = \hat{T} [\dot{U}_2] \\
&= \int_{t_i}^t dt_1 M_2(t, t_1) \quad (\text{C.4})
\end{aligned}$$

$$\begin{aligned}
\dot{\kappa}_3(t) &= \hat{T} [\dot{U}_3 - \dot{U}_1 U_2 - \dot{U}_2 U_1 + \dot{U}_1 U_1^2] = \hat{T} [\dot{U}_3] \\
&= \int_{t_i}^t dt_1 \int_{t_i}^{t_1} dt_2 M_3(t, t_1, t_2), \quad (\text{C.5})
\end{aligned}$$

It is to be noted that due to the special choice of $\langle \tilde{L}(t) \rangle = 0$, one has $U_1 = \dot{U}_1 = 0$. In addition the chronological operator is not explicitly required as the integral limits take care of this aspect. For the $\dot{\kappa}_4(t)$ term some further algebra may be required though:

$$\begin{aligned}
\dot{\kappa}_4(t) &= \hat{T} [\dot{U}_4 - \dot{U}_2 U_2] \quad (\text{C.6}) \\
&= \hat{T} \left[\int_{t_i}^t dt_1 \int_{t_i}^{t_1} dt_2 \int_{t_i}^{t_2} dt_3 M_4(t, t_1, t_2, t_3) \right] \\
&\quad - \hat{T} \left[\int_{t_i}^t dt_1 M_2(t, t_1) \int_{t_i}^t dt_2 \int_{t_i}^{t_2} dt_3 M_2(t_2, t_3) \right] \\
&= \int_{t_i}^t dt_1 \int_{t_i}^{t_1} dt_2 \int_{t_i}^{t_2} dt_3 M_4(t, t_1, t_2, t_3) \\
&\quad - \hat{T} \left[\int_{t_i}^t dt_1 \int_{t_i}^t dt_2 \int_{t_i}^{t_2} dt_3 M_2(t, t_1) M_2(t_2, t_3) \right]
\end{aligned}$$

It is not evident to remove the \hat{T} operator from the last line as the integral limits do not coincide with the needed time-ordering $t > t_1 > t_2 > t_3 > t_i$. Some transformations are required to arrive at a triple-integral with the proper limits. To this end one can make use of the following identity:

$$\int_b^a dx \int_x^a dy f(x, y) = \int_b^a dx \int_b^x dy f(y, x). \quad (\text{C.7})$$

Adopting temporarily the notation, $M_2(t_i, t_j) = M_{ij}$ and dropping the \hat{T} operator each time that conforms with the integral limits, for the last line of Eq. (C.6), one has

$$\begin{aligned}
& \hat{T} \left[\int_{t_i}^t dt_1 \int_{t_i}^{t_1} dt_2 \int_{t_i}^{t_2} dt_3 M_{01} M_{23} \right] + \hat{T} \left[\int_{t_i}^t dt_1 \int_{t_1}^t dt_2 \int_{t_i}^{t_2} dt_3 M_{01} M_{23} \right] \\
&= \int_{t_i}^t dt_1 \int_{t_i}^{t_1} dt_2 \int_{t_i}^{t_2} dt_3 M_{01} M_{23} + \hat{T} \left[\int_{t_i}^t dt_1 \int_{t_1}^t dt_2 \int_{t_i}^{t_1} dt_3 M_{01} M_{23} \right] \\
&\quad + \hat{T} \left[\int_{t_i}^t dt_1 \int_{t_1}^t dt_2 \int_{t_1}^{t_2} dt_3 M_{01} M_{23} \right] \\
&= \int_{t_i}^t dt_1 \int_{t_i}^{t_1} dt_2 \int_{t_i}^{t_2} dt_3 M_{01} M_{23} + \int_{t_i}^t dt_1 \int_{t_i}^{t_1} dt_2 \int_{t_i}^{t_2} dt_3 M_{02} M_{13} \\
&\quad + \hat{T} \left[\int_{t_i}^t dt_1 \int_{t_i}^{t_1} dt_2 \int_{t_2}^{t_1} dt_3 M_{02} M_{13} \right] \\
&= \int_{t_i}^t dt_1 \int_{t_i}^{t_1} dt_2 \int_{t_i}^{t_2} dt_3 M_{01} M_{23} + \int_{t_i}^t dt_1 \int_{t_i}^{t_1} dt_2 \int_{t_i}^{t_2} dt_3 M_{01} M_{23} \\
&\quad + \int_{t_i}^t dt_1 \int_{t_i}^{t_1} dt_2 \int_{t_1}^{t_2} dt_3 M_{03} M_{12},
\end{aligned}$$

Now replacing the integral of Eq. (C.6) one can arrive at the final expression:

$$\dot{\kappa}_4(t) = \int_{t_i}^t dt_1 \int_{t_i}^{t_1} dt_2 \int_{t_i}^{t_2} dt_3 [M_4(t, t_1, t_2, t_3) - M_2(t, t_1)M_2(t_2, t_3) \quad (C.8)$$

$$- M_2(t, t_2)M_2(t_1, t_3) - M_2(t, t_3)M_2(t_1, t_2)] \quad (C.9)$$

Note that for stochastic fields with Gaussian statistics and in the case of commutative matrices, one has $\dot{\kappa}_3 = \dot{\kappa}_4 = 0$ if the properties of the non-vanishing multitime moments [114] are considered:

$$M_{ijkl\dots mn} = \sum M_{i'j'} M_{k'l'} \cdots M_{m'n'}, \quad n \text{ even} \quad (C.10)$$

where $(i', j'), (k', l'), \dots, (m', n')$ pairs are all possible combinations of the indices $(i, j, k, l, \dots, m, n)$.

One may continue towards the higher-order cumulant expressions along similar lines if needed. Alternative methods for their calculations in terms of the moments may also be found in the original literature [85, 114].

Appendix D

Derivation of $S_{1t}(\delta)$ and $S_{2t}(0)$

D.1 Gaussian AC

The complex field envelope of the FEL considered as Gaussian, is of the form

$$\mathcal{E}(t) = \mathcal{E}_0(t)\epsilon(t)$$

where the deterministic envelope is of the form

$$\mathcal{E}_0(t) = \mathcal{E}_0 e^{-\frac{\chi t^2}{2\tau_p^2}}$$

where $\chi = 1 - ik$ and $k = \frac{1}{\sqrt{3}}$. The random fluctuations of the FEL are gathered into $\epsilon(t)$ whose autocorrelation is given by

$$\langle \epsilon(t)\epsilon^*(t - \tau) \rangle = e^{-\frac{\tau^2}{2\tau_c^2}}$$

Using these, one can now proceed to calculate the required integrals.

D.1.1 Closed form expression of $S_{1t}(\delta)$ - Gaussian AC

The above expressions for the FEL field are inserted into the integral of S_{1t} to obtain,

$$\begin{aligned}
S_{1t}(\delta) &= \int_0^\infty \langle \mathcal{E}(t) \mathcal{E}^*(t-\tau) \rangle e^{-\delta\tau} d\tau \\
&= \int_0^\infty \mathcal{E}_0(t) \mathcal{E}_0^*(t-\tau) \langle \epsilon(t) \epsilon^*(t-\tau) \rangle e^{-\delta\tau} d\tau \\
&= \int_0^\infty \mathcal{E}_0 e^{-\frac{\chi t^2}{2\tau_p^2}} \mathcal{E}_0 e^{-\frac{\chi^*(t-\tau)^2}{2\tau_p^2}} e^{-\frac{\tau^2}{2\tau_c^2}} e^{-\delta\tau} d\tau \\
&= \mathcal{E}_0^2 \int_0^\infty e^{-\frac{\chi t^2}{2\tau_p^2}} e^{-\frac{\chi^*(t^2+\tau^2-2t\tau)}{2\tau_p^2}} e^{-\frac{\tau^2}{2\tau_c^2}} e^{-\delta\tau} d\tau \\
&= \underbrace{\mathcal{E}_0^2 e^{-t^2/\tau_p^2}} \int_0^\infty e^{-\frac{\chi^*(\tau^2-2t\tau)}{2\tau_p^2}} e^{-\frac{\tau^2}{2\tau_c^2}} e^{-\delta\tau} d\tau \\
&= \langle \mathcal{I}(t) \rangle \underbrace{\int_0^\infty e^{-a\tau^2+b\tau} d\tau}
\end{aligned}$$

where $a = \frac{\chi^*}{2\tau_p^2} + \frac{1}{2\tau_c^2}$ and $b = -\delta + \frac{\chi^*t}{\tau_p^2}$. The under-braced expression is well known and is given by

$$\int_0^\infty e^{-a\tau^2+b\tau} d\tau = \underbrace{\frac{\sqrt{\pi}}{2\sqrt{a}}}_{(i)} \underbrace{e^{\frac{b^2}{4a}}}_{(ii)} \underbrace{\left(1 + \operatorname{erf}\left(\frac{b}{2\sqrt{a}}\right)\right)}_{(iii)}$$

There are three parts in this integral. One by one, they are evaluated in the following. Before that, two new variables are defined for simplicity.

$$M = \frac{\tau_p}{\tau_{coh}} \quad ; \quad \tau_{coh} = \frac{\tau_p \tau_c}{\sqrt{\tau_p^2 + \tau_c^2}} \quad \lambda = \frac{1}{\sqrt{2\frac{ik}{M^2} + 1}}$$

(i)

$$\begin{aligned}
\frac{\sqrt{\pi}}{2\sqrt{a}} &= \frac{\sqrt{\pi}}{2\sqrt{\frac{\chi^*}{2\tau_p^2} + \frac{1}{2\tau_c^2}}} = \frac{\sqrt{\pi}\tau_p}{\sqrt{2}\sqrt{\chi^* + \frac{\tau_p^2}{\tau_c^2}}} \\
&= \frac{\sqrt{\pi}\tau_p}{\sqrt{2}\sqrt{ik + 1 + \underbrace{\frac{\tau_p^2}{\tau_c^2}}_{M^2}}} = \frac{\sqrt{\pi}\tau_p}{\sqrt{2}\sqrt{ik + M^2}} = \sqrt{\pi} \underbrace{\left(\frac{\tau_p}{M}\right)^{\tau_{coh}}}_{\tau_{coh}} \underbrace{\left(\frac{1}{\sqrt{2(\frac{ik}{M^2} + 1)}}\right)}_{\lambda} \\
\Rightarrow \boxed{\frac{\sqrt{\pi}}{2\sqrt{a}} = \sqrt{\pi}\tau_{coh}\lambda}
\end{aligned}$$

(ii) Let the argument of the exponential $b^2/4a$ be evaluated as

$$\begin{aligned}
\frac{b^2}{4a} &= \left(\frac{\chi^* t}{\tau_p^2} - \delta \right)^2 \frac{1}{4 \left(\frac{\chi^*}{2\tau_p^2} + \frac{1}{2\tau_c^2} \right)} = \left(\frac{\chi^* t}{\tau_p^2} - \delta \right)^2 \frac{\tau_p^2}{2 \left(\chi^* + \frac{\tau_p^2}{\tau_c^2} \right)} \\
&= \left(\frac{\chi^* t}{\tau_p} - \delta \tau_p \right)^2 \frac{1}{2 \left(ik + 1 + \frac{\tau_p^2}{\tau_c^2} \right)} = \left(\frac{\chi^* t}{\tau_p} - \delta \tau_p \right)^2 \frac{1}{2(ik + M^2)} \\
&= \left(\frac{\chi^* t}{M\tau_p} - \delta \frac{\tau_p}{M} \right)^2 \underbrace{\left(\frac{1}{2 \left(\frac{ik}{M^2} + 1 \right)} \right)}_{\lambda^2} \\
\Rightarrow \frac{b^2}{4a} &= \lambda^2 \left(\frac{\chi^* t}{M\tau_p} - \delta \tau_{coh} \right)^2
\end{aligned}$$

(iii) It turns out that the magnitude of argument of $\text{erf}\left(\frac{b}{2\sqrt{a}}\right)$ is nothing but the magnitude of the square root of the above term. Therefore one obtains

$$\boxed{\text{erf}\left(\frac{b}{2\sqrt{a}}\right) = \text{erf}\left(\lambda \left(\frac{\chi^* t}{M\tau_p} - \delta \tau_{coh} \right)\right)}$$

Combining the results from the three boxed parts, one obtains

$$S_{1t}(\delta) = \langle \mathcal{I}(t) \rangle \sqrt{\pi} \tau_{coh} \lambda \underbrace{e^{\lambda^2 \left(\frac{\chi^* t}{M\tau_p} - \delta \tau_{coh} \right)^2} \left[1 + \text{erf}\left(\lambda \left(\frac{\chi^* t}{M\tau_p} - \delta \tau_{coh} \right)\right)\right]}_{w(z)}$$

Assigning the variable $z = \lambda \left(\frac{\chi^* t}{M\tau_p} - \delta \tau_{coh} \right)$ and using the function $w(z) = e^{z^2} (1 + \text{erf}(z))$, one can turn the above expression into

$$\boxed{S_{1t}(\delta) = \tau_{coh} \sqrt{\pi} \langle \mathcal{I}(t) \rangle \lambda w\left(\lambda \left(\frac{\chi^* t}{M\tau_p} - \delta \tau_{coh} \right)\right)} \quad (\text{D.1})$$

D.1.2 Closed form expression of $S_{2t}(0)$ - Gaussian AC

This is relatively simple due to $\delta = 0$ in the integral.

$$\begin{aligned}
S_{2t}(0) &= \int_0^\infty \overbrace{\langle \mathcal{I}(t)\mathcal{I}(t-\tau) \rangle - \langle \mathcal{I}(t) \rangle \langle \mathcal{I}(t-\tau) \rangle}^{\text{for Gaussian random processes} = |\langle \mathcal{E}(t)\mathcal{E}^*(t-\tau) \rangle|^2} d\tau \\
&= \int_0^\infty |\langle \mathcal{E}(t)\mathcal{E}^*(t-\tau) \rangle|^2 d\tau \\
&= \int_0^\infty |\mathcal{E}_0(t)\mathcal{E}_0^*(t-\tau)\langle \epsilon(t)\epsilon^*(t-\tau) \rangle|^2 d\tau \\
&= \int_0^\infty |\mathcal{E}_0 e^{-\frac{\chi t^2}{2\tau_p^2}} \mathcal{E}_0 e^{-\frac{\chi^*(t-\tau)^2}{2\tau_p^2}} e^{-\frac{\tau^2}{2\tau_c^2}}|^2 d\tau \\
&= \int_0^\infty \mathcal{E}_0^4 e^{-\frac{t^2}{\tau_p^2}} e^{-\frac{(t-\tau)^2}{\tau_p^2}} e^{-\frac{\tau^2}{\tau_c^2}} d\tau \\
&= \int_0^\infty \mathcal{E}_0^4 e^{-\frac{t^2}{\tau_p^2}} e^{-\frac{(t^2+\tau^2-2t\tau)}{\tau_p^2}} e^{-\frac{\tau^2}{\tau_c^2}} d\tau \\
&= \int_0^\infty \underbrace{\mathcal{E}_0^4 e^{-\frac{2t^2}{\tau_p^2}}}_{\langle \mathcal{I}(t) \rangle^2} e^{-\frac{(\tau^2-2t\tau)}{\tau_p^2}} e^{-\frac{\tau^2}{\tau_c^2}} d\tau \\
&= \langle \mathcal{I}(t) \rangle^2 \int_0^\infty e^{-\tau^2 \left(\frac{1}{\tau_p^2} + \frac{1}{\tau_c^2} \right)} e^{\tau \frac{2t}{\tau_p^2}} d\tau \\
&= \langle \mathcal{I}(t) \rangle^2 \int_0^\infty e^{-p\tau^2 + q\tau} d\tau
\end{aligned}$$

where $p = \left(\frac{1}{\tau_p^2} + \frac{1}{\tau_c^2} \right)$ and $q = \frac{2t}{\tau_p^2}$. Using the already explored integral form, i.e.,

$$\int_0^\infty e^{-p\tau^2 + q\tau} d\tau = \underbrace{\frac{\sqrt{\pi}}{2\sqrt{p}}}_{(iv)} \overbrace{e^{\frac{q^2}{4p}}}_{(v)} \underbrace{\left(1 + \operatorname{erf}\left(\frac{q}{2\sqrt{p}}\right) \right)}_{(vi)}$$

one obtains the following.

(iv)

$$\begin{aligned}
\frac{\sqrt{\pi}}{2\sqrt{p}} &= \frac{\sqrt{\pi}}{2\sqrt{\left(\frac{1}{\tau_p^2} + \frac{1}{\tau_c^2}\right)}} = \frac{\sqrt{\pi}}{2} \overbrace{\left(\frac{\tau_p \tau_c}{\sqrt{\tau_p^2 + \tau_c^2}} \right)}^{\tau_{coh}} \\
\implies \boxed{\frac{\sqrt{\pi}}{2\sqrt{p}} = \tau_{coh} \frac{\sqrt{\pi}}{2}}
\end{aligned}$$

(v) The argument of the exponential $q^2/4p$ is given by

$$\begin{aligned}
\frac{q^2}{4p} &= \left(\frac{2t}{\tau_p^2}\right)^2 \frac{1}{\left(\frac{1}{\tau_p^2} + \frac{1}{\tau_c^2}\right)} \frac{1}{4} = \left(\frac{At^2}{\tau_p^4}\right) \overbrace{\left(\frac{\tau_p^2 \tau_c^2}{(\tau_p^2 + \tau_c^2)}\right)}^{\tau_{coh}^2} \frac{1}{A} \\
&= \left(\frac{t^2}{\tau_p^2}\right) \underbrace{\frac{\tau_{coh}^2}{\tau_p^2}}_{\frac{1}{M^2}} = \left(\frac{t^2}{\tau_p^2}\right) \frac{1}{M^2} \\
\Rightarrow \boxed{\frac{q^2}{4p} = \left(\frac{t^2}{M^2 \tau_p^2}\right)}
\end{aligned}$$

(vi) The argument in $\text{erf}\left(\frac{q}{2\sqrt{p}}\right)$ is nothing but the square root of the above term, i.e.,

$$\boxed{\text{erf}\left(\frac{q}{2\sqrt{p}}\right) = \text{erf}\left(\frac{t}{M\tau_p}\right)}$$

Combining the results from the three boxed parts, one obtains

$$S_{2t}(0) = \langle \mathcal{I}(t) \rangle^2 \tau_{coh} \frac{\sqrt{\pi}}{2} e^{\frac{t^2}{M^2 \tau_p^2}} \left(1 + \text{erf}\left(\frac{t}{M\tau_p}\right)\right)$$

Assigning the variable $z = \frac{t}{M\tau_p}$ and using the function $w(z) = e^{z^2}(1 + \text{erf}(z))$, one can turn the above expression into

$$\boxed{S_{2t}(0) = \tau_{coh} \sqrt{\pi} \frac{\langle \mathcal{I}(t) \rangle^2}{2} w\left(\frac{t}{M\tau_p}\right)} \quad (\text{D.2})$$

D.2 Lorentzian AC

The field envelope remains the same but the AC form is changed here.

$$\langle \epsilon(t) \epsilon^*(t - \tau) \rangle = e^{-\frac{|\tau|}{2\tau_c}}$$

Using this and the fact that no chirp is included in the main text i.e., $\chi = 1$, one can now proceed to calculate the required integrals.

D.2.1 Closed form expression of $S_{1t}(\delta)$ - Lorentzian AC

The above expressions for the FEL field are inserted into the integral of S_{1t} to obtain,

$$\begin{aligned}
S_{1t}(\delta) &= \int_0^\infty \langle \mathcal{E}(t) \mathcal{E}^*(t-\tau) \rangle e^{-\delta\tau} d\tau \\
&= \int_0^\infty \mathcal{E}_0(t) \mathcal{E}_0^*(t-\tau) \langle \epsilon(t) \epsilon^*(t-\tau) \rangle e^{-\delta\tau} d\tau \\
&= \int_0^\infty \mathcal{E}_0 e^{-\frac{t^2}{2\tau_p^2}} \mathcal{E}_0 e^{-\frac{(t-\tau)^2}{2\tau_p^2}} e^{-\frac{|\tau|}{\tau_c}} e^{-\delta\tau} d\tau \\
&= \mathcal{E}_0^2 \int_0^\infty e^{-\frac{t^2}{2\tau_p^2}} e^{-\frac{(t^2+\tau^2-2t\tau)}{2\tau_p^2}} e^{-\frac{\tau}{\tau_c}} e^{-\delta\tau} d\tau \\
&= \underbrace{\mathcal{E}_0^2 e^{-t^2/\tau_p^2}}_{(i)} \int_0^\infty e^{-\frac{(\tau^2-2t\tau)}{2\tau_p^2}} e^{-\frac{\tau}{\tau_c}} e^{-\delta\tau} d\tau \\
&= \langle \mathcal{I}(t) \rangle \underbrace{\int_0^\infty e^{-a\tau^2+b\tau} d\tau}_{(ii)}
\end{aligned}$$

where $a = \frac{1}{2\tau_p^2}$ and $b = -\delta - \frac{1}{2\tau_c} + \frac{t}{\tau_p}$. Defining a new term for simplifying the coming expressions,

$$\tau_\delta = \frac{t}{\tau_p} - \left(\frac{1}{2\tau_c} + \delta\right)\tau_p$$

the under-braced expression, already given above, can be evaluated as

$$\int_0^\infty e^{-a\tau^2+b\tau} d\tau = \underbrace{\frac{\sqrt{\pi}}{2\sqrt{a}}}_{(i)} \underbrace{e^{\frac{b^2}{4a}}}_{(ii)} \underbrace{\left(1 + \operatorname{erf}\left(\frac{b}{2\sqrt{a}}\right)\right)}_{(iii)}$$

(i)

$$\begin{aligned}
\frac{\sqrt{\pi}}{2\sqrt{a}} &= \frac{\sqrt{\pi}}{2\sqrt{\frac{1}{2\tau_p^2}}} = \frac{\sqrt{\pi}\tau_p}{\sqrt{2}} \\
\Rightarrow \boxed{\frac{\sqrt{\pi}}{2\sqrt{a}} = \frac{\sqrt{\pi}\tau_p}{\sqrt{2}}}
\end{aligned}$$

(ii) Let the argument of the exponential $b^2/4a$ be evaluated as

$$\begin{aligned}
\frac{b^2}{4a} &= \frac{\left(\delta + \frac{1}{2\tau_c} - \frac{t}{\tau_p}\right)^2}{4\left(\frac{1}{2\tau_p^2}\right)} = \tau_p^2 \frac{\left(\delta + \frac{1}{2\tau_c} - \frac{t}{\tau_p}\right)^2}{2} \\
&= \frac{\left(\delta\tau_p + \frac{\tau_p}{2\tau_c} - \frac{\tau_p t}{\tau_p}\right)^2}{2} = \left(\frac{\tau_\delta}{\sqrt{2}}\right)^2 \\
\Rightarrow \boxed{\frac{b^2}{4a} = \left(\frac{\tau_\delta}{\sqrt{2}}\right)^2}
\end{aligned}$$

(iii) Noticing that $\tau_\delta = \frac{t}{\tau_p} - (\frac{1}{2\tau_c} + \delta)\tau_p$ and $b = \delta + \frac{1}{2\tau_c} - \frac{t}{\tau_p}$ one obtains

$$\boxed{\operatorname{erf}\left(\frac{b}{2\sqrt{a}}\right) = \operatorname{erf}\left(\frac{\tau_\delta}{\sqrt{2}}\right)}$$

Combining the results from the three boxed parts, one obtains

$$S_{1t}(\delta) = \langle \mathcal{I}(t) \rangle \frac{\sqrt{\pi}\tau_p}{\sqrt{2}} \underbrace{\left(\frac{\tau_\delta}{\sqrt{2}}\right)^2 \left[1 + \operatorname{erf}\left(\frac{\tau_\delta}{\sqrt{2}}\right)\right]}_{w(z)}$$

Assigning the variable $z = \left(\frac{\tau_\delta}{\sqrt{2}}\right)$ and using the function $w(z) = e^{z^2}(1 + \operatorname{erf}(z))$, one can turn the above expression into

$$\boxed{S_{1t}(\delta) = \langle \mathcal{I}(t) \rangle \frac{\sqrt{\pi}\tau_p}{\sqrt{2}} w\left(\frac{\tau_\delta}{\sqrt{2}}\right)} \quad (\text{D.3})$$

D.2.2 Closed form expression of $S_{2t}(0)$ - Lorentzian AC

This is relatively simple due to $\delta = 0$ in the integral.

$$\begin{aligned} S_{2t}(0) &= \int_0^\infty \overbrace{\left(\langle \mathcal{I}(t)\mathcal{I}(t-\tau) \rangle - \langle \mathcal{I}(t) \rangle \langle \mathcal{I}(t-\tau) \rangle\right)}^{\text{for Gaussian random processes} = |\langle \mathcal{E}(t)\mathcal{E}^*(t-\tau) \rangle|^2} d\tau \\ &= \int_0^\infty |\langle \mathcal{E}(t)\mathcal{E}^*(t-\tau) \rangle|^2 d\tau \\ &= \int_0^\infty |\mathcal{E}_0(t)\mathcal{E}_0^*(t-\tau)\langle \epsilon(t)\epsilon^*(t-\tau) \rangle|^2 d\tau \\ &= \int_0^\infty |\mathcal{E}_0 e^{-\frac{t^2}{2\tau_p^2}} \mathcal{E}_0 e^{-\frac{(t-\tau)^2}{2\tau_p^2}} e^{-\frac{\tau}{2\tau_c}}|^2 d\tau \\ &= \int_0^\infty \mathcal{E}_0^4 e^{-\frac{t^2}{\tau_p^2}} e^{-\frac{(t-\tau)^2}{\tau_p^2}} e^{-\frac{\tau}{\tau_c}} d\tau \\ &= \int_0^\infty \mathcal{E}_0^4 e^{-\frac{t^2}{\tau_p^2}} e^{-\frac{(t^2+\tau^2-2t\tau)}{\tau_p^2}} e^{-\frac{\tau}{\tau_c}} d\tau \\ &= \int_0^\infty \underbrace{\mathcal{E}_0^4 e^{-\frac{2t^2}{\tau_p^2}}}_{\langle \mathcal{I}(t) \rangle^2} e^{-\frac{(\tau^2-2t\tau)}{\tau_p^2}} e^{-\frac{\tau}{\tau_c}} d\tau \\ &= \langle \mathcal{I}(t) \rangle^2 \int_0^\infty e^{-\frac{\tau^2}{\tau_p^2}} e^{-\tau\left(\frac{1}{\tau_c} - \frac{2t}{\tau_p^2}\right)} d\tau \\ &= \langle \mathcal{I}(t) \rangle^2 \int_0^\infty e^{-p\tau^2+q\tau} d\tau \end{aligned}$$

where $p = \frac{1}{\tau_p^2}$ and $q = -\frac{1}{\tau_c} + \frac{2t}{\tau_p^2}$. Using the already explored integral form, i.e.,

$$\int_0^\infty e^{-p\tau^2+q\tau} d\tau = \underbrace{\frac{\sqrt{\pi}}{2\sqrt{p}}}_{(iv)} \underbrace{e^{\frac{q^2}{4p}}}_{(v)} \underbrace{\left(1 + \operatorname{erf}\left(\frac{q}{2\sqrt{p}}\right)\right)}_{(vi)}$$

one obtains the following.

(iv)

$$\begin{aligned} \frac{\sqrt{\pi}}{2\sqrt{p}} &= \frac{\sqrt{\pi}}{2\sqrt{\frac{1}{\tau_p^2}}} = \frac{\tau_p\sqrt{\pi}}{2} \\ \implies \boxed{\frac{\sqrt{\pi}}{2\sqrt{p}} &= \frac{\tau_p\sqrt{\pi}}{2}} \end{aligned}$$

(v) The argument of the exponential i.e., $q^2/4p$ is given by

$$\begin{aligned} \frac{q^2}{4p} &= \left(\frac{1}{\tau_c} - \frac{2t}{\tau_p^2}\right)^2 \frac{1}{\frac{1}{\tau_p^2}} \frac{1}{4} = \left(\frac{1}{\tau_c} - \frac{2t}{\tau_p^2}\right)^2 \tau_p^2 \frac{1}{4} \\ &= \left(\frac{\tau_p}{2\tau_c} - \frac{t}{\tau_p}\right)^2 \\ \implies \boxed{\frac{q^2}{4p} &= \left(\frac{\tau_p}{2\tau_c} - \frac{t}{\tau_p}\right)^2 = \tau_0^2} \end{aligned}$$

(vi) The argument in $\operatorname{erf}\left(\frac{q}{2\sqrt{p}}\right)$ is nothing but the square root of the above term, i.e.,

$$\boxed{\operatorname{erf}\left(\frac{q}{2\sqrt{p}}\right) = \operatorname{erf}(\tau_0)}$$

Combining the results with the understanding that $\tau_0 = \tau_{\delta=0}$, from the three boxed parts, one obtains

$$S_{2t}(0) = \langle \mathcal{I}(t) \rangle^2 \frac{\tau_p\sqrt{\pi}}{2} \underbrace{e^{\tau_0^2} (1 + \operatorname{erf}(\tau_0))}_{(v)}$$

Assigning the variable $z = \tau_0$ and using the function $w(z) = e^{z^2}(1 + \operatorname{erf}(z))$, one can turn the above expression into

$$\boxed{S_{2t}(0) = \langle \mathcal{I}(t) \rangle^2 \frac{\tau_p\sqrt{\pi}}{2} w(\tau_0)} \quad (\text{D.4})$$

Appendix E

Atomic units - conversion

Some useful factors of conversion from atomic units to the other units are given below

Parameters	Description	Values (a.u.)	Value (other units)
a_0	Bohr radius	1	0.529×10^{-10} m
ω	energy	1	27.211 eV
α	fine structure constant	1/137	1/137
c	speed of light in vacuum	137	3×10^{-8} ms ⁻¹
t	time	41.34	1 fs
\hbar	reduced Planck constant	1	6.58×10^{-16} eV-s
I_0	peak intensity	1	3.509×10^{16} W/cm ²

Table E.1: Useful conversion factors relating to atomic units.